

University of Southampton Research Repository  
ePrints Soton

Copyright © and Moral Rights for this thesis are retained by the author and/or other copyright owners. A copy can be downloaded for personal non-commercial research or study, without prior permission or charge. This thesis cannot be reproduced or quoted extensively from without first obtaining permission in writing from the copyright holder/s. The content must not be changed in any way or sold commercially in any format or medium without the formal permission of the copyright holders.

When referring to this work, full bibliographic details including the author, title, awarding institution and date of the thesis must be given e.g.

AUTHOR (year of submission) "Full thesis title", University of Southampton, name of the University School or Department, PhD Thesis, pagination



Faculty of Natural and Environmental Sciences

School of Chemistry

**Probing the Early Activation Mechanism of Olefin  
Oligomerisation Catalysis using Molybdenum,  
Scandium and Chromium Halide Complexes**

By Stuart A. Bartlett

A Thesis Submitted for the Degree of Doctor of Philosophy

November 2012



UNIVERSITY OF SOUTHAMPTON

ABSTRACT

FACULTY OF NATURAL AND ENVIRONMENTAL SCIENCES  
SCHOOL OF CHEMISTRY

Doctor of Philosophy

**Probing the Early Activation Mechanism of Olefin Oligomerisation Catalysis  
using Molybdenum, Scandium and Chromium Halide Complexes**

By Stuart A. Bartlett

The efficient catalytic conversion of small molecules into more complex species by clean, energy efficient processes is of high commercial demand. The selective trimerisation and tetramerisation of ethene to produce the linear alpha-olefins (LAOs) 1-hexene and 1-octene, respectively, are of major significance due to the importance in the production of linear low-density polyethylene (LLDPE).

The activation of  $[MX_3(L)]$  ( $M = Mo, Sc, Cr; X = Cl, Br^*$ ;  $L$  = tridentate ligands with  $S_3$ ,  $N_3$ , SNS and PNP donor sets) by  $AlMe_3$ , based around the industrially important  $[CrCl_3(L)]$  catalysts for selective oligomerisation of alkenes, has been investigated by K-edge X-ray absorption (XAS), UV–Visible and NMR spectroscopies. Time-resolved stopped-flow Mo XAS with UV-Vis spectroscopy, in combination with a newly developed anaerobic freeze-quench approach, established the complete alkylation of the Mo centres and a slower, stepwise sequence for  $[MoBr_3(L)]$ . Sc K-edge XAS with  $^{45}Sc$  and  $^{27}Al$  NMR measurements revealed a possible ethene polymerisation pathway *via* a chloro bridged alumino scandium species. The novel freeze-quench approach, which can trap reaction solutions within 1 second of mixing to allow long data acquisition, was applied to the industrially important  $[CrCl_3(SNS)]$  and  $[CrCl_3(PNP)]$  complexes to yield a four coordinate  $[Cr^{II}Cl(SNS)]$  species and five coordinate  $[Cr^{II}Cl_2Me(PNP)]$  upon reaction with  $AlMe_3$ . This demonstrates the power of the freeze-quench technique in identifying new reactive and short lived intermediates within homogeneous catalysis.

\*Bromides only investigated on molybdenum.

## Table of Contents

LIST OF FIGURES.....	VII
LIST OF SCHEMES.....	XVII
LIST OF TABLES.....	XXI
LIST OF EQUATIONS .....	XXIII
DECLARATION OF AUTHORSHIP .....	XXIV
ACKNOWLEDGEMENTS .....	XXV
LIST OF ABBREVIATIONS.....	XXVI
INTRODUCTION .....	1
1.1 LINEAR ALPHA OLEFINS.....	2
1.1.1 Products .....	2
1.1.2 Industrial Production .....	3
1.1.3 Technology .....	4
1.1.4 Markets .....	4
1.2 PRINCIPLES OF CATALYSIS .....	4
1.2.1 Catalytic Pathway.....	5
1.2.2 Catalyst Types.....	6
1.3 HARD-SOFT ACID-BASE (HSAB) THEORY .....	6
1.3 TRANSITION METAL CHEMISTRY.....	7
1.3.1 Scandium .....	7
1.3.1.1 Scandium Macroyclic Compounds.....	8
1.3.1.2 Scandium Cyclopentadienyl Complexes.....	9
1.3.2 Chromium.....	9
1.3.2.1 Low valent Chromium Carbonyl Complexes.....	10
1.3.2.2 Chromium(II) Chemistry .....	11
1.3.2.3 Chromium (III) Chemistry .....	13
1.3.2.4 Chromium (IV)/(V) .....	13
1.3.2.4 Chromium(VI) Chemistry .....	15
1.3.3 Molybdenum .....	16
1.3.3.1 Low Valent Molybdenum Complexes.....	17
1.3.3.2 High Valent Molybdenum Complexes .....	17
1.3.3.3 Molybdenum Multiple bonds .....	18
1.4 ETHENE POLYMERISATION.....	19
1.4.1 Ziegler-Natta Polymerisation .....	19
1.5 ETHENE OLIGOMERISATION.....	20
1.5.1 Nickel-Catalysed Ethene Oligomerisation.....	20
1.5.2 Shell Higher Olefin Process .....	22
1.5.3 Selective Ethene Trimerisation .....	23
1.5.4 The Phillips Ethene Trimerisation Catalyst .....	27
1.5.5 The Sasol Ethene Trimerisation Catalyst .....	29
1.5.6 Ethene Trimerisation by Titanium and Tantalum .....	30
1.5.6.1 Titanium Catalysts .....	30
1.5.6.2 Tantalum Catalysts .....	32
1.5.7 Ethylene Tetramerisation Catalyst .....	32
1.6 ROLE OF THE CO-CATALYST .....	36
1.6.1 Types of Co-Catalyst .....	36
1.6.1.1 Aluminium Alkyls .....	36
1.6.1.2 Perfluoroaryl Boranes.....	37
1.6.1.3 Trityl Aluminates and Borates .....	38
1.6.2 Activation.....	38
1.6.2.1 Alkyl Abstraction .....	38
1.6.2.2 Ligand Exchange .....	39
1.6.2.3 One Electron Oxidation .....	40
1.7 CONCLUSION .....	40
1.8 AIMS .....	42
1.9 REFERENCES .....	43
EXPERIMENTAL TECHNIQUES.....	51

<b>2.1 INTRODUCTION .....</b>	52
<b>2.2 NUCLEAR MAGNETIC RESONANCE SPECTROSCOPY .....</b>	52
<b>2.2.1 Quadrupolar Nuclei .....</b>	52
<b>2.2.1.1 <math>^{27}\text{Al}</math> NMR Spectroscopy .....</b>	53
<b>2.2.1.2 <math>^{45}\text{Sc}</math> NMR Spectroscopy .....</b>	53
<b>2.3 INFRA RED SPECTROSCOPY .....</b>	54
<b>2.3.1 Group Theory .....</b>	55
<b>2.4 ULTRA-VIOLET - VISIBLE (UV-VIS) SPECTROSCOPY .....</b>	56
<b>2.5 X-RAY ABSORPTION FINE STRUCTURE (XAFS) SPECTROSCOPY .....</b>	58
<b>2.5.1 Introduction .....</b>	58
<b>2.5.2 EXAFS Theory .....</b>	59
<b>2.5.3 X-ray Absorption Near Edge Structure (XANES) Spectroscopy .....</b>	64
<b>2.7 REFERENCES .....</b>	67
<b>VALIDATION OF THE STOPPED-FLOW INSTRUMENT AND FREEZE-QUENCH ACCESSORY BY CHROMIUM (III) UV-VIS SPECTROSCOPY AND MOLYBDENUM (III) EXAFS ANALYSIS.....</b>	69
<b>3.1 INTRODUCTION.....</b>	70
<b>3.1.1 The Stopped-flow Instrument .....</b>	70
<b>3.1.2 Analysis of Iron and Nickel Catalytic Pathways .....</b>	71
<b>3.1.3 Analysis of Palladium Catalytic Pathways .....</b>	73
<b>3.1.4 Analysis of Copper Catalysed Aryl Coupling Reaction .....</b>	76
<b>3.2 AIMS .....</b>	78
<b>3.3 RESULTS AND DISCUSSION.....</b>	79
<b>3.3.1 Details and Modifications of the BioLogic Stopped-flow Instrument .....</b>	79
<b>3.3.2 Titration of <math>\text{AlMe}_3</math> using the Quench-flow Setup.....</b>	82
<b>3.3.3 Validation by 5 mM <math>[\text{CrCl}_3(\text{decyl-SNS})] + 10 \text{ AlMe}_3</math> in toluene .....</b>	84
<b>3.3.4 Validation by 25 mM <math>[\text{MoCl}_3(\text{decyl-SNS})] + 20 \text{ AlMe}_3</math> in Toluene .....</b>	86
<b>3.3.5 The Freeze-quench Accessory .....</b>	87
<b>3.3.5.1 Validation of the Freeze-quench Accessory.....</b>	90
<b>3.3.5.2 Test of oxygen using <math>[\text{Cp}_2\text{TiCl}_2]\text{ZnCl}_2</math> .....</b>	90
<b>3.3.5.3 Analysis of <math>[\text{MoBr}_3(\text{SBz})]</math> by EXAFS analysis.....</b>	90
<b>3.4 CONCLUSION .....</b>	92
<b>3.5 REFERENCES .....</b>	92
<b>A MO K-EDGE QEXAFS STUDY INTO THE MECHANISM OF SELECTIVE OLEFIN OLIGOMERISATION CATALYSIS USING STOPPED-FLOW FREEZE-QUENCH TECHNIQUES.....</b>	96
<b>4.1 INTRODUCTION.....</b>	97
<b>4.1.1 Alkene Metathesis .....</b>	97
<b>4.1.2 Epoxidation of Alkenes .....</b>	103
<b>4.1.3 Ethene Oligomerisation .....</b>	106
<b>4.2 AIMS .....</b>	106
<b>4.3 RESULTS AND DISCUSSION.....</b>	108
<b>4.3.1 Synthesis of Mo(III) Halide Complexes .....</b>	108
<b>4.3.2 Characterisation – FT-IR and UV-Vis Spectroscopy.....</b>	111
<b>4.4 MO K-EDGE EXAFS ANALYSES.....</b>	113
<b>4.4.1 Solid State and Solution Complexes .....</b>	113
<b>4.4.2 End state analysis .....</b>	119
<b>4.4.3 Time-Resolved EXAFS Spectroscopy .....</b>	123
<b>4.4.4 Freeze-quench study of the alkylation of <math>[\text{MoBr}_3(\text{SBz})]</math>.....</b>	125
<b>4.5 CONCLUSION .....</b>	127
<b>4.6 EXPERIMENTAL.....</b>	127
<b>4.6.1 X-ray Crystallography .....</b>	130
<b>4.6.2 XAFS Experimental .....</b>	132
<b>4.7 REFERENCES .....</b>	134
<b>SC(III) COMPLEXES WITH NEUTRAL <math>\text{N}_3</math>- AND SNS-DONOR LIGANDS – A SPECTROSCOPIC STUDY OF THE ACTIVATION OF ETHENE POLYMERISATION CATALYSTS.....</b>	139
<b>5.1 INTRODUCTION.....</b>	140
<b>5.1.1 Sc Complexes for Ethene Polymerisation Catalysis .....</b>	140

<b>5.1.2 <math>^{45}\text{Sc}</math> NMR Spectroscopy .....</b>	<b>146</b>
<b>5.2 AIMS .....</b>	<b>147</b>
<b>5.3 RESULTS AND DISCUSSION.....</b>	<b>148</b>
<b>5.3.1 Investigation of <math>\text{R}_3\text{-tacn}</math> Complexes by Multinuclear NMR .....</b>	<b>149</b>
5.3.1.1 Reaction of $\text{R}_3\text{-tacn}$ Complexes with MeLi.....	152
5.3.1.2 Reaction $\text{R}_3\text{-tacn}$ Complexes with $\text{AlMe}_3$ .....	154
<b>5.3.2 Investigation of <math>\text{R-SNS}</math> Complexes by Multinuclear NMR .....</b>	<b>155</b>
5.3.2.1 Reactions $\text{R-SNS}$ Complexes with MeLi.....	157
5.3.2.2 Reactions $\text{R-SNS}$ Complexes with $\text{AlMe}_3$ .....	160
<b>5.3.3 Ethene Polymerisation Catalysis Testing .....</b>	<b>161</b>
<b>5.3.4 XAFS Measurements and Analysis .....</b>	<b>163</b>
5.3.4.1 Complexes in the Solid State and in Solution.....	163
5.3.4.2 Reactions of $[\text{ScCl}_3(\text{L}_3)]$ with MeLi.....	165
5.3.4.3 Reaction of $[\text{ScCl}_3(\text{decyl-SNS})]$ with $\text{AlMe}_3$ .....	168
<b>5.4 CONCLUSIONS .....</b>	<b>171</b>
<b>5.5 EXPERIMENTAL.....</b>	<b>173</b>
<b>5.5.1 Preparations .....</b>	<b>173</b>
<b>5.5.2 Catalysis Testing.....</b>	<b>176</b>
<b>5.5.3 XAFS Experimentation.....</b>	<b>177</b>
<b>5.6 REFERENCES .....</b>	<b>177</b>
<b>FREEZE-QUENCH CR K-EDGE EXAFS: INSIGHTS INTO THE EARLY ACTIVATION OF CHROMIUM CATALYSED ETHENE OLIGOMERISATION.....</b>	<b>182</b>
<b>6.1 INTRODUCTION.....</b>	<b>183</b>
<b>6.1.1 Chromium SNS .....</b>	<b>183</b>
<b>6.1.2 Chromium PNP .....</b>	<b>190</b>
<b>6.2 AIMS .....</b>	<b>191</b>
<b>6.3 RESULTS AND DISCUSSION.....</b>	<b>192</b>
<b>6.3.1 Synthesis of Chromium Complexes .....</b>	<b>192</b>
<b>6.3.2 Cr K-edge XAFS analysis .....</b>	<b>192</b>
6.3.2.1 Freeze-quench $[\text{CrCl}_3(\text{decyl-SNS})] + 20 \text{ AlMe}_3$ in Toluene .....	194
6.3.2.2 $[\text{CrCl}_3(\text{decyl-SNS})] + 4 \text{ MeLi}.$ .....	199
6.3.2.3 $[\text{CrCl}_3(\text{decyl-S}_3)] + 20 \text{ AlMe}_3.$ .....	201
6.3.2.4 $[\text{CrCl}_3(\text{PNP})(\text{THF})] + 20 \text{ AlMe}_3$ .....	204
<b>6.4 CONCLUSION .....</b>	<b>207</b>
<b>6.5 EXPERIMENTAL.....</b>	<b>209</b>
<b>6.5.1 XAFS Experimental.....</b>	<b>210</b>
<b>6.6 REFERENCES .....</b>	<b>211</b>
<b>FINAL DISCUSSION AND CONCLUSIONS.....</b>	<b>214</b>
<b>7.3 REFERENCES .....</b>	<b>217</b>
<b>SUPPLEMENTARY .....</b>	<b>219</b>
<b>8.1 CHAPTER 4 .....</b>	<b>220</b>
<b>8.2 CHAPTER 5 .....</b>	<b>228</b>
<b>8.3 CHAPTER 6 .....</b>	<b>230</b>
<b>8.4 REFERENCES .....</b>	<b>233</b>

## List of Figures

**Fig. 1.1** Graph displaying difference of activation energy ( $\Delta_A G$ ) with and without use of a catalyst and the Gibbs overall energy of reaction  $\Delta_R G$  between reactants (A) and products (B) for a hypothetical case.

**Fig. 1.2** Scandium alkyl five-coordinate complex with porphyrin ring.

**Fig. 1.3** Examples of  $[\text{Cr}(\text{CO})_3(\text{S}_3)]$  type complexes.

**Fig. 1.4** X-Ray structure of  $[\text{CrH}_4(\text{dmpe})_2]$ .

**Fig. 1.5** Square pyramidal Cr(V) oxide complexes with macrocyclic tetraamido-*N* ligand.

**Fig. 1.6** X-ray structure of  $[\text{Cr}(\text{N}^t\text{Bu}_2)_2(\eta^2\text{-}o\text{-C}_6\text{H}_4[(\text{CHSiMe}_3)_2])$ .

**Fig. 1.7** SHOP for production of  $\text{C}_{10\text{-}14}$   $\alpha$ -olefins.

**Fig. 1.8** Crystal structures of chromocyclo-pentane and heptane complexes.

**Fig. 1.9** Chromium(I) pyrrolyl sandwich complex active for selective ethene trimerisation.

**Fig. 1.10** Displaying dimeric  $[(\eta^5\text{-}2,3,4,5\text{-Me}_4\text{C}_4\text{N}(\text{AlClMe}_2))\text{Cr}(\mu\text{-Me})]_2$  catalyst for selective ethene trimerisation.

**Fig. 1.11**  $[\text{CrCl}_3(\text{HN}(\text{CH}_2\text{CH}_2\text{PR}_2)_2)]$  catalyst.

**Fig. 1.12**  $[\text{CrCl}_3(\text{SNS-R})]$  catalyst.

**Fig. 1.13** Titanium functionalised Cp complex for ethene trimerisation.

**Fig. 1.14** Highly active non-Cp based Ti ethene trimerisation catalyst.

**Fig. 1.15** Phosphinoamine ligand for ethene trimerisation and tetramerisation.

**Fig. 1.16** Tetralithium tetrabutanediyldichromate which results in 1-octene liberation upon thermolysis.

**Fig. 1.17** Two possible formations for selective 1-octene production by Cr ethene oligomerisation catalyst.

**Fig. 1.18** Proposed structures of methylaluminoxane oligomer.

**Fig. 1.19** Publications on trimerisation and tetramerisation of ethene by year (upto June 2010).

**Fig. 2.1** Generic isomers of *fac*- (F) and *mer*- (M) six-coordinate complexes.

**Fig. 2.2** Tanabe-Sugano diagram showing  $^4F$  ground state splitting in an octahedral field.

**Fig. 2.3** Energy level diagram for a  $d^3$  transition metal in  $O_h$  and  $C_{3v}$  environments.

**Fig. 2.4** Photoelectric effect: incident X-ray is absorbed by core level electron, which is then ejected as a photo-electron into the continuum.

**Fig. 2.5** Showing the XAFS spectrum of a Cr foil .

**Fig. 2.6** Isolated EXAFS of a Cr foil.

**Fig. 2.7** Fe K-edge XANES spectra of Fe metal and Fe compounds.

**Fig. 2.8** Cr K-edge XANES spectra for octahedral  $Cr^{3+}$  and tetrahedral  $Cr^{6+}$ .

**Fig. 3.1** Schematic of a typical stopped-flow design.

**Fig. 3.2** Active Ni propene dimerisation catalyst proposed by EXAFS analysis.

**Fig. 3.3** Trimeric Ni intermediate suggested by EDE analysis for the dimerisation of propene.

**Fig. 3.4** Schematic of stopped-flow instrument set-up for UV-Vis and simultaneous XAFS measurements.

**Fig. 3.5** Photograph showing the stopped-flow instrument on B18.

**Fig. 3.6** Photograph showing observation head with optical fibre connectors, sealed entries to syringes and waste tube.

**Fig. 3.7** UV-Vis spectra showing reaction of 5 mM [CrCl<sub>3</sub>(decyl-SNS)] + 10 AlMe<sub>3</sub> in toluene at 2 s intervals.

**Fig. 3.8** UV-Vis spectra showing reaction of 5 mM [CrCl<sub>3</sub>(decyl-SNS)] + 10 AlMe<sub>3</sub> in toluene at rate of 2 ms/spectrum.

**Fig. 3.9** UV-Vis spectra showing reaction of 1mM [MoCl<sub>3</sub>(decyl-SNS)] + 20 AlMe<sub>3</sub> in toluene.

**Fig. 3.10** UV-Vis spectra showing reaction of 25mM [MoCl<sub>3</sub>(decyl-SNS)] + 20 AlMe<sub>3</sub> in toluene.

**Fig. 3.11** Schematic of the freeze-quench accessory connected to the stopped-flow unit.

**Fig. 3.12** Displaying freeze-quench add-on allowing for easy air/moisture free sample collection.

**Fig. 3.13** Photographs showing set-up of the freeze quench and sample under cryostream in sealed Kapton® tube.

**Fig. 3.14** Mo K-edge  $k^2$ -weighted EXAFS and Fourier transform data showing the comparison of 20 mM [MoBr<sub>3</sub>(SBz)] collected in the liquid cell and collected by the freeze quench.

**Fig. 3.15** Mo K-edge  $k^2$ -weighted EXAFS and Fourier transform analysis of 20 mM [MoBr<sub>3</sub>(SBz)] toluene solution in liquid cell with fits.

**Fig. 4.1** Schrock catalyst.

**Fig. 4.2** X-ray crystal structure of tungstanocyclobutane ring product upon reaction of [W(CH<sup>t</sup>Bu)(NAr)(O<sup>t</sup>Bu)<sub>2</sub>] with 2,3-Bis(trifluoro)norbornadiene.

**Fig. 4.3** Displaying Mo chiral metathesis catalysts reviewed by Schrock.

**Fig. 4.4** Displaying active epoxidation catalyst [CpMoO<sub>2</sub>Cl] and inactive  $\eta^2$ -peroxo species [CpMo(O<sub>2</sub>)OCl].

**Fig. 4.5** Multiple bonded Mo dimer from reaction of [Mo(CO)<sub>3</sub>(SNS)] with [Ag(CH<sub>2</sub>Cl<sub>2</sub>)<sub>2</sub>][Al(OC(CF<sub>3</sub>)<sub>3</sub>)<sub>4</sub>].

**Fig. 4.6** UV-Vis spectra of 5 mmol [MoCl<sub>3</sub>(THF)<sub>3</sub>] in THF and CH<sub>2</sub>Cl<sub>2</sub>.

**Fig. 4.7** Showing structure of the synthesised Mo(III) complexes with coordinated ligands.

**Fig. 4.8** Structure of [MoCl<sub>3</sub>(HN(CH<sub>2</sub>CH<sub>2</sub>S<sup>t</sup>Bu)<sub>2</sub>)].

**Fig. 4.9** Structure of [MoCl<sub>3</sub>([9]aneS<sub>3</sub>)].

**Fig. 4.10** Displaying FT-IR spectra of [MoCl<sub>3</sub>(decyl-SNS)] as Nujol mull and free ligand decyl-SNS.

**Fig. 4.11** Displaying FT-IR spectra for  $[\text{MoCl}_3(\text{decyl-SNS})]$  and  $[\text{MoCl}_3(\text{THF})_3]$  as Nujol mulls.

**Fig. 4.12** Mo K-edge  $k^1$ -weighted Fourier transform EXAFS data displaying subsequent scans collected for solid  $[\text{MoBr}_3(\text{decyl-SNS})]$ .

**Fig. 4.13** Mo K-edge  $k^2$ -weighted EXAFS and Fourier transform data and fits for  $[\text{MoCl}_3(\text{decyl-SNS})]$  solid and solution.

**Fig. 4.14** Mo K-edge  $k^2$ -weighted Fourier transform EXAFS data for  $[\text{MoCl}_3(\text{decyl-SNS})]$  in toluene and  $[\text{MoCl}_3(\text{decyl-SNS})] + 20$  equivs.  $\text{AlMe}_3$  in the solution cell.

**Fig. 4.15** Mo K-edge  $k^2$ -weighted Fourier transform EXAFS data for  $[\text{MoCl}_3(\text{SBz})]$  in the solution cell; + 20 equivs.  $\text{AlMe}_3$  in the solution cell; + 4 equivs.  $\text{AlMe}_3$  in the stopped-flow cuvette; + 8 equivs.  $\text{AlMe}_3$  in the stopped-flow cuvette.

**Fig. 4.16** Mo K-edge  $k^2$ -weighted Fourier transform EXAFS data for a solution of  $[\text{MoBr}_3(\text{SBz})]$  in the solution cell; + 20 equivs.  $\text{AlMe}_3$  in the solution cell; + 20 equivs.  $\text{AlMe}_3$  in the stopped-flow cuvette; + 20 equivs.  $\text{AlMe}_3$  freeze-quenched after 5 s; + 20 equivs.  $\text{AlMe}_3$  freeze-quenched after 5 min.

**Fig. 4.17** Combined time-resolved UV–Vis and QEXAFS data of the reaction of  $[\text{MoCl}_3(\text{decyl-SNS})] + 20$  equivs of  $\text{AlMe}_3$ .

**Fig. 4.18** Mo K-edge  $k^3$ -weighted Fourier transform EXAFS data for  $[\text{MoCl}_3(\text{SBz})] + 32$  equivs.

**Fig. 5.1** Displaying crystal structure for  $[\text{ScCl}_3(\text{Me}_3\text{-[9]aneN}_3)]$ .

**Fig. 5.2** Dimeric yttrium hydrido complex.

**Fig. 5.3** Displaying  $^{45}\text{Sc}$  NMR spectra for  $[\text{ScCl}_3(\text{Me}_3\text{-tacn})]$  in (THF/D<sub>2</sub>O capillary) and  $[\text{Sc}(\text{Me})_3(\text{Me}_3\text{-tacn})]$  in Tol-D<sub>8</sub>.

**Fig. 5.4** Displaying  $^1\text{H}$  and  $^{13}\text{C}$  NMR spectra for  $[\text{Sc}(\text{Me})_3(\text{Me}_3\text{-tacn})]$  in Tol-D<sub>8</sub>.

**Fig. 5.5** Proposed complex formed with  $[\text{ScCl}_3(\text{Me}_3\text{-tacn})] + 10 \text{ AlMe}_3$  in toluene.

**Fig. 5.6** Displaying  $^1\text{H}$  and  $^{13}\text{C}$  NMR spectra for  $[\text{ScCl}_3(^t\text{Bu-SNS})]$  in  $\text{CDCl}_3$ .

**Fig. 5.7** Displaying  $^1\text{H}$  (top) and  $^{13}\text{C}\{^1\text{H}\}$  (bottom) NMR for  $[\text{ScCl}_3(^t\text{Bu-SNS})] + 4 \text{ MeLi}$  in Tol-D<sub>8</sub> (reacted at -78 °C, measured at room temperature).

**Fig 5.8** Displaying two complexes formed from the reaction of  $[\text{ScCl}_3(\text{THF})_3]$  and the lithiated free ligand PN(Li)P.

**Fig. 5.9** Sc K-edge  $k^2$ -weighted EXAFS and Fourier transform data and for  $[\text{ScCl}_3(\text{decyl-SNS})]$  solid, solution in toluene and  $[\text{ScCl}_3(^t\text{Bu-SNS})]$  solid.

**Fig. 5.10** Sc K-edge  $k^2$ -weighted Fourier transform EXAFS data for  $[\text{ScCl}_3(\text{Me}_3\text{-tacn})]$  and  $[\text{ScCl}_3(\text{decyl-SNS})]$  solid and with 3.5 mol. equivs. MeLi in THF.

**Fig. 5.11** Sc K-edge XANES spectra for  $[\text{ScCl}_3(\text{decyl-SNS})]$  solution, with 10 mol. equiv.  $\text{AlMe}_3$  frozen after 1 s, with 10 mol. equiv.  $\text{AlMe}_3$  at ambient temperature, with 3.5 mol. equiv. MeLi.

**Fig. 5.12** Sc K-edge  $k^1$ -weighted Fourier transform EXAFS data for  $[\text{ScCl}_3(\text{decyl-SNS})]$  solution and with 10 mol. equiv.  $\text{AlMe}_3$ , with further addition of 1 mol. equiv. of  $[\text{Ph}_3\text{C}][\text{Al}\{\text{OC}(\text{CF}_3)_3\}_4]$ , and with further addition of 100 mol. equivs. 1-hexene.

**Fig. 5.13** Sc K-edge normalised XANES spectra for  $[\text{ScCl}_3(\text{decyl-SNS})]$  solution and with 10 mol. equiv.  $\text{AlMe}_3$ , with further addition of 1 mol. equivs.  $[\text{Ph}_3\text{C}][\text{Al}\{\text{OC}(\text{CF}_3)_3\}_4]$ , with further addition of 100 mol. equivs. 1-hexene.

**Fig. 6.1** Chromium dimer complex formed after addition of 10  $\text{AlMe}_3$  to  $[\text{CrCl}_3(\text{Cy-SNS})]$ .

**Fig. 6.2** Isolated product from reaction of  $[\text{CrCl}_2(\text{THF})_2] + \text{Cy-SNS} + \text{AlEt}_2\text{Cl}$ .

**Fig. 6.3** Self-activating catalyst formed from  $[\text{CrCl}_3(2,6-(^t\text{BuSCH}_2)_2\text{-py})]$  and  $\text{AlMe}_3$ .

**Fig. 6.4** Crystal structure for  $[\text{CrCl}(\text{^tBu-SNS})]_2$  with bridging amide.<sup>[6]</sup>

**Fig. 6.5** Isolated monomeric divalent Cr(PNP) species upon reaction with 10 equivalents of  $\text{AlMe}_3$ .

**Fig. 6.6** Cr K-edge  $k^2$ -weighted EXAFS and Fourier transform data (blue) and fits (red) for  $[\text{CrCl}_3(\text{decyl-SNS})]$  in toluene.

**Fig. 6.7** Cr K-edge  $k^2$ -weighted Fourier transform EXAFS data for  $[\text{CrCl}_3(\text{decyl-SNS})]$  (blue),  $[\text{CrCl}_3(\text{decyl-SNS})] + 20 \text{ AlMe}_3$ , freeze-quenched at 1 s (red) and  $[\text{CrCl}_3(\text{decyl-SNS})] + 4 \text{ MeLi}$  in the XAFS solution cell (green), in toluene.

**Fig. 6.8** Activated  $[\text{CrCl}_3(\text{decyl-SNS})]$  catalyst proposed by XAFS.

**Fig. 6.9** Cr K-edge normalised XANES spectra for  $[\text{CrCl}_3(\text{decyl-SNS})]$  (blue),  $[\text{CrCl}_3(\text{decyl-SNS})] + 20 \text{ AlMe}_3$ , freeze-quenched at 1 s (red) and  $[\text{CrCl}_3(\text{decyl-SNS})] + 4 \text{ MeLi}$  in the XAFS cell (green), in toluene.

**Fig. 6.10** UV-Vis spectra showing reaction of 5 mM  $[\text{CrCl}_3(\text{decyl-SNS})] + 10 \text{ AlMe}_3$  in toluene at 2 s intervals, with red spectrum representing start point and blue representing last collected spectrum (red = 2s, black = 2s intervals, Blue = 29 s; green arrow = direction of time).

**Fig. 6.11** UV-Vis spectra showing reaction of 5 mM  $[\text{CrCl}_3(\text{decyl-SNS})] + 10 \text{ AlMe}_3$  in toluene at rate of 2 ms/spectrum (black = unreacted complex, red = 1.120 s, blue = 1.122 s).

**Fig. 6.12** Cr K-edge  $k^2$ -weighted Fourier transform EXAFS data for  $[\text{CrCl}_3(\text{decyl-S}_3)]$  in toluene (blue),  $[\text{CrCl}_3(\text{decyl-S}_3)] + 20 \text{ AlMe}_3$ , freeze-quenched at 1 s (red) and  $[\text{CrCl}_3(\text{decyl-S}_3)] + 20 \text{ AlMe}_3$  freeze-quenched at 5 min (blue).

**Fig. 6.13** Displaying XANES region for  $[\text{CrCl}_3(\text{decyl-S}_3)]$  (blue),  $[\text{CrCl}_3(\text{decyl-SNS})] + 20 \text{ AlMe}_3$  at 1 s (green) and  $[\text{CrCl}_3(\text{decyl-S}_3)] + 20 \text{ AlMe}_3$  at 5 min (red).

**Fig. 6.14** Cr K-edge  $k^2$ -weighted Fourier transform EXAFS data for solid  $[\text{CrCl}_3(\text{PNP})(\text{THF})]$  in BN,  $[\text{CrCl}_3(\text{PNP})(\text{THF})] + 20 \text{ AlMe}_3$ , freeze-quenched at 1 min and  $[\text{CrCl}_3(\text{PNP})(\text{THF})] + 20 \text{ AlMe}_3$  freeze-quenched at 5 min.

**Fig. 6.15** Displaying XANES region for solid  $[\text{CrCl}_3(\text{PNP})(\text{THF})]$ ,  $[\text{CrCl}_3(\text{PNP})(\text{THF})] + 20 \text{ AlMe}_3$  at 1 min and  $[\text{CrCl}_3(\text{PNP})(\text{THF})] + 20 \text{ AlMe}_3$  at 5 min.

**Fig. 6.16** Cr K-edge  $k^2$ -weighted EXAFS and Fourier transform data and fits for  $[\text{CrCl}_3(\text{PNP})(\text{THF})] + 20 \text{ AlMe}_3$  freeze-quenched at 5 min.

**Fig. S4.1** Mo K-edge  $k^2$ -weighted EXAFS and Fourier transform data and fits for  $[\text{MoCl}_4(\text{THF})_2]$  in BN.

**Fig. S4.2** Mo K-edge  $k^2$ -weighted EXAFS and Fourier transform data and fits for  $[\text{MoBr}_3(\text{THF})_3]$  in BN.

**Fig. S4.3** Mo K-edge  $k^2$ -weighted EXAFS and Fourier transform data and fits for  $[\text{MoCl}_3(\text{tBu-SNS})]$  in BN.

**Fig. S4.4** Mo K-edge  $k^2$ -weighted EXAFS and Fourier transform data and fits for  $[\text{MoCl}_3([9]\text{aneS}_3)]$  in BN.

**Fig. S4.5** Mo K-edge  $k^2$ -weighted EXAFS and Fourier transform data and fits for  $[\text{MoCl}_3([9]\text{aneN}_3)]$  in BN.

**Fig. S4.6** Mo K-edge  $k^2$ -weighted EXAFS and Fourier transform data and fits for  $[\text{Mo}(\text{CO})_6]$  in BN.

**Fig. S4.7** Mo K-edge  $k^2$ -weighted EXAFS and Fourier transform data and fits for [Mo(CO)<sub>4</sub>(norbornadiene)] in BN.

**Fig. S4.8** Mo K-edge  $k^2$ -weighted EXAFS and Fourier transform data and fits for [MoO<sub>2</sub>(S<sub>2</sub>NEt<sub>2</sub>)<sub>2</sub>] in BN.

**Fig. S4.9** Mo K-edge  $k^2$ -weighted EXAFS and Fourier transform data and fits for [MoO<sub>2</sub>Cl<sub>2</sub>(Ph<sub>3</sub>PO)<sub>2</sub>] in BN.

**Fig. S4.10** Mo K-edge  $k^2$ -weighted EXAFS and Fourier transform data and fits for [MoO<sub>2</sub>Cl<sub>2</sub>(Me<sub>3</sub>PO)<sub>2</sub>] in BN.

**Fig. S4.11** Mo K-edge  $k^2$ -weighted EXAFS and Fourier transform data and fits for [MoO<sub>2</sub>Br<sub>2</sub>(Me<sub>3</sub>PO)<sub>2</sub>] in BN.

**Fig. S4.11** Mo K-edge  $k^2$ -weighted EXAFS and Fourier transform data and fits for [MoO<sub>2</sub>Br<sub>2</sub>(Me<sub>3</sub>PO)<sub>2</sub>] in BN.

**Fig. S5.1** Sc K-edge  $k^2$ -weighted EXAFS and Fourier transform data and fits of [ScCl<sub>3</sub>(Me<sub>3</sub>-tacn)] solid and with 3.5 mol. equivs. MeLi in THF.

**Fig. S5.2** Sc K-edge  $k^2$ -weighted EXAFS and Fourier transform data and fits for [ScCl<sub>3</sub>(decyl-SNS)] with 3.5 mol. equivs. MeLi in THF.

**Fig. S5.3** Sc K-edge  $k^2$ -weighted EXAFS and Fourier transform data and fits for [ScCl<sub>3</sub>(decyl-SNS)] solution with 10 mol equiv. AlMe<sub>3</sub>, with further addition of 1 mol equivs. [Ph<sub>3</sub>C][Al{OC(CF<sub>3</sub>)<sub>3</sub>}<sub>4</sub>], with further addition of 100 mol equivs. 1-hexene.

**Fig. S6.1** Cr K-edge  $k^2$ -weighted EXAFS and Fourier transform data and fits for [CrCl<sub>3</sub>(decyl-SNS)] + 20 AlMe<sub>3</sub> at 1 s in toluene.

**Fig. S6.2** Cr K-edge  $k^2$ -weighted EXAFS and Fourier transform data and fits for [CrCl<sub>3</sub>(decyl-SNS)] + 4 MeLi in toluene.

**Fig. S6.3** Cr K-edge  $k^2$ -weighted EXAFS and Fourier transform data and fits for [CrCl<sub>3</sub>(decyl-S<sub>3</sub>)] in toluene.

**Fig. S6.4** Cr K-edge  $k^2$ -weighted EXAFS and Fourier transform data and fits for [CrCl<sub>3</sub>(decyl-S<sub>3</sub>)] + 20 AlMe<sub>3</sub> at 1 s in toluene.

**Fig. S6.5** Cr K-edge  $k^2$ -weighted EXAFS and Fourier transform data and fits for [CrCl<sub>3</sub>(decyl-S<sub>3</sub>)] + 20 AlMe<sub>3</sub> at 1 s in toluene.

**Fig. S6.6** Cr K-edge  $k^2$ -weighted EXAFS and Fourier transform data and fits for [CrCl<sub>3</sub>(PNP)(THF)] in BN.

**Fig. S6.7** Cr K-edge  $k^2$ -weighted EXAFS and Fourier transform data and fits for [CrCl<sub>3</sub>(PNP)(THF)] + 20 AlMe<sub>3</sub> at 1 min.

## List of Schemes

**Scheme 1.1** Synthesis of  $[(C_5Me_5)ScCl]$ .

**Scheme 1.2** Ethene insertion into  $[(C_5Me_5)_2ScH]$ .

**Scheme 1.3** Coupling of aldehyde and vinyl bromide by  $CrCl_2$ .

**Scheme 1.4**  $CrCl_2$  promoted cyclisation in the synthesis of Asperdiol.

**Scheme 1.5** Stereoselective coupling mechanism of an aldehyde and an alkene using  $CrCl_2$ .

**Scheme 1.6** Mechanism of alkene insertion by a homogeneous Ziegler-Natta catalyst.

**Scheme 1.7** Synthesis of SHOP catalyst used to give a Shulz-Flory distribution of  $\alpha$ -olefins.

**Scheme 1.8** Formation of active Ni-H species for ethene oligomerisation.

**Scheme 1.9** Catalytic cycle of ethene oligomerisation by nickel hydrido species.

**Scheme 1.10** Manyik proposed metallocycle growth mechanism with chromium.

**Scheme 1.11** Briggs proposed cycle for selective ethene trimerisation.

**Scheme 1.12** Metallocycle pathway for the production of 1-hexene.

**Scheme 1.13** 1-Hexene D/H scrambling as produced *via* the Cossee-Arlman chain growth mechanism.

**Scheme 1.14** Metallocycle formation arising from the dimeric chromium pyrrolyl complex to give 1-hexene.

**Scheme 1.15** Proposed ethene trimerisation route by TaCl<sub>5</sub>.

**Scheme 1.16** Displaying two routes of the tantalum metallacycloheptane decomposition to yield 1-hexene.

**Scheme 1.17** Suggested Philips catalytic route for the polymerisation of ethene.

**Scheme 1.18** Suggested bimetallic route for the selective production of 1-octene.

**Scheme 1.19** Formation of cationic zirconium ethene polymerisation catalyst.

**Scheme 1.20** Stepwise methyl abstraction by B(C<sub>6</sub>F<sub>5</sub>)<sub>3</sub> on zirconium metallocene

**Scheme 1.21** Ligand exchange and subsequent alkyl abstraction by MAO.

**Scheme 1.22** Oxidation of an active olefin titanium complex by ferrocenium tetrakis(pentafluorophenyl)borate.

**Scheme 1.23** Possible Cr-based metallocycle reaction pathways as reviewed by Agapie.

**Scheme 3.1** Proposed catalytic cycle for the dimerisation of propene by [Ni(acac)(ethyl)(propene)] precursor.

**Scheme 3.2** Reaction scheme showing formation of the palladium four coordinate catalytic precursor for allyl alkylation.

**Scheme 3.3** Suggested reaction pathway of allyl alkylation by palladium catalysis.

**Scheme 3.4** Palladium catalysed coupling under study by EDE/QEXAFS spectroscopy.

**Scheme 3.5** Suggested palladium species present in equilibrium in pre-catalytic solution.

**Scheme 3.6** Suggested palladium species present in catalytic solution at 75 °C.

**Scheme 3.7** Proposed catalytic cycle for the Cu(II)-catalysed arylation of imidazole and phenyl boronic acid.

**Scheme 3.8** Scheme showing titration method of AlMe<sub>3</sub> by pyridine.

**Scheme 4.1** Metathesis reaction and ring-open metathesis polymerisation.

**Scheme 4.2** Synthesis of Mo Schrock catalyst.

**Scheme 4.3** Reaction pathway of ring-open metathesis polymerisation.

**Scheme 4.4** mCPBA type epoxidation of olefin by molybdenum catalyst.

**Scheme 4.5** Mimoun proposed epoxidation pathway and Sharpless epoxidation pathway.

**Scheme 4.6** Displaying the Thiel type epoxidation pathway.

**Scheme 4.7** Proposed reaction of Mo complexes upon activation with AlMe<sub>3</sub>.

**Scheme 5.1** Mechanism of Ziegler-Natta α-olefin polymerisation.

**Scheme 5.2** Showing method of synthesis towards dimeric scandium metallocene for Ziegler-Natta polymerisation.

**Scheme 5.3** Showing synthesis of methylated scandium β-diketimido complex.

**Scheme 5.4** Reaction of scandium dimethyl β-diketimido complex with 0.5, 1 and 2 equivalents of B(C<sub>6</sub>F<sub>5</sub>)<sub>4</sub>.

**Scheme 5.5** Synthesis of new [M(CH<sub>2</sub>SiMe<sub>3</sub>)(N<sub>3</sub>)] type complexes.

**Scheme 5.6** Synthesis of scandium bis(alkyl) 2-pyridinemethanamido complex.

**Scheme 5.7** General reaction scheme for scandium catalysts.

**Scheme 5.8** Showing formation of five coordinate scandium SNS complex and subsequent alkylation by MeLi.

**Scheme 5.9** Proposed reaction pathways of  $[\text{ScCl}_3(\text{decyl-SNS})]$  by  $\text{AlMe}_3 + [\text{Ph}_3\text{C}][\text{Al}\{\text{OC}(\text{CF}_3)_3\}_4]$  for olefin polymerisation.

**Scheme 6.1** Reduction of  $[\text{CrCl}_3(\text{Cy-SNS})]$  with iso-butyl aluminoxane (i-BAO) to give chromium(II) dimer.

**Scheme 6.2** Oxidation of Cr(II) precursor giving oxidised dimeric  $[\text{Cr}(\text{SNS})\text{Cl}]_2^{2+}$ .

**Scheme 6.3** Synthesis of  $[\text{CrCl}_3(2,6-(\text{CySCH}_2)_2-\text{py})]$  complex.

**Scheme 6.4** Proposed mechanism towards the production of 1-hexene from the isolated self-activating chromium catalyst.

**Scheme 6.5** Proposed mechanistic cycles of Cr-SNS complex for selective ethene trimerisation; neutral Cr(I)  $\rightarrow$  Cr(III) and cationic Cr(II)  $\rightarrow$  Cr(IV) cycles.

**Scheme 6.6** Reaction scheme of  $[\text{CrCl}_3(\text{decyl-S}_3)] + 20 \text{ AlMe}_3$  as proposed by freeze-quench Cr K-edge EXAFS spectroscopy.

**Scheme 6.7** Reaction of  $[\text{CrCl}_3(\text{PNP})(\text{THF})]$  with 20  $\text{AlMe}_3$  as proposed by Cr K-edge EXAFS analysis.

## List of Tables

**Table 1.1** Displaying the global LAO capacity of each company and plant as of 2007.

**Table 1.2** Showing the classification of different Lewis Acids and Bases.

**Table 2.1** Table of chemical shifts for selected aluminium alkyls and chlorides relevant to this work observed in  $^{27}\text{Al}$  NMR spectroscopy.

**Table 2.2** Table of chemical shifts for selected scandium(III) species species observed by  $^{45}\text{Sc}$  NMR spectroscopy.

**Table 2.3** Reducible representation of *mer*-isomer (M) for  $\Gamma_{\text{M-X}}$ .

**Table 2.4** Reducible representation of *fac*-isomer (F) for  $\Gamma_{\text{M-X}}$ .

**Table 3.1** Results for Mo K-edge EXAFS analysis of  $[\text{MoBr}_3(\text{SBz})]$  sample in the liquid cell.

**Table 4.1** Mo K-edge EXAFS data analyses results on  $[\text{MoCl}_3(\text{SBz})]$  complex.

**Table 4.2** Mo K-edge EXAFS data analyses results on  $[\text{MoCl}_3(\text{decyl-SNS})]$  complex.

**Table 4.3** Mo K-edge EXAFS data analyses results on  $[\text{MoBr}_3(\text{SBz})]$  complex.

**Table 4.4** Crystal data and structure refinement details.

**Table 4.5** Selected bond lengths ( $\text{\AA}$ ) and angles ( $^{\circ}$ ) for  $[\text{MoCl}_3(\text{HN}(\text{CH}_2\text{CH}_2\text{S}^{\text{t}}\text{Bu})_2)]$ .

**Table 4.6** Selected bond lengths ( $\text{\AA}$ ) and angles ( $^{\circ}$ ) for  $[\text{MoCl}_3([9]\text{aneS}_3)]$ .

**Table 5.1**  $^{45}\text{Sc}$  NMR solution data for  $[\text{ScCl}_3(\text{R}_3\text{-tacn})]$  before and after addition of metal methyl reagents.

**Table 5.2**  $^{27}\text{Al}$  NMR solution data for  $[\text{ScCl}_3(\text{L}_3)] + 10 \text{ AlMe}_3$ .

**Table 5.3**  $^{45}\text{Sc}$  NMR solution data for  $[\text{ScCl}_3(\text{SNS-R})]$  before and after addition of metal methyls.

**Table 5.4** Results of catalyst testing with ethene.

**Table 5.5** Sc K-edge EXAFS data analyses for  $[\text{ScCl}_3(\text{R-SNS})]$  and  $[\text{ScCl}_3(\text{Me}_3\text{-tacn})]$ .

**Table 5.6** Sc K-edge EXAFS data analyses of  $[\text{ScCl}_3(\text{L})] + 3.5 \text{ MeLi}$  in toluene ( $\text{L} = \text{decyl-SNS, Me}_3\text{-tacn}$ ).

**Table 5.7** Sc K-edge EXAFS data analyses for  $[\text{ScCl}_3(\text{decyl-SNS})]$  upon activation in toluene.

**Table 6.1** Cr K-edge EXAFS data analyses for solutions of  $[\text{CrCl}_3(\text{L})]$  in toluene

**Table 6.2** Cr K-edge EXAFS data analyses for the reaction of  $[\text{CrCl}_3(\text{decyl-SNS})]$  with 20 equivs.  $\text{AlMe}_3$  in toluene, freeze-quenched after 1 s.

**Table 6.3** Cr K-edge EXAFS data analyses for the reaction of  $[\text{CrCl}_3(\text{decyl-SNS})]$  with 4 mol equivs.  $\text{MeLi}$  in toluene.

**Table 6.4** Cr K-edge EXAFS data analyses for the reaction of  $[\text{CrCl}_3(\text{decyl-S}_3)]$  with 20 equivs.  $\text{AlMe}_3$  in toluene, freeze-quenched after 1 s and 5 min.

**Table 6.5** Cr K-edge EXAFS data analyses for the reaction of  $[\text{CrCl}_3(\text{PNP})(\text{THF})]$  with 20 equivs.  $\text{AlMe}_3$  in toluene, freeze-quenched after 1 min and 5 min.

## **List of Equations**

**Equation 1.1** Turnover frequency.

**Equation 2.1** Beer Lambert Law.

**Equation 2.2** Beer-Lambert Law (integration of Equation 2.1).

**Equation 2.3** Dependence of absorption coefficient  $\mu$ .

**Equation 2.4** Showing how EXAFS is derived from XAFS spectrum.

**Equation 2.5** The plane wave theory EXAFS equation.

# **Declaration of Authorship**

I, Stuart A. Bartlett,

declare that this thesis and the work presented in it are my own and has been generated by me as the result of my own original research.

Probing the Early Activation Mechanism of Olefin Oligomerisation Catalysis using Molybdenum, Scandium and Chromium Halide Complexes

I confirm that:

1. This work was done wholly or mainly while in candidature for a research degree at this University;
2. Where any part of this thesis has previously been submitted for a degree or any other qualification at this University or any other institution, this has been clearly stated;
3. Where I have consulted the published work of others, this is always clearly attributed;
4. Where I have quoted from the work of others, the source is always given. With the exception of such quotations, this thesis is entirely my own work;
5. I have acknowledged all main sources of help;
6. Where the thesis is based on work done by myself jointly with others, I have made clear exactly what was done by others and what I have contributed myself;
7. Either none of this work has been published before submission, or parts of this work have been published as:
  - a. S. A. Bartlett, P. P. Wells, M. Nachtegaal, A. J. Dent, G. Cibin, G. Reid, J. Evans and M. Tromp, *J. Catal.* **2011**, 284, 247-258.
  - b. S. A. Bartlett, G. Cibin, A. J. Dent, J. Evans, M. J. Hanton, G. Reid, R. P. Tooze and M. Tromp, *Dalton Trans.*, **2013**, 42, 2213-2223.

Signed:.....

Date:.....

## Acknowledgements

Firstly, I would like to thank my supervisors, Prof. G. Reid, Prof. J. Evans and Prof. M. Tromp. All of whom provided guidance, knowledge, inspiration and time for me and the project as a whole. I only hope I managed to meet their expectations and beyond for this project. I would also like to thank my advisor Prof. W. Levason, again for his guidance and time, especially during  $^{45}\text{Sc}$  NMR studies.

I would also like to thank current and past members of my research group for their constant support and advice, especially to Sarah Hobbs, Rowena Thomas, Luke Ollivere, Jamie Frew, Chitra Gurnani, Andrew Jolleys, Christianne Wicking, Paolo Farina and George Sanderson. I would also like to thank Jamie Frew, Peter Wells and Richard Isley for their assistance during beamtimes.

Special thanks go to Dr Peter Wells for coming into the project and helping to move it forward and also to Dr Marek Jura, who I learned so much from within my first six months. Both these people I hold in the highest regard and hope to remain friends far into the future.

I would like to thank all my family for their unwavering support and the immense help they have provided during my whole time at university. I would also like to acknowledge my very close friends David Barrett, Stuart Wakefield, Christopher Robinson and Richard Harrision who would regularly turn up like a tornado over many weekends.

I would like to acknowledge Kate Sillis for her high level of patience and incredible support during my PhD. I am also very grateful to her family for their support.

I would also like to acknowledge The ESRF for provision of beamtime and the staff with their help. The Swiss Light Source, PSI, Villigen, Switzerland along with Marteen Nachtegaal and associated staff, The Diamond Light Source for beamtime along with Andy Dent, Giannantonio Cibin, Stephen Parry. I gratefully acknowledge the EPSRC. Dr. M. Webster and Dr W. Zhang are gratefully acknowledged for help with the X-ray crystallography.

I would like to acknowledge Sasol including Prof. R. Tooze and Dr. M. Hanton for their help and involvement with catalyst testing.

**Dedicated to the memory of Lee Winter, 1986 – 2004.**

## List of Abbreviations

- acac – Acetylacetone
- AlMe<sub>3</sub> – Trimethylaluminium
- <sup>i</sup>BAO - Iso-butyl aluminoxane
- <sup>t</sup>Bu - C(CH<sub>3</sub>)<sub>3</sub>
- CH<sub>2</sub>Cl<sub>2</sub> - Dichlorethane
- Cp – Cyclopentadiene
- Cr-2-EH - Chromium (III)2-ethylhexanoate
- DABCO - 1,4-diazabicyclo(2.2.2)octane
- decyl-S<sub>3</sub> - S(CH<sub>2</sub>CH<sub>2</sub>S<sup>n</sup>C<sub>10</sub>H<sub>21</sub>)<sub>2</sub>
- decyl - <sup>n</sup>C<sub>10</sub>H<sub>21</sub>
- DME – Dimethoxyethane
- EDE - Energy dispersive EXAFS
- EDXAFS - Energy Dispersive X-ray Absorption Fine Structure
- EPR - Electron paramagnetic resonance
- equiv. - Equivalents
- Et, ethyl - CH<sub>2</sub>CH<sub>3</sub>
- Et<sub>2</sub>O - Diethyl ether
- EXAFS - Extended X-ray Absorption Fine Structure
- FTIR - Fourier Transform Infrared
- FQ - Freeze-quench
- Fig. – Figure
- LAO – Linear Alpha Olefins
- LLDPE – Linear low density polyethylene
- MAO - Methylaluminoxane
- mCPBA - meta-Chloroperoxybenzoic acid
- Me, Methyl - CH<sub>3</sub>
- MeCN – Acetonitrile
- MMAO/PMAO/DMAO - Modified methylaluminoxane
- nacnac - 2,6-<sup>i</sup>Pr<sub>2</sub>C<sub>6</sub>H<sub>3</sub>)NC(<sup>t</sup>Bu)]<sub>2</sub>CH
- NMP - N-methyl-2-pyrrolidone
- NMR - Nuclear magnetic resonance
- N<sub>2</sub>P<sub>2</sub> - <sup>t</sup>BuN(H)SiMe<sub>2</sub>N(CH<sub>2</sub>CH<sub>2</sub>P<sup>i</sup>Pr<sub>2</sub>)<sub>2</sub>

OEP - Octaethylporphyrin  
otf - On-the-fly  
PE - Polyethylene  
Ph - Phenyl  
PhCl – Chlorobenzene  
phen - 1,10-phenanthroline  
 $P_2N$  -  $N[2-P(CHMe_2)2-4\text{-methylphenyl}]_2$  or  $Li-N(Si(Me_2)CH_2P(^iPr)_2)_2$   
PNP - R-N(PPh<sub>2</sub>)<sub>2</sub>  
Py - Pyridine  
QEXAFS - Quick Extended X-ray Absorption Fine Structure  
ROMP - Ring open metathesis polymerisation  
salen - Bis(salicylaldehyde)ethylenediamine  
SBz – S(CH<sub>2</sub>CH<sub>2</sub>SCH<sub>2</sub>-*p*-C<sub>6</sub>H<sub>4</sub>-C[CH<sub>3</sub>]<sub>3</sub>)<sub>2</sub>  
SHOP – Shell Higher Olefin Process  
SNS – HN(CH<sub>2</sub>CH<sub>2</sub>S-R)<sub>2</sub>  
tacn - Triazacyclononane  
TBHP - Tert-butyl hydroperoxide  
THF – Tetrahydrofuran  
TMC - 1,4,8,11-tetramethyl-1,4,8,11-tetraazacyclotetradecane  
TMEDA – Tetramethylethylenediamine  
TOF – Turnover Frequency  
Uv-Vis - Ultraviolet-Visible  
XAFS - X-ray Absorption Fine Structure  
XANES - X-ray Absorption near edge structure  
XAS - X-ray Absorption Spectroscopy  
XRD - X-ray diffraction

*“...No, it is impossible; it is impossible to convey the life-sensation of any given epoch of one’s existence – that which makes its truth, its meaning – its subtle and penetrating essence. It is impossible. We live, as we dream – alone...”*

- Marlow, Heart of Darkness.



**1.**

**Introduction.**

## 1.1 Linear Alpha Olefins

Linear  $\alpha$ -olefins (LAO) are a class of unsaturated, straight-chain hydrocarbons with a single double bond in the  $\alpha$ -position, with the general formula  $C_nH_{2n}$ . The world-wide demand for olefins is driven by consumer goods, for which the highest percentages are consumed in the making of linear low density polyethylene (LLDPE).

The most important of the LAOs are ethene ( $C_2H_4$ ) and propene ( $C_3H_6$ ). The majority of ethene and propene is produced by thermal cracking of hydrocarbon feedstocks. These are the basic building blocks to longer chain LAOs and are essential in the petrochemical market.<sup>[1]</sup>

### 1.1.1 Products

At the end of 2007, the global capacity of LAOs was at 3.4 m tonnes/year ( $t\text{ a}^{-1}$ ). The four largest consumer markets use  $\sim 84\%$  of the global consumption of LAOs. These areas include; for use as co-monomers for polyethylene and poly  $\alpha$ -olefins (56%), surfactants (12%), synthetic lubricants (11%) and petroleum additives (5%). The other 16% consumption is for plasticiser alcohols, alkenyl succinic anhydride, oil field chemicals and synthetic acids.<sup>[2]</sup>

Because of the reactive double bond, LAOs can be readily converted into many useful consumer goods. Many common transformations include oxidation, hydroformylation, oligomerisation, polymerisation, addition, alkylation and sulfonation.

For example, detergent alcohols represent high value products that are incorporated into speciality markets, such as surfactants, cosmetics and toiletries. These are formed by a two step process from the LAO precursor. First is hydroformylation of the LAO to yield the subsequent aldehyde, which can be easily reduced to the primary alcohol. Further reaction with ethylene oxide forms a variety of ethyloxalates which can be used as surfactants or be further derivatised.<sup>[3]</sup> LAOs of  $C_{12-18}$  can be converted to sulfates for the use as surfactants in the detergent industry. These products require high solubility across a wide temperature range and robustness in solution still allowing biodegradability. With the use of co-surfactants and modification of the hydrophobic tail, these targets can be achieved.<sup>[3b]</sup>

### 1.1.2 Industrial Production

Three companies dominate the global market of LAO production. These are Chevron Phillips (CPChem), INEOS and Shell. These produce full range LAOs using ethene oligomerisation processes. In addition, other production capacities are also available from companies such as Idemitsu, Mitsubishi, Sasol and Nizhnekamskneftekhim. All produce LAOs with an even number of carbon chain length except Sasol, which can produce C<sub>5-8</sub> using coal-based synthetic fuels.<sup>[3b, 4]</sup> The production capacities of these companies are shown in Table 1.1.

**Table 1.1** Displaying the global LAO capacity of each company and plant as of 2007.<sup>[2]</sup>

Company	LAO Production	Location	Capacity (kt a <sup>-1</sup> )
Sinopec	1-Hexene	Yanhua, China	50
Chevron Phillips	Full Range	Texas, USA	705
DOW Chemical	1-Octene	Tarragona, Spain	50
Idemitsu Petrochemical	Full Range	Ichihara, Japan	63
INEOS	Full Range	Feluy, Belgium	300
	Full Range	Alberta, Canada	250
Mitsubishi Chemical	Full Range	Kurashiki, Japan	60
Nizhnekamskneftekhim	Full Range	Nizhnekamsk, Russia	186
Q-Chem	1-Hexene	Mesaieed, Qatar	47
SABIC	Full Range	Al-Jubail, Saudi Arabia	150
Sasol	1-C <sub>5</sub> and 1-C <sub>6</sub>	Sasolburg, South Africa	230
	1-Octene	Sasolburg, South Africa	96
Shell	Full Range	Louisiana, USA	920
	Full Range	Stanlow, UK	330

At the end of 2005, INEOS closed its 505,000 t a<sup>-1</sup> LAO plant in Texas, USA. Since then four new production plants have started. In 2006, Sinopec Beijing Yanhua Petrochemical Company opened a 50,000 t a<sup>-1</sup> 1-hexene plant in China, which uses ethene trimerisation technology. In 2007, SABIC opened a full range 150,000 t a<sup>-1</sup> LAO plant in Al-Jubail, Saudi Arabia. In 2007, DOW Chemical opened a 50,000 t a<sup>-1</sup>

1-octene plant in Tarragonia, Spain in 2007 which uses a butadiene feedstock. In 2009, Q-Chem (a jointly owned company by CPChem and Qatar Petroleum) opened a full range 350,000 t a<sup>-1</sup> LAO plant in Mesaieed, Qatar. There are also plans in place by Sasol to open a new 1-octene plant in 2013, at 100,000 t a<sup>-1</sup>.<sup>[2, 4-5]</sup>

### **1.1.3 Technology**

The LAOs are mainly produced by catalytic oligomerisation of ethene. In many cases a mixture of linear C<sub>4</sub> - 20+ chain lengths are synthesised, usually dictated by a Shulz – Flory mathematical distribution. Selective chain lengths or ‘on-purpose’ technology provide certain discrete chain lengths, but full range production dominates. There are processes held by Shell, INEOS, CPChem, Sasol, SABIC and Idemitsu, some of which are discussed below in this chapter. The focus of research has now shifted to developing single chain lengths over full range production.<sup>[2]</sup>

### **1.1.4 Markets**

The LAO market has faced challenges during the start of the 21<sup>st</sup> century after an initial boost in 1999-2001. The market slowed because of rising raw material and energy costs due to a global economic recession, where increased prices were passed onto consumers. Despite this, demand recovered in 2005 as hurricanes disrupted LAO produced along the Gulf coast and with permanent closure of the INEOS Texas production plant, representing ~ 14% of LAO production. Demand continues to grow since 2005 and more so for specific chain lengths of 1-hexene and 1-octene.<sup>[4]</sup> The outlook could be problematic if oil prices remain high, but long term prospects are good for companies based in the Middle East and Asia.<sup>[2]</sup>

## **1.2 Principles of Catalysis<sup>[6]</sup>**

In order to understand how catalysts produce various length LAOs, a brief discussion of the principles of catalysis is required.

A catalyst is a substance that increases the rate of reaction without itself undergoing any permanent chemical changes. It is both a reactant and product of reaction. Catalysts are often used in key steps to produce a variety of synthetically

challenging chemicals. Understanding the mechanisms of catalytic reactions or cycles has always been an area of huge academic and industrial importance to help in the design of catalysts to provide high rates of reaction and specificities to give low amounts of unwanted by-products.

The efficiency of a catalyst can be defined by its turnover frequency (TOF). This frequency relates to the rate of reaction as a function of catalyst loading. The TOF is related to rate of reaction ( $k$ ) as given in Equation 1.1. This means a highly active catalyst will have a large TOF.

$$\text{TOF} = \frac{k}{[\text{Q}]}$$

TOF = Turnover frequency.

$k$  = rate of reaction.

[Q] = concentration of catalyst.

### **Equation 1.1 Turnover frequency.**

#### **1.2.1 Catalytic Pathway**

One of the main principles of a catalyst is the ability to regenerate its active form. The catalytic pathway must follow a cycle that consumes reactants, forms products and regenerates the catalytic species. In many cases the pre-catalyst undergoes changes to form the active species which is rarely isolated. A catalyst increases the reaction rate by introducing new pathways with a lower Gibbs energy of activation,  $\Delta_A G$  (Fig. 1.1). During this cycle a catalyst can undergo insertion or elimination reactions, oxidation or reduction at the metal, ligand substitution or dissociation.

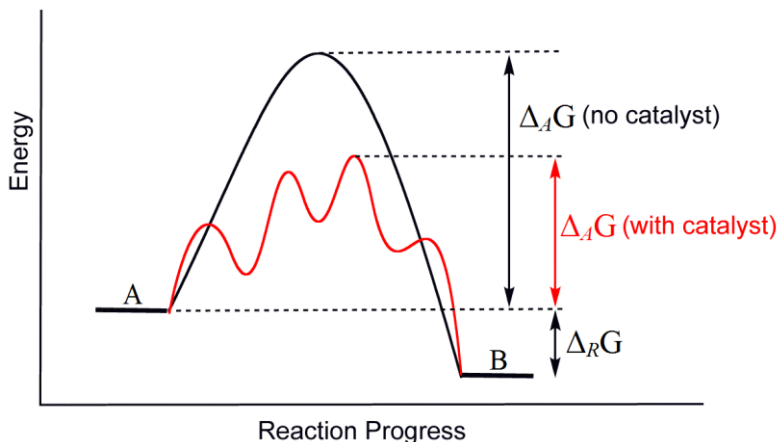


**Fig. 1.1** Graph displaying difference of activation energy ( $\Delta_A G$ ) with and without use of a catalyst and the Gibbs overall energy of reaction  $\Delta_R G$  between reactants (A) and products (B) for a hypothetical case.

### 1.2.2 Catalyst Types

Two main classes of catalyst exist, heterogeneous and homogeneous. The former is very popular in industry because of two main principles, robustness and ease of separation. Many are robust at high a temperature which makes them accessible to a range of operating conditions and, because they exist in a different phase to the product and reactants, separation of the product from the catalyst is very easy. This will be the extent of the discussion of heterogeneous systems as the main focus of this research is into homogeneous systems.

Homogeneous catalysts are often highly selective towards the formation of specific products. Homogeneous catalysts are usually more accessible for study because spectroscopic characterisation is often easier in solution than on a surface.

### 1.3 Hard-Soft Acid-Base (HSAB) Theory

The ligand environment of a transition metal homogeneous catalyst can be crucial in dictating how a metal behaves in a catalytic mechanism. This section summarises how this theory can help predict how a variety of different metals and ligands (Lewis acids and Lewis bases respectively) can interact.<sup>[7]</sup>

There are a large variety of Lewis acids and bases, for which many factors influence the interaction between electron pair donors and acceptors. HSAB theory predicts that hard metals (acids) will favour coordination to hard ligands (bases) and vice versa. This helps in predicting how different Lewis acids and bases from across the periodic table will interact. This theory is not absolute as some elements are borderline soft or hard, but nevertheless provides a useful rule of thumb.

The binding strength between a hard acid and a base will increase as the bonding becomes more ionic in character. The opposite is true of a soft acid, so bonding between a soft acid and base increases with increasing covalency. Table 1.2 shows the classification of several acids and bases.<sup>[8]</sup>

**Table 1.2** Showing the classification of different Lewis Acids and Bases.<sup>[8]</sup>

	<b>Hard</b>	<b>Borderline</b>	<b>Soft</b>
<b>Acids</b>	H <sup>+</sup> , Li <sup>+</sup> , Na <sup>+</sup> , K <sup>+</sup> Be <sup>2+</sup> , Mg <sup>2+</sup> , Ca <sup>2+</sup> , Cr <sup>2+</sup> , Cr <sup>3+</sup> , Sc <sup>3+</sup> , Al <sup>3+</sup> SO <sub>3</sub> , BF <sub>3</sub>	Fe <sup>2+</sup> , Co <sup>2+</sup> , Ni <sup>2+</sup> Cu <sup>2+</sup> , Zn <sup>2+</sup> , Pb <sup>2+</sup> SO <sub>2</sub> , BBr <sub>3</sub>	Cu <sup>+</sup> , Ag <sup>+</sup> , Au <sup>+</sup> , Tl <sup>+</sup> , Hg <sup>+</sup> Pd <sup>2+</sup> , Cd <sup>2+</sup> , Pt <sup>2+</sup> , Hg <sup>2+</sup> BH <sub>3</sub>
<b>Bases</b>	F, OH <sup>-</sup> , H <sub>2</sub> O, NH <sub>3</sub> CO <sub>3</sub> <sup>2-</sup> , NO <sub>3</sub> <sup>-</sup> , O <sup>2-</sup> SO <sub>4</sub> <sup>2-</sup> , PO <sub>4</sub> <sup>3-</sup> , ClO <sub>4</sub> <sup>-</sup>	NO <sub>2</sub> <sup>-</sup> , SO <sub>3</sub> <sup>2-</sup> , Br <sup>-</sup> N <sub>3</sub> <sup>-</sup> , N <sub>2</sub> C <sub>6</sub> H <sub>5</sub> N, SCN <sup>-</sup>	H <sup>-</sup> , R <sup>-</sup> , CN <sup>-</sup> , CO, I <sup>-</sup> SCN <sup>-</sup> , R <sub>3</sub> P, C <sub>6</sub> H <sub>6</sub> R <sub>2</sub> S

### 1.3 Transition Metal Chemistry

This section is a brief introduction into the three transition metals that form the basis of this research; scandium, chromium and molybdenum. In addition to this, directly relevant catalytic systems are further discussed for each transition metal as an introduction to that chapter (Chapter 4 – Mo; Chapter 5 – Sc; Chapter 6 – Cr).

#### 1.3.1 Scandium

Scandium is the first member of the 3d transition metals, with the electronic configuration of [Ar] 3d<sup>1</sup> 4s<sup>2</sup>. It has been relatively little studied compared to many of the other first row transition metals; this is in part due to its high expense because

although it is not a rare element, it has an even distribution in the earth, with no rich ores available. As it has only one stable oxidation state (+3, d<sup>0</sup>), this restricts any redox chemistry and the d<sup>0</sup> configuration usually leads to colourless complexes and limits spectroscopic investigations. The Sc(III) ion is highly oxophilic and is considered a very hard ion. It is the largest of the 3+ transition metal ions of the first row with radius = 0.745 Å for 6-coordination. As a result Sc(III) is known to exhibit a large range of coordination numbers, 3 – 9, although six coordinate is the most common.<sup>[9]</sup>

### 1.3.1.1 Scandium Macroyclic Compounds

A review of related Sc(III) macrocyclic complexes relevant to the scandium research of this thesis is presented in the introduction to Chapter 5. This section serves as an introduction to the chemistry of Sc(III) macrocyclic complexes. Scandium complexes with octaethylporphyrin (OEP)H<sub>2</sub> to form a 5-coordinate, 10-electron compound.<sup>[10]</sup> Reaction of the Li<sub>2</sub>(OEP) + [ScCl<sub>3</sub>(THF)<sub>3</sub>] in refluxing toluene gives >90% of [ScCl(OEP)]. This can then be treated with [Mg(Me)<sub>2</sub>(dioxane)] to give the alkylated [ScMe(OEP)]. The Sc(III) ion is too large to coordinate within the porphyrin and so it sits above the N<sub>4</sub> plane with the further coordinating ligand forced into the *cis*-configuration (Fig. 1.2).

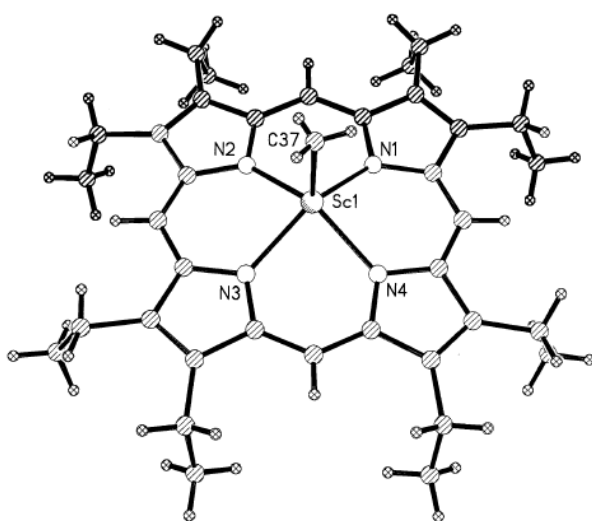
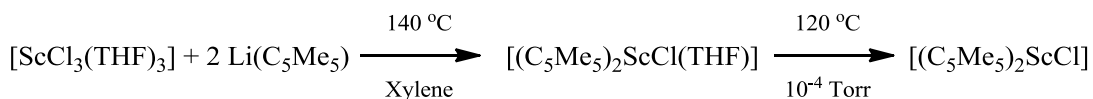


**Fig. 1.2** Scandium alkyl five-coordinate complex with porphyrin ring.<sup>[10-11]</sup>

### 1.3.1.2 Scandium Cyclopentadienyl Complexes

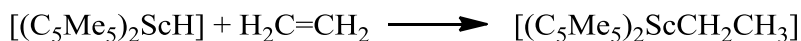
Bercaw *et al.*<sup>[12]</sup> synthesised the first pentamethyl scandocene complex,  $[(C_5Me_5)_2ScCl]$  (Scheme 1.1).



### Scheme 1.1 Synthesis of $[(C_5Me_5)_2ScCl]$ .

The  $[(C_5Me_5)_2ScCl]$  undergoes alkylation with LiR ( $R = Me, C_6H_5, o\text{-}C_6H_5\text{-}Me$ ) to give the subsequent  $[(C_5Me_5)_2ScR]$  complexes. The alkylated species can undergo further transformations including hydrogenolysis with  $H_2$  in THF to form  $[(C_5Me_5)_2ScH(THF)]$ , which can then react with unsaturated substrates such as ethene and propene at  $-80\text{ }^\circ C$ .<sup>[13]</sup>

$[(C_5Me_5)_2ScH]$  can oligomerise ethene or propene to give a Poisson distribution of odd number oligomers. Initial insertion by ethene into the Sc-H bond was rapid but it was found that the insertion rate of ethene decreased with increasing strength of the scandium-alkyl bond (Scheme 1.2).<sup>[14]</sup>



### Scheme 1.2 Ethene insertion into $[(C_5Me_5)_2ScH]$ .

Further derivatives of these catalysts are discussed in the introduction to Chapter 5.

### 1.3.2 Chromium

Naturally occurring chromium is Cr(III) and mined as iron chromite ( $FeCr_2O_4$ ), as this is the most stable oxidation state in the environment. Chromium has long been known to exist as 0 to +6 oxidation states. The most common oxidation states are 0, +3 and +6.<sup>[15]</sup>

### 1.3.2.1 Low Valent Chromium Carbonyl Complexes

$\text{Cr}(0)$  is a stable oxidation state of chromium and in many cases,  $\text{Cr}(0)$  forms hexacoordinate species to form highly stable 18-electron complexes, such as  $[\text{Cr}(\text{CO})_6]$  and  $[\text{Cr}(\text{bipy})_3]$ .<sup>[16]</sup>

$\text{Cr}(0)$  is a relatively unexplored oxidation state for ethene oligomerisation. The Tosoh Corporation filed a number of patents for ligands with  $\text{Cr}(\text{CO})_3$  complexes.<sup>[17]</sup> The most prominent of these was a  $[\text{Cr}(\text{CO})_3(1,3,5\text{-trimethylbenzene})]$  complex, which in the presence of dibutyl sulphide and  $^t\text{Bu}_3\text{Al}$  at a ratio of 1:10:20 gave an activity of 70,900 g/g Cr/h with overall selectivity of 85% 1-C<sub>6</sub>.<sup>[18]</sup>

Much of the work in this thesis makes use of thioether ligand complexes and their subsequent impact on catalysis. The low valent  $\text{Cr}(0)$  oxidation state generally favours soft,  $\sigma$ -donor/ $\pi$ -acceptor ligands, often including CO. Many such complexes have been reported, including those with neutral tridentate sulfur (thioether) ligands, as shown in (Fig. 1.3).<sup>[19]</sup> The tripodal thioether complex was synthesised *in situ* from  $[\text{Cr}(\text{CO})_3(\text{MeCN})_3]$  in presence of the ligand. This complex was relatively unstable compared to the Mo(0) analogue and thus was never isolated. The complex was found to readily convert to the  $[\text{Cr}(\text{CO})_4(\eta^2\text{-tripodal S}_3)]$ . The corresponding [9]aneS<sub>3</sub> (1,4,7-trithiacyclononane) complex was found to be more robust and synthesised from  $[\text{Cr}(\text{CO})_6]$  and NaBH<sub>4</sub> in the presence of [9]aneS<sub>3</sub> to give the corresponding *fac*-octahedral  $[\text{Cr}(\text{CO})_3([9]\text{aneS}_3)]$  complex.

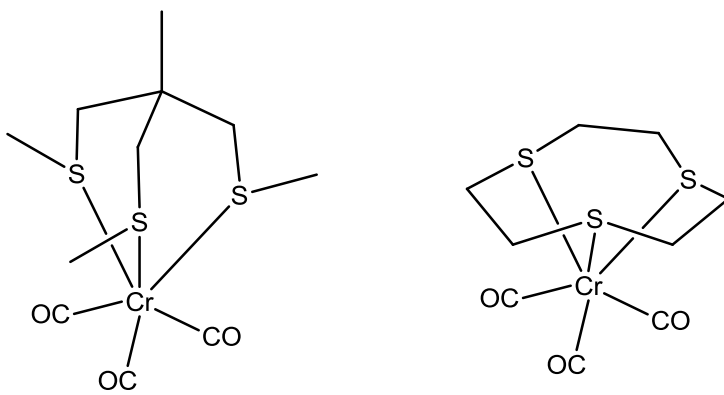


**Fig. 1.3** Examples of  $[\text{Cr}(\text{CO})_3(\text{S}_3)]$  type complexes.<sup>[19]</sup>

Considering the relatively weak coordination of the sulfur demonstrated by the tripodal S<sub>3</sub> ligand, perhaps the observed increase in activity of  $[\text{Cr}(\text{CO})_3(1,3,5\text{-trimethylbenzene})]$

trimethylbenzene)] in the presence of dibutyl sulfide, is provided by a weak coordination of dibutyl sulfide, essentially providing a vacant coordination site on the activated complex.

In 2007, Cr(0) and Cr(I) carbonyl complexes with PNP and dppe ligands were investigated (PNP =  $i\text{PrN}(\text{PPh}_2)_2$ , dppe =  $\text{Ph}_2\text{PC}_2\text{H}_4\text{PPh}_2$ ).<sup>[20]</sup> Synthesis of the Cr(0)  $[\text{Cr}(\text{CO})_4(\text{PNP})]$  complex from  $[\text{Cr}(\text{CO})_6] + \text{PNP}$ , gave very low activity for ethene oligomerisation but oxidising to Cr(I) using  $\text{Ag}[\text{Al}(\text{OC}\{\text{CF}_3\}_3)_4]$  to give the corresponding  $[\text{Cr}(\text{CO})_4(\text{PNP})][\text{Al}(\text{OC}\{\text{CF}_3\}_3)_4]$  complex gave activities up to 120,000 g/g Cr/h for ethene oligomers  $\text{C}_6$  (~ 20%) and  $\text{C}_8$  (~ 70%). This lends support to the theory of a Cr(I)/Cr(III) active cycle for selective ethene oligomerisation.

### 1.3.2.2 Chromium(II) Chemistry

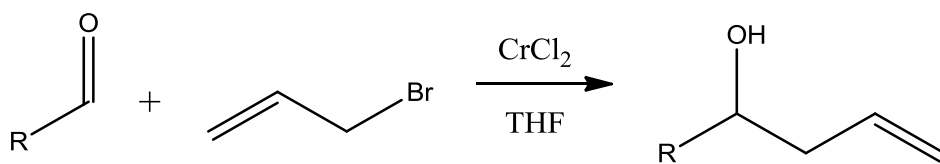
Chromium (II) complexes tend to form distorted structures such as a distorted trigonal bipyramidal geometry with tripodal ligands,<sup>[21]</sup> for example  $[\text{Cr}(\{\text{Et}_2\text{N C}_2\text{H}_4\}_2\text{NC}_2\text{H}_4\text{PPh}_2)\text{X}]^+$  (where X = Br or I). These are typically high-spin with two expected d-d transitions observed in the UV-Vis spectra. Also distorted tetrahedral complexes are also known, such as  $[\text{CrCl}_2(\text{MeCN})_2]$  and  $[\text{CrI}_2(\text{OPPh}_3)_2]$ .<sup>[16]</sup>

Distorted octahedral complexes are also observed where two ligands are usually situated farther from the metal than the other four.  $\text{CrCl}_2$  displays four chlorides at 2.39 Å and two at 2.90 Å. Similar distortions are seen for  $\text{CrF}_2$  and  $\text{CrBr}_2$ .  $\text{Cr}_2\text{F}_5$  contains both  $\text{Cr}^{2+}$  and  $\text{Cr}^{3+}$  in octahedral sites. The octahedron about  $\text{Cr}^{2+}$  is highly distorted with four short 1.96 – 2.01 Å bonds and two long 2.57 Å bonds.<sup>[16]</sup> The 3+ oxidation state is also considerably more inert towards ligand substitution relative to the 2+ oxidation state based upon ligand exchange rates.<sup>[22]</sup> This distortion and reactivity around  $\text{Cr}^{2+}$  can be explained by its electronic structure.

As  $\text{Cr}^{2+}$  is commonly high spin  $d^4$  ( $t_{2g}^3, e_{2g}^1$ ), Jahn-Teller distortions are expected in an octahedral field. This leads to one allowed electronic d-d transition for an octahedral field which leads to several superimposed transitions because of Jahn-Teller distortion.

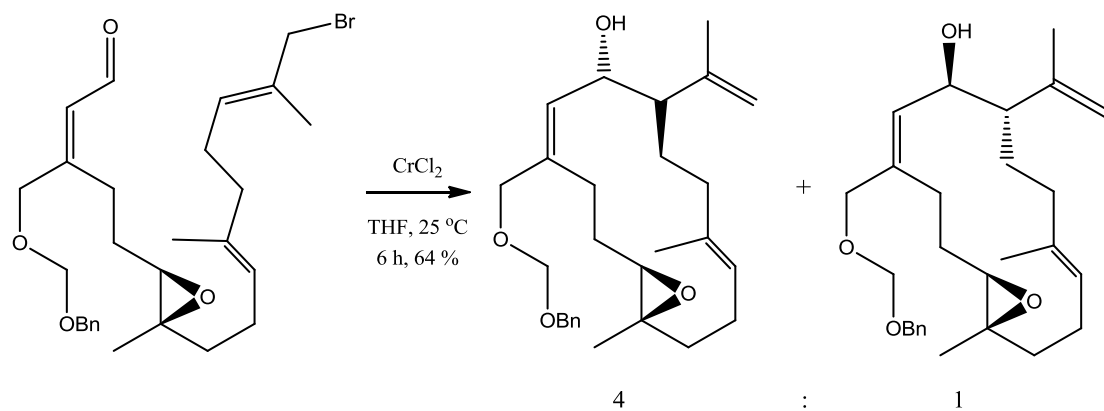
Chromium (II) salts have been widely used as reducing agents.<sup>[23]</sup> Hiyama examined the use of  $\text{CrCl}_2$  with allyl halides to form organochromium intermediates for carbon-carbon bond formation (Scheme 1.3).<sup>[24]</sup>  $\text{CrCl}_2$  displays a high

chemoselectivity as esters, cyano groups and epoxides are tolerated in the coupling step and aldehydes react preferentially in the presence of ketones.<sup>[25]</sup>



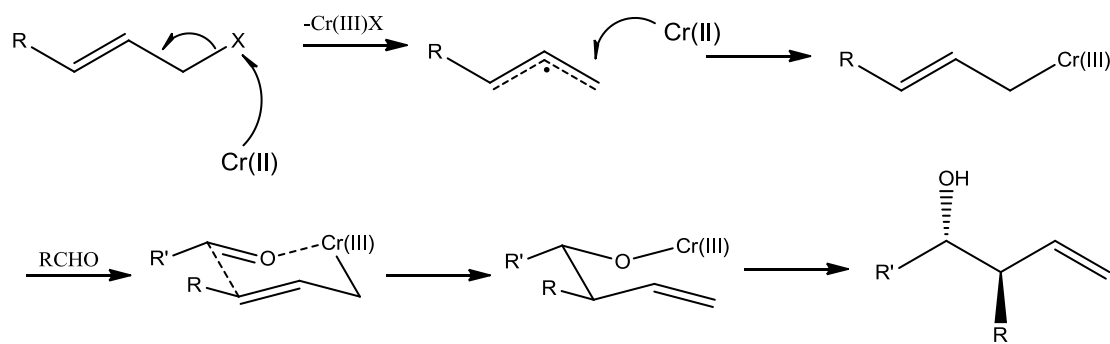
**Scheme 1.3** Coupling of aldehyde and vinyl bromide by  $\text{CrCl}_2$ .<sup>[24]</sup>

A good example of this is the Still's and Mobilio's synthesis of marine cembranoid antitumor agent Asperdiol.<sup>[26]</sup> This displays regio- and stereo-selectivity and compatibility of an epoxide group (Scheme 1.4).



**Scheme 1.4**  $\text{CrCl}_2$  promoted cyclisation in the synthesis of Asperdiol.<sup>[26]</sup>

The  $\text{CrCl}_2$  is thought to remove the halogen in a one electron oxidation to give an allyl radical. This is then rapidly reduced by a second Cr(II) species, forming the allyl chromium(III) species. The regio- and stereo-selectivity is thought to be a result of a chair formation transition state upon coordination of the aldehyde. The Cr atom is located at the least sterically hindered end, to which the aldehyde coordinates through the oxygen lone pair. The R group of the aldehyde will then adopt the equatorial position to avoid interaction of the Cr ligands. The Cr(III) species is thought to be hexacoordinate containing two chlorides and two solvent molecules (Scheme 1.5).<sup>[27]</sup>



**Scheme 1.5** Stereoselective coupling mechanism of an aldehyde and an alkene using  $\text{CrCl}_2$ .<sup>[27]</sup>

### 1.3.2.3 Chromium (III) Chemistry

The  $\text{Cr(III)}$  is the most common oxidation state for chromium and thousands of hexacoordinate complexes are known. Considering the electronic structure of  $\text{Cr}^{3+}$  in an octahedral field, a stabilisation is gained by having one electron in each of the lowest energy d-orbitals ( $t_{2g}^3$ ,  $e_{2g}^0$ ), which would explain why octahedral  $\text{Cr}^{3+}$  complexes are so favourable. Many examples are discussed in the later sections of this introduction and in the introduction section of Chapter 6.

Other coordination numbers are known such as three coordinate planer complex  $[\text{Cr}(\text{N}^t\text{Pr}_2)_3]$ .<sup>[28]</sup>  $\text{CrCl}_3$  can also form adducts with ethers, amines and phosphines to give  $\text{CrCl}_3 \cdot 2/3 \text{ L}$  complexes. The  $[\text{CrCl}_3(\text{NMe}_3)_2]$  adduct is trigonal bipyramidal with axial amine groups.<sup>[29]</sup>

### 1.3.2.4 Chromium (IV)/(V)

$\text{Cr(IV)}$  is a relatively unusual oxidation state of chromium. In aqueous solutions it is known to readily disproportionate to  $\text{Cr(III)}/\text{Cr(VI)}$  species.<sup>[30]</sup> Stable  $\text{Cr(IV)}$ -C/N/O compounds are known such as  $[\text{Cr}(\text{CH}_2\text{SiMe}_3)_4]$ ,<sup>[31]</sup>  $[\text{Cr}(\text{NEt}_2)_4]$  and  $[\text{Cr}(\text{O}^t\text{Bu})_4]$ .<sup>[32]</sup> These are blue, volatile, monomeric paramagnetic substances. The  $[\text{Cr}(\text{CH}_2\text{SiMe}_3)_4]$  complex is formed by the oxidation of  $[\text{CrCl}_3(\text{THF})_3]$  using  $\text{Me}_3\text{SiCH}_2\text{MgCl}$ . The dialkyl amide,  $[\text{Cr}(\text{NEt}_2)_4]$  is formed in a similar manner using  $\text{LiNEt}_2$ . These complexes display distorted tetrahedral structures.

An example of a rare  $[\text{CrH}_4(\text{dmpe})_2]$  ( $\text{dmpe} = \text{bis}(\text{dimethylphosphino})\text{ethane}$ ) complex was isolated and characterised by X-ray crystallography (Fig. 1.4).<sup>[33]</sup> This

forms an eight-coordinate Cr(IV) tetrahydrido species in a dodecahedral arrangement and was synthesised from the Cr(II) species  $[\text{CrCl}_2(\text{dmpe})_2]$  by reaction with  $^n\text{BuLi}$  in the presence of  $\text{H}_2$ . It is presumed the complex is formed *via* a Cr-butyl species, where a  $\beta$ -hydride transfer step gives the chromium hydride with release of the olefin.

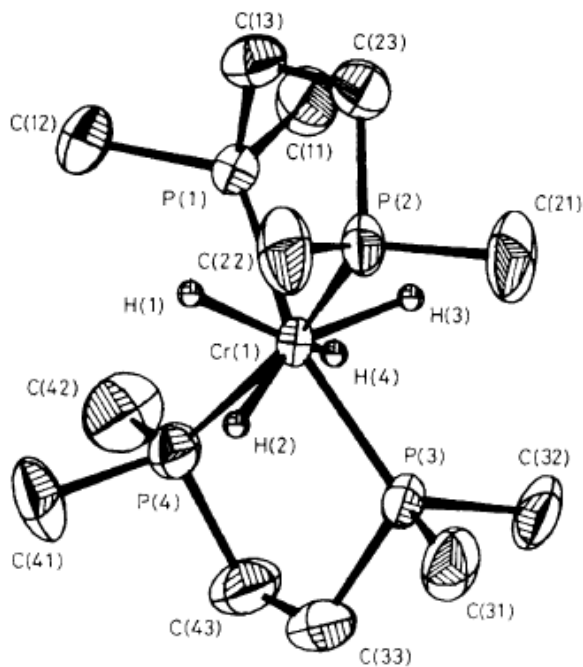


**Fig. 1.4** X-Ray structure of  $[\text{CrH}_4(\text{dmpe})_2]$ .<sup>[33]</sup>

The Cr(V) oxidation state is also a lesser known oxidation state, with most of the known complexes containing a chromyl group.<sup>[34]</sup> One such example is a square pyramidal complex based on an  $\text{N}_4$  macrocycle (Fig. 1.5).<sup>[35]</sup> This was formed from the reaction of  $\text{CrCl}_2$  and isobutylhydroperoxide reagent in the presence of the lithiated form of the ligand. The CrO bond was identified using X-ray crystallography with a distance of 1.57 Å.

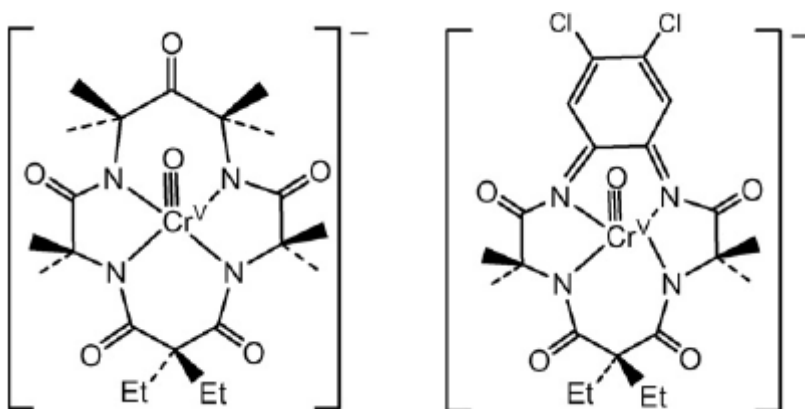


**Fig. 1.5** Square pyramidal Cr(V) oxide complexes with macrocyclic tetraamido-*N* ligand.<sup>[35]</sup>

Further examples of Cr(V) complexes containing nitrogen donor ligands include  $[\text{CrO}(\text{salen})]^{+}$ ,<sup>[36]</sup> distorted octahedral  $[\text{CrO}(\text{TMC})(\text{OCH}_3)]^{2+}$ ,<sup>[37]</sup> and  $[\text{CrO}_2(\text{phen})_2]^{+}$ ,<sup>[38]</sup> complexes (salen = bis(salicylaldehyde)ethylenediamine; TMC = 1,4,8,11-tetramethyl-1,4,8,11-tetraazacyclotetradecane; phen = 1,10-phenanthroline).

#### 1.3.2.4 Chromium(VI) Chemistry

Chromium(VI) is a common oxidation state of chromium, being  $3d^0$ . These complexes are usually chromates and act as strong oxidising agents. The compound  $\text{CrO}_3$  forms a yellow tetrahedral chromate ion  $\text{CrO}_4^{2-}$  at pH 6, a  $\text{HCrO}_4^-$  and an orange-red dichromate  $\text{Cr}_2\text{O}_7^{2-}$  at pH 2-6 and  $\text{H}_2\text{CrO}_4$  below pH 1.<sup>[39]</sup>

When considering the proposed cycle for ethene oligomerisation, high valent chromium metallocycles are very plausible. One such study involved the synthesis of Cr(VI) alkyl and metallocycle complex.<sup>[40]</sup> This was made possible by using the more stable  $[\text{Cr}(\text{N}^t\text{Bu})_2(\text{OSiMe}_3)_2]$  precursor over the more toxic  $\text{CrO}_2\text{Cl}_2$ . This was readily converted to  $[\text{Cr}(\text{N}^t\text{Bu})_2(\text{Py})\text{Br}_2]$  complex by 2 mol. equivs. of  $\text{SiMe}_3\text{Br}$  in pyridine in 90% yield. Use of pyridine was advantageous as it allowed crystallisation of the product.

Alkylation of  $[\text{Cr}(\text{N}^t\text{Bu})_2(\text{Py})\text{Br}_2]$  by reaction with 2 mol. equivs. of  $\text{Me}_3\text{SiCH}_2\text{MgCl}$  gave the  $[\text{Cr}(\text{N}^t\text{Bu})_2(\text{CH}_2\text{SiMe}_3)_2]$  complex cleanly. The alkyl analogue  $[\text{Cr}(\text{N}^t\text{Bu})_2(\text{CH}_2\text{CMe}_3)_2]$  prepared by the same method was identified by  $^1\text{H}$  and  $^{13}\text{C}$  NMR spectroscopy, but could not be isolated cleanly.<sup>[40]</sup>

Reaction of  $[\text{Cr}(\text{N}^t\text{Bu})_2(\text{Py})\text{Br}_2]$  with  $o\text{-C}_6\text{H}_4[(\text{CHSiMe}_3)_2\text{Li}\text{-TMEDA}]$  (TMEDA = tetramethylethyldiamine) in ether gave the  $[\text{Cr}(\text{N}^t\text{Bu})_2(\eta^2\text{-}o\text{-C}_6\text{H}_4[(\text{CHSiMe}_3)_2])]$  metallocyclic complex in 64% yield. The X-ray structure is shown in Fig. 1.6.<sup>[40]</sup>

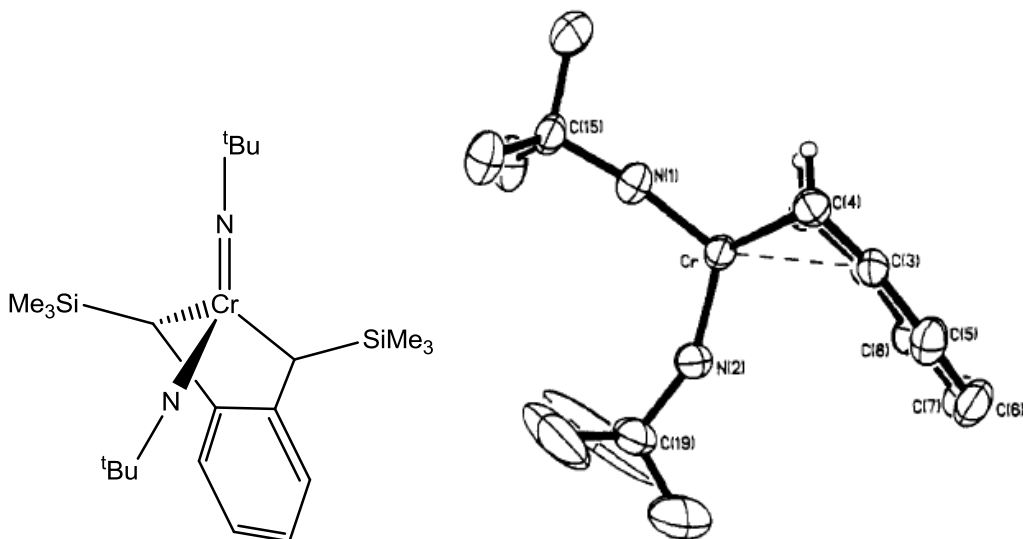


**Fig. 1.6** X-ray structure of  $[\text{Cr}(\text{N}^t\text{Bu})_2(\eta^2\text{-}o\text{-C}_6\text{H}_4[(\text{CHSiMe}_3)_2])]$ , where  $\text{SiMe}_3$  groups have been omitted for clarity.<sup>[40]</sup>

The  $t\text{BuN}$  ligands adopt a *cis* formation around the Cr ion as it is thought this minimises competition of  $\pi$ -backbonding into the metal d-orbitals. This backbonding allows stabilisation of the observed chromium complexes and as such, suppresses their reactivities.<sup>[40]</sup>

### 1.3.3 Molybdenum<sup>[16]</sup>

Molybdenum has found use across a huge range of chemistry, physics and biology due to its chemical versatility. Molybdenum is chiefly mined as molybdenite ( $\text{MoS}_2$ ) or molybdates, such as wulfenite ( $\text{PbMoO}_4$ ).

Molybdenum chemistry can exhibit significantly different chemistry from that of chromium. Cr(VI) is a powerful oxidant whereas Mo(VI) and W(VI) are relatively stable and not easily reduced, forming extensive series of polynuclear oxa-anions. Second and third row transition metal elements are often more prone to forming metal-metal bonds more often than their first row counterparts.

Heavier elements tend to give low-spin complexes as the 4d-orbital is spatially larger than the 3d-orbital. When the orbital is doubly occupied, a 4d-orbital will experience less electronic repulsions relative to a 3d-orbital. Also a given set of ligands produce a larger d-orbital splitting for 4d than 3d-orbitals, increased by about 25-50%. The magnetic measurements are usually much more complex, where first row transition metal elements are often straightforward. The second and third row transition metal elements exhibit high spin-orbit coupling constants at room temperature for magnetic moment measurements, increasing the difficulty for their interpretation. For the first row elements, the spin-orbit coupling constant is much lower at room temperature, allowing for their more straightforward analysis.

Below is a brief introduction into some of the coordination chemistry based around examples of molybdenum halide complexes.

### 1.3.3.1 Low Valent Molybdenum Complexes

Low valent Mo complexes can be formed from  $[\text{Mo}(\text{CO})_6]$  starting material. Reacting  $[\text{Mo}(\text{CO})_6]$  with  $\text{Cl}_2$  gives  $[\text{Mo}(\text{CO})_4\text{Cl}_2]$ . This reacts readily with  $\text{Ph}_3\text{P}$  and  $\text{Ph}_3\text{As}$  to give the corresponding  $[\text{Mo}(\text{Ph}_3\text{P})_2(\text{CO})_3\text{Cl}_2]$ .<sup>[41]</sup>  $[\text{Mo}(\text{CO})_4\text{Cl}_2]$  also reacts with isocyanides to give seven coordinate  $[\text{Mo}(\text{CNR})_5\text{X}_2]$ .<sup>[42]</sup>  $[\text{Mo}(\text{CO})_6]$  can react directly with N, P and As donors to displace one to four CO groups. Further reaction of these with  $\text{X}_2$  (where  $\text{X}_2 = \text{Cl}, \text{Br}, \text{I}$ ) affords six or seven coordinate Mo(I – III) complexes.<sup>[16]</sup> Using  $[\text{MoCl}_4(\text{EtCN})_2]$  instead of  $[\text{Mo}(\text{CO})_6]$  gives similar non-CO containing complexes.<sup>[43]</sup>

Reaction of  $[\text{Mo}(\text{CO})_3(\text{cycloheptatriene})]$  with  $\text{HN}(\text{C}_2\text{H}_4\text{SEt})_2$  gave the corresponding  $[\text{Mo}(\text{CO})_3(\text{HN}\{\text{C}_2\text{H}_4\text{SEt}\}_2)]$ .<sup>[44]</sup> This complex is discussed in more detail in the introduction to Chapter 4 as this is relevant to Mo(SNS) research.

### 1.3.3.2 High Valent Molybdenum Complexes

Mo(VI) organometallics have found great importance in homogeneous catalysis as ring opening metathesis catalyst. This is discussed in depth within the introduction of Chapter 4. This section serves as a brief introduction into some high valent Mo coordination compounds.

[MoCl<sub>5</sub>] provides an easy route to many Mo(IV) coordination compounds, by reduction to [MoCl<sub>4</sub>(Et<sub>2</sub>O)<sub>2</sub>].<sup>[45]</sup> This can be reacted in the presence of several ligand types to give a range of Mo(IV) complexes, for example a seven coordinate [MoCl<sub>4</sub>(HN{C<sub>2</sub>H<sub>4</sub>S-decyl})<sub>2</sub>].<sup>[44]</sup> Mo(IV) complexes can display a range of coordination complexes including a distorted tetrahedral [Mo(NMe<sub>2</sub>)<sub>4</sub>], octahedral [Mo(NCS)<sub>6</sub>]<sup>2-</sup>,<sup>[16]</sup> oxo-Mo(IV) complex [MoOCl<sub>2</sub>(PMe<sub>2</sub>Ph)<sub>3</sub>].<sup>[46]</sup>

[MoCl<sub>5</sub>] has a high propensity to abstract oxygen to form a range of Mo(V) compounds such as [MoOCl<sub>3</sub>(OSMe<sub>2</sub>)<sub>2</sub>] and [MoOCl<sub>3</sub>(Ph<sub>3</sub>PO)<sub>2</sub>]. These can be formed from reaction of MoCl<sub>5</sub> + Me<sub>2</sub>SO or Ph<sub>3</sub>PO. Nearly all Mo(V) oxo compounds contain MoO, Mo<sub>2</sub>O<sub>3</sub> or Mo<sub>2</sub>O<sub>4</sub> units.<sup>[16]</sup>

Many Mo(VI) are dioxo-complexes. These are binuclear oxo complexes with Mo=O terminal groups and Mo-O-Mo bridging units as observed for K<sub>2</sub>[Mo<sub>2</sub>O<sub>5</sub>(C<sub>2</sub>O<sub>4</sub>)<sub>2</sub>(H<sub>2</sub>O)<sub>2</sub>].<sup>[16]</sup>

### 1.3.3.3 Molybdenum Multiple bonds

The chemistry of Mo(4d<sup>3</sup>)-Mo(4d<sup>3</sup>) multiply bonded complexes is diverse and can provide a range of reactivity dictated by the Mo-Mo bonding.<sup>[47]</sup>

Mo-Mo triply bonded structures such as Mo<sub>2</sub>L<sub>6</sub> adopt ethane like staggered geometries.<sup>[47]</sup> These complexes are common for anionic ligands such as SiMe<sub>3</sub><sup>-</sup>,<sup>[48]</sup> NR<sub>2</sub><sup>-</sup>,<sup>[49]</sup> and OR<sup>-</sup>.<sup>[50]</sup> The Mo-Mo triple bond length is usually between 2.15 – 2.30 Å. The Mo-Mo triple bond consists of one σ-bond and two π-bonds derived from the overlapping z<sup>2</sup> orbitals (σ-bond) and both xz and yz orbitals giving the two degenerate π bonds. The three Mo-L σ-bonds overlap with the metal s, p<sub>x</sub> and p<sub>y</sub> orbitals, leaving the d<sub>x<sup>2</sup>-y<sup>2</sup></sub> and xy orbitals available for π-bonding with ligands such as NMe<sub>2</sub> that have filled π-orbitals. This bonding is reflected by NMe<sub>2</sub> lying more in the plane to the Mo-Mo bond. This allows π-bonding of Me<sub>2</sub>N (p) and Mo (d) without disruption of the Mo-Mo π-bonding.<sup>[49]</sup> This is supported by molecular orbital calculations and photoelectron spectroscopy.<sup>[51]</sup> Many of these multiply bonded Mo complexes undergo a variety of reactions at mild conditions and in many cases, the multiple bonding of Mo is retained.

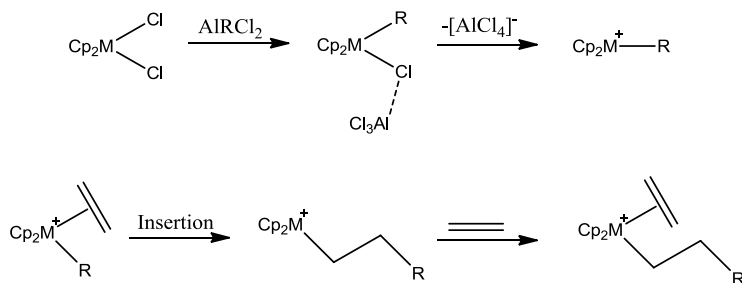
## 1.4 Ethene Polymerisation

Ethene polymerisation is the process of forming new carbon-carbon bonds to give high molecular weight polyethylene.<sup>[52]</sup> One of the most important classes of alkene polymerisation catalysis processes is the Ziegler-Natta process.

### 1.4.1 Ziegler-Natta Polymerisation

Most polyolefins are produced by the Ziegler-Natta heterogeneous catalyst, based on supported-TiCl<sub>4</sub> with trialkylaluminum activator. This exhibits high activity for ethene and propylene polymerisation and has been used since the 1950s.<sup>[53]</sup> This type of polymerisation was attempted to be homogenised using a [Cp<sub>2</sub>TiCl<sub>2</sub>] (Cp = cyclopentadienyl) and dialkylaluminum chloride as a co-catalyst. This system gave very little activity for ethene polymerisation, but was used to give insights into the more active systems.<sup>[54]</sup> A remarkable increase in activity for polyethylene production was discovered by Sinn when a small amount of water was added to [Cp<sub>2</sub>ZrMe<sub>2</sub>] and AlMe<sub>3</sub>, which was inactive before the addition of H<sub>2</sub>O.<sup>[55]</sup> It was found that the addition of water gave methylaluminoxanes (MAO), via partial hydrolysis of AlMe<sub>3</sub>, which was responsible for the increased activity of polymerisation.<sup>[56]</sup> Polymers produced using this catalyst had molecular weights between 100,000 and 200,000 and [Cp<sub>2</sub>ZrCl<sub>2</sub>] metallocene give activities of 3200 kg PE/g Zr / h.

The accepted mechanism for Ziegler–Natta alkene polymerisation is insertion of the alkene to the cationic metallocene catalyst as shown in Scheme 1.6, known as the Cossee-Arlman mechanism.<sup>[57]</sup> The aluminium activator first alkylates the metallocene pre-catalyst and then further removes a halide to yield the active cationic species. Coordination of an alkene, such as ethene, can then be inserted into the alkyl ligand in a non-redox process. This process can occur until a chain termination step occurs to give the metal hydride after a β-hydride elimination step.



**Scheme 1.6** Mechanism of alkene insertion by a homogeneous Ziegler-Natta catalyst ( $\text{M} = \text{Zr}, \text{Ti}$ ;  $\text{Cp} = \text{Cyclopentadienyl}$ ).<sup>[57c]</sup>

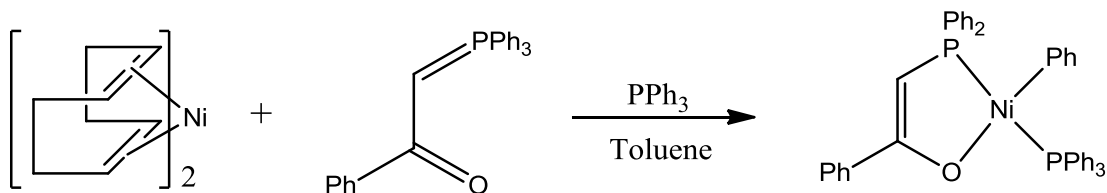
## 1.5 Ethene Oligomerisation

Oligomerisation is the conversion of a monomer (a molecule of low RMM) to an oligomer (a molecule of intermediate RMM).<sup>[52]</sup> In terms of ethene conversion, there are two main mechanisms of oligomerisation; a Shulz-Flory distribution, usually consisting of oligomers ranging from  $\text{C}_{4-40}$ , and selective ethene oligomerisation, where a process is put in place to produce one particular chain length selectively.

A discussion of the main homogeneous catalysts used for both full range and selective oligomerisation processes follow. The nickel-catalysed ethene oligomerisation gives a Shulz-Flory distribution and the chromium-catalysed process is able to produce selective trimerisation and tetramerisation of ethene.

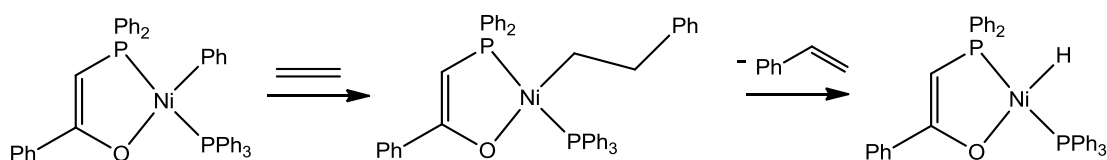
### 1.5.1 Nickel-Catalysed Ethene Oligomerisation

Nickel(II) catalysts of the general formula  $[\text{NiPh}(\text{L})(\text{L}')]$  ( $\text{L} = \text{tertiary phosphine}$ ;  $\text{L}' = \text{Ph}_3\text{P}=\text{CHC(O)Ph}$ ) have been used for over three decades as highly efficient catalysts for the production of linear  $\alpha$ -olefins.<sup>[58]</sup> These were first introduced by Keim to be suitable for ethene oligomerisation and have since been used in the Shell Higher Olefin Process (SHOP) as discussed below.<sup>[59]</sup> These catalysts are synthesised by oxidative addition of a keto-stabilised phosphorus ylide to  $[\text{Ni}(\text{cod})_2]$  ( $\text{cod} = \text{cycloocta-1,5-diene}$ ) with transfer of a phenyl group from the phosphorus to the Ni. (Scheme 1.7). This catalyst can convert 10-100 bar ethene at 50 °C to give olefins of 99% linearity, with >95%  $\alpha$ -olefins. This produces 48%  $\text{C}_{6-8}$  and 52%  $\text{C}_{10-18}$ .



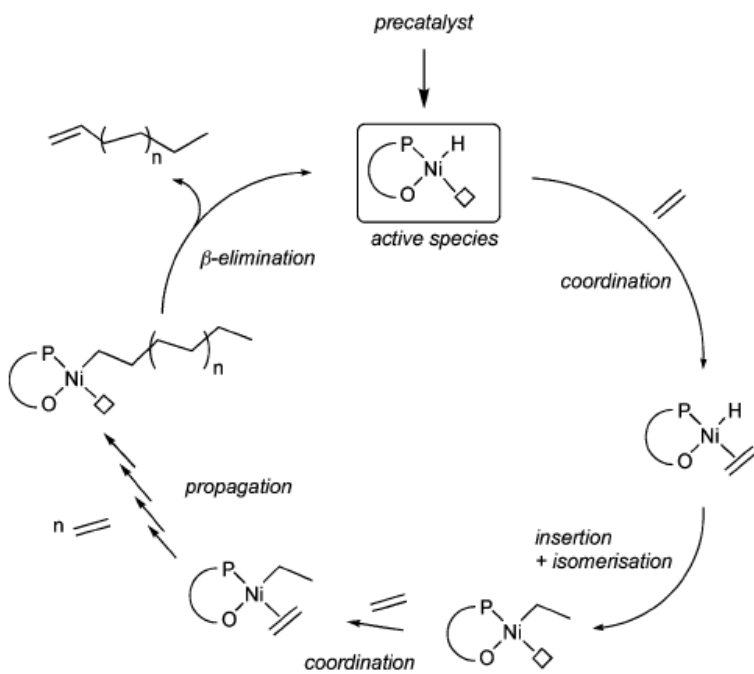
**Scheme 1.7** Synthesis of SHOP catalyst used to give a Shulz-Flory distribution of  $\alpha$ -olefins.<sup>[59a]</sup>

The pre-catalyst must undergo activation to form the active species. This occurs during the oligomerisation process where ethene is inserted into the Ni-Ph bond and subsequent loss of styrene produces the active hydride species (Scheme 1.8).<sup>[60]</sup>



**Scheme 1.8** Formation of active Ni-H species for ethene oligomerisation.<sup>[60]</sup>

The catalytic pathway of the nickel hydride is shown in Scheme 1.9. It is thought to proceed by a chain growth mechanism. Upon coordination of ethene, it undergoes migratory insertion with the hydride to produce the  $\text{Ni-CH}_2\text{CH}_3$  species.<sup>[61]</sup> This creates a vacant site to allow coordination of ethene and further insertion until chain termination by  $\beta$ -hydride elimination, producing the  $\alpha$ -olefin and nickel hydride.



**Scheme 1.9** Catalytic cycle of ethene oligomerisation by nickel hydrido species.<sup>[58]</sup>

### 1.5.2 Shell Higher Olefin Process

The Shell Higher Olefin Process is an industrial scale production of desired C<sub>10-14</sub>  $\alpha$ -olefins by the Shell Oil Company, making use of the nickel catalysed ethene oligomerisation route.<sup>[59a]</sup> This process consists of three steps, ethene oligomerisation, isomerisation and co-metathesis to produce  $\alpha$ -olefins of the range C<sub>10-14</sub> (Fig. 1.7).

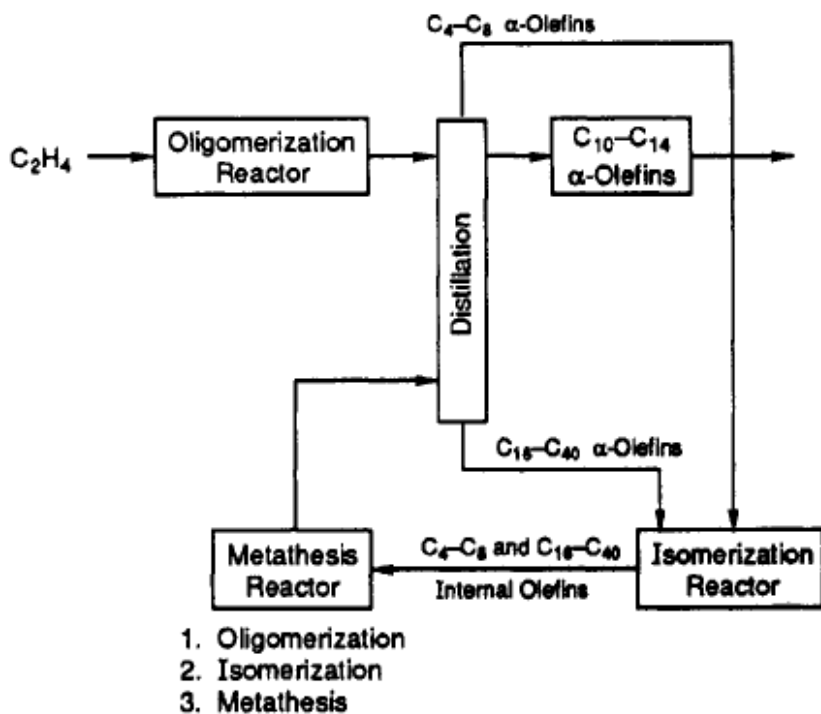


**Fig. 1.7** SHOP for production of C<sub>10-14</sub> α-olefins.<sup>[59b]</sup>

The first step uses a nickel catalyst generated from a keto-stabilised phosphorus ylide (Scheme 1.8).<sup>[59a]</sup> These oligomerisation catalysts are dissolved in solvents that are largely immiscible with α-olefins, making for easy separation and allows for any excess ethene and Ni catalysts to be recycled. As these catalysts produce a Shulz-Flory distribution of α-olefins ranging C<sub>4-40</sub>, these are split into three fractions; C<sub>4-8</sub>, desired C<sub>10-14</sub> and C<sub>16-40</sub>. The light and heavy fractions are fed back into the process for further reactions.

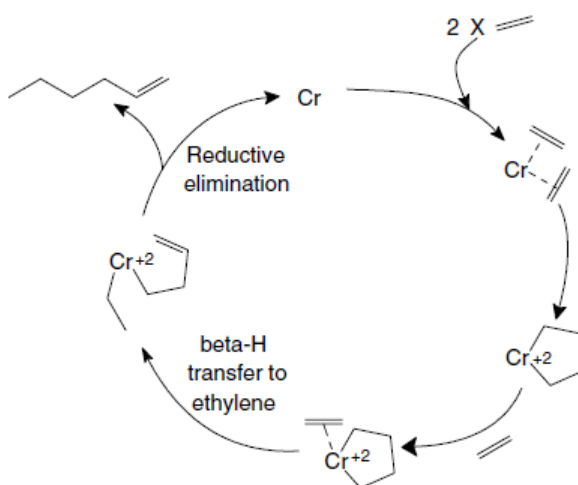
First is isomerisation, where the recycled α-olefins are converted to internal olefins. These converted olefins are then fed into a metathesis reactor where short and long chain internal olefins disproportionate. These newly formed internal olefins can then react with further ethene to obtain α-olefins where the process can continue.<sup>[62]</sup>

### 1.5.3 Selective Ethene Trimerisation

The originally proposed mechanism for alpha olefin production was the Cossee-Arlman chain growth mechanism (Scheme 1.6). At closer inspection, this mechanism does not allow for the high selectivity that has been observed by

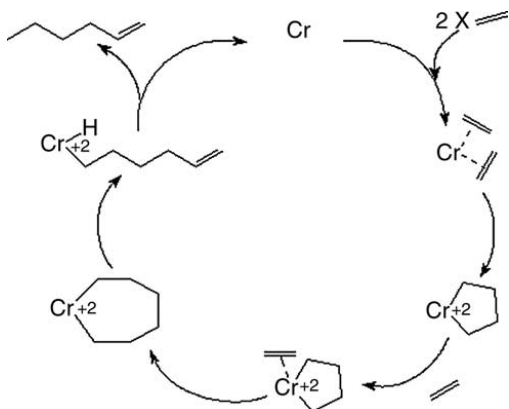
trimerisation catalysts, instead giving high molecular weight polyalkenes as given by the Zieger-Natta catalysts.

Manyik *et al.* first proposed the formation of a chromium metallocycle to give selective trimerisation in 1977 (Scheme 1.10).<sup>[63]</sup> It was proposed that a chromocyclopentane intermediate undergoes a  $\beta$ -hydride transfer, followed by insertion of ethene to allow reductive elimination of 1-hexene. This was derived from the investigation of a chromium (III)2-ethylhexanoate (Cr-2-EH) ethene polymerisation catalyst. The polyethylene production was assumed to be formed by ethene insertion into an alkyl chain and the 1-hexene was identified as being produced through a separate pathway. It was found that changing the pressure and temperature of the system could inhibit selective 1-hexene formation but polyethylene was still being produced.



**Scheme 1.10** Manyik proposed metallocycle growth mechanism with chromium.<sup>[63]</sup>

In 1989,<sup>[64]</sup> a 3 component system of Cr-2-EH, hydrolysed triisobutylaluminium and dimethoxyethane in heptane, was found to produce 1-hexene selectively up to 74% at 1.2 mol/mol Cr/s. Here, the generally accepted chromometallocycle pathway was first outlined by Briggs to give selective 1-hexene. This route favours the formation of a chromocycloheptane intermediate, where ethene insertion is favoured over  $\beta$ -hydride transfer of the chromocyclopentane. This species does undergo reductive elimination to give a chromium hydride and 1-hexene selectively (Scheme 1.11).



**Scheme 1.11** Briggs proposed cycle for selective ethene trimerisation.<sup>[64]</sup>

Crystal structures have been obtained to provide evidence of five- and seven-membered chromometallocycles (Fig. 1.8).<sup>[65]</sup> The seven-membered ring decomposes readily to liberate 1-hexene. In addition to this, chromium hydride systems have also been identified by X-ray crystallography.<sup>[66]</sup>

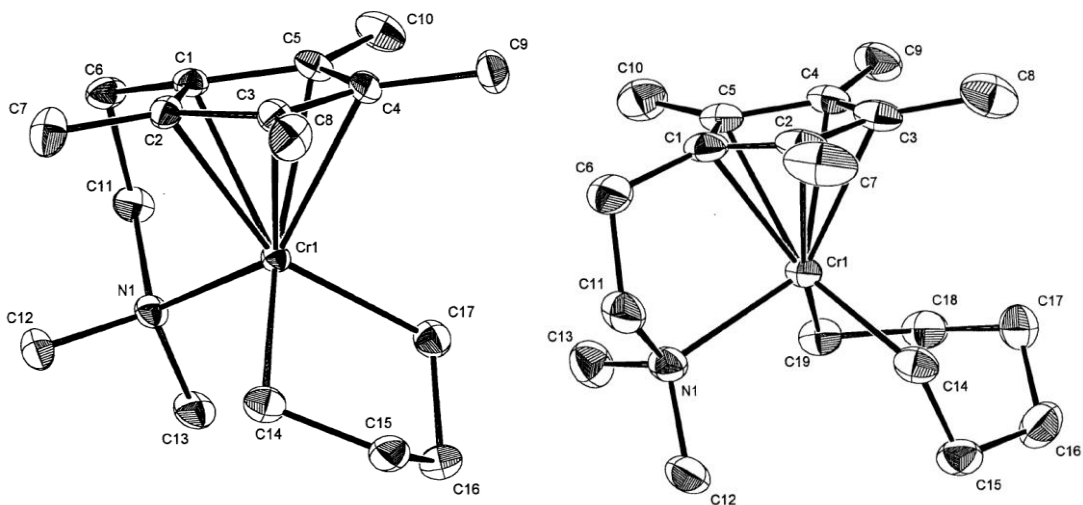
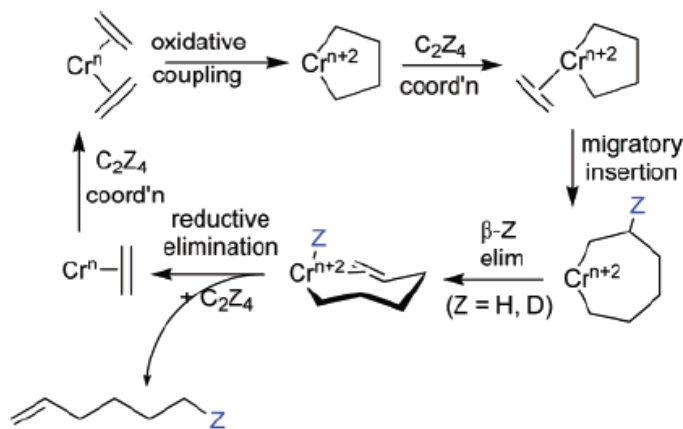


**Fig. 1.8** Crystal structures of chromocyclo-pentane and -heptane complexes.<sup>[65]</sup>

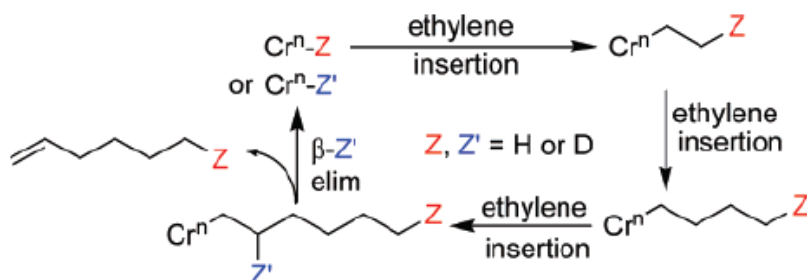
A deuterium study was undertaken to give weight to the proposed metallocycle growth pathway. Using a ratio of 1:1 C<sub>2</sub>H<sub>4</sub> and C<sub>2</sub>D<sub>4</sub>, a 1:3:3:1 mix of

$C_6H_{12}$ ,  $C_6H_8D_4$ ,  $C_6H_4D_8$  and  $C_6D_{12}$  respectively would be present only for the metallocycle route and so no H/D scrambling would be seen (Scheme 1.12).<sup>[67]</sup> The hydride on the metal is transferred back on to the same alkene during the reductive elimination step, so only even numbers of deuterium are expected.



**Scheme 1.12** Metallocycle pathway for the production of 1-hexene ( $Z$  indicates migratory H/D atom).<sup>[67]</sup>

The Cossee mechanism would give complex H/D mixtures and odd numbers of deuteriated hexenes would be seen (Scheme 1.13). This arises as the hydride on the metal is generated once the oligomer is liberated and then it transfers to the next coordinated ethene placed at the end of each new oligomer chain, causing a H/D scrambling effect. From the experimental results, only even numbers of deuterium were observed indicating a metallocycle mechanism.



**Scheme 1.13** 1-Hexene D/H scrambling as produced *via* the Cossee-Arlman chain growth mechanism.<sup>[67]</sup>

### 1.5.4 The Phillips Ethene Trimerisation Catalyst

This is the first commercialised selective ethene trimerisation process and the first trimerisation catalyst to yield selectively 1-hexene to higher than 90%.<sup>[68]</sup> Chevron Phillips successfully commercialised this process in 2003.<sup>[69]</sup>

The selective trimerisation of ethene was first discovered in the late 1980s when the catalytic properties of chromium pyrrolyl complexes were being investigated. The catalyst is formed from chromium(III) 2-ethylhexanoate (Cr-2-EH) and sodium pyrrolide in the presence of electron donor solvents, such as THF. The major product formed is an inorganic polymer, containing bridging amido pyrrolyl ligands. This was found to be active towards ethene oligomerisation at 25 mol. equivs. of trimethylaluminium to yield 83% 1-hexene and less than 2% polyethylene.<sup>[17]</sup> By 1999 this had improved to an activity exceeding 94,000 g/g Cr in 30 min. This was achieved using a mixture of Cr-2-EH, 2,5-dimethyl pyrrole, diethylaluminium chloride and triethylaluminium to yield a total 93% 1-hexene.<sup>[70]</sup>

In 2008, Gambarotta used a similar system to the Phillips trimerisation catalyst, a chromium(I) metal sandwich between two phenyl moieties, which was determined by X-ray crystallography (Fig. 1.19). For this complex, only Cr(I) gave high selectivity for 1-hexene as observed for the Phillips systems.<sup>[71]</sup>

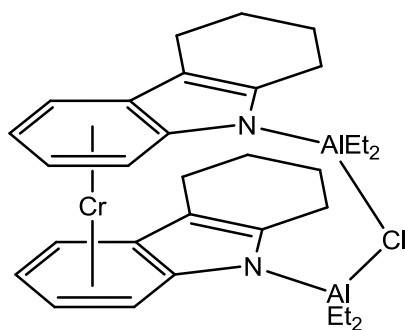


**Fig. 1.9** Chromium(I) pyrrolyl sandwich complex active for selective ethene trimerisation.<sup>[71]</sup>

In toluene, this complex was found to be catalytically inactive, which was supposed to form a  $[\text{Cr}(\text{I})(\pi\text{-arene})]$  complex. It was proposed that using the solvent methylcyclohexane allowed for a similar dissociation of the chromium from the

ligand except without the unfavourable competition from other  $\pi$ -donors, allowing for the coordination of ethene.

The same group prepared a dimeric, divalent chromium complex with one aluminato-pyrrolyl ring per chromium (Fig. 1.10).<sup>[72]</sup> This complex gave an activity of  $1.2 \times 10^6 \text{ g mol}^{-1} \text{ h}^{-1}$  and a 97.5% selectivity of C<sub>6</sub>. The Cr(II) dimer is proposed to undergo a disproportionation reaction in the presence of ethene to form the transient monovalent Cr species (Scheme 1.14).

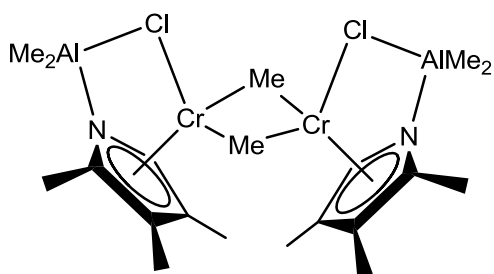
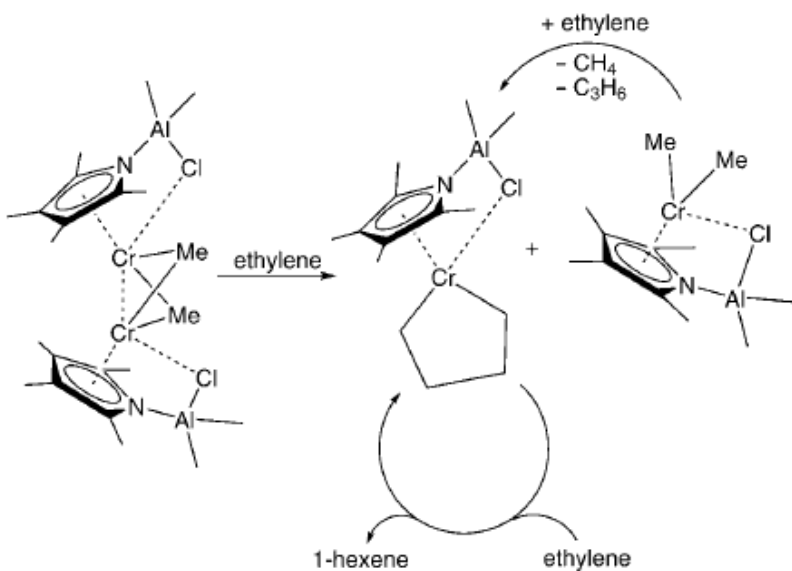


**Fig. 1.10** Displaying dimeric  $[(\eta^5\text{-}2,3,4,5\text{-Me}_4\text{C}_4\text{N}(\text{AlClMe}_2))\text{Cr}(\mu\text{-Me})]_2$  catalyst for selective ethene trimerisation.<sup>[72]</sup>



**Scheme 1.14** Metallocycle formation arising from the dimeric chromium pyrrolyl complex to give 1-hexene.<sup>[72]</sup>

In 2010, an EPR study of  $[\text{Cr}(\text{acac})_3]/\text{pyrrolyl}/\text{AlEt}_3/\text{AlEt}_2\text{Cl}$  systems found two active species in solution.<sup>[73]</sup> These were proposed as  $\text{Cr(III)-(pyrrolyl)}_x\text{Cl}_y\text{Et}_z\text{L}$  and  $\text{Cr(I)-(pyrrolyl)L}$  ( $\text{L}$  = unknown ligand). The maximum concentration of these species in the sample did not exceed 20% and so, the majority of the Cr species is thought to be an EPR silent Cr(II) species. This research investigated a low activity  $[\text{Cr}(\text{acac})_3]:\text{AlEt}_3$  (1:30) system and compared with the significantly more active  $[\text{Cr}(\text{acac})_3]:\text{AlEt}_3:\text{pyrrolyl}$  (1:30:3). The more active solution gave higher levels of Cr(I) species. As pyrrolyl has been shown to promote ethene trimerisation, this led to the theory that Cr(III) is initially reduced to Cr(II) which then leads to the active Cr(I) catalyst, as higher levels are observed in the more active systems.

### 1.5.5 The Sasol Ethene Trimerisation Catalyst

In 2003, a Cr(III) chloride complex with a tridentate  $\text{HN}(\text{CH}_2\text{CH}_2\text{PR}_2)_2$  ligand gave a high activity and selectivity for 1-hexene (Fig. 1.11).<sup>[74]</sup> The best activities were observed where  $\text{R}$  = ethyl, which gave the lowest steric requirement of the tested analogues (others include Ph and Cy). A 48,000 TOF (per h) of ethene conversion was achieved at 23  $\mu\text{mol}$  of Cr loading, 340 mol equivs. of MAO to give 98%  $\text{C}_6$  of which 98.9% was 1- $\text{C}_6$ . The activity continually increased as MAO was increased up to 850 mol equivs. (69,000  $\text{TOF h}^{-1}$ ), although  $\text{C}_6$  selectivity dropped to 94%. At runs of 100 °C, ethene uptake dropped off dramatically after 30 min, suggesting deactivation. At 80 °C, high activity and selectivity remained and the ethene uptake continued over 60 min.

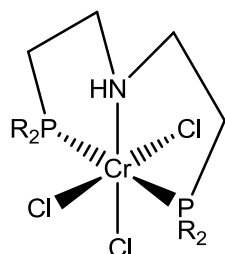


**Fig. 1.11**  $[\text{CrCl}_3(\text{HN}(\text{CH}_2\text{CH}_2\text{PR}_2)_2)]$  catalyst ( $\text{R} = \text{Ph}, \text{Cy}, \text{Et}$ ).<sup>[74]</sup>

A follow up study by the same group replaced the phosphorus donors for sulfur atoms in the neutral tridentate SNS-donor ligand (Fig. 1.12).<sup>[75]</sup> This ligand type

can be synthesised at a much lower cost than the phosphine analogue with the added advantages of much lower toxicity and sensitivity to oxidation.

This complex gave improved activities and selectivities towards selective ethene trimerisation. Where R = ethyl, an activity of 160,000 g/g Cr/h was achieved ( $300,000 \text{ TOF h}^{-1}$ ), 98.4% of C<sub>6</sub> of which 99.7% was 1-C<sub>6</sub>. This was obtained with a low catalyst loading of 5 µmol and 280 mol equivs. of MAO. Using the more soluble <sup>n</sup>decyl derivative allowed for a much lower co-catalyst loading, but still gave very high selectivities and activity. At 50 mol equivs. of MAO, 98.7% C<sub>6</sub>, of which 1-C<sub>6</sub> = 99.8% and an activity of 86,000 g/g Cr/h was achieved.

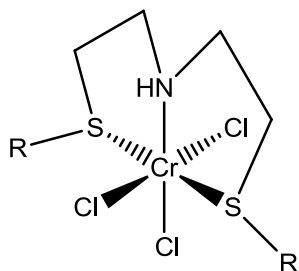


**Fig. 1.12** [CrCl<sub>3</sub>(SNS-R)] catalyst (R = Me, Et, <sup>n</sup>Bu, <sup>n</sup>decyl).<sup>[75]</sup>

This ligand type is one of the main themes of the research presented in this thesis as it is a very active Sasol homogeneous catalyst. The introduction of Chapter 6 discusses recently published literature concerning the activation of these types of catalysts.

### 1.5.6 Ethene Trimerisation by Titanium and Tantalum

Earlier transition metals have also been known to trimerise ethylene. Two of the more notable examples are discussed below.

#### 1.5.6.1 Titanium Catalysts

Certain titanium catalysts are known to provide a high activity for ethene trimerisation. Using Cp based arene stabilised titanium complexes can give a TOF of ~ 240,000 h<sup>-1</sup>, with a selectivity up to 90% of 1-hexene (Fig. 1.13).<sup>[76]</sup>

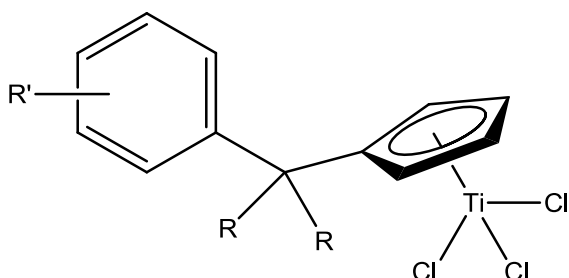


**Fig. 1.13** Titanium functionalised Cp complex for ethene trimerisation.<sup>[76]</sup>

Based on theoretical modelling, the catalyst is activated by MAO to give a Ti(II) cation *via* alkylation, insertion and  $\beta$ -hydride elimination. This provides a Ti(II)/Ti(IV) catalytic pathway. The arene pendant group serves as a hemilabile donor group to stabilise the Ti centre, which provides a changing coordination number throughout the cycle ( $\eta^1$ ,  $\eta^3$ ,  $\eta^6$ ).<sup>[77]</sup>

Theoretical studies by Hagen predicted the major side product of polyethylene (PE) (present ~1–2%) was being formed by two species during the ethene trimerisation pathway.<sup>[78]</sup> PE formation occurs during the activation process with MAO, where the partially alkylated species  $[(R-C_5H_4)TiClMe]^+$  promotes PE. This can be avoided by pre-treatment of the catalyst with an alkylating agent to give the fully substituted species. PE is also produced during the catalytic cycle which is thought to arise from the degradation of the Ti catalyst to form a Ti-H species.

A non-Cp based Ti catalyst gave very high activity for the trimerisation of ethene using a tridentate phenoxyimine ligand (Fig. 1.14).<sup>[79]</sup> With MAO, a TOF in excess of  $12 \times 10^6 \text{ h}^{-1}$  with a 92% 1-hexene selectivity was achieved.

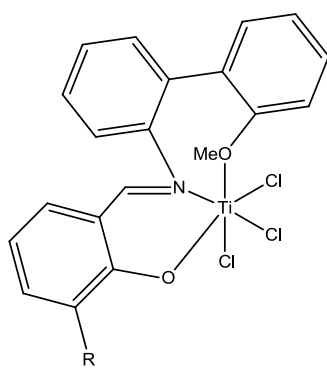
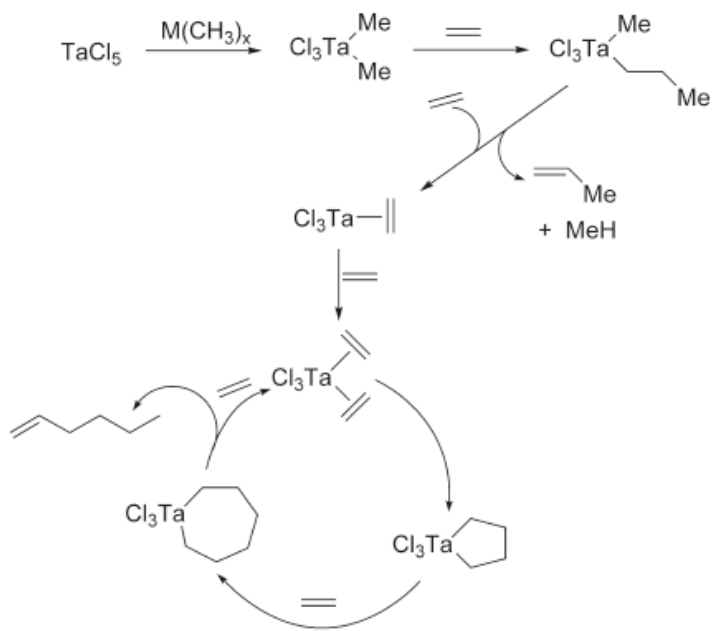


**Fig. 1.14** Highly active non-Cp based Ti ethene trimerisation catalyst (R = adamantyl).<sup>[79]</sup>

### 1.5.6.2 Tantalum Catalysts

In 2001,  $\text{TaCl}_5$  with an alkylating agent gave trimerisation of ethene with a high selectivity of 1-hexene, with a modest TOF  $500 \text{ h}^{-1}$ . The intermediates of this catalysis were studied by  $^1\text{H}$  NMR (Scheme 1.15),<sup>[80]</sup> where the initiating species was found to be  $\text{Cl}_3\text{TaMe}_2$ . This was also supported by theoretical studies which predicted 1-hexene is liberated through a concerted process.<sup>[81]</sup> This is discussed in more detail in the next section to provide some perspective on ethene tetramerisation.



**Scheme 1.15** Proposed ethene trimerisation route by  $\text{TaCl}_5$  ( $\text{M} = \text{AlR}_3$ ,  $\text{ZnR}_2$ ,  $\text{SnR}_4$ ).<sup>[80, 82]</sup>

### 1.5.7 Ethylene Tetramerisation Catalysis

In 2002, the use of an *ortho*-methoxy substituted diphosphinous amide ligand with  $[\text{CrCl}_3(\text{THF})_3]$  gave a high activity for ethylene trimerisation (Fig. 1.15).<sup>[83]</sup> This

complex displayed a high activity of 1,033,200 g/g Cr/h<sup>-1</sup>, with C<sub>6</sub> = 90%, of which 1-C<sub>6</sub> = 90%. This was found to be extremely stable and no deactivation was observed over 1 h. Removal of the *ortho*-substitution on the phenyl ring gave researchers at Sasol a catalyst that produced 70.7% 1-octene at a selectivity of 97.9% (Fig. 1.15).<sup>[84]</sup> It was suggested that 1-octene is produced by further insertion of ethene into the metallocycloheptane to give the metallocyclononane derivative.

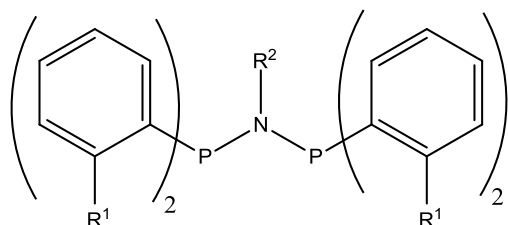
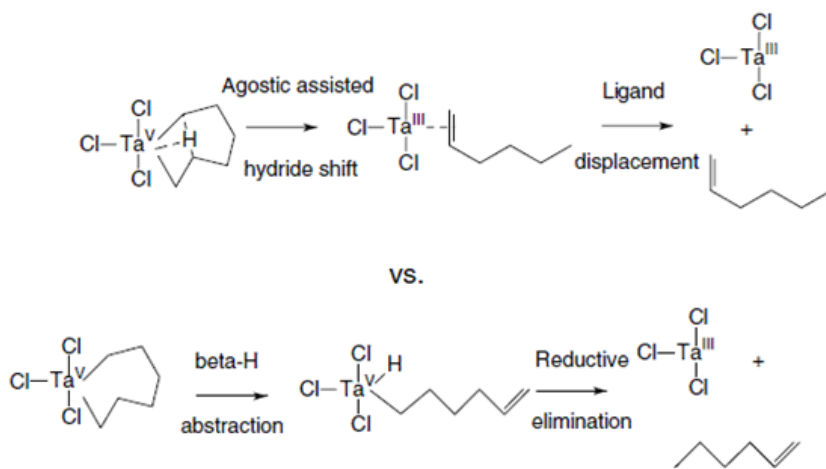


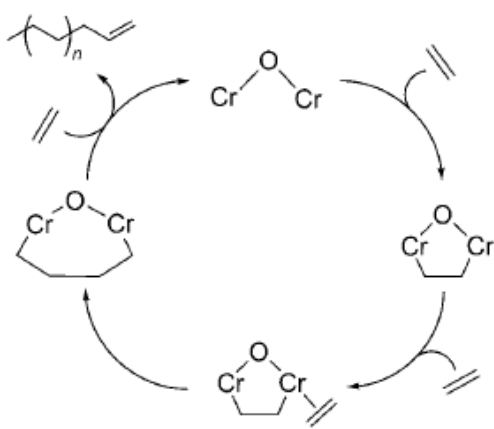
**Fig. 1.15** Phosphinoamine ligand for ethene trimerisation and tetramerisation (R<sup>1</sup> = OMe, R<sup>2</sup> = Me (trimerisation);<sup>[83]</sup> R<sup>1</sup> = H, R<sup>2</sup> = i-Pr (tetramerisation)<sup>[84]</sup>).

Prior to this, it was thought insertion of ethylene into a chromocycloheptane to give the nine-membered metallocycle was unlikely. A computational study of the [TaCl<sub>3</sub>(Me)<sub>2</sub>]<sup>[80]</sup> selective trimerisation catalyst confirmed formation of a tantalum metallocycloalkanes for trimerisation are energetically possible.<sup>[81]</sup> This study also suggested decomposition of the tantalum metallocycloheptane ring occurs *via* a concerted hydride transfer over the two step reductive elimination pathway (Scheme 1.16). Dimerisation of ethene was disfavoured because the concerted step is not possible for the tantalum metallocyclopentane intermediate. Further insertion into a tantalum metallocloheptane to form the tantalum metallocyclononane and beyond was also disfavoured over the more energetically favourable reductive elimination step. The formation of a tantalum metallocycloheptane was calculated at 13 kcal mol<sup>-1</sup>, ethene insertion to form the larger ring was calculated at 36.2 kcal mol<sup>-1</sup> whereas concerted release of 1-hexene was calculated lower at 25.5 kcal mol<sup>-1</sup>. Similar studies by Blok *et al.* echoed the unfavourable formation of larger rings for titanium catalysts.<sup>[85]</sup> It was supposed that similar results would be expected for the Cr derivatives.

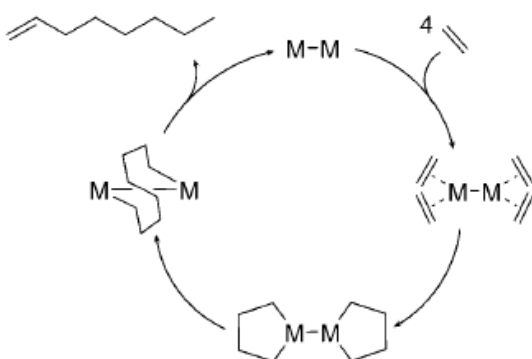


**Scheme 1.16** Displaying two routes of the tantalum metallacycloheptane decomposition to yield 1-hexene.<sup>[17, 81]</sup>

In 2010, a bimetallic route for the selective production of 1-octene by  $[\text{CrCl}_3(\text{PNP})(\text{THF})]$  was suggested by SABIC.<sup>[86]</sup> Bimetallic routes have been suggested before for the polymerisation of ethene, e.g. for the heterogeneous  $\text{CrO}_3/\text{SiO}_2$  Phillips ethene polymerisation catalyst<sup>[87]</sup> by IR analysis<sup>[88]</sup> and DFT<sup>[89]</sup> studies (Scheme 1.17). A similar route for the selective production of 1-octene was proposed (Scheme 1.18). This route avoids the energetically unfavourable formation of the metallocyclononane as suggested previously.<sup>[81, 85]</sup>



**Scheme 1.17** Suggested Philips catalytic route for the polymerisation of ethene.<sup>[86]</sup>



**Scheme 1.18** Suggested bimetallic route for the selective production of 1-octene.<sup>[86]</sup>

Thermolysis of a quadruply bonded bimetallic chromium cyclo alkyl species, as shown in Fig. 1.16 produced 1-octene, whereas thermolysis of the monometallic chromocyclopentane only gave 1-butene and ethene.<sup>[86]</sup>

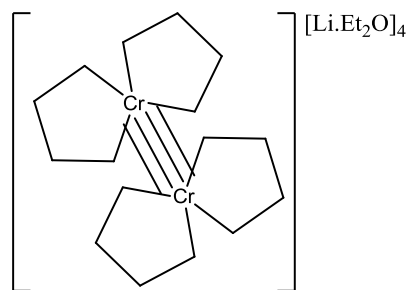


**Fig. 1.16** Tetralithium tetrabutanediylidichromate which results in 1-octene liberation upon thermoysis.

In 2012, a highly selective chromium ethene tetramerisation catalyst was discovered, giving selectivity up to 91% 1-C<sub>8</sub>.<sup>[90]</sup> This was achieved using a phosphoramine ligand (Fig. 1.17),  $[\text{CrCl}_2(\text{THF})_2]$  precursor, 500 equivs. DMAO to give a moderate activity of 1800 g/g Cr/h<sup>-1</sup>. Using  $[\text{CrCl}_3(\text{THF})_3]$  and DMAO/AlEt<sub>3</sub> (500/100) gave a significant increase in the activity to 25,500 g/g Cr/h<sup>-1</sup>, and selectivity of 1-C<sub>8</sub> to 88%. Using the shorter chain analogue, Ph<sub>2</sub>PNR(CH<sub>2</sub>)<sub>2</sub>NRPPh<sub>2</sub> produces (and in some instances favours) larger quantities of C<sub>6</sub>. It was proposed that the shorter ligand produces the monomeric chromium catalyst giving variable results,

and the longer chain analogue produces a dimeric chromium catalyst capable of producing high selectivities of C<sub>8</sub> (Fig. 1.17).

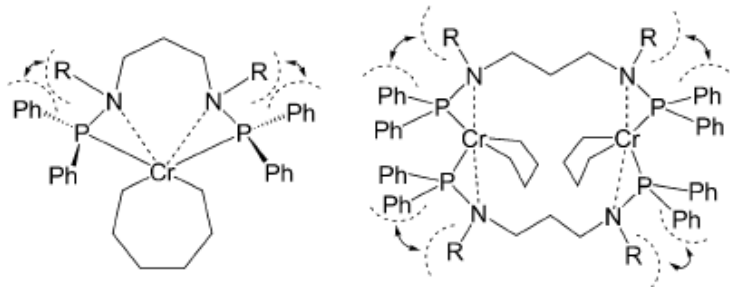


**Fig. 1.17** Two possible formations for selective 1-octene production by Cr ethene oligomerisation catalyst ( $R = Et, iPr$ ).

## 1.6 Role of the Co-catalyst

These are commonly formed from main group organometallic species and play a crucial role in activation of pre-catalysts for ethylene polymerisation. The main functions of the co-catalysts are as alkylating reagents, as a Lewis acid to form a non-coordination anion and possibly act as an oxidant or reductant.

### 1.6.1 Types of Co-Catalyst

Many types of co-catalysts have been studied and are known to have positive effects in one system and give detrimental effects in another. This section aims to give a general introduction to some of the more common additives.

#### 1.6.1.1 Aluminium Alkyls

Aluminium alkyls such as AlR<sub>3</sub> and AlClR<sub>2</sub>, are one of the main components for the highly active Ziegler-Natta polymerisation systems.<sup>[54b]</sup> Sinn found that by adding H<sub>2</sub>O to the inactive Cp<sub>2</sub>ZrMe<sub>2</sub>/AlMe<sub>3</sub>, a high activity was then observed for ethene polymerisation.<sup>[55]</sup> This led to the discovery of a highly efficient activator, an oligomeric methyl aluminoxane (MAO).<sup>[56, 91]</sup>

MAO consists of  $[\text{Al}(\text{R})\text{O}]_n$  subunits ( $n \approx 5\text{--}20$ ), from the controlled hydrolysis of  $\text{AlMe}_3$  and gives highly active catalysts for olefin polymerisation.<sup>[92]</sup> The exact composition of MAO is still unclear. It varies the activities of a catalyst depending on the  $\text{H}_2\text{O}$  source and the reaction conditions of its synthesis. Some structures were proposed based on structural studies of iso-butylaluminoxane, for which species can be isolated easier and so, allows for X-ray crystallography (Fig. 1.18).<sup>[93]</sup>

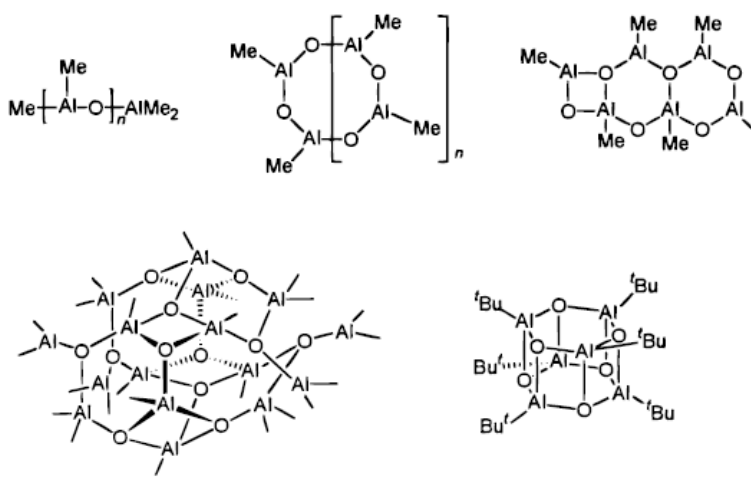


**Fig. 1.18** Proposed structures of methylaluminoxane oligomer.<sup>[93]</sup>

MAO can be synthesised using different methods to provide certain advantages. Modified MAO (MMAO) is synthesised by the controlled hydrolysis of  $\text{AlMe}_3$  and  ${}^t\text{Bu}_3\text{Al}$  to improve solubility in non-polar solvents and allow for easier storage. Residual  $\text{AlMe}_3$  can have a detrimental effect in some catalyst systems. Therefore PMAO-IP, a modified MAO to give low amounts of  $\text{AlMe}_3$ , can be synthesised by reacting  $\text{AlMe}_3$  using non-hydrolytic means, i.e. using  $\text{Me}_3\text{COH}$ . Thermal conversion of this product gives purer MAO.<sup>[92b]</sup>

### 1.6.1.2 Perfluoroaryl Boranes

$\text{B}(\text{C}_6\text{F}_5)_3$  with Group 4 metallocenes have been used to promote highly active olefin polymerisation catalysts and allow for X-ray crystallography of cationic metallocenes.<sup>[94]</sup> These organometallics exhibit high Lewis acidity and the anionic complexes can act as large non-coordinating, inert counter ions. Since their discovery,

the use in academic and industrial research is massive and as such, many variations are now available.<sup>[92b]</sup> Some examples of their use are discussed below.

### 1.6.1.3 Trityl Aluminates and Borates

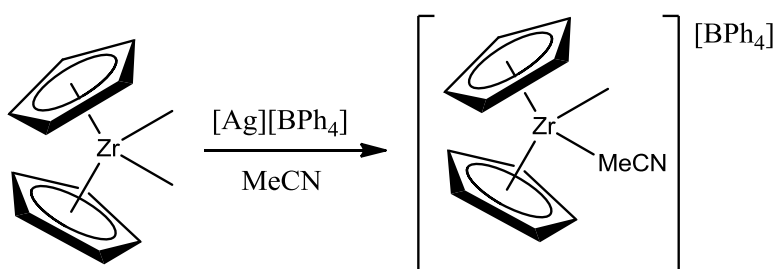
The trityl cation,  $\text{Ph}_3\text{C}^+$ , is a powerful oxidising reagent and also, as a Lewis acid, acts as alkyl and hydride abstractor. These perform as effective co-catalysts alongside weakly-coordinating anions such as tetra-arylborates ( $[\text{B}(\text{C}_6\text{F}_5)_4]$ )<sup>[95]</sup> and tetra-alkoxy aluminates ( $[\text{Al}(\text{OR})_4]$ ).<sup>[96]</sup> Again many variations on these types have been synthesised.<sup>[92b]</sup>

## 1.6.2 Activation

Co-catalysts are considered to play three major roles in the initial stages during the activation of the pre-catalyst; abstractive cleavage of M-R, ligand exchange and subsequent extraction and a one electron oxidation process.

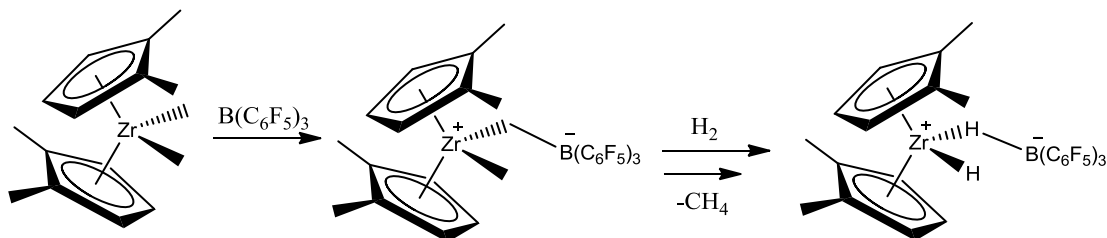
### 1.6.2.1 Alkyl Abstraction

The neutral  $[\text{Cp}_2\text{ZrR}_2]$  complex can undergo alkyl abstraction using  $\text{Ag}^+$  in the presence of a donor ligand to form Lewis base stabilised cationic  $[(\text{Cp})_2\text{ZrR(L)}]^+$  complex (Scheme 1.19),<sup>[97]</sup> which is active for ethene polymerisation.<sup>[98]</sup> To help isolate these types of complexes, use of large noncoordinating, unreactive Lewis bases help to stabilise the salt.



**Scheme 1.19** Formation of cationic zirconium ethene polymerisation catalyst.

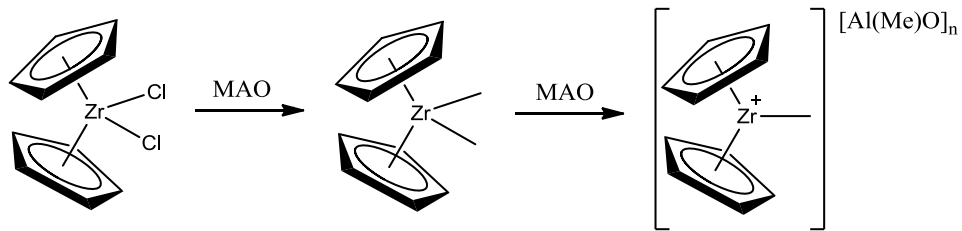
The neutral  $\text{B}(\text{C}_6\text{F}_5)_3$  Lewis acid can also abstract an alkyl group. A study showed its ability to oxidise zirconium in non-coordinating solvents to give the cationic bridging methyl complex<sup>[94]</sup> and, with follow up of hydrogenolysis, leads to the stepwise formation of the mono, then di-hydrido zirconium metallocene complex (Scheme 1.20).<sup>[99]</sup>



**Scheme 1.20** Stepwise methyl abstraction by  $\text{B}(\text{C}_6\text{F}_5)_3$  on zirconium metallocene.

### 1.6.2.2 Ligand Exchange

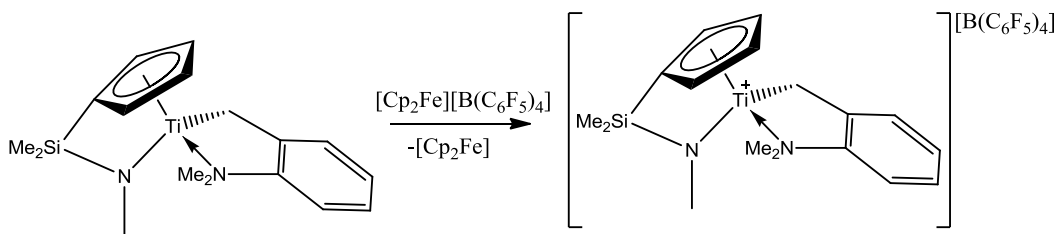
MAO can provide ligand exchange and abstraction to form the active ethene polymerisation catalyst from  $[(\text{Cp})_2\text{ZrCl}_2]$ . At first it provides a rapid initial ligand exchange to generate the dialkyl zirconium metallocene, followed by the formation of the cationic species by removal of an alkyl group (Scheme 1.21).<sup>[92b]</sup> It is assumed the aluminium centres in MAO have a high capacity for extraction of chloride and the methyl from zirconium to yield the active  $\text{Zr}^+-\text{R}$  species as seen by  $^{13}\text{C}$  and  $^{91}\text{Zr}$  NMR analysis.<sup>[100]</sup>



**Scheme 1.21** Ligand exchange and subsequent alkyl abstraction by MAO.

### 1.6.2.3 One Electron Oxidation

Without extraction of an alkyl group or halide, the role of the co-catalyst can be to perform a one-electron oxidation, as observed for a functionalised Cp Ti(III) complex. This can be activated by ferrocenium tetrakis(pentafluorophenyl)borate to oxidise Ti(III) to the cationic Ti(IV) which is a highly active ethene polymerisation catalyst (Scheme 1.23).<sup>[92b]</sup>



**Scheme 1.22** Oxidation of an active olefin titanium complex by ferrocenium tetrakis(pentafluorophenyl)borate.

### 1.7 Conclusion

Since the first report of ethene oligomerisation to 1-hexene at 1% selectivity by chromium, more than 30 years later this has now given rise to a huge area of research where selectivities for 1-hexene has risen to >95%. A wide variety of ligands have now been discovered that can promote selective oligomerisation, these include aromatics, heteroaromatics and multidentates. Although many of these systems present a challenge in characterisation due to their paramagnetic nature, this has been overcome by using studies on ligand design, organometallic synthesis, isotope labelling and computational studies.<sup>[17]</sup>

Interest in selective oligomerisation of ethene has seen a big increase over the last 10 years, which coincides with the publication of selective 1-octene catalysis. Interest is likely to continue as industry drives towards selective processes to produce high value co-monomers such as 1-hexene and 1-octene (Fig. 1.19).

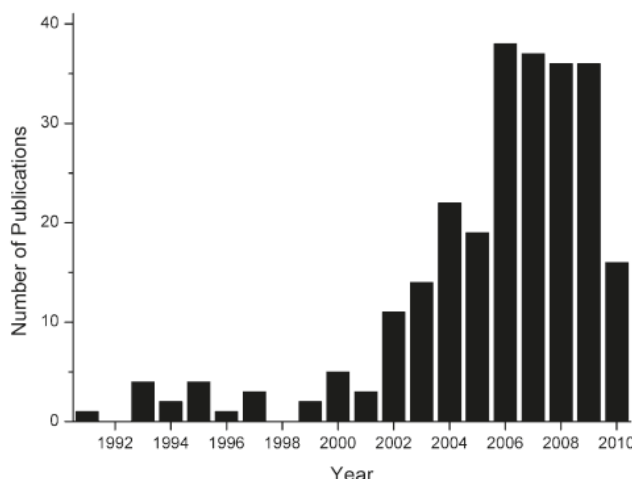
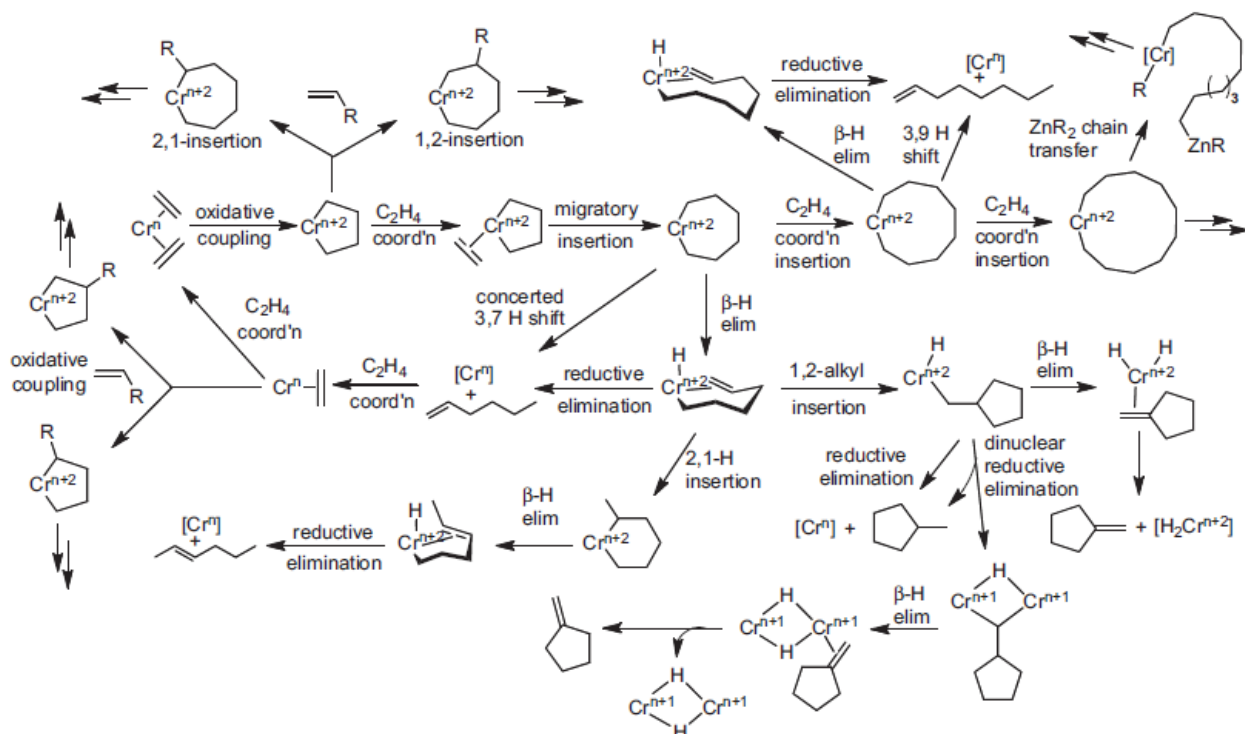


**Fig. 1.19** Publications on trimerisation and tetramerisation of ethene by year (up to June 2010).<sup>[82]</sup>

Such a large diversity is observed in allowing selective production of oligomers and this can then lead to a very complex picture to encompass all these possibilities as observed in a recent review by Agapie,<sup>[101]</sup> and so it can be seen why this is still a vibrant area of academic and industrial research today (Scheme 1.23).



**Scheme 1.23** Possible Cr-based metallocycle reaction pathways as reviewed by Agapie.<sup>[101]</sup>

## **1.8 Aims**

This research project has three main aims; (i) development of the XAFS stopped-flow technique for application in identification of transient intermediates for homogeneous catalytic processes; (ii) identifying highly reactive intermediate species formed during the activation of ethene oligomerisation and polymerisation catalysts; (iii) to synthesise new inorganic molybdenum and scandium halide complexes using N<sub>3</sub> and mixed S and N donor tridentate ligands and probe their utility in ethene polymerisation.

By developing the XAFS/stopped-flow/UV-Vis technique, it allows the reaction of AlMe<sub>3</sub> with ethene oligomerisation catalysts to be followed in time by XAFS and UV-vis spectroscopy simultaneously. By combining these techniques it may be possible to identify new species formed after activation by AlMe<sub>3</sub> at specific time periods. In addition to this, a newly developed freeze-quench technique can be used to freeze reaction mixtures at predetermined time periods to allow for XAFS analysis over long acquisition times and for soft X-ray edges. This requires modification of the stopped-flow instrument to exclude air and moisture, which must be validated first before real experiments can be undertaken.

Once this technique has been established, it can be utilised to trap and identify species that are being formed from reaction of the AlMe<sub>3</sub> and the ethene oligomerisation catalysts, such as [CrCl<sub>3</sub>(SNS)]. This can be analysed at different steps of the reaction to follow the reaction profile and thus provide evidence to support an activation pathway leading to the active catalytic species.

Under analysis are the transition metals molybdenum, which allows for better XAFS analysis because of its hard X-ray edge and slower reaction kinetics, scandium which allows for <sup>45</sup>Sc, <sup>1</sup>H and <sup>13</sup>C NMR analysis due to its diamagnetic nature, and chromium, which is the most active and most studied metal for ethene trimerisation. New inorganic materials have been synthesised for scandium and molybdenum to aid in the study of activation by AlMe<sub>3</sub>.

## **1.9 References**

- [1] <http://www.kbr.com/Technologies/Olefins/>, KBR, **2012**.
- [2] <http://www.icis.com/Articles/2008/02/18/9101114/chemical-profile-alpha-olefins.html>, ICIS, **18 Feb. 2008**.
- [3] a) <http://www.cpchem.com>; Chevron Phillips Chemical Company, **2012**; b) <http://www.cchange.ac.za/?cat=19> University of Cape Town, **Feb. 2012**.
- [4] ALPHA-OLEFINS - WORLD MARKETS; <http://www.colin-houston.com/files/Alpha-Olefin%20-%20World%20Markets,%202005-2015.pdf>; Colin A. Houston and Associates, **2006**.
- [5] a) <http://www.qchem.com.qa>, Qatar Chemical Company Ltd, **2012**; b) <http://www.sasol.com> Sasol, **2012**.
- [6] a) D. F. Shriver and P. W. Atkins, *Inorganic Chemistry*, Oxford University Press, Oxford, **1999 p437**; b) R. Whyman, *Applied Organometallic Chemistry and Catalysis*, Oxford University Press, Oxford, **2001**.
- [7] R. G. Pearson, *J. Chem. Educ.* **1968**, *45*, 581.
- [8] R. G. Pearson, *Coord. Chem. Rev.* **1990**, *100*, 403-425.
- [9] S. A. Cotton, *Polyhedron* **1999**, *18*, 1691-1715.
- [10] J. Arnold, C. G. Hoffman, D. Y. Dawson and F. J. Hollander, *Organomet.* **1993**, *12*, 3645-3654.
- [11] P. R. Meehan, D. R. Aris and G. R. Willey, *Coord. Chem. Rev.* **1999**, *181*, 121-145.
- [12] M. E. Thompson and J. E. Bercaw, *Pure Appl. Chem.* **1984**, *56*, 1-11.
- [13] M. E. Thompson, S. M. Baxter, A. R. Bulls, B. J. Burger, M. C. Nolan, B. D. Santarsiero, W. P. Schaefer and J. E. Bercaw, *J. Am. Chem. Soc.* **1987**, *109*, 203-219.
- [14] B. J. Burger, M. E. Thompson, W. D. Cotter and J. E. Bercaw, *J. Am. Chem. Soc.* **1990**, *112*, 1566-1577.

- [15] J. Barnhart, *Regul. Toxicol. Pharm.* **1997**, *26*, S3-S7.
- [16] F. A. Cotton and G. Wilkinson, *Advanced Inorganic Chemistry*, John Wiley & Sons USA, **1972**.
- [17] J. T. Dixon, M. J. Green, F. M. Hess and D. H. Morgan, *J. Organomet. Chem.* **2004**, *689*, 3641-3668.
- [18] M. Oguri, H. Mimura, T. Aoyama, H. Okada and Y. Koie **JP 11092407**, **1999**.
- [19] A. J. Barton, J. Connolly, W. Levason, A. Menda-Jalon, S. D. Orchard and G. Reid, *Polyhedron* **2000**, *19*, 1373-1379.
- [20] A. J. Ruckridge, D. S. McGuinness, R. P. Tooze, A. M. Z. Slawin, J. D. A. Pelletier, M. J. Hanton and P. B. Webb, *Organomet.* **2007**, *26*, 2782-2787.
- [21] F. Mani and L. Sacconi, *Inorg. Chim. Acta* **1970**, *4*, 365-366.
- [22] a) L. Helm and A. E. Merbach, *Chem. Rev.* **2005**, *105*, 1923-1960; b) K. M. Smith, *Coord. Chem. Rev.* **2006**, *250*, 1023-1031.
- [23] J. R. Hanson, *Synthesis* **1974**, 1-8.
- [24] Y. Okude, S. Hirano, T. Hiyama and H. Nozaki, *J. Am. Chem. Soc.* **1977**, *99*, 3179-3181.
- [25] D. M. Hodgson, *J. Organomet. Chem.* **1994**, *476*, 1-5.
- [26] W. C. Still and D. Mobilio, *J. Org. Chem.* **1983**, *48*, 4785-4786.
- [27] J. K. Kochi, *Organometallic Mechanisms and Catalysis*, Academic Press, New York, **1978**.
- [28] E. C. Alyea, J. S. Basi, D. C. Bradley and M. H. Chisholm, *Chem. Commun.* **1968**, 495-495.
- [29] J. S. Wood, *Inorg. Chem.* **1968**, *7*, 852-859.
- [30] K. Nag and S. N. Bose, *Struct. Bond.* **1985**, *63*, 153-197.

- [31] G. Yagupsky, W. Mowat, A. Shortland and G. Wilkinson, *J. Chem. Soc. Chem. Comm.* **1970**, 1369.
- [32] E. C. Alyea, J. S. Basi, D. C. Bradley and M. H. Chisholm, *J. Chem. Soc. A* **1971**, 772-776.
- [33] J. E. Salt, G. S. Girolami, G. Wilkinson, M. Motevalli, M. Thornton-Pett and M. B. Hursthouse, *Dalton Trans.* **1985**, 685-692.
- [34] M. Mitewa and P. R. Bontchev, *Coord. Chem. Rev.* **1985**, 61, 241-272.
- [35] T. J. Collins, C. Slebodnick and E. S. Uffelman, *Inorg. Chem.* **1990**, 29, 3433-3436.
- [36] G. Chaka and A. Bakac, *Dalton Trans.* **2009**, 318-321.
- [37] J. Cho, J. Woo, J. Eun Han, M. Kubo, T. Ogura and W. Nam, *Chem. Sci.* **2011**, 2, 2057-2062.
- [38] C. L. Weeks, A. Levina, C. T. Dillon, P. Turner, R. R. Fenton and P. A. Lay, *Inorg. Chem.* **2004**, 43, 7844-7856.
- [39] J. H. Espenson and J. R. Pladziewicz, *Inorg. Chem.* **1971**, 10, 634-637.
- [40] N. Meijboom, C. J. Schaverien and A. G. Orpen, *Organomet.* **1990**, 9, 774-782.
- [41] R. Colton and I. Tomkins, *Aust. J. Chem.* **1966**, 19, 1143-1146.
- [42] F. Bonati and G. Minghetti, *Inorg. Chem.* **1970**, 9, 2642-2644.
- [43] a) J. R. Moss and B. L. Shaw, *J. Chem. Soc. A* **1970**, 595-601; b) A. V. Butcher and J. Chatt, *J. Chem. Soc. A* **1970**, 2652-2656.
- [44] S. P. Downing, M. J. Hanton, A. M. Z. Slawin and R. P. Tooze, *Organomet.* **2009**, 28, 2417-2422.
- [45] F. Stoffelbach, D. Saurenz and R. Poli, *Eur. J. Inorg. Chem.* **2001**, 2699-2703.
- [46] L. Manojlovic-Muir, *J. Chem. Soc. A* **1971**, 2796-2800.
- [47] M. H. Chisholm, *Accounts Chem. Res.* **1990**, 23, 419-425.

- [48] F. Huq, W. Mowat, A. Shortland, A. C. Skapski and G. Wilkinson, *J. Chem. Soc. Chem. Comm.* **1971**, 1079-1080.
- [49] M. H. Chisholm, F. A. Cotton, B. A. Frenz, W. W. Reichert, L. W. Shive and B. R. Stults, *J. Am. Chem. Soc.* **1976**, *98*, 4469-4476.
- [50] M. H. Chisholm, F. A. Cotton, C. A. Murillo and W. W. Reichert, *Inorg. Chem.* **1977**, *16*, 1801-1808.
- [51] B. E. Bursten, F. A. Cotton, J. C. Green, E. A. Seddon and G. G. Stanley, *J. Am. Chem. Soc.* **1980**, *102*, 4579-4588.
- [52] IUPAC *Compendium of Chemical Terminology*, **2005**.
- [53] Y. Imanishi and N. Naga, *Prog. Polym. Sci.* **2001**, *26*, 1147-1198.
- [54] a) G. Natta, P. Pino, G. Mazzanti and U. Giannini, *J. Am. Chem. Soc.* **1957**, *79*, 2975-2976; b) D. S. Breslow and N. R. Newburg, *J. Am. Chem. Soc.* **1957**, *79*, 5072-5073.
- [55] A. Andresen, H.-G. Cordes, J. Herwig, W. Kaminsky, A. Merck, R. Mottweiler, J. Pein, H. Sinn and H.-J. Vollmer, *Angew. Chem. Int. Edit.* **1976**, *15*, 630-632.
- [56] H. Sinn, W. Kaminsky, H.-J. Vollmer and R. Woldt, *Angew. Chem. Int. Edit.* **1980**, *19*, 390-392.
- [57] a) H. Weiss, M. Ehrig and R. Ahlrichs, *J. Am. Chem. Soc.* **1994**, *116*, 4919-4928; b) P. Cossee, *J. Catal.* **1964**, *3*, 80-88; c) R. F. Jordan, *J. Chem. Educ.* **1988**, *65*, 285.
- [58] P. Kuhn, D. Semeril, D. Matt, M. J. Chetcuti and P. Lutz, *Dalton Trans.* **2007**, 515-528.
- [59] a) W. Keim, F. H. Kowaldt, R. Goddard and C. Krüger, *Angew. Chem. Int. Edit.* **1978**, *17*, 466-467; b) J. Skupinska, *Chem. Rev.* **1991**, *91*, 613-648.
- [60] W. Keim, *New J. Chem.* **1987**, *11*, 531-534.
- [61] U. Müller, W. Keim, C. Krüger and P. Betz, *Angew. Chem. Int. Edit.* **1989**, *28*, 1011-1013.

- [62] B. Reuben and H. Wittcoff, *J. Chem. Educ.* **1988**, 65, 605.
- [63] R. M. Manyik, W. E. Walker and T. P. Wilson, *J. Catal.* **1977**, 47, 197-209.
- [64] J. R. Briggs, *Chem. Commun.* **1989**, 674-675.
- [65] R. Emrich, O. Heinemann, P. W. Jolly, C. Krüger and G. P. J. Verhovnik, *Organomet.* **1997**, 16, 1511-1513.
- [66] L. A. MacAdams, G. P. Buffone, C. D. Incarvito, J. A. Golen, A. L. Rheingold and K. H. Theopold, *Chem. Commun.* **2003**, 1164-1165.
- [67] T. Agapie, J. A. Labinger and J. E. Bercaw, *J. Am. Chem. Soc.* **2007**, 129, 14281-14295.
- [68] W. K. Reagen *Process for olefin polymerization*, 90115317 EP-A- 0 250 999; US-A- 3 887 494, EP, **1995**.
- [69] *Alpha Olefins (02/03-4), PERP Report, Nexant Chem Systems*, **2004**.
- [70] J. W. Freeman, J. L. Buster and R. D. Knudsen *Olefin Production*, US 5856257, **1999**.
- [71] A. Jabri, C. B. Mason, Y. Sim, S. Gambarotta, T. J. Burchell and R. Duchateau, *Angew. Chem. Int. Edit.* **2008**, 47, 9717-9721.
- [72] I. Vidyaratne, G. B. Nikiforov, S. I. Gorelsky, S. Gambarotta, R. Duchateau and I. Korobkov, *Angew. Chem. Int. Edit.* **2009**, 48, 6552-6556.
- [73] I. Y. Skobelev, V. N. Panchenko, O. Y. Lyakin, K. P. Bryliakov, V. A. Zakharov and E. P. Talsi, *Organomet.* **2010**, 29, 2943-2950.
- [74] D. S. McGuinness, P. Wasserscheid, W. Keim, C. Hu, U. Englert, J. T. Dixon and C. Grove, *Chem. Commun.* **2003**, 334-335.
- [75] D. S. McGuinness, P. Wasserscheid, W. Keim, D. Morgan, J. T. Dixon, A. Bollmann, H. Maumela, F. Hess and U. Englert, *J. Am. Chem. Soc.* **2003**, 125, 5272-5273.
- [76] B. Hessen, *J. Mol. Catal. A Chem* **2004**, 213, 129-135.

- [77] a) T. J. M. de Bruin, L. Magna, P. Raybaud and H. Toulhoat, *Organomet.* **2003**, 22, 3404-3413; b) S. Tobisch and T. Ziegler, *Organomet.* **2003**, 22, 5392-5405.
- [78] H. Hagen, W. P. Kretschmer, F. R. van Buren, B. Hessen and D. A. van Oeffelen, *J. Mol. Catal. A Chem.* **2006**, 248, 237-247.
- [79] Y. Suzuki, S. Kinoshita, A. Shibahara, S. Ishii, K. Kawamura, Y. Inoue and T. Fujita, *Organomet.* **2010**, 29, 2394-2396.
- [80] C. Andes, S. B. Harkins, S. Murtuza, K. Oyler and A. Sen, *J. Am. Chem. Soc.* **2001**, 123, 7423-7424.
- [81] Z.-X. Yu and K. N. Houk, *Angew. Chem. Int. Edit.* **2003**, 42, 808-811.
- [82] D. S. McGuinness, *Chem. Rev.* **2011**, 111, 2321-2341.
- [83] A. Carter, S. A. Cohen, N. A. Cooley, A. Murphy, J. Scutt and D. F. Wass, *Chem. Commun.* **2002**, 858-859.
- [84] A. Bollmann, K. Blann, J. T. Dixon, F. M. Hess, E. Killian, H. Maumela, D. S. McGuinness, D. H. Morgan, A. Neveling, S. Otto, M. Overett, A. M. Z. Slawin, P. Wasserscheid and S. Kuhlmann, *J. Am. Chem. Soc.* **2004**, 126, 14712-14713.
- [85] A. N. J. Blok, P. H. M. Budzelaar and A. W. Gal, *Organomet.* **2003**, 22, 2564-2570.
- [86] S. Peitz, B. R. Aluri, N. Peulecke, B. H. Müller, A. Wöhl, W. Müller, M. H. Al-Hazmi, F. M. Mosa and U. Rosenthal, *Chem. Eur. J.* **2010**, 16, 7670-7676.
- [87] K. H. Theopold, *Eur. J. Inorg. Chem.* **1998**, 1998, 15-24.
- [88] B. Rebenstorf and R. Larsson, *J. Mol. Catal.* **1981**, 11, 247-256.
- [89] Ø. Espelid and K. J. Børve, *J. Catal.* **2002**, 206, 331-338.
- [90] Y. Shaikh, K. Albahily, M. Sutcliffe, V. Fomitcheva, S. Gambarotta, I. Korobkov and R. Duchateau, *Angew. Chem. Int. Edit.* **2012**, 51, 1366-1369.
- [91] H. Sinn and W. Kaminsky *Ziegler-Natta Catalysis, Volume 18* Eds.: F. G. A. Stone and W. Robert), Academic Press, **1980**, pp. 99-149.

- [92] a) W. Kaminsky, K. Külper, H. H. Brintzinger and F. R. W. P. Wild, *Angew. Chem. Int. Edit.* **1985**, *24*, 507-508; b) E. Y.-X. Chen and T. J. Marks, *Chem. Rev.* **2000**, *100*, 1391-1434.
- [93] M. R. Mason, J. M. Smith, S. G. Bott and A. R. Barron, *J. Am. Chem. Soc.* **1993**, *115*, 4971-4984.
- [94] X. Yang, C. L. Stern and T. J. Marks, *J. Am. Chem. Soc.* **1994**, *116*, 10015-10031.
- [95] X. Yang, C. L. Stern and T. J. Marks, *J. Am. Chem. Soc.* **1991**, *113*, 3623-3625.
- [96] I. Krossing, H. Brands, R. Feuerhake and S. Koenig, *J. Fluorine Chem.* **2001**, *112*, 83-90.
- [97] R. F. Jordan, W. E. Dasher and S. F. Echols, *J. Am. Chem. Soc.* **1986**, *108*, 1718-1719.
- [98] R. F. Jordan, C. S. Bajgur, R. Willett and B. Scott, *J. Am. Chem. Soc.* **1986**, *108*, 7410-7411.
- [99] X. Yang, C. L. Stern and T. J. Marks, *Angew. Chem. Int. Edit.* **1992**, *31*, 1375-1377.
- [100] a) A. R. Siedle, W. M. Lamanna, R. A. Newmark and J. N. Schroepfer, *J. Mol. Catal. A Chem.* **1998**, *128*, 257-271; b) I. Tritto, S. X. Li, M. C. Sacchi, P. Locatelli and G. Zannoni, *Macromolecules* **1995**, *28*, 5358-5362.
- [101] T. Agapie, *Coord. Chem. Rev.* **2011**, *255*, 861-880.



**2.**

## **Experimental Techniques.**

## 2. 1 Introduction

This chapter aims to explain the major spectroscopic techniques which have been used within this research. The techniques discussed were used to identify, characterise and confirm newly synthesised complexes and also to follow reaction profiles of metal complexes to help identify new species in solution.

### 2.2 Nuclear Magnetic Resonance Spectroscopy<sup>[1]</sup>

NMR spectroscopy is one of the most common techniques in chemistry for determining structural information of new compounds. The most routinely probed nuclei include <sup>1</sup>H, <sup>13</sup>C, <sup>19</sup>F and <sup>31</sup>P NMR. The NMR studies within this research also probe the less commonly studied <sup>45</sup>Sc and <sup>27</sup>Al quadrupolar nuclei as discussed below.

#### 2.2.1 Quadrupolar Nuclei

Use of quadrupolar nuclei ( $I \geq 1$ ) is a relatively less studied area of NMR spectroscopy than that of the  $I = \frac{1}{2}$  nuclei, <sup>1</sup>H, <sup>13</sup>C, <sup>19</sup>F and <sup>31</sup>P, because many are much less sensitive and have large quadrupole moments, leading to significant line broadening resulting from fast quadrupolar relaxation. It should also be noted that line width is also a function of temperature and concentration. The standard reference for <sup>27</sup>Al NMR spectroscopy,  $[\text{Al}(\text{H}_2\text{O})_6]^{3+}$ , has been shown to have line widths from  $\sim 2 - 100$  Hz depending on sample conditions despite its regular octahedral geometry.

Within this work (as described in Chapter 5) two quadrupolar nuclei were studied by NMR spectroscopy, <sup>27</sup>Al and <sup>45</sup>Sc, in order to provide additional evidence for the species present at various stages of the reaction. Probing of a quadrupolar nucleus can sometimes cause difficulties due to sensitivity and complex splitting patterns. The <sup>27</sup>Al and <sup>45</sup>Sc however are sensitive NMR nuclei and can provide important structural information or insights into reaction mechanisms. Both of these are discussed further.

### 2.2.1.1 $^{27}\text{Al}$ NMR Spectroscopy

The  $^{27}\text{Al}$  nucleus ( $I = 5/2$ ) is 100 % abundant and has an NMR frequency of 26.057 MHz (relative to  $^1\text{H}$  NMR at 100 MHz) with a low quadrupole moment of  $0.149 \cdot 10^{-28} \text{ m}^2$ . For these reasons,  $^{27}\text{Al}$  is a relatively well studied NMR nucleus. The chemical shift range is commonly divided into three regions (as referenced by  $[\text{Al}(\text{H}_2\text{O})_6]^{3+}$ ); octahedral aluminium species (-50 – 50 ppm), tetrahedral aluminium species (40 – 150 ppm) and alkylaluminum compounds ( $\geq 150$  ppm). Therefore, the chemical shift is a good indication of the coordination number, but it is also influenced by its ligand environment. In general the  $^{27}\text{Al}$  NMR chemical shift is higher for alkylaluminums than the tetrahalides and their adducts (Table 2.1).

Line broadening in the  $^{27}\text{Al}$  NMR spectrum can arise from exchanging ligands at Al, although ligand exchange tends to be slow on the NMR timescale because  $\text{Al}^{3+}$  has a strong interaction with electron donors due to its relatively high Lewis acidity arising from its large charge-to radius ratio. Line broadening in  $^{27}\text{Al}$  NMR spectroscopy can also arise from non-zero electric field gradients (EFG) set-up by an asymmetry of ligand arrangements.

**Table 2.1** Table of chemical shifts for selected aluminium alkyls and chlorides relevant to this work observed in  $^{27}\text{Al}$  NMR spectroscopy (reference  $[\text{Al}(\text{H}_2\text{O})_6]^{3+}$ ).<sup>[1a, 2]</sup>

Aluminium Compound (solvent)	$\delta$ (ppm)
$\text{Al}_2\text{Cl}_6$ (toluene)	91
$\text{AlCl}_4^-$ (ether)	10
$\text{AlMe}_3$ (toluene)	157
$\text{Al}_2\text{Me}_3\text{Cl}_3$ (pure)	93

### 2.2.1.2 $^{45}\text{Sc}$ NMR Spectroscopy

The  $^{45}\text{Sc}$  nucleus ( $I = 7/2$ ) is 100 % abundant and is highly sensitive ( $D_c = 1709$ ) with an NMR frequency of 24.330 MHz and a moderate quadrupole moment of  $0.22 \cdot 10^{-28} \text{ m}^2$ .  $^{45}\text{Sc}$  is a seldom studied by NMR spectroscopy, but an overview of the studies most relevant to this work is discussed in Chapter 5. The only stable oxidation state of Sc is  $3+$  ( $d^0$ ), therefore electronic spectroscopy provides little information

compared to Cr(III) and Mo(III) species. However the diamagnetic nature of the Sc(III) ion means that NMR spectroscopy offers an alternative method for providing structural information.

Due to the quadrupolar nature of  $^{45}\text{Sc}$ , low symmetry Sc(III) complexes are unlikely to be detected by  $^{45}\text{Sc}$  NMR spectroscopy because of the non-zero EFG, thus significantly increasing the rates of relaxation and increasing line widths. Despite this, complexes close to  $\text{O}_\text{h}$ ,  $\text{T}_\text{d}$  and  $\text{C}_{3v}$  symmetry have been shown to have an EFG close to 0 and so, should be observable by  $^{45}\text{Sc}$  NMR studies.<sup>[1a]</sup> Even so, the precise combination of ligands has a significant effect on both the chemical shift and the observed line width - as seen in the studies in Chapter 5. Table 2.2 lists a set of scandium(III) chloride species with their  $^{45}\text{Sc}$  NMR chemical shifts and line widths.

**Table 2.2** Table of chemical shifts for selected scandium(III) species species observed by  $^{45}\text{Sc}$  NMR spectroscopy (reference  $[\text{Sc}(\text{H}_2\text{O})_6]^{3+}$ ).<sup>[1a, 3]</sup>

Scandium Compound	$\delta$ (ppm)	$W_{1/2}$ (Hz)
$[\text{ScCl}_3(\text{Ph}_2\text{MePO})_3]$	123	1100
$[\text{ScCl}_3(\text{Ph}_3\text{PO})_3]$	121	1400
$[\text{ScCl}_2(\text{Ph}_2\text{MePO})_4]\text{Cl}$	80	2000
$[\text{ScCl}_2(\text{Me}_3\text{PO})_4]\text{Cl}$	85	360
$\text{ScCl}_3$ in MeCN	204	-
$\text{ScCl}_3$ in THF	203	-

### 2.3 Infra red Spectroscopy<sup>[4]</sup>

Infrared spectroscopy is another commonly used spectroscopic technique to provide information on chemical groups and bonds. All samples were made up as a mull in Nujol and analysed on CsI plates using a Perkin Elmer FT-IR Spectrum 100 spectrometer.

The main focus in this work is the metal-halide stretching region, typically in the far-infrared ( $500\text{-}200\text{ cm}^{-1}$ ) region. Consideration of metal-halogen bonds in group theory allows the number of bands expected for a specific geometry to be predicted, thus providing a useful structural probe.

### 2.3.1 Group Theory

By identifying the symmetry elements present in a molecule, its point group can be determined. Using the relevant character tables and the reduction formula leads to prediction of the IR active bands for that molecule. Examples using two of the common geometries observed in this research are presented below:  $C_{2v}$  *mer*-[MX<sub>3</sub>Y<sub>3</sub>] and  $C_{3v}$  *fac*-[MX<sub>3</sub>Y<sub>3</sub>] (Fig. 2.1).

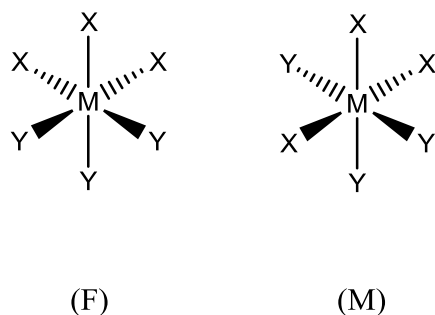


**Fig. 2.1** Generic isomers of *fac*- (F) and *mer*- (M) six-coordinate complexes.

Consideration of how the M-X bonds move during these symmetry operations allows the reducible representation to be derived (Table 2.3 and 2.4).

**Table 2.3** Reducible representation of *mer*-isomer (M) for  $\Gamma_{M-X}$ .

$C_{2v}$	$E$	$C_2$	$\sigma_v(xz)$	$\sigma_v(xz)$
$\Gamma_{M-X}$	3	1	3	1

**Table 2.4** Reducible representation of *fac*-isomer (F) for  $\Gamma_{M-X}$ .

$C_{3v}$	$E$	$2C_3$	$3\sigma_v(xz)$
$\Gamma_{M-X}$	3	0	1

The reduction formula can be applied to give the Mulliken symbols and active IR bands as follows:

→ (M) = 2 A<sub>1</sub>(z) + B<sub>1</sub> (x) (3 active bands in the infrared)

→ (F) = A<sub>1</sub> (z) + E (x,y) (2 frequencies in the infrared)

## 2.4 Ultra-violet - Visible (UV-Vis) Spectroscopy<sup>[4b, 5]</sup>

UV-Vis spectroscopy is a study of transitions involved in the rearrangement of valence electrons, which is modulated by the energy of the UV and visible part in the electromagnetic spectrum. This technique is extensively used within inorganic chemistry as it can help determine oxidation state from d-d transitions within the metal, also other transitions arising from transfer of electrons from metal-to-ligand or vice versa are also identified by UV-Vis spectroscopy.

In practice, a solution of the analyte is made up to a known concentration (typically 1 – 5 mmol). The solution can then be placed in a quartz cell within the spectrometer and detected by UV-Vis spectroscopy. This provides the energy of the electronic transitions, usually as a function of wavelength and their capacity for absorbance of UV-Vis light, which is a function of the extinction coefficient. The extinction coefficient can be found using the Beer-Lambert Law (Equation 2.1):

$$A = -\log_{10} \left( \frac{I}{I_0} \right) = \varepsilon lc$$

*A* = absorbance

*I*<sub>0</sub> = Initial intensity

*I* = Intensity

*c* = concentration (mol dm<sup>-3</sup>)

*ε* = extinction coefficient (mol<sup>-1</sup> dm<sup>3</sup> cm<sup>-1</sup>)

*l* = pathlength (cm)

### Equation 2.1 Beer Lambert Law.

The basis of the UV-Vis spectroscopic analysis in this research focuses on transition metals with 3d<sup>3</sup> (Cr(III)) or 4d<sup>3</sup> (Mo(III)) configurations. Using the Russell-

Saunders coupling scheme gives the free ion  $^4F$  ground state term for both. This leads to a  $^4A_{2g}$  ground state term in an octahedral field, leading to three spin-allowed d-d transitions, two low energy triplet states  $^4T_{2g} + ^4T_{1g}$  also from the  $^4F$  ground state, and a third triplet state  $^4T_{1g}$ , derived from a  $^4P$  excited state, which is the highest energy term. The two lowest energy terms, split by interelectronic repulsions as determined by Racah parameters can provide the  $10 D_q$  octahedral splitting term derived from the relevant Tanabe-Sugano diagram (Fig. 2.2). The magnitude of this splitting is influenced by the ligands around the metal.

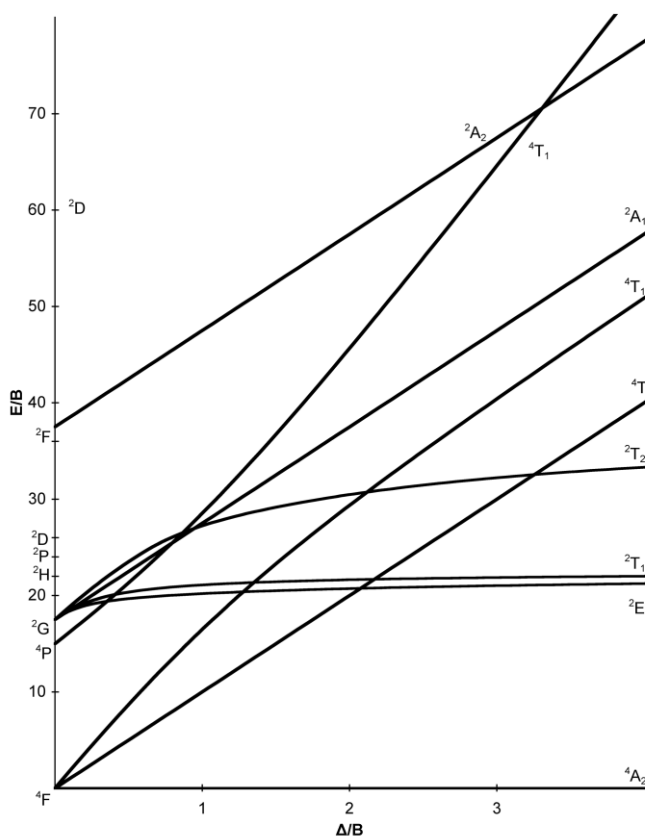


**Fig. 2.2** Tanabe-Sugano diagram showing  $^4F$  ground state splitting in an octahedral field.<sup>[5b]</sup>

The theory discussed here is generally for purely octahedral complexes and becomes significantly more difficult when considering systems of lower symmetry. Fig. 2.3 shows how the states are further split from  $O_h$  to  $C_{3v}$ . In practice, because of the broad transitions that arise in UV-Vis spectra, these extra transitions are unlikely to be observed.<sup>[6]</sup>

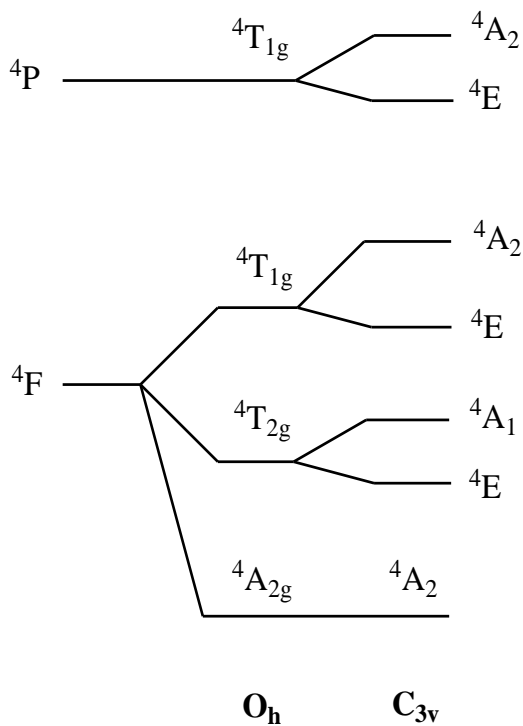


**Fig. 2.3** Energy level diagram for a  $d^3$  transition metal in  $O_h$  and  $C_{3v}$  environments.<sup>[6]</sup>

## 2.5 X-ray Absorption Fine Structure (XAFS) Spectroscopy

### 2.5.1 Introduction

X-ray Absorption Fine Structure (XAFS) is the modulation of an atom's X-ray absorption probability influenced by its chemical and physical state. How an element absorbs X-rays at, or near the binding energy of a core level electron of an atom, is influenced by its oxidation state and coordination chemistry. XAFS encompasses the two parts of the X-ray absorption spectrum: X-ray Absorption Near Edge Structure (XANES) and Extended X-ray Absorption Fine Structure (EXAFS) spectroscopy.

The inherent advantage of the XAFS technique is that it is element specific and, as every atom contains core electrons, it can in theory be used for every element in the periodic table. Because the absorption of the element is determined by its chemistry, it can be used as a tool to determine its oxidation state, coordination number, distance of neighbouring atoms and their identity. XAFS can be measured on

many sample types i.e. powder, solution, crystal etc. The technique can also be used for trace analysis in dilute systems.

For XAFS measurements, an intense and tuneable energy X-ray source is required and so, many experiments are carried out at synchrotron facilities around the world. The analysis of the data can be challenging and not always straightforward but recent advances in software have aided in gaining accurate and precise analysis.

### 2.5.2 EXAFS Theory

This technique makes use of the photoelectric effect. This is the process by which an X-ray is absorbed by an electron in the 1s or 2p orbital (K or L level) (Fig. 2.4). The binding energy of the electron must be of lower than the energy of the incident photon to be ejected. Any excess energy is used as kinetic energy by the photo-electron as it is ejected from the atom.

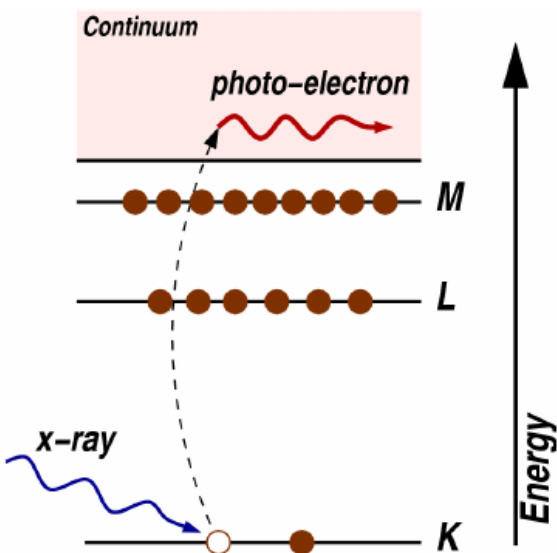


**Fig. 2.4** Photoelectric effect: incident X-ray is absorbed by core level electron, which is then ejected as a photo-electron into the continuum.<sup>[7]</sup>

The probability of X-rays absorbed at and above the absorption edge by a particular sample is determined by Beer's Law and the absorption coefficient,  $\mu$  (Equation 2.2). The absorption coefficient is dependent on the factors shown in

Equation 2.3. This demonstrates how the atomic number has a big influence on absorption coefficient over the absorption edge.

$$I = I_0 e^{-\mu t}$$

$I_0$  = Incident X-ray intensity

$t$  = Sample thickness

$I$  = Intensity transmitted through the sample

$\mu$  = Absorption coefficient

### Equation 2.2 Intensity dependence on absorption coefficient.

$$\mu \approx \frac{\rho Z^4}{AE^3}$$

$\mu$  = Absorption coefficient

$\rho$  = Density

$Z$  = Atomic number

$A$  = Atomic mass

$E$  = X-ray energy

### Equation 2.3 Dependence of absorption coefficient $\mu$ .

When a photo-electron is ejected, a sharp rise in  $\mu$  is observed. This is known as the absorption edge. The XAFS is concerned with the intensity of  $\mu$  as a function of energy (eV) near, at and above the absorption edge. Once the photo-electron is ejected, the atom enters an excited state. This excited state can decay by any one of two mechanisms, fluorescence or the Auger effect. Fluorescence occurs when an electron in a higher energy orbital moves to fill the empty core hole. This process emits an X-ray at a defined energy. The Auger Effect is the ejection of a second electron as another electron moves to fill the empty core hole. Both methods can be used to study  $\mu$ , but fluorescence is the more common method. Generally XAFS is measured in transmission or fluorescence mode.

Extended X-ray absorption fine structure (EXAFS) is concerned with oscillations over the absorption edge. The EXAFS  $\chi(E)$ , is extrapolated using Equation 2.4 and shown in Fig. 2.5.

$$\chi(E) = \frac{\mu(E) - \mu_0(E)}{\Delta\mu_0(E)}$$

$\chi(E)$  = Extended X-ray absorption fine structure (EXAFS)

$\mu(E)$  = Measured absorption coefficient

$\mu_0(E)$  = Background function representing absorption of single isolated atom

$\Delta\mu_0(E)$  = Absorption edge jump

**Equation 2.4** Showing how EXAFS is derived from XAFS spectrum.

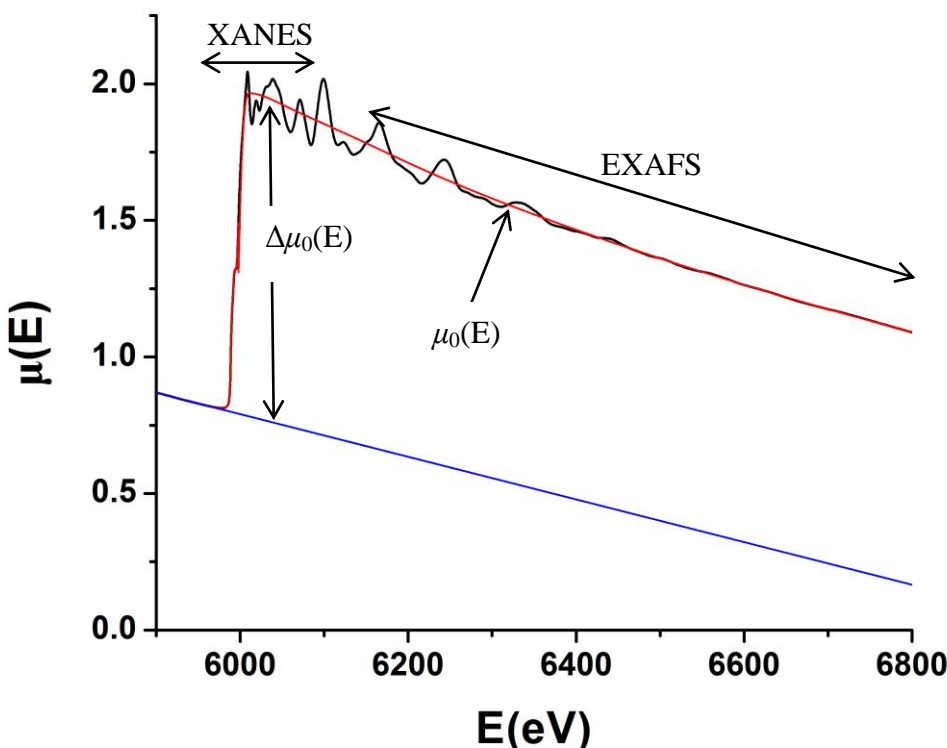


**Fig. 2.5** Showing the XAFS spectrum of a Cr foil (blue). Above: showing separate regions of X-ray absorption near edge structure (XANES) and EXAFS spectroscopy. Also showing background function  $\mu_0(E)$  (red), and edge-step  $\Delta\mu_0(E)$  (pre-edge background subtraction – blue).

EXAFS analysis considers photoelectrons in terms of its wave function. Therefore, its energy is converted to wavenumber,  $k (\text{\AA}^{-1})$ . An example of the derived EXAFS  $\chi(k)$ , for a Cr foil is shown in Fig. 2.6. This shows the EXAFS oscillations and how they decay with increasing  $k$ . To emphasise different parts of the EXAFS,  $k$  can be multiplied by the power of 2 or 3 ( $k^2$  or  $k^3$ ) (Fig. 2.6).

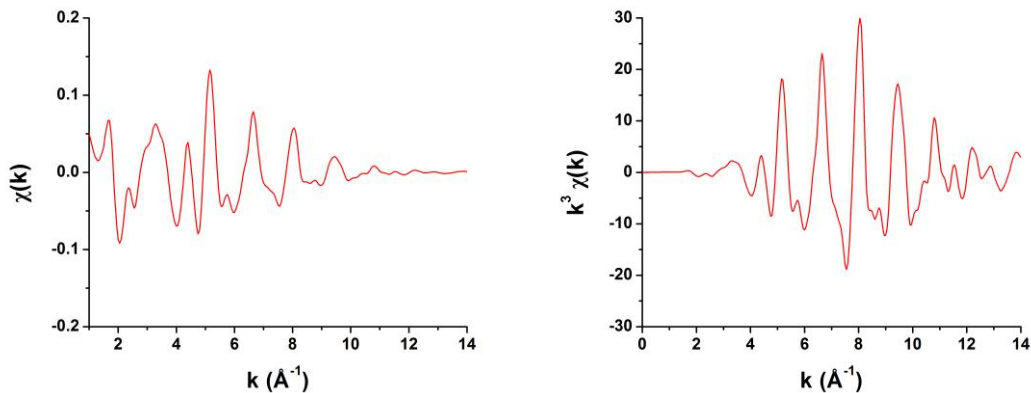


**Fig. 2.6** Left: Isolated EXAFS of a Cr foil. Right:  $k$ -weighted EXAFS,  $k^3 \chi(k)$ .

The different frequencies and amplitudes in the EXAFS correspond to backscattering of photoelectron by neighbouring atoms, which cause constructive and destructive wave interference. This signal can be deconvoluted and analysed to provide information on the coordination number, distance and type of neighbour around the absorbing atom. This is modelled using the EXAFS equation (Equation 2.5).

The underlying methodology of single electron scattering to yield structural information by EXAFS theory was first recognised by Sayers *et al.*<sup>[8]</sup> This was further developed to give the more formal derivation of the EXAFS formula as seen in Equation 2.5.<sup>[9]</sup> This equation is based on the small atom approximation, that the outgoing spherical photoelectron wave is treated as a plane wave in the vicinity of the backscatterers.<sup>[10]</sup> This enables an expression relating EXAFS intensity  $\chi$ , to photoelectron wave vector  $k$ .

$$\chi(k) = \frac{1/k \sum_j S N_j |f_j(\pi, k)|}{R_j^2} \exp(-2\sigma_j^2 k^2) \exp(-2R_j/\lambda) \sin[2kR_j + 2\delta + \alpha_j]$$

$S$	- Amplitude reduction factor.
$N_j$	- Number of equivalent backscatters in each shell, $j$ .
$R_j$	- Interatomic distance between absorber and backscatterer.
$f_j(\pi, k)$	- Backscattering amplitude of backscattering atom.
$\sigma_j^2$	- Mean square variation of $R_j$ .
$\lambda$	- Elastic mean free path.
$\delta$	- Phase shift arising from absorber.
$\alpha_j$	- Phase shift arising from backscatterer.

### Equation 2.5 The plane wave theory EXAFS equation.

Plane wave theory is the summation of a series of damped sine waves, where each wave is derived from equivalent backscatters producing an interference pattern. The terms from the equation relate to phase and dampening of EXAFS oscillations. These terms are explained below.

#### - Phase Shift - $\sin[2kR_j + 2\delta + \alpha_j]$

The ejected photoelectron from the X-ray absorber experiences a phase shift influenced by inner bound electrons of the atom ( $\delta$ ). This phase shift is also experienced during backscattering by neighbouring atoms ( $\alpha_j$ ). The photoelectron undergoes a final phase shift again from the central atom and so, these shifts give the term  $\sin[2kR_j + 2\delta + \alpha_j]$  (where  $2kR_j$  term is the wave progression). The backscattering amplitude of an atom is calculated from the phase shift and is  $k$  dependent. The backscattering amplitude will increase with increasing atomic number, Z.

#### - Debye-Waller Factor - $\exp(-2\sigma_j^2 k^2)$

This term relates to the disorder and precision of  $R_j$ . This defines the magnitude of dampening of the EXAFS oscillations as they are broadened. This term is increased by uncertainties of interatomic distance between backscatterers and

absorbing atom. A high Debye-Waller factor illustrates a high degree of dampening and therefore a low overall contribution.

These uncertainties arise from static disorder, such as a large range in the distance between atoms within one shell, and dynamic disorder, caused by vibrations of coordinated atoms. In this case, the dynamic disorder is approximated as a Gaussian distribution, but in many cases this is not true as most vibrations will not be truly harmonic.

#### - Multiple Excitation Amplitude Reduction Factor – $S$

As a photoelectron is ejected from the absorbing atom, the excess energy it possesses can excite or even eject a further electron from the atom. This produces an overall shift in phase and energy of the EXAFS contribution. This results in dampening of the experimental EXAFS data,  $S$ . The degree of dampening is dependent upon the nature of the absorber only and less influenced by its chemical environment. Therefore  $S$  is considered to be constant for edges of the same element, once it has been established by known compounds.

#### - Mean Free Path - $\exp(-2R_j/\lambda)$

A photoelectron has a finite lifetime as the wave loses energy to its surroundings by inelastic scattering. This leads to a decrease in the interaction between outgoing and backscattering photoelectron by reducing coherency and the strength of interference patterns.

### 2.5.3 X-ray Absorption Near Edge Structure (XANES) Spectroscopy

X-ray absorption near edge structure (XANES) spectroscopy is the analysis of features just before, at and just over the absorption edge (Fig. 2.7). It is sensitive to the oxidation state and geometry of the metal in question. At low  $k$ , the EXAFS equation breaks down therefore XANES analysis is required.

When comparing samples, the XANES is useful at the very least in comparison of edge shift and pre-edge features. These can be an indication of changes in symmetry and oxidation state changes of the metal in question (Fig. 2.7).

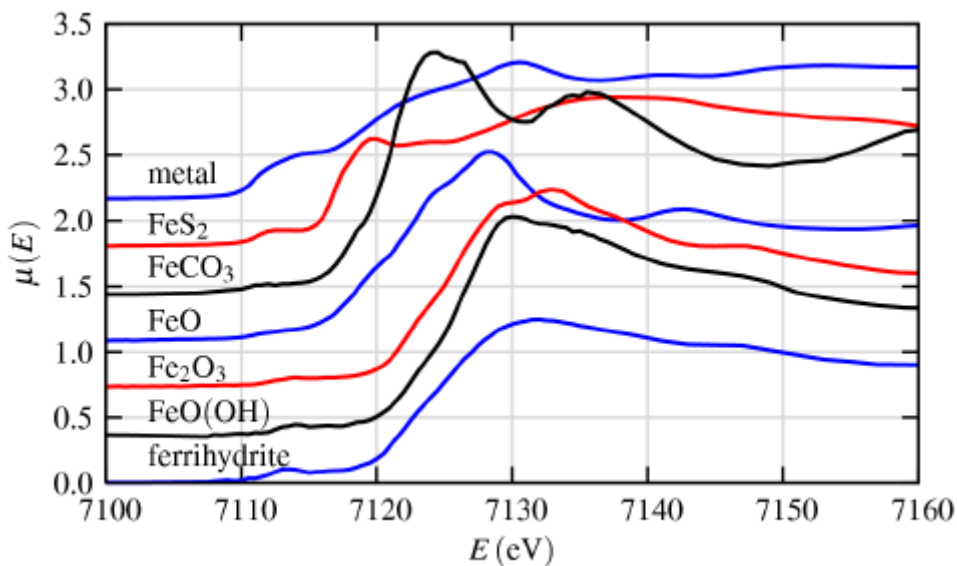


**Fig. 2.7** Fe K-edge XANES spectra of Fe metal and Fe compounds.<sup>[7]</sup>

In XANES spectroscopy, as the X-ray is absorbed, the core level electron is not ejected from the atom but can possibly be promoted to the next orbital quantum number ( $l$ ), as given by the rule  $\Delta l = \pm 1$ . When considering a transition metal, the p-orbital is filled and by this law, absorption of the X-ray should not occur, yet this absorption is still seen.

When comparing Cr<sup>3+</sup> and Cr<sup>6+</sup> oxides, such as octahedral Cr<sub>2</sub>O<sub>3</sub> (Cr<sup>3+</sup>) and tetrahedral CrO<sub>3</sub> (Cr<sup>6+</sup>), the metal will have either an empty or partially filled d-orbital valence shell, which would be reflected by the Cr K-edge position of the metal states, as observed in Fig. 2.8, there is a significant shift between Cr<sup>3+</sup> and Cr<sup>6+</sup>. The edge position is not solely governed by oxidation state, it can also reflect geometry and its surrounding ligands (Fig 2.8).

Along with charge transfer effects, the 1s(Cr) to 4p(Cr) transition can be observed because of the hybridisation of the 4p(Cr) shell and the 3d(Cr) shell. Therefore the stronger this hybridisation, the more p in character the d-orbitals become, the stronger the intensity of the 1s to 4p transition. This demonstrates how these pre-edge features can be dramatically altered depending on the coordination environment surrounding the metal.

For Cr<sup>6+</sup>, a strong pre-edge absorption is observed. This arises from a charge transfer between Cr to O. There is a high degree of overlap with the p-orbitals on the oxygen and so an intense charge transfer band is seen.

For  $\text{Cr}^{3+}$ , only weak pre-edge absorption features are observed because this metal has a partially filled valence shell,  $3d^3$ , giving an octahedral crystal field splitting term. This means there is a low overlap of the oxygen p-orbitals with the metal and the observed transitions are the low probability  $1s \rightarrow 4p$  transition. From this theory XANES can be qualitatively interpreted for its coordination chemistry and in turn an interpretation of crystal field splitting.

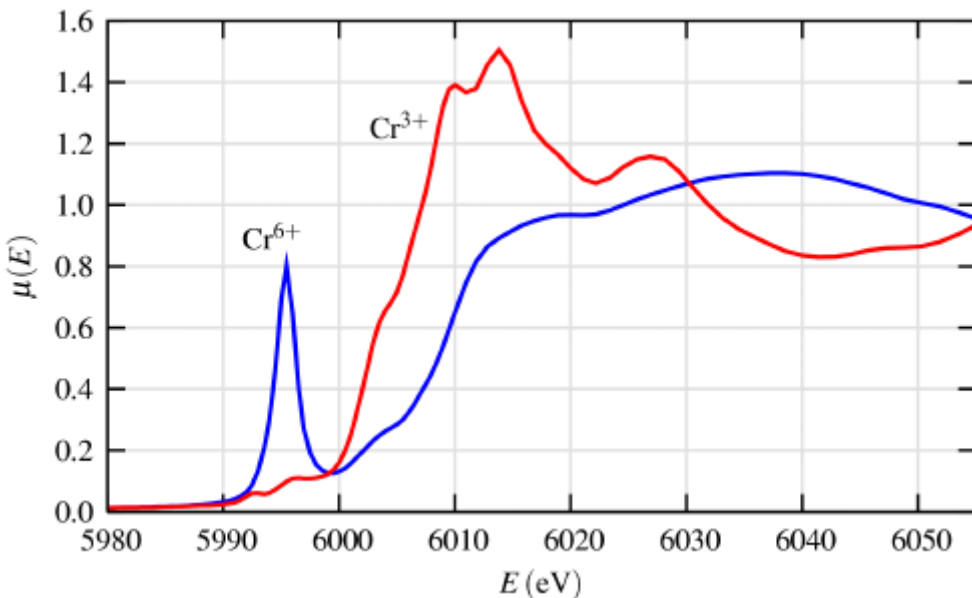


**Fig. 2.8** Cr K-edge XANES spectra for octahedral  $\text{Cr}^{3+}$  and tetrahedral  $\text{Cr}^{6+}$ .<sup>[7]</sup>

The edge shift can help in determining the oxidation state of a metal. Use of good model data of purely one oxidation state can provide a visual interpretation of the degree of oxidation or reduction of a sample. Model data can also provide ‘finger print’ comparison by comparing sample and model data. Detailed XANES analysis is now a possibility but is beyond the scope of the work presented here.<sup>[11]</sup>

## 2.7 References

- [1] a) J. Mason, *M multinuclear NMR*, Springer, New York and London, **1987**; b) J. A. Iggo, *NMR Spectroscopy in Inorganic Chemistry*, Oxford University Press, Oxford, **2000**; c) W. Kemp, *NMR in Chemistry: A Multinuclear Introduction*, Macmillan Education Ltd., Hong Kong, **1986**.
- [2] D. E. O'Reilly, *J. Chem. Phys.* **1960**, 32.
- [3] M. C. Popham, *Complexes of the Group 3 Metal Salts and Titanium Halides with Tertiary Pnictogen Oxides and Crown Ether Ligands*, PhD Thesis, University of Southampton, Southampton, **2003**.
- [4] a) A. Vincent, *Molecular Symmetry and Group Theory*, John Wiley & Sons, London, **1977**; b) E. A. V. Ebsworth, D. W. H. Rankin and S. Cradock, *Structural Methods in Inorganic Chemistry*, Blackwell Scientific Publications, Great Britain, **1987**.
- [5] a) A. K. Brisdon, *Inorganic Spectroscopic Methods*, Oxford University Press, Oxford, **1998**; b) D. F. Shriver and P. W. Atkins, *Inorganic Chemistry*, Oxford University Press, Oxford, **1999 p437**.
- [6] A. B. P. Lever, *Inorganic Electronic Spectroscopy*, Elsevier, Amsterdam, **1984**.
- [7] M. Newville, *Fundamentals of XAFS*, Consortium for Advanced Radiation Sources, University of Chicago, **2008**.
- [8] D. E. Sayers, E. A. Stern and F. W. Lytle, *Phys. Rev. Lett.* **1971**, 27, 1204-1207.
- [9] P. A. Lee and J. B. Pendry, *Phys. Rev. B* **1975**, 11, 2795-2811.
- [10] S. J. Gurman, *J. Phys C Solid State* **1988**, 21, 3699.
- [11] D. C. Koningsberger and R. Prins, *X-ray Absorption: Principles, Applications, Techniques of EXAFS, SEXAFS and XANES*, in *Chemical Analysis*, John Wiley & Sons, **1988**.



## **Chapter 3.**

**Validation of the Stopped-Flow Instrument and  
Freeze-quench Accessory by Chromium (III) UV-Vis  
Spectroscopy and Molybdenum (III) EXAFS  
Analysis.**

### 3.1 Introduction

This section aims to introduce the stopped-flow instrument and discuss previous research where it has been used to help identify transition metal complexes.

#### 3.1.1 The Stopped-flow Instrument

The stopped-flow instrument is, in essence, a system for rapid mixing of reagents (in solution) and real time monitoring of reactant/product concentrations. Common problems of normal solution phase reactions include slow mixing of reagents or identifying short lifetime intermediate states; these can be addressed by the use of a stopped-flow instrument. Utilising sophisticated flow systems which provide fast flow rates (for good mixing) and low dead times (point from mixing of reagents to detection), the stopped-flow is an advanced mixing instrument and can be coupled with an appropriate detection method to be used as a strong tool in identifying short lived reaction intermediates.

The system works by injection of two or more reagents from separate syringes into a mixing chamber, which in turn fills an effluent syringe at the end of the system. Once this end syringe fills to a pre-determined point, a backstop is hit which halts the flow of the system. Between the point of mixing and the effluent syringe, a detector can be placed (commonly a UV-Vis absorption spectrophotometer) where monitoring of reactant/product concentration can be performed (Fig. 3.1). <sup>[1]</sup>

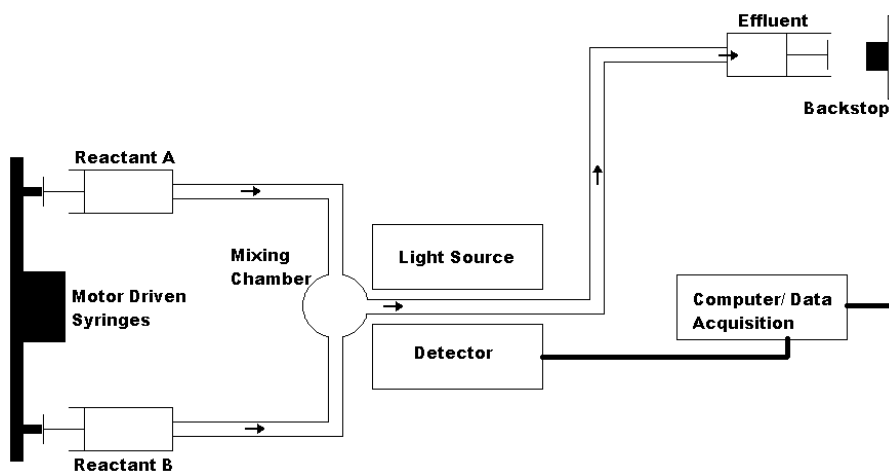


**Fig. 3.1** Schematic of a typical stopped-flow design (arrows indicating direction of flow).

Typically, the stopped-flow system is coupled with UV-Vis spectroscopy to follow reactions and help in identifying any changes of electronic absorption within the d-orbital manifold or the charge transfer bands of a complex. This method allows for very fast detection (ms time scale) and subsequent analysis can be used to establish reaction kinetics. The stopped-flow system is a flexible instrument where many detection methods can be employed. Along with UV-Vis spectroscopy, other detection methods include small angle X-ray and neutron scattering to study mechanisms of surfactant self assembly,<sup>[2]</sup> also for the study of protein folding by stopped-flow FT-IR, NMR and circular dichroism spectroscopies.<sup>[3]</sup>

In 1990,<sup>[4]</sup> a new detection method of Energy Dispersive X-ray Absorption Fine Structure (EDXAFS) spectroscopy was employed with the rapid mixing provided by the stopped-flow system.<sup>[5]</sup> EDXAFS allows for fast acquisition of XAFS data, as it allows a wide X-ray energy range to be recorded simultaneously without mechanical motion during measurements. As there are no moving components, energy scales and focusing of the beam become incredibly stable. The main limitations of EDXAFS are in keeping the energy of the beam travelling in the correct direction, originating from the polychromator, to the crystal, to detection. This then puts constraints on morphology and structure of the sample. Secondly, this technique does not allow detection by de-excitation techniques (i.e. fluorescence required particularly for soft X-rays). As large energy ranges strike the sample simultaneously, these signals become flooded,<sup>[6]</sup> although it is possible now to overcome this limitation albeit at reduced time-resolution (seconds) in comparison to normal EDXAFS measurements (milliseconds).<sup>[7]</sup> Examples of the use of these experiments using EDXAFS spectroscopy have been reported previously<sup>[6,8]</sup> and some cases are discussed below.

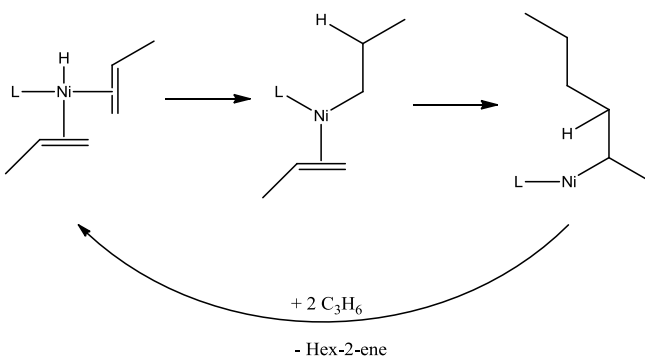
### 3.1.2 Analysis of Iron and Nickel Catalytic Pathways

The oxidation of hydroquinone by iron(III) perchlorate was studied using EDXAFS/stopped-flow technique.<sup>[4]</sup> This is a redox reaction and is thought to occur through a single electron oxidation step, forming a free radical semiquinone intermediate.<sup>[9]</sup> The Fe K-edge XANES of this reaction reflected the reduction of the

ferric ion, forming a Fe(III)-hydroquinone intermediate, with the end-state matching the ferrous cation,  $[\text{Fe}(\text{H}_2\text{O})_6]^{2+}$ .

This set-up had now proved useful in identifying short lived intermediate species and so, it was put to use in probing other catalytic pathways.

The dimerisation of propene by  $[\text{Ni}(\text{acac})_2]$  (acac = acetylacetone) to form linear hexenes in the presence of weak Lewis acids, such as  $\text{AlEt}_2(\text{OEt})$  was investigated. It was found that at  $0\text{ }^\circ\text{C}$ , the catalytic solution changed reversibly from yellow to a catalytically inactive green solution.<sup>[10]</sup>  $[\text{Ni}(\text{ethyl})(\text{acac})]$  was suggested as the active (yellow) intermediate, stabilised by the presence of an  $\alpha$ -olefin. The suggested mechanism is shown in Scheme 3.1.



**Scheme 3.1** Proposed catalytic cycle for the dimerisation of propene by  $[\text{Ni}(\text{acac})(\text{ethyl})(\text{propene})]$  precursor (L = ligand).<sup>[10]</sup>

In 1996, Bogg *et al.*<sup>[11]</sup> repeated this experiment and followed it by Energy Dispersive EXAFS (EDE) spectroscopy. Scanning XAFS revealed the green inactive solution to be a trimeric  $[\text{Ni}(\text{acac})_2]_3$  complex ( $-70\text{ }^\circ\text{C}$ ) and the active (yellow) solution ( $5\text{ }^\circ\text{C}$ ) to be either one of the monomers in Fig. 3.2. Using a modified low temperature cell fitted with syringe drivers to provide continuous or interrupted flow mixing, EDE analysis agreed with the previously collected scanning XAFS data. This method found the lead up to the trimeric/monomeric equilibrium was rapid (40 s at  $0\text{ }^\circ\text{C}$ ), where after 4.75 mins at  $0\text{ }^\circ\text{C}$ , a trimeric intermediate was identified by EDE. This species had undergone partial substitution of the acac ligand from the  $[\text{Ni}(\text{acac})_2]_3$  by alkene and alkyl ligands. (Fig. 3.3).

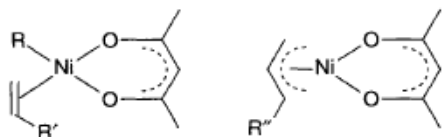


**Fig. 3.2** Active Ni propene dimerisation catalyst proposed by EXAFS analysis.<sup>[11]</sup>

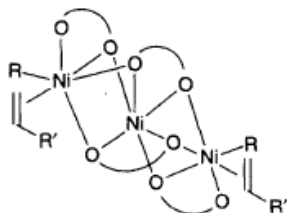


**Fig. 3.3** Trimeric Ni intermediate suggested by EDE analysis for the dimerisation of propene ( $O-O = acac$ ).<sup>[11]</sup>

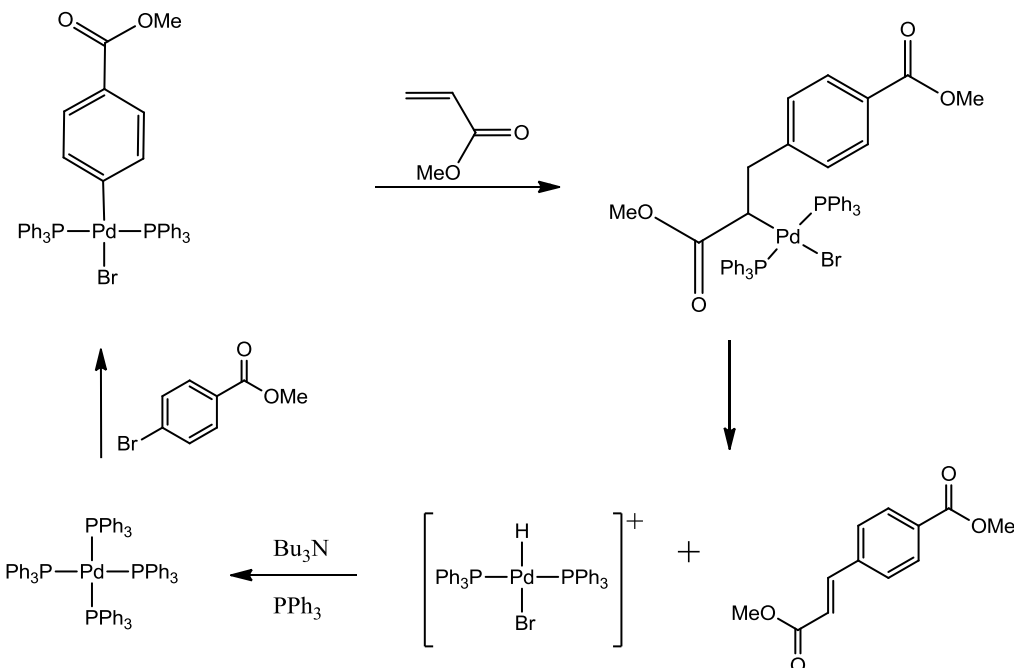
In a further study of this Ni system in 2002, the same group used the EDE/stopped-flow technique to look at the 1-hexene di/tri-merisation,<sup>[12]</sup> in a solution of  $[Ni(dpm)_2] / AlEt_2(OEt) / hex-1-ene$  (1:2:20) ( $dpm = ^{t}Bu-C(O)CH_2C(O)-^{t}Bu$ ). After 20 min at 0 °C, EXAFS analysis indicated the coordination of one dpm ligand and three carbons at 2.07 Å, giving the same Ni species as presented in Fig. 3.2. This analysis gives evidence for a mechanism of alkene catenation by insertion into a Ni-alkyl bond as suggested in Scheme 3.1. Using the EDE/stopped-flow technique, an initial change in the coordination sphere of  $[Ni(dpm)_2]$  was observed after 32 s. Between 32 s to 320 s only minor changes were observed, thought to be reordering of the Ni coordination for di/tri-merisation of 1-hexene as shown as an equilibrium of the  $\eta^3$ -enyl complex in Fig. 3.2.

### 3.1.3 Analysis of Palladium Catalytic Pathways

Palladium catalysts have been used for many years to produce new carbon-carbon bonds, although the exact palladium species in solution has seldom been isolated. In one such example, a four coordinate palladium complex has demonstrated its ability to alkylate allyl substrates (Scheme 3.2 and 3.3).<sup>[13]</sup>



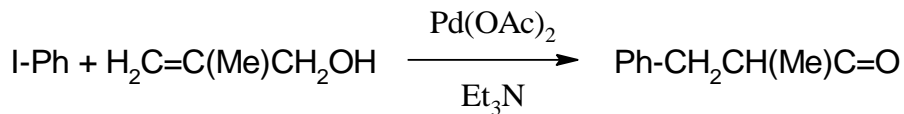
**Scheme 3.2** Reaction scheme showing formation of the palladium four coordinate catalytic precursor in a Heck Coupling.



**Scheme 3.3** Suggested reaction pathway of Heck Coupling by palladium catalysis.<sup>[13]</sup>

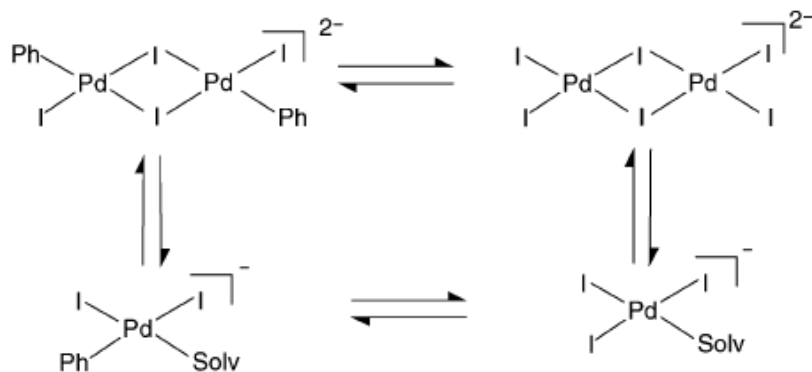
Using palladium acetate as the catalytic precursor (Scheme 3.4), an investigation of the active palladium species of this pathway was analysed using both EDE and Quick EXAFS (QEXAFS).<sup>[14]</sup>

$[\text{Pd(OAc)}_2]$  is trimeric by XRD.<sup>[15]</sup> In a solution of *N*-methyl-2-pyrrolidone (NMP), no evidence of  $\text{Pd}^{\cdots}\text{Pd}$  contributions were found by XAFS, suggesting that NMP breaks up the trimer to yield the monomeric form.



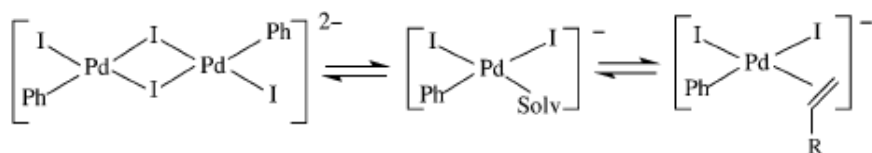
**Scheme 3.4** Palladium catalysed coupling under study by EDE/QEXAFS spectroscopy.

Analysis of the pre-catalytic solution ( $\text{Pd(OAc)}_2 + \text{I-Ph} + \text{NR}_3$  [ $\text{R} = \text{Et, Me}$ ] in NMP) by EXAFS spectroscopy shows the palladium complex coordinates to 3.2 iodides at  $2.62 \text{ \AA}$ . A small shoulder was observed in the Fourier transform of the EXAFS, suggesting the coordination of light atom scatterers from the phenyl ring or the solvent NMP at around  $2 \text{ \AA}$ . This evidence suggests the equilibrium exists as shown in Scheme 3.5.



**Scheme 3.5** Suggested palladium species present in equilibrium in pre-catalytic solution (Solv = NMP).

The addition of 2-methylprop-2-en-1-ol to the solution, at  $75 \text{ }^\circ\text{C}$  initiates the catalysis, lasting for 1 h. The XAFS analysis of the catalytic solution gave a two coordinate carbon shell and an iodine shell of coordinate *ca.* 2. This analysis suggests an equilibrium exists between the Pd dimer and the olefin coordinated monomer (Scheme 3.6).

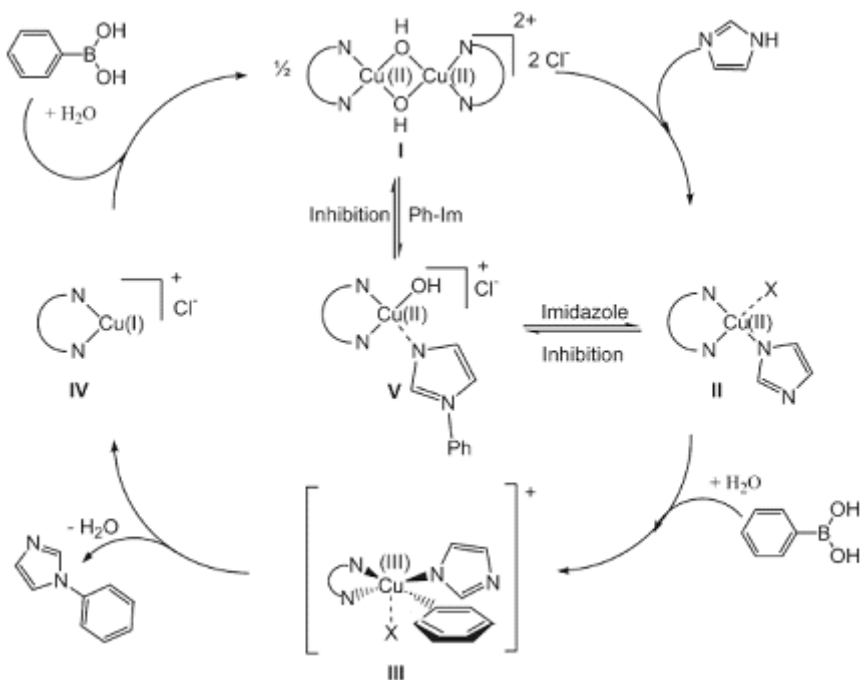


**Scheme 3.6** Suggested palladium species present in catalytic solution at 75 °C.

Although there was no direct evidence of the Pd dimer by EDE/QEXAFS (as a Pd···Pd shell neither improves or deteriorates fit), removal of all volatiles from the catalytic solution gave a single crystal of  $[Pd_2I_6][NR_3H]_2$ . The reason no Pd···Pd shell was observed by EXAFS was thought to be because palladium complexes have a tendency to bridge and so, the low frequency bending of this bridged unit would give a high dynamic Debye Waller factor, meaning the Pd···Pd shell will become difficult to detect at higher temperatures. It is postulated the opening of the bridged unit provides a vacant site for the alkene to coordinate before insertion into Pd-C bond.<sup>[14a]</sup>

### 3.1.4 Analysis of Copper Catalysed Aryl Coupling Reaction

Another study investigated the mechanism of Cu(II)-catalysed aryl coupling reaction. By using EDXAFS and UV-Vis, also incorporating EPR and NMR techniques, a complex catalytic pathway was proposed and supported for the  $[Cu(OH)(TMEDA)]_2$  (TMEDA = tetramethylethylenediamine) catalytic coupling of imidazole and phenyl boronic acid to produce the single phenyl-imidazole product (Scheme 3.7).<sup>[16]</sup>



**Scheme 3.7** Proposed catalytic cycle for the Cu(II)-catalysed arylation of imidazole and phenyl boronic acid.<sup>[16]</sup>

For each Cu species shown in the cycle (**I – V**), EDXAFS data was collected along with UV-Vis, EPR and <sup>11</sup>B and <sup>1</sup>H NMR spectroscopy. In time EDXAFS and UV-Vis spectroscopy was able to decipher the formation of the monomer along with the oxidation and various coordination states of many of the Cu species within the cycle. Analysis of the results showed the imidizole undergoes deprotonation to give [Cu(TMEDA)(Imidizole)(Imidozolate)] complex **II**, where a further imidizole is weakly coordinated to provide an easily dissociated ‘vacant site’. This intermediate is thought to react with an ‘activated’ phenylboric acid species to form the Cu intermediate **III** and then undergo a possible reductive elimination step to give the Cu(I) species **IV**.

The combined stopped-flow and XAFS approach has proven itself to be an insightful technique for probing catalytic cycles across a range of homogeneous transition metal complexes using a variety of different chemical reagents. Use of the stopped-flow unit with the observation head allows for fast reactions to be observed accurately by UV-Vis spectroscopy, with the addition of the XAFS to give structural and electronic information specific to the metal being probed. The literature discussed above displays an array of previously undiscovered intermediates to provide

information of key steps, allowing the proposal of complete catalytic pathways. One limitation to this technique is poor signal-to-noise data collection for fast XAFS acquisition. Yet this is now much improved and sure to enhance over time with the improvements of beam flux and collimation at synchrotrons, enabling high quality data collection of sub-second intermediates.

One of the purposes of the work in this thesis is to establish an XAFS cell which allows ‘trapping’ (stabilisation) of intermediate species present at various stages of activation and catalysis, by development of rapid quenching to effectively pause reactions. Once the catalytic intermediate is ‘trapped’, XAFS detection can be performed in fluorescence mode with long data acquisition times as required for low energy systems like Cr. The development of such an XAFS quench cell can trap highly reactive transients on a sub-second time-scale and allow structural identification. Complementing this technique with established stopped-flow EXAFS spectroscopy procedures and more standard techniques (i.e. IR, UV-Vis spectroscopies.) can provide, in principle, an in-depth study of any homogeneous process and catalytic cycles. Although freeze-quench (also in combination with stopped-flow methodologies) is used frequently for biological and bio-inorganic systems,<sup>[17]</sup> the research presented across this thesis requires an anaerobic approach to reliably study the homogeneous catalysis cycle in question, which requires considerable modifications to the apparatus which are discussed below.

### **3.2 Aims**

The work of this chapter aims to discuss how reliable, reproducible results can be achieved using a stopped-flow instrument and freeze quench accessory. This is an integral part to all later work in the following chapters, where using a stopped-flow instrument has allowed us to gain important insights into ethene oligomerisation or polymerisation catalysis. Presented here are detailed workings of the stopped-flow apparatus, its validation and the adaptation required for housing air and moisture sensitive chemistry. In addition, performing titrations of a highly moisture sensitive compound, trimethylaluminium ( $\text{AlMe}_3$ ), provided an indication of the concentrations which were able to be handled reliably in the stopped-flow instrument and so, give a good indication of its lifetime.

In order to establish the reliability of the results from the stopped-flow instrument, the reaction of  $[\text{CrCl}_3(\text{decyl-SNS})]$  (decyl-SNS =  $\text{HN}(\text{CH}_2\text{CH}_2\text{SC}_{10}\text{H}_{21})_2$ ) and 10 mol equivalents of  $\text{AlMe}_3$  was followed using the UV-Vis/stopped-flow set-up and compared with data collected using a Perkin-Elmer Lambda 19 UV-Vis instrument, where results have been previously published.<sup>[18]</sup> Furthermore, new chemistry of  $[\text{MoCl}_3(\text{decyl-SNS})]$  and 20 mol equivalents of  $\text{AlMe}_3$  was performed again using the UV-Vis/stopped-flow setup and Lambda 19 spectrometer, within a gas tight quartz cell under an inert nitrogen atmosphere.

In order to validate the freeze quench accessory, a titanium metallocene complex<sup>[19]</sup> was passed through the system,<sup>16,17</sup> injected into a sealed Kapton® tube to confirm the absence of  $\text{O}_2/\text{H}_2\text{O}$ . Once established, a solution of  $[\text{MoBr}_3(\text{SBz})]$  ( $\text{SBz} = \text{S}(\text{CH}_2\text{CH}_2\text{SCH}_2-\text{C}_6\text{H}_4-p\text{-C}(\text{CH}_3)_3)_2$ ) was injected in the same manner and frozen. At which point EXAFS data was collected, and later analysed to establish that the complex had remained intact.

### 3.3 Results and Discussion

#### 3.3.1 Details and Modifications of the BioLogic Stopped-flow Instrument

The stopped-flow instrument (SFM400/QS, Biologic, France) consists of four syringes which can be filled with reagents or solvent.<sup>[16, 20]</sup> The system is computer controlled and allows injection of very precise volumes with controlled injection rates (and thus injection times). The solutions are injected using stepper motors via the delay lines and mixers into a cuvette or capillary, depending on the requirement. A lower limit of 19 ms dead time (point of mixing to first detection) can be achieved.<sup>[21]</sup> Specially designed quartz cuvettes allow time-resolved XAFS experiments to be performed on the injected mixtures. Use of cuvettes with two transmission pathways perpendicular to each other, allows the addition of a complementary technique, like UV-Vis spectroscopy, to be performed simultaneously (Fig. 3.4).<sup>[16]</sup> An optical fibre UV-Vis spectrometer (MCS-UV-VIS-NIR 1/500-3 Fast Diode Array Detector, BioLogic, France), specially customised for the stopped-flow instrument, was used for these studies. This spectroscopy technique was used to perform time-resolved UV-Vis studies in the laboratory as well as combined XAFS/UV-Vis experiments at the synchrotron. Due to the air and moisture sensitive nature of the chemistry, the entire

stopped-flow apparatus was connected to a Schlenk line, allowing us to work under an argon atmosphere (Figs. 3.5 and 3.6). To ensure the stopped-flow instrument was completely air and moisture free, a careful cleaning and passivating procedure was employed before every experiment. The internal components of the stopped-flow instrument were manufactured in KelF® (polychlorotrifluorethyene), with Kalrez® (perfluoroelastomer) rings, to ensure full chemical compatibility. Originally, the internal components were manufactured from PEEK® (polyether ether ketone) until it was discovered early on that this polymer type dissolved slowly in AlMe<sub>3</sub> solutions, at which point it was replaced with KelF®.

There are two extra modes of operation; the addition of a freeze-quench accessory, which will be discussed later in the chapter and quenched-flow mode. The quenched-flow mode is designed to allow collection of a sample after mixing, allowing analysis by additional methods. The quenched-flow set-up was utilised to determine AlMe<sub>3</sub> concentrations.

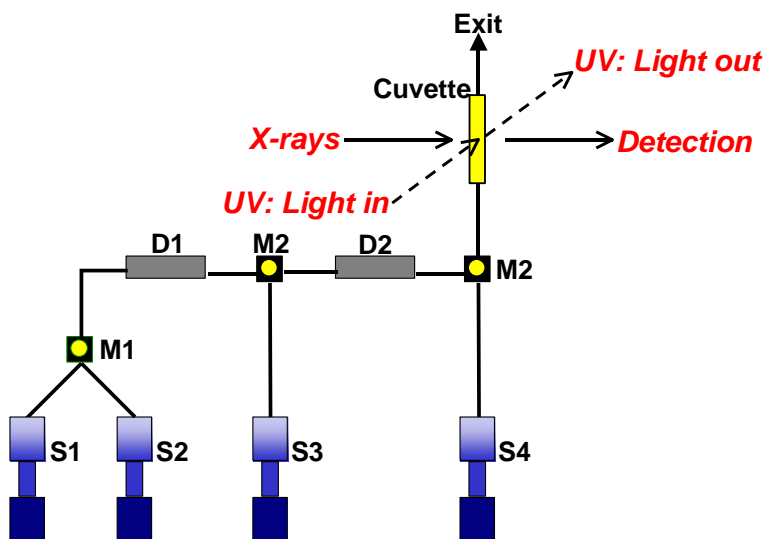


**Fig. 3.4** Schematic of stopped-flow instrument set-up for UV-Vis and simultaneous XAFS measurements (S = syringe, M = mixer, D = delay line).<sup>[20]</sup>

Exclusion of air and moisture is essential to probe the activation pathways. The stopped-flow instrument required alterations to ensure this was achievable. All entries to syringes were fitted with plastic screws connected to PTFE tubing with a needle attached. These were then placed into sealed Schlenk vessels under a positive

pressure of argon. The exit was sealed with a rubber tube leading to a round bottom flask, under positive pressure of argon. This is shown in Figs. 3.5 and 3.6. The passivation of the instrument is detailed in the next section.

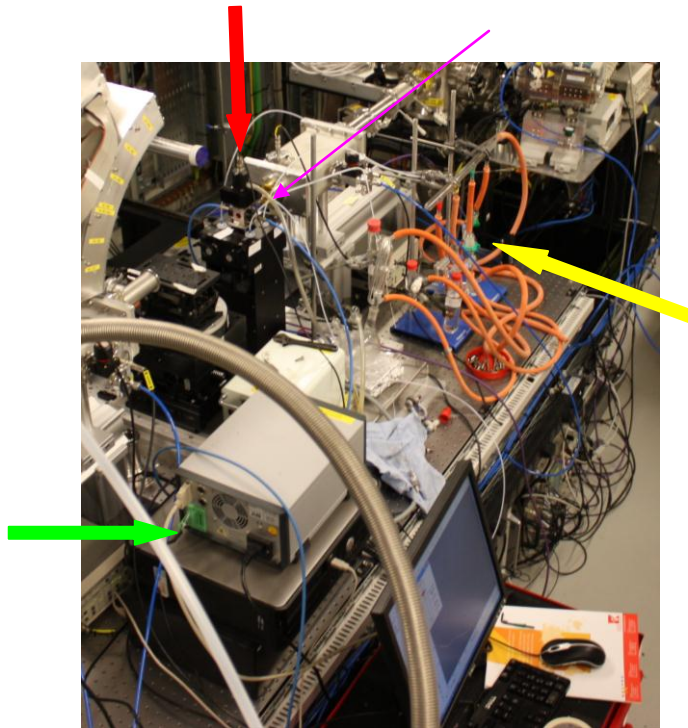


**Fig. 3.5** Photograph showing the stopped-flow instrument on B18 beamline at the Diamond Light Source. The red arrow pointing to the position of stopped-flow instrument, yellow arrow pointing to attached Schlenk line, green arrow pointing to UV-Vis spectrometer and computer and the pink arrow displays direction of X-rays from synchrotron.

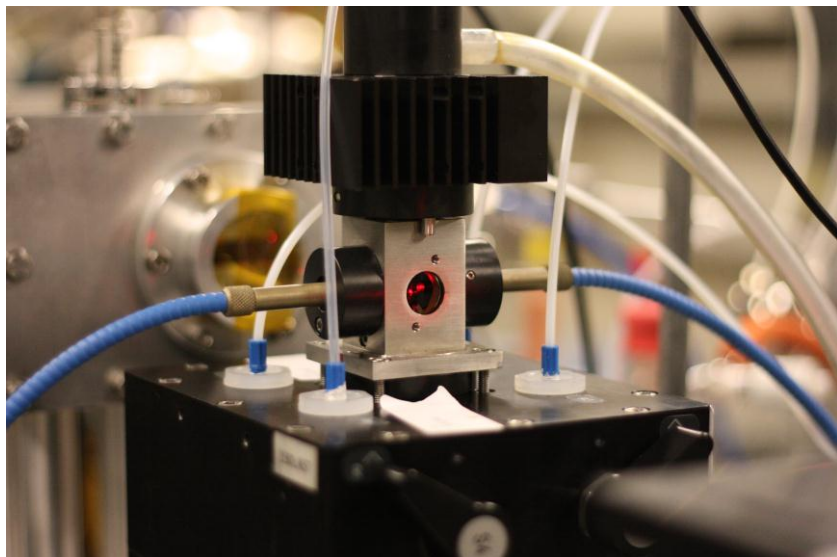


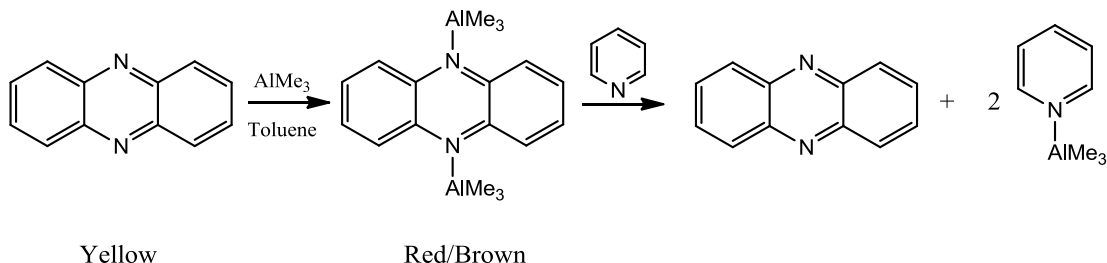
**Fig. 3.6** Photograph showing observation head with optical fibre connectors, sealed entries to syringes and waste tube.

As confirmation that this stopped-flow system was capable of excluding air and moisture satisfactorily, AlMe<sub>3</sub> was titrated at regular intervals as stated below, with no loss of concentration.

### 3.3.2 Titration of AlMe<sub>3</sub> using the Quench-flow Setup

Many reactions within the stopped-flow instrument will involve the use of AlMe<sub>3</sub>. Therefore it is of high importance that the concentration of this reagent remains constant when moving through the stopped-flow system and when contained for periods of time in the syringes. To confirm this, a titration method was established by using the quench-flow mode.

The titration of AlMe<sub>3</sub> is a published procedure, where a yellow solution of phenazine in dry toluene is used as an indicator.<sup>[22]</sup> To this, a known amount of AlMe<sub>3</sub> was added which coordinates to phenazine to give a red/brown solution, indicating an excess of AlMe<sub>3</sub>. The solution was then titrated with dry pyridine, which firstly coordinates to excess AlMe<sub>3</sub>, then substitutes the coordinated AlMe<sub>3</sub> from the phenazine. Once all AlMe<sub>3</sub> is removed from the phenazine, the solution returns to yellow (Scheme 3.8).



**Scheme 3.8** Scheme showing titration method of  $\text{AlMe}_3$  by pyridine.<sup>[22]</sup>

Before the titration, the quench-flow system first required purging of air and moisture (passivation follows the same method in the stopped-flow mode). This was done by placing all attaching stopped-flow syringe needles into sealed Schlenk tubes with a positive pressure of argon. The syringes were filled with dry argon and pushed through the quench-flow, with this repeated five times. Dry degassed toluene was taken up into all syringes and this was pushed through the quench-flow set-up. The syringes were ‘washed’ with their subsequent reagents (phenazine, pyridine or AlMe<sub>3</sub> solutions) and pushed through the quench-flow to remove any impurities or toluene residues. The syringes could then be filled with the required reagents and the titrations could begin.

In the quench-flow mode, a certain volume was required to be put to waste (minimum 250 µl) to ensure the correct volume was collected. The solution could then be collected into a purged, clear syringe. For example, 100 µl of the phenazine indicator solution was collected, followed by AlMe<sub>3</sub>, 250 µl of 1 M solution in toluene. This mixture was then titrated by pyridine (50 µl of 0.5 M pyridine solution in toluene). As the collection vessel is clear, colour changes were easily observed to determine the end point. The syringe was easily removed and disposed of, to be replaced and the titration repeated.

A previously titrated solution of AlMe<sub>3</sub> in toluene (titrated using standard Schlenk apparatus) was then introduced into the quench-flow set-up and titrated. The results indicated that solutions of 1.0 M AlMe<sub>3</sub> and below were constant, with no decrease over the measured time (5 hours, measured every hour). Each measurement matched the previously determined value from the Schlenk line titration. When using a solution of 1.5 M, the initial titration was lower than the pre-determined value and decreased over time. Therefore a 1.0 M solution of AlMe<sub>3</sub> was used as the highest

concentration, which was stable for at least 5 hours in the stopped-flow instrument, which was sufficient for the later experiments.

### 3.3.3 Validation by 5 mM [CrCl<sub>3</sub>(decyl-SNS)] + 10 AlMe<sub>3</sub> in toluene

As analysis of [CrCl<sub>3</sub>(decyl-SNS)] and 10 mol equiv. of AlMe<sub>3</sub> by UV-Vis spectroscopy has been previously published,<sup>[18]</sup> this same chemistry was performed within the stopped-flow system. This made for a good reaction for the validation of the stopped-flow instrument.

Based on an approximately octahedral complex (O<sub>h</sub> symmetry can be considered as further splitting by C<sub>2v</sub> is not observed due to broad transitions). The analysis of the reaction by stopped-flow UV-Vis spectroscopy shows two d-d transitions for the precursor complex at 456 and 657 nm for the [CrCl<sub>3</sub>(decyl-SNS)], being <sup>4</sup>T<sub>2g</sub> ← <sup>4</sup>A<sub>2g</sub> (v<sup>1</sup>) and <sup>4</sup>T<sub>1g</sub> ← <sup>4</sup>A<sub>2g</sub> (v<sup>2</sup>); the <sup>4</sup>T<sub>1g</sub> ← <sup>4</sup>A<sub>2g</sub> transition at higher energy is obscured by CT transitions. The energy band between these two transitions gives 10 Dq ~ 1583 cm<sup>-1</sup>. This is consistent with UV-Vis analysis of related complexes described previously.<sup>[18]</sup>

UV-Vis data collected using the stopped-flow diode array indicated a very rapid initial reaction of [CrCl<sub>3</sub>(decyl-SNS)] with 10 mol equiv. of AlMe<sub>3</sub>, detected at 1.122 s. At this time frame, clear changes had already occurred considering the relative absorbance of the two observed d-d bands (Fig. 3.7). The time frame given by the UV-Vis computer has to be considered with a small uncertainty as the solution may not be completely homogeneous and still turbulent at this point

Once the complex has reacted, we see two transitions that are blue-shifted from the original 456 and 657 nm to 425 and 617 nm respectively. As suggested previously,<sup>[23]</sup> this could arise from the substitution of chloride for methyl groups (Fig. 3.8). Chapter 6 discusses these spectra further in the context of structures as proposed by EXAFS analysis.

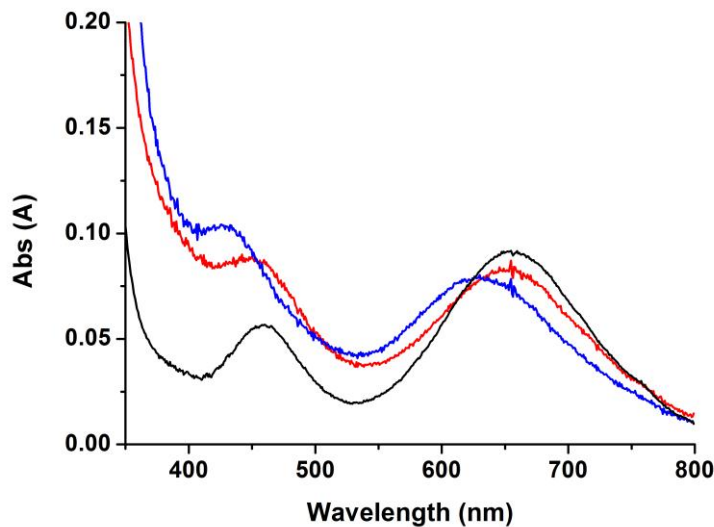


**Fig. 3.7** UV-Vis spectra showing reaction of 5 mM  $[\text{CrCl}_3(\text{decyl-SNS})] + 10 \text{ AlMe}_3$  in toluene at rate of 2 ms/spectrum (black = unreacted complex, red = 1.120 s, blue = 1.122 s).

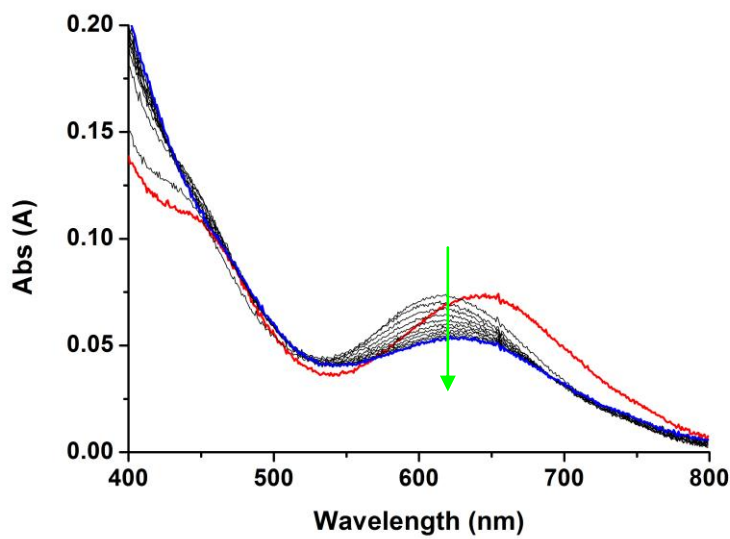


**Fig. 3.8** UV-Vis spectra showing reaction of 5 mM  $[\text{CrCl}_3(\text{decyl-SNS})] + 10 \text{ AlMe}_3$  in toluene at 2 s intervals, with red spectrum representing start point and blue representing last collected spectrum (red = 0s, black = 2s intervals, Blue = 29 s; green arrow = direction of time).

### 3.3.4 Validation by 25 mM [MoCl<sub>3</sub>(decyl-SNS)] + 20 AlMe<sub>3</sub> in Toluene

The reaction of [MoCl<sub>3</sub>(decyl-SNS)] with 20 mol equiv. of AlMe<sub>3</sub> was monitored using a Perkin-Elmer Lambda 19 UV-Vis spectrometer using a gas tight quartz cell, under inert N<sub>2</sub> atmosphere (Fig. 3.9). The same reaction was repeated using stopped-flow UV-Vis diode array to give similar results (Fig. 3.10).

The complex [MoCl<sub>3</sub>(decyl-SNS)] exhibits one transition at 464 nm. This is assumed to be the lowest energy  $^4T_{2g} \leftarrow ^4A_{2g}$  or  $^4T_{1g} \leftarrow ^4A_{2g}$  transition as it occurs at lower energy for the Cr(III) analogue.<sup>[24]</sup> The d-d transitions of the Mo complex would be expected to occur at higher energy due to larger orbital separations (i.e. 4d-transition metal complexes always form low spin complexes due to bigger d-d orbital splitting relative to 3d-transition metals complexes).

After reaction of [MoCl<sub>3</sub>(decyl-SNS)] with 20 mol equiv. of AlMe<sub>3</sub>, a new transition at 596 nm is observed, with the loss of the original transition. From the EXAFS analysis of this reaction (Chapter 4), it suggests the [MoCl<sub>3</sub>(decyl-SNS)] complex undergoes complete substitution of chloride for methyl groups by the AlMe<sub>3</sub> (as seen for the Cr analogue). The reaction of [CrCl<sub>3</sub>(decyl-SNS)] with 10 mol equiv. of AlMe<sub>3</sub> shifts the transitions to higher energies, whereas the Mo exhibits a lower energy transition.

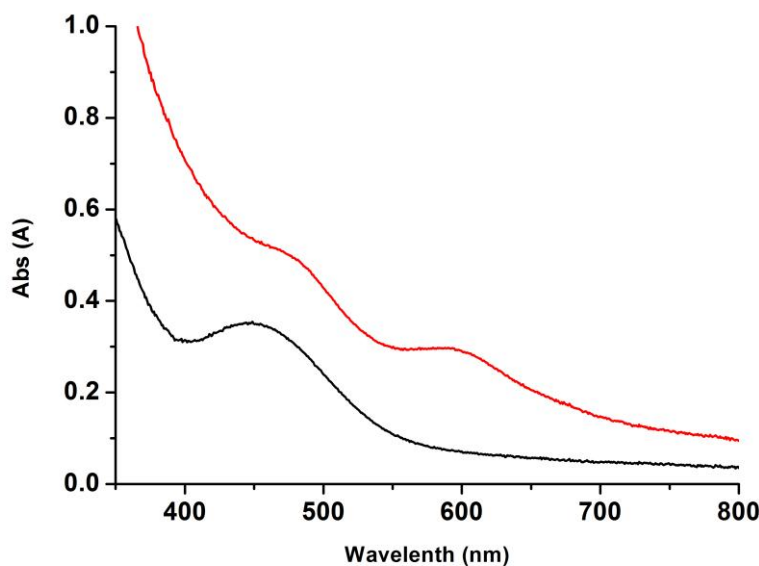


**Fig. 3.9** UV-Vis spectra showing reaction of 1mM [MoCl<sub>3</sub>(decyl-SNS)] + 20 AlMe<sub>3</sub> in toluene (black = unreacted complex, red = *ca.* 5 mins).

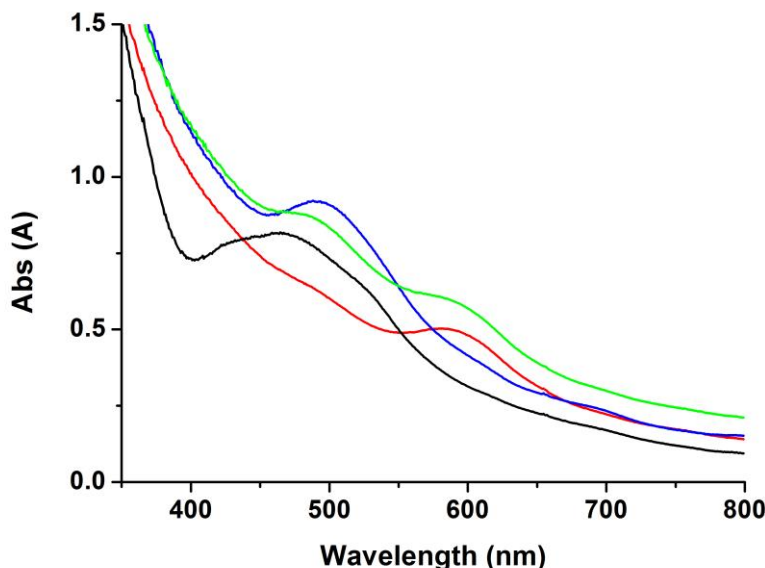


**Fig. 3.10** UV-Vis spectra showing reaction of 25mM [MoCl<sub>3</sub>(decyl-SNS)] + 20 AlMe<sub>3</sub> in toluene (black = unreacted complex, blue = 1 min, green = 2.5 min, red = 7 min).

### 3.3.5 The Freeze-quench Accessory

Development of the freeze-quench (FQ) XAFS cell has permitted measurements by quenching of catalyst mixtures. This is intended for probing early stages of activation and catalysis in the true trimerisation and tetramerisation mixtures and to provide a more detailed understanding of individual stages of the cycle(s). The stopped-flow system has demonstrated its performance in controlled and reproducible injection of accurate mixtures for millisecond time scales (see introduction section). Therefore, the set-up as developed for the freeze-quench system is based on the stopped-flow XAFS spectroscopic approach.<sup>[12, 16]</sup>

The standard freeze-quench accessory available from BioLogic was originally developed for non-sensitive aqueous solution reactions, which involved spraying through air into isopentane (unmodified schematic shown in Fig. 3.11).<sup>[25]</sup> Because of the air and moisture sensitivity of the organometallic chemistry in the present study,

this was not a viable option. So, an XAFS measurement cell has been developed for the freeze-quench system to be attached to the stopped-flow instrument (Fig. 3.12). This enables a Kapton® (polyimide) capillary to be mounted into a custom holder which attaches to the standard BioLogic freeze-quench accessory. The implement allows direct injection into the Kapton® tube while argon gas is flowed around the spray exit and tube inlet and prevents ingress of air (or moisture) into the sample (Fig. 3.13). A Kapton® tube, 4.2 mm x 200 mm (as received – cut to varied desired lengths) with wall thickness of 0.07 mm, was sealed with a plug and immersed into liquid nitrogen contained within a Dewar (before and during injection). The reaction mixture was then injected and frozen directly. The injection and freezing time was estimated to be below 1 second. For XAFS experimentation the tube containing the frozen sample was placed into a holder aligned in the X-ray beam, while being cooled continuously using a Cryostream (100 K). By setting up the appropriate cryostream flow-rate, ice formation on the outside of the capillary is limited (although this is not crucial for the high energy Mo XAFS data as obtained in this study, but would be very problematic for softer edges like the 3d transition metals involved in the Cr and Sc systems).

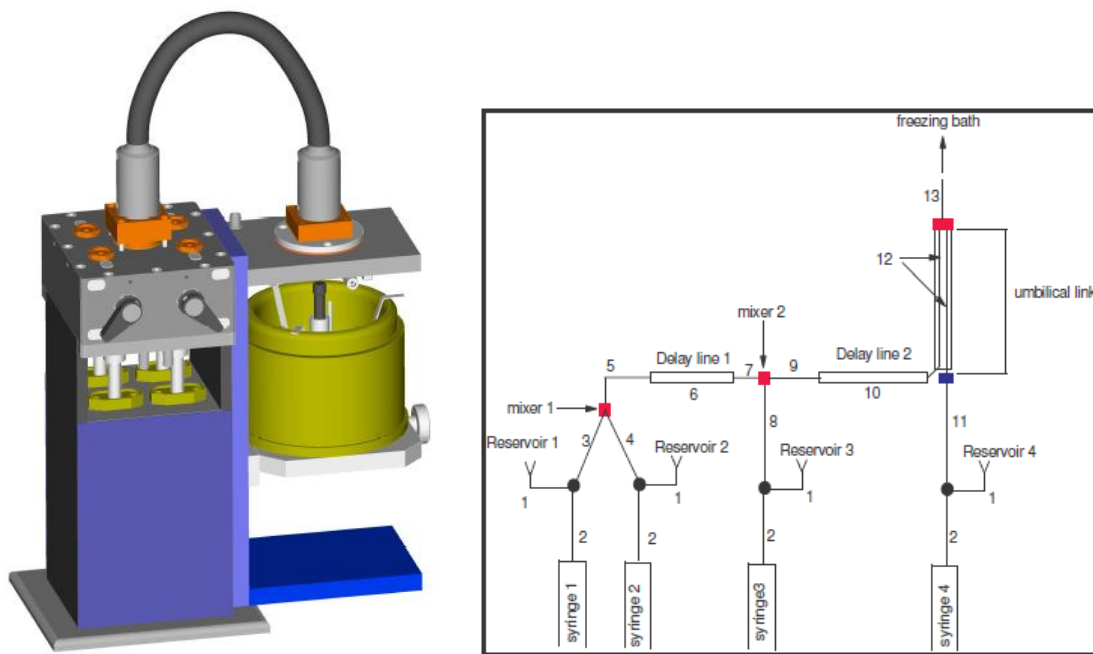


**Fig. 3.11** Schematic of the freeze-quench accessory connected to the stopped-flow unit.<sup>[25]</sup>

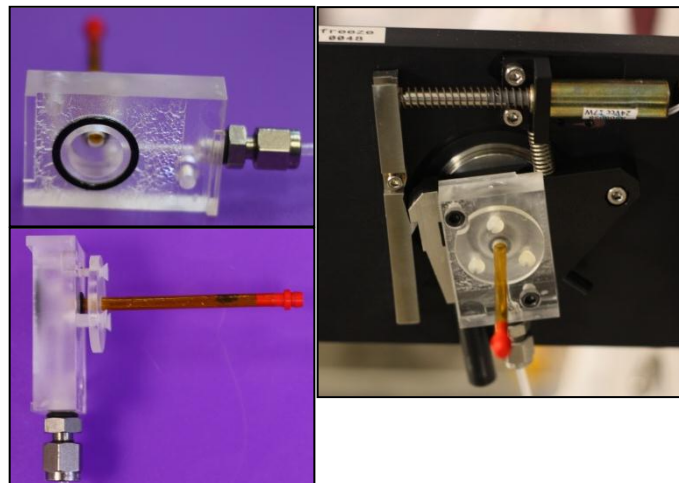


**Fig. 3.12** Displaying freeze-quench add-on allowing for easy air/moisture free sample collection.

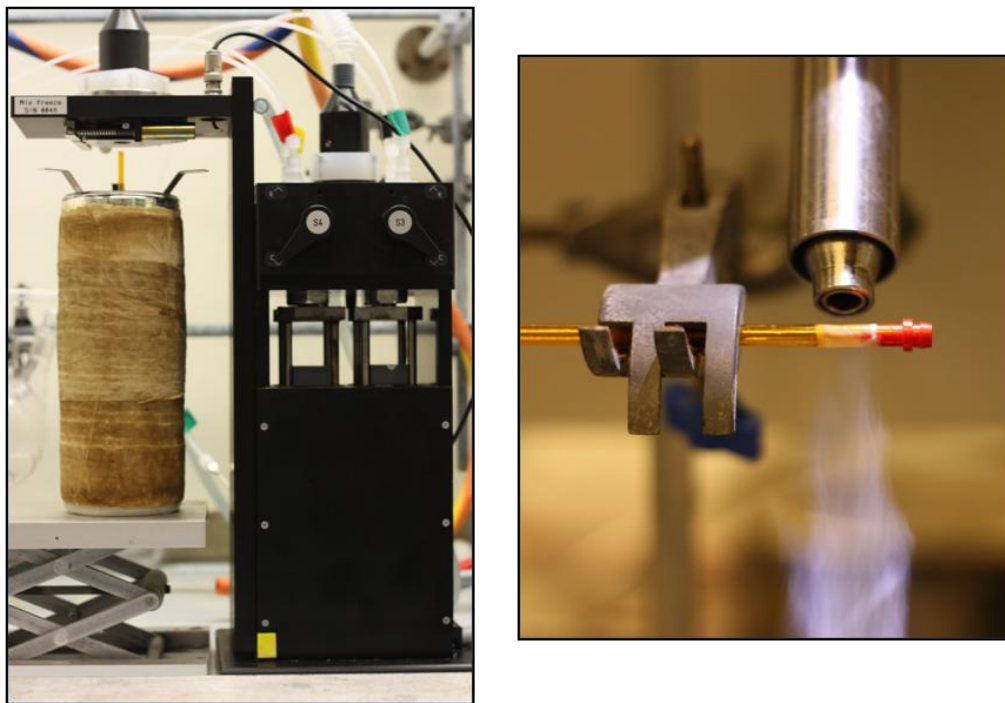


**Fig. 3.13** Photographs showing set-up of the freeze-quench (left) and sample under cryostream in sealed Kapton® tube (right).

### 3.3.5.1 Validation of the Freeze-quench Accessory

To establish if air and moisture sensitive samples could be collected and frozen intact using the stopped-flow freeze-quench system, two methods were employed and discussed below.

### 3.3.5.2 Test of oxygen using $[\text{Cp}_2\text{TiCl}]_2\text{ZnCl}_2$

Reaction of  $[\text{Cp}_2\text{TiCl}]$  with zinc in toluene produces the highly oxygen sensitive complex  $[\text{Cp}_2\text{TiCl}]_2\text{ZnCl}_2$ . This complex is regularly used in glove-boxes as a chemical indicator for oxygen levels. The initial complex is blue/green at levels below 5 ppm oxygen, turning to yellow or orange at higher oxygen levels once the complex has oxidised, from Ti(III) to Ti(IV).<sup>[19a]</sup> It has also been used as a visual aid when inducting students to the workings of Schlenk line apparatus and techniques, particularly when learning to set-up oxygen free environments.<sup>[19b]</sup>

This proved a very useful chemical to test the procedures for the stopped-flow freeze-quench technique to test the anaerobic conditions of the instrument. The aforementioned passivation was followed and the titanium complex was loaded into a syringe of the stopped-flow unit. This was then ejected in the same manner as a sample collection into a Kapton® tube under argon. Once collected the complex had remained blue/green, indicating the oxygen level to be < 5 ppm.

### 3.3.5.3 Analysis of $[\text{MoBr}_3(\text{SBz})]$ by EXAFS analysis.

The complex  $[\text{MoBr}_3(\text{SBz})]$  ( $\text{SBz} = \text{S}(\text{CH}_2\text{CH}_2\text{SCH}_2-p\text{-C}_6\text{H}_4\text{-C}(\text{CH}_3)_3)_2$ ) was dissolved in toluene and passed through the system and measured by Mo K-edge EXAFS as the final validation step. Once frozen, the data were compared to the same complex measured in the previously validated XAS liquid cell.<sup>[18]</sup> Below are plots of the Mo K-edge EXAFS data that were collected within the two cells, comparing both samples, with appropriate fit data presented in the table below (Figs. 3.14 and 3.15, Table 3.1).

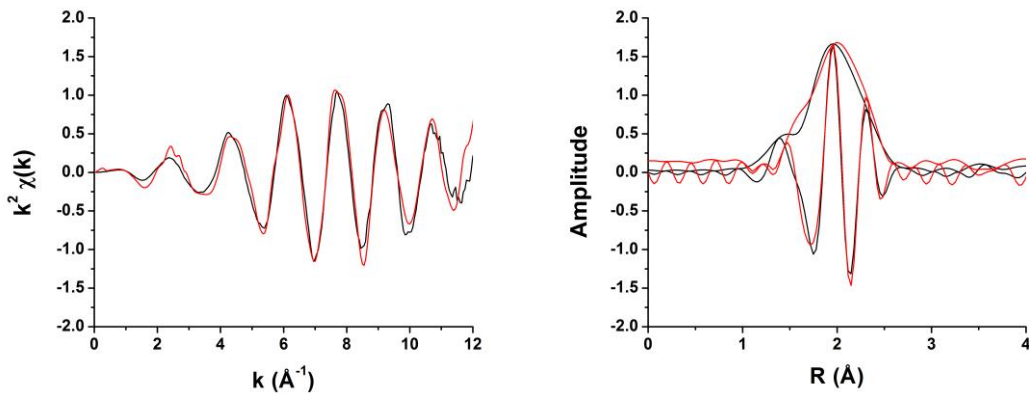


**Fig. 3.14** Mo K-edge  $k^2$ -weighted EXAFS and Fourier transform data showing the comparison of 20 mM [MoBr<sub>3</sub>(SBz)] collected in the liquid cell (Black) and collected by the freeze-quench (Red).

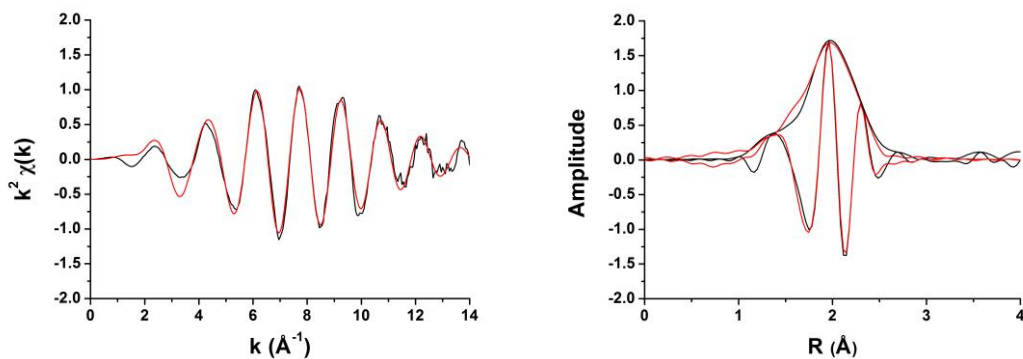


**Fig. 3.15** Mo K-edge  $k^2$ -weighted EXAFS and Fourier transform analysis of 20 mM [MoBr<sub>3</sub>(SBz)] toluene solution in liquid cell (black) with fits (red).

**Table 3.1** Results for Mo K-edge EXAFS analysis of [MoBr<sub>3</sub>(SBz)] sample in the liquid cell.

Abs – Scat	CN	R(Å)	$2\sigma^2 (\text{\AA}^{-2})$	Fitting Parameters
Mo – S	3 <sup>a</sup>	2.45(2)	0.003(1)	$1.7 < k < 14.2$ , $1.2 < R < 2.6$ , Amp = 0.85, E <sub>0</sub> = -4(1),
Mo - Br	3 <sup>a</sup>	2.55(1)	0.006(1)	R = 0.007

<sup>a</sup>Fixed parameters.

The EXAFS data shows that both samples are the same, albeit the freeze-quench data giving poorer signal-to-noise (average of two scans). The complex in the liquid XAS cell was averaged over five scans, therefore after data averaging, giving better signal-to-noise. This allowed a good fit for this data set, giving three sulfur contributions at 2.45 Å and three bromides at 2.55 Å with low uncertainties.

### 3.4 Conclusion

The stopped-flow instrument is a versatile piece of apparatus that can be implemented across a range of science. The work in this chapter has shown how it can be used and modified for the research of inorganic mechanisms. The introduction section has discussed how the stopped-flow system has evolved to probe catalytic intermediates using a combination of methods and in-time analyses. We have built on these former practices to ensure the research of a highly air sensitive chromium ethene oligomerisation pathway can be achieved using a combined XAFS/UV-Vis approach. The addition of a new freeze-quench technique (for use in organometallic chemistry) allows freezing of reactions to allow fluorescence XAFS data collection. This chapter details the rigorous validation techniques to ensure air and moisture are excluded from the stopped-flow freeze-quench system and the chemistry is able to survive from setup through to analysis. New methods have been developed and comparisons with previously published data have been employed to confirm all new methodologies and apparatus to produce reproducible and reliable results.

*Experimental details for this chapter are provided in later experimental sections within this research (Chapters 4 and 6).*

### 3.5 References

- [1] M. J. Pilling and P. W. Seakins, *Reaction Kinetics*, Oxford University Press, **1995**.
- [2] I. Grillo, *Curr. Opin. Colloid In.* **2009**, *14*, 402-408.
- [3] a) H. Fabian and D. Naumann, *Methods* **2004**, *34*, 28-40; b) W. A. McGee and L. J. Parkhurst, *Anal. Biochem.* **1990**, *189*, 267-273; c) C. Frieden, S. D. Hoeltzli and I. J. Ropson, *Protein Sci.* **1993**, *2*, 2007-2014; d) B. Ranjbar and P. Gill, *Chem. Biol. Drug Des.* **2009**, *74*, 101-120.

- [4] N. Yoshida, T. Matsushita, S. Saigo, H. Oyanagi, H. Hashimoto and M. Fujimoto, *J. Chem. Soc. Chem. Comm.* **1990**, 354-356.
- [5] T. Matsushita and R. P. Phizackerley, *Jpn. J. Appl. Phys.* **1981**, 20.
- [6] S. Pascarelli and O. Mathon, *Phys. Chem. Chem. Phys.* **2010**, 12, 5535-5546.
- [7] S. Pascarelli, T. Neisius and S. De Panfilis, *J. Synchrotron Radiat.* **1999**, 6, 1044-1050.
- [8] S. Pascarelli, O. Mathon, M. Munoz, T. Mairs and J. Susini, *J. Synchrotron Radiat.* **2006**, 13, 351-358.
- [9] J. H. Baxendale, H. R. Hardy and L. H. Sutcliffe, *T. Faraday Soc.* **1951**, 47, 963-973.
- [10] J. R. Jones and T. J. Symes, *J. Chem. Soc. C* **1971**, 1124-1130.
- [11] D. Bogg, M. Conyngham, J. M. Corker, A. J. Dent, J. Evans, R. C. Farrow, V. L. Kambhampati, A. F. Masters, D. N. McLeod, C. A. Ramsdale and G. Salvini, *Chem. Comm.* **1996**, 647-648.
- [12] M. B. B. Abdul Rahman, P. R. Bolton, J. Evans, A. J. Dent, I. Harvey and S. Diaz-Moreno, *Faraday Discuss.* **2002**, 122, 211-222.
- [13] R. F. Heck, *Accounts Chem. Res.* **1979**, 12, 146-151.
- [14] a) J. Evans, L. O'Neill, V. L. Kambhampati, G. Rayner, S. Turin, A. Genge, A. J. Dent and T. Neisius, *J. Chem. Soc. Dalton Trans.*, **2002**, 2207; b) A. J. Dent, *Top. Catal.* **2002**, 18, 27-35.
- [15] A. C. Skapski and M. L. Smart, *J. Chem. Soc. Chem. Comm.* **1970**, 658.
- [16] M. Tromp, G. P. F. van Strijdonck, S. S. van Berkel, A. van den Hoogenband, M. C. Feiters, B. de Bruin, S. G. Fiddy, A. M. J. van der Eerden, J. A. van Bokhoven, P. W. N. M. van Leeuwen and D. C. Koningsberger, *Organomet.* **2010**, 29, 3085-3097.
- [17] O. Kleifeld, A. Frenkel, J. M. Martin and I. Sagi, *Nat. Struct. Biol.* **2003**, 10, 98.

- [18] J. O. Moulin, *X-Ray Absorption Spectroscopy for the Study of a Homogeneous Catalysis System based Upon Chromium*, Ph. D Thesis, University of Southampton, Southampton, **2006**.
- [19] a) D. G. Sekutowski and G. D. Stucky, *Inorg. Chem.* **1975**, *14*, 2192-2199; b) S. J. N. Burgmayer, *J. Chem. Educ.* **1998**, *75*, 460.
- [20] M. Tromp, *Developments of Time-Resolved XAFS Techniques: Applications in Homogeneous Catalysis*, Ph. D. Thesis, Utrecht, The Netherlands, **2004**.
- [21] BioLogic, *SFM-400 User's Manual*, BioLogic Science Instruments, **2008**.
- [22] D. E. Jordan, *Anal. Chem.* **1968**, *40*, 2150-2153.
- [23] J. O. Moulin, J. Evans, D. S. McGuinness, G. Reid, A. J. Rucklidge, R. P. Tooze and M. Tromp, *Dalton Trans.* **2008**, 1177-1185.
- [24] S. F. A. Kettle, *Physical Inorganic Chemistry*, Spektrum Academic Publishers, **1996**.
- [25] BioLogic, *Mix & freeze quench accessory User's Manual*, BioLogic Science Instruments, **2010**.



## **Chapter 4.**

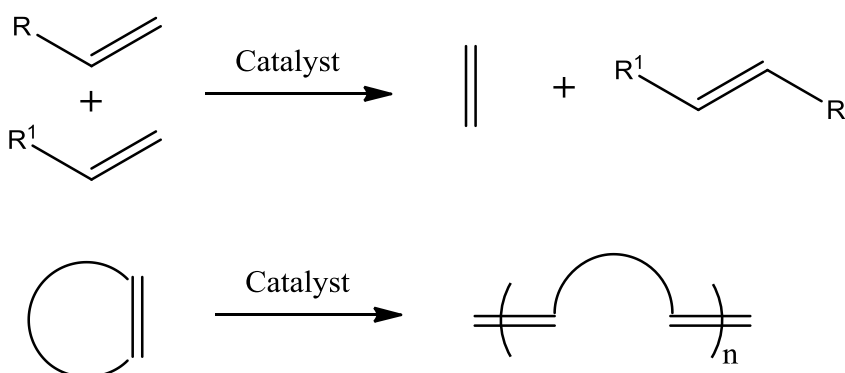
**A Mo K-edge QEXAFS Study into the Mechanism of  
Selective Olefin Oligomerisation Catalysis using  
Stopped-flow Freeze-quench Techniques.**

## 4.1 Introduction

This chapter aims to demonstrate new research into the organometallic chemistry of molybdenum using an array of characterisation techniques. To introduce this, examples of how molybdenum has been used as an active metal for olefin catalysis are discussed.

### 4.1.1 Alkene Metathesis

The alkene metathesis pathway has proven to be an extremely useful reaction within organic chemistry, providing highly functionalised alkenes and polymers. Scheme 4.1 demonstrates how alkenes undergo structural redistribution by alkene metathesis.



**Scheme 4.1** Metathesis reaction (top) and ring-open metathesis polymerisation (ROMP) (bottom).

One of the most notable homogeneous catalysts for ring-open metathesis polymerisation (ROMP) is the Schrock catalyst shown in Fig. 4.1.<sup>[1]</sup> The new C-C bond formation can be catalysed at mild conditions, with high specificity and turnover numbers.

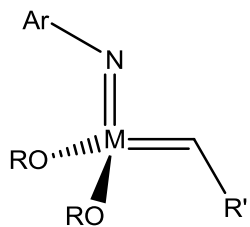
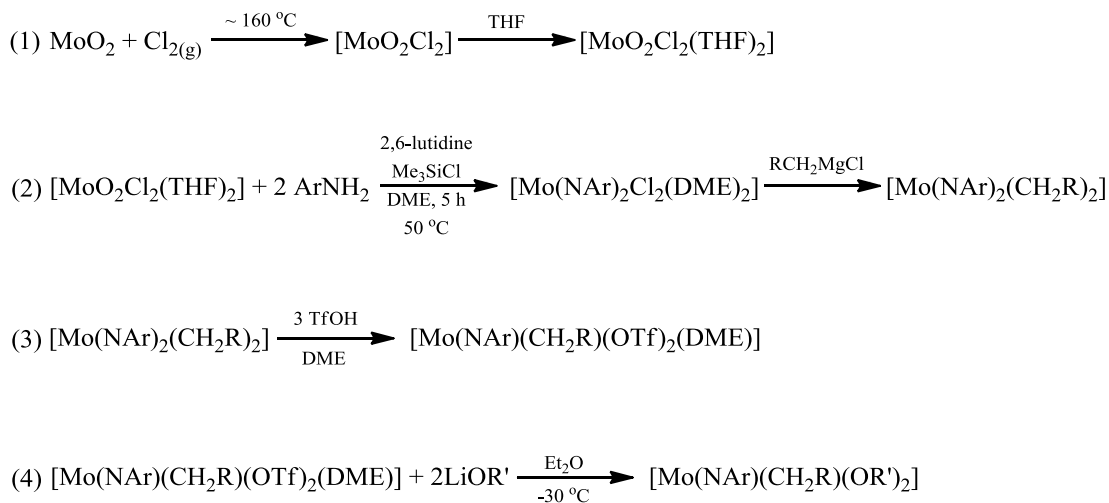


**Fig. 4.1** Schrock catalyst ( $R = C(CH_3)_3, C(CF_3)_3, C(CF_3)_2CH_3$ ;  $M = W$  or  $Mo$ ).

This is a ‘living’ catalysis system, which is so called when the rate of initiation is equal to or greater than the rate of propagation, each monomer adds irreversibly, chain transfer is slow relative to the propagation and well defined homopolymers or ‘block’ polymers are formed.<sup>[2]</sup> The first example of a ‘living’ catalyst was a titanium complex, a bis(cyclopentadienyl) titanocyclobutane type catalyst for the polymerisation of olefins.<sup>[3]</sup>

The Schrock type ROMP catalyst can be ‘tuned’ accurately to be highly active for polymerisation of ring strained monomer alkenes. These catalysts consist of a four coordinate, high oxidation state transition metal (typically Mo or W (VI)). This low coordination state allows relatively small substrates to react with the metal to give a five coordinated intermediate metallocyclobutane complex.

Synthesis of the Mo catalyst is shown in Scheme 4.2.<sup>[4]</sup> Use of the precursor  $[Mo(NAr)_2(CH_2R)_2]$  (the W analogue can also be used for the synthesis of the subsequent W complexes)<sup>[5]</sup> allows synthesis of the different analogues (2). After protonation of one imido group, the ligand leaves as a salt and the complex is stabilised by the coordination of DME (dimethoxyethane) to allow the loss of  $RCH_3$ , rather than forming the unstable  $[Mo(NAr)(CH_2R)(OTf)_2]$  complex (3). Coordination of two bulky alkoxide ligands to the intermediate  $[Mo(NAr)(CH_2R)(OTf)_2(DME)]$  results in the loss of DME to form the 4 coordinate catalyst  $[Mo(NAr)(CHR)(OR)_2]$  (4).



**Scheme 4.2** Synthesis of Mo Schrock catalyst ( $\text{R} = {^t\text{Bu}}$  or  $\text{Ph}(\text{Me})_2\text{C}$ ;  $\text{OR}' = \text{OCMe}(\text{CF}_3)$ ,  $\text{OC}(\text{Me})_2\text{Ph}$ ,  $\text{O}^t\text{Bu}$ ,  $\text{OAr}$ .  $\text{Ar} = \text{aryl}$ ,  $\text{DME} = \text{dimethoxyethane}$ ,  $\text{OTf} = \text{OSO}_2\text{C}_6\text{H}_4\text{CF}_3$ ).<sup>[4]</sup>

Coordination of bulky imido and alkoxide ligands to the catalyst prevents intermolecular reactions and ligand scrambling. These internal rearrangements are a common cause of catalytic degradation, destroying the active alkylidene ligand.<sup>[2]</sup>

Crystal structures of tungsten species  $[\text{W}(\text{CHPh})(\text{NAr})(\text{OC}(\text{CF}_3)_2\text{CH}_3)_2]$ <sup>[5a]</sup> and  $[\text{W}(\text{CH}^t\text{Bu})(\text{NAr})(\text{O}^t\text{Bu})_2]$ <sup>[5b]</sup> show a pseudo tetrahedral arrangement, with a  $\text{W}=\text{N}-\text{C}$  bond angle of  $\sim 170^\circ$ . The  $\beta$ -C of the alkylidene lies in the same plane as N, W and  $\alpha$ -C atoms, pointing towards the N atom, as the syn rotamer.

Although these complexes are isostructural, the activity for the metathesis of cis-2-pentene at  $25^\circ\text{C}$  was found to be very different. The  $-\text{OC}(\text{CF}_3)_2\text{CH}_3$  complex gives a rate of  $\sim 10^3$  turnovers per minute and the  $-\text{O}^t\text{Bu}$  analogue gives 2 turnovers per minute. This reason for the observed difference is the electrophilicity between the two complexes. The metal-olefin interaction is described as an electrophilic attack, so the  $-\text{OC}(\text{CF}_3)_2\text{CH}_3$  as the more electronegative substituent, makes the catalyst more electrophilic, thus better for attack.<sup>[5a, 6]</sup>

These complexes are known to perform ROMP catalysis of norbornene. They do not react readily with ordinary olefins but rapidly with strained alkenes such as those contained within norbornenes, thus providing selectivity.  $[\text{W}(\text{CH}^t\text{Bu})(\text{NAr})(\text{O}^t\text{Bu})_2]$  can polymerise norbornene as low as  $-80^\circ\text{C}$ . This can give polymer chain length ( $x$ ) up to 500, giving a Poisson distribution around  $x$ . The

average chain length is a narrow range indicating an irreversible polymerisation mechanism.<sup>[7]</sup>

Polymerisation can be terminated by aldehydes, such as benzaldehyde, to give a metal oxide in a Wittig-type reaction step. This ‘caps’ the polymer and kills the catalyst. Use of styrene instead makes chain transfer rapid and produces a new alkylidene catalyst.<sup>[8]</sup>

The Diels-Alder reaction provides a route to a large number of highly functionalised norbornenes. The molybdenum Schrock catalyst can polymerise a large array of functionalised norbornenes, and –dienes at the least sterically hindered double bond.<sup>[9]</sup> Tungsten has not been found to polymerise many norbornenes that contain a variety of functionalities, as referenced by Schrock.<sup>[2]</sup> This is thought to be because the tungsten alkylidene possibly reacts rapidly with the functionality on the substrate relative to that of the Mo derivative. Also the tungstacyclobutane ring is possibly more stable than the Mo analogue. Moreover such a complex was isolated and determined crystallographically. The monomer 2,3-Bis(trifluoro)norbornadiene was added to  $[W(CH^tBu)(NAr)(O^tBu)_2]$  at -30 °C to give an intermediate, a square pyramidal metallocycle (Fig. 3.2).<sup>[10]</sup>

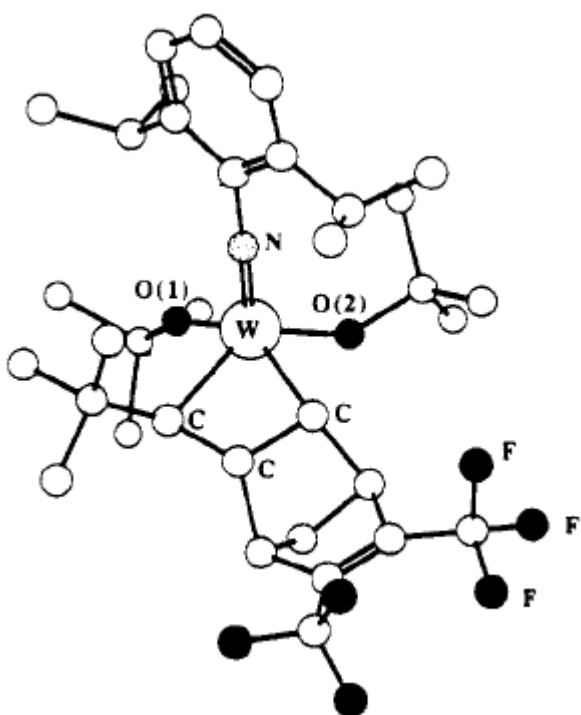
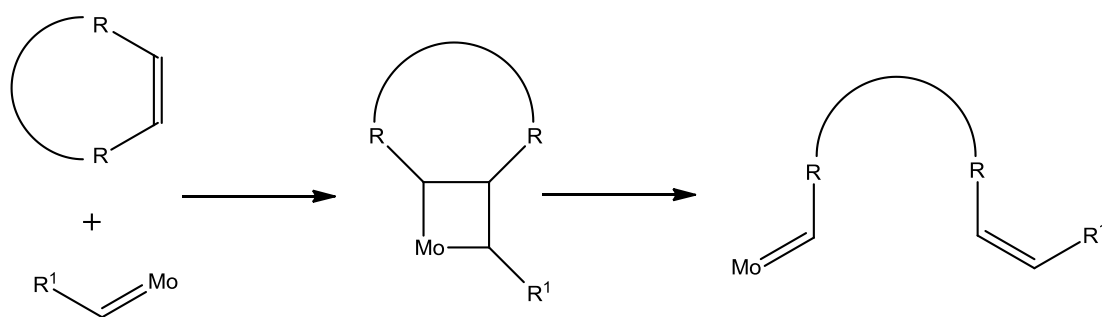


**Fig. 4.2** X-ray crystal structure of tungstanocyclobutane ring product upon reaction of  $[W(CH^tBu)(NAr)(O^tBu)_2]$  with 2,3-Bis(trifluoro)norbornadiene.<sup>[10]</sup>

The ROMP initiation step proceeds by the coordination of a cyclic olefin monomer to the metal carbene complex. The olefin and metal complex undergo a [2+2] cycloaddition to form a metallocyclobutane intermediate. This cyclic intermediate undergoes cyclo-reversion to form a new metal alkylidene with the ring-opened monomer, forming a growing polymer chain. Propagation proceeds through the same process as the ring-opened monomer and is included into the growing polymer chain (Scheme 4.3). The cycle continues until, either all the monomer is consumed, an equilibrium has been reached or the catalyst is quenched. Addition of an unsaturated ether releases the polymer from the metal complex otherwise degradation of the polymer product can occur (by inter- or intra- molecular chain transfer) and metal residues can contaminate the final product.<sup>[11]</sup>



**Scheme 4.3** Reaction pathway of ring-open metathesis polymerisation.

Since the development of these highly active metathesis catalysts, much work has been published as can be seen by simple literature searches for ROMP, giving 100s of review articles. Referenced here are a few review articles for a comprehensive overview of many developments across tungsten, ruthenium, molybdenum and tantalum catalysts.<sup>[12]</sup> A thorough review for recent advances in molybdenum metathesis by Schrock and Hoveyda discuss the variations for molybdenum catalysis,<sup>[12f]</sup> a selection of these chiral variations is shown in Fig. 4.3.

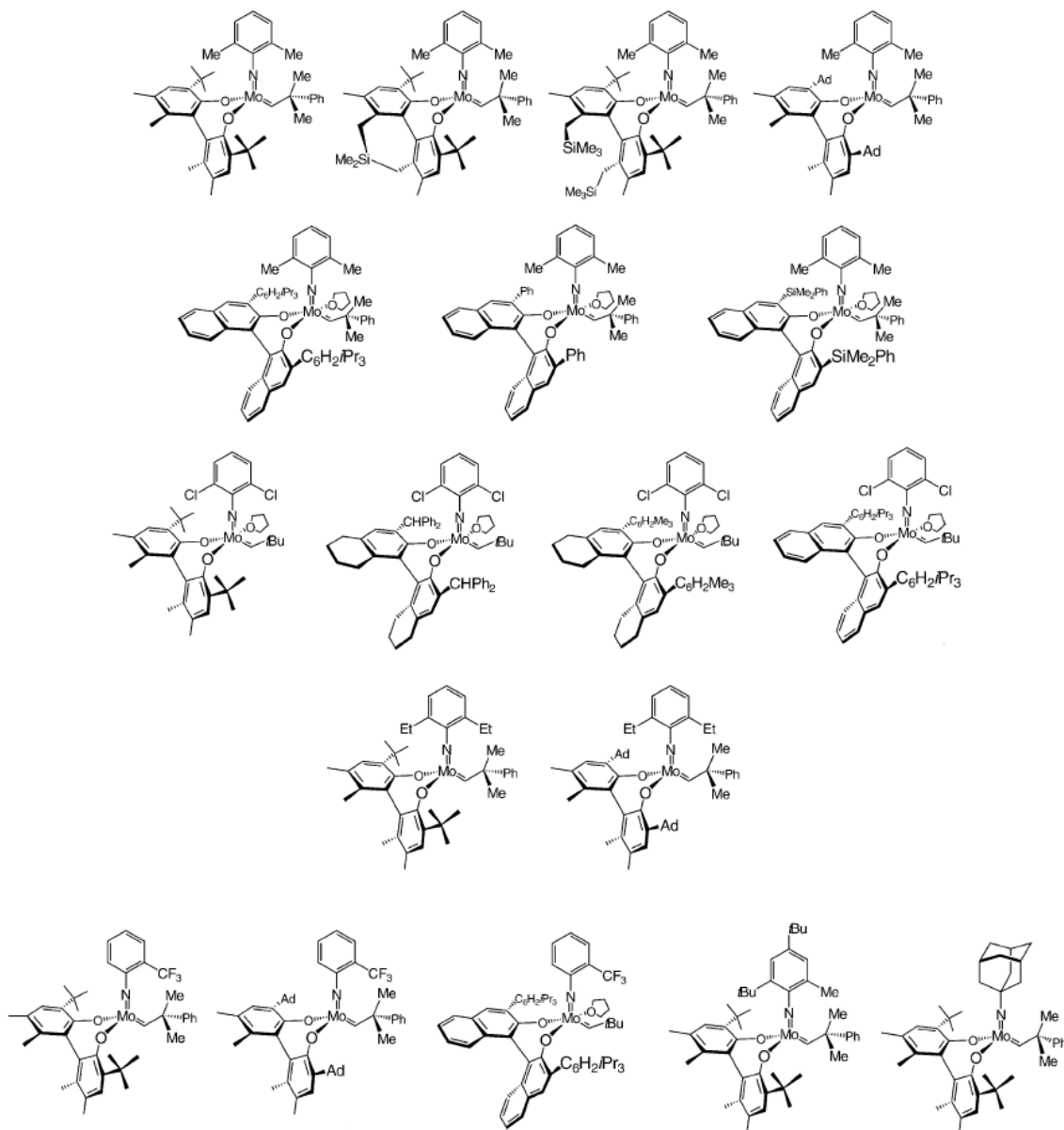


**Fig. 4.3** Displaying a selection of Mo chiral metathesis catalysts reviewed by Schrock.<sup>[12f]</sup>

To expand on one example, the chiral  $[\text{Mo}(\text{CHCMe}_2\text{Ph})(\text{N}-\text{C}_6\text{H}_3-[m-\text{iPr}]_2)([\pm]-\text{BINO}(\text{SiMe}_2\text{Ph})_2)]$  is a highly selective catalyst for *cis*-poly(2,3-bis(trifluoromethyl)norbornadiene) and *cis*-poly(2,3-dicarbomethoxynorbornadiene). This catalyst gave > 99 % *cis*-conformation and *cis*-tacticity of the polymers at room temperature with yield of 97 % after 8 hrs.<sup>[13]</sup>

#### 4.1.2 Epoxidation of Alkenes

For large scale production of epoxides, finding active catalysts that provide olefin epoxidation has become an important area of research. One of the most common molybdenum homogeneous catalyst was first synthesised in 1960s,  $[\text{CpMoO}_2\text{Cl}]$  ( $\text{Cp}$  = cyclopentadienyl).<sup>[14]</sup> Upon activation with tert-butyl hydroperoxide (TBHP), it can facilitate the epoxidation of a range of olefins, although its activation with  $\text{H}_2\text{O}_2$  gave no catalysis. This was attributed to the formation of a  $\eta^2$ -peroxy species, which was isolated by reaction with TBHP and found to be catalytically inactive, suggesting this was not an intermediate step within the active catalytic cycle (Fig. 4.4).<sup>[15]</sup>

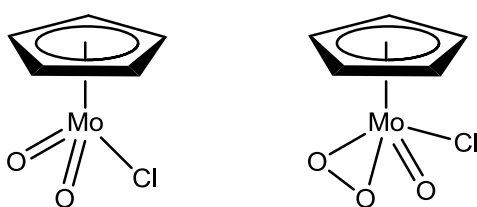
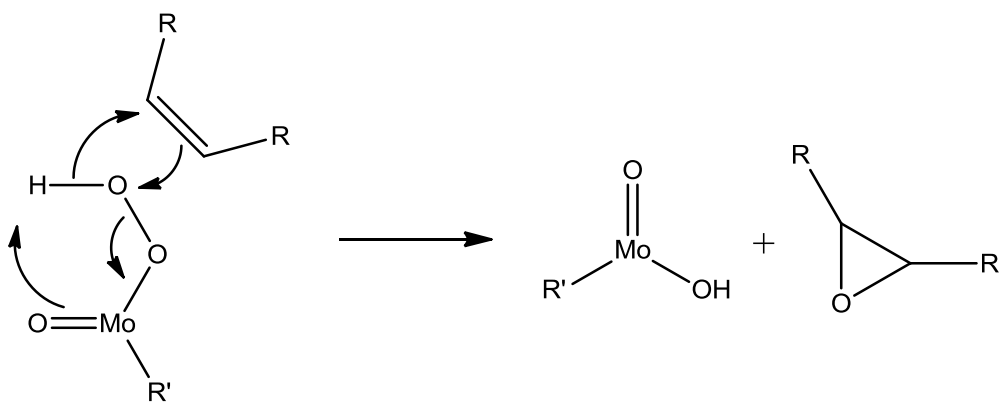


**Fig. 4.4** Displaying active epoxidation catalyst  $[\text{CpMoO}_2\text{Cl}]$  (left) and inactive  $\eta^2$ -peroxy species  $[\text{CpMo}(\text{O}_2)\text{OCl}]$  (right).

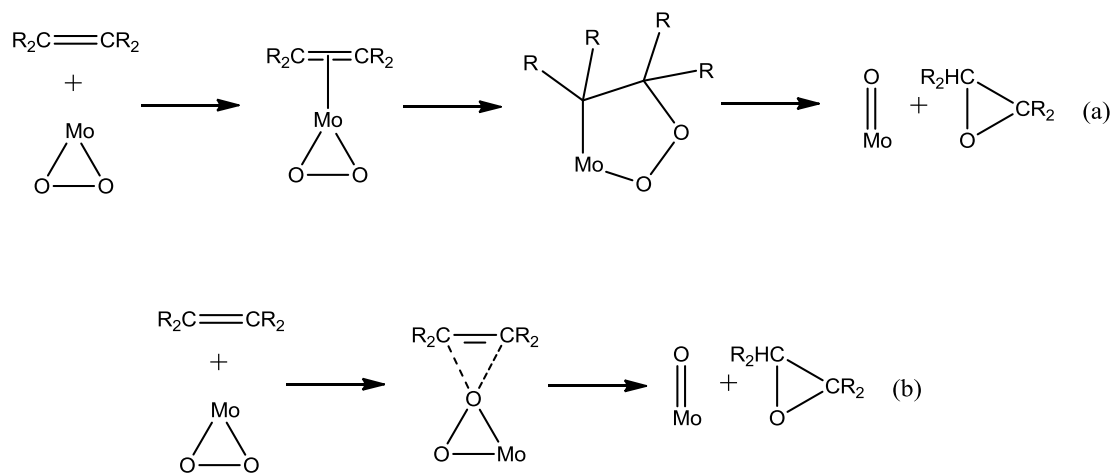
Investigations of catalysts incorporating substituted Cp rings for epoxidation of cyclooctene, such as  $[(\eta^5\text{-C}_5(\text{CH}_2\text{Ph})_5)\text{MoO}_2\text{Cl}]$ , gave 100 % conversion over 4 h at 55 °C, 1 % mol. catalyst and TBHP. Carbonyl analogues were also active towards catalytic epoxidation. These pre-catalysts have the additional advantage of being more stable than the dioxo-analogues, and so become more easily stored and handled.<sup>[16]</sup>

Over recent years there has been much discussion of the route of olefin epoxidation by  $[\text{CpMoO}_2\text{Cl}]$ .<sup>[17]</sup> Considering the purely organic reaction, oxidation of an olefin by a per-acid, i.e. *meta*-chloroperoxybenzoic acid (mCPBA), it is possible a similar route is followed (Scheme 4.4). But this pathway would favour oxidation by  $\text{H}_2\text{O}_2$ , as the active species can easily be regenerated by hydrogen peroxide from R-Mo-OH by ligand exchange. This would suggest  $\text{H}_2\text{O}_2$  would be the better oxidant.<sup>[18]</sup>

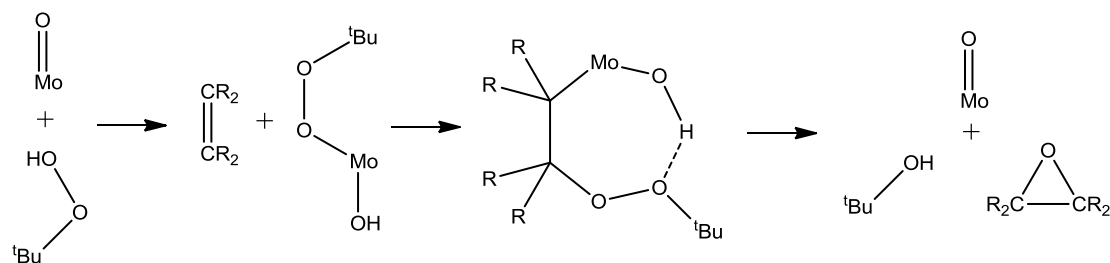


**Scheme 4.4** mCPBA type epoxidation of olefin by molybdenum catalyst.<sup>[18]</sup>

In all cases, experimental evidence has proved TBHP provides much better oxidation over  $\text{H}_2\text{O}_2$ , while the latter significantly decreases the activity or inhibits the catalysis. Two proposed mechanisms for olefin epoxidation have been analysed by several computational and DFT studies.<sup>[18-19]</sup> The stepwise Mimoun pathway<sup>[20]</sup> (Scheme 4.5 (a)) was calculated to give a higher activation barrier at the point of the olefin incorporation into the peroxy group on the metal, compared to the concerted transfer as suggested by Sharpless.<sup>[21]</sup> Yudanov found that decomposition of the metallocyclopentane led to aldehyde or ketone formation instead of the epoxide.<sup>[19e]</sup> The Sharpless concerted step (Scheme 4.5 (b)) was then calculated to be the favourable pathway. Neither of these routes account for the selectivity of TBHP over  $\text{H}_2\text{O}_2$  and each route contains the  $[\text{Mo}(\text{O}_2)]$  species, previously seen to be catalytically inactive. From a slight modification of a previous route by Thiel,<sup>[22]</sup> a DFT calculation suggested a route from a  $\text{Mo}=\text{O}$  species, avoiding the inactive  $\text{Mo}(\text{O}_2)$  species (Scheme 4.6).<sup>[17d]</sup>



**Scheme 4.5** Mimoun proposed epoxidation pathway (a) and Sharpless epoxidation pathway (b).



**Scheme 4.6** Displaying the Thiel type epoxidation pathway.

In terms of homogeneous catalysis, molybdenum has proven to be a versatile transition metal as demonstrated by its range of oxidation states, coordination number and geometries; hence several pathways have been proposed for catalytic production of epoxides. It has also shown an affinity for conversion of olefins to more functional products. The research in this chapter investigates the activation of lower oxidation state Mo(III) complexes (compared with VI examples shown above), analogous to highly active Cr(III), towards olefin oligomerisation catalysis. In 2009, the investigation of molybdenum for ethene oligomerisation was investigated and this is discussed below.

### 4.1.3 Ethene Oligomerisation

A range of Mo(SNS) ( $\text{SNS} = \text{HN}(\text{CH}_2\text{CH}_2\text{SR})_2$ , R = Et, decyl) complexes were synthesised and tested for their activity towards ethene oligomerisation catalysis.<sup>[23]</sup> These included  $[\text{Mo}(\text{CO})_3(\text{SNS})]$ , which converted to the Mo(I) dimer complex  $[(\text{SNS})\text{Mo}]_2$  (Fig. 4.5) upon reaction with  $[\text{Ag}(\text{CH}_2\text{Cl}_2)_2][\text{Al}(\text{OC}(\text{CF}_3)_3)_4]$ . In addition to these,  $[\text{MoCl}_3(\text{SNS})]$  and  $[\text{MoCl}_4(\text{SNS})]$  complexes were also tested for ethene oligomerisation.

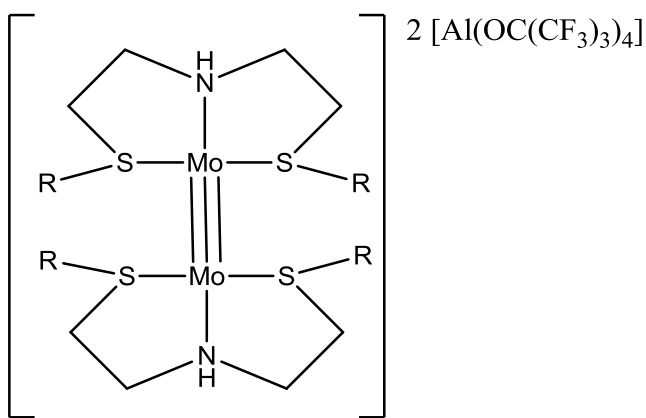


**Fig. 4.5** Multiple bonded Mo dimer from reaction of  $[\text{Mo}(\text{CO})_3(\text{SNS})]$  with  $[\text{Ag}(\text{CH}_2\text{Cl}_2)_2][\text{Al}(\text{OC}(\text{CF}_3)_3)_4]$  (R = Et, decyl).

All catalysts tested gave low activity and high amounts of C<sub>4</sub> and polyethylene. The high amounts of C<sub>4</sub> were forming at the Al centres of the activator as test were ran without the Mo complexes and similar high levels of C<sub>4</sub> were produced. These poor results (compared to the high selectivity and activity of Cr analogues) were attributed to the softer nature of Mo over Cr. It was also noted that a loss of colour from the Mo complexes in solution was observed in preliminary reactions with aluminium activators. It was suggested this arose from dissociation of the ligand from the metal.<sup>[23]</sup>

### 4.2 Aims

A set of Mo(III) halide complexes has been synthesised to help investigate the Cr(III) catalysed ethene trimerisation pathway, by determining their reaction with

$\text{AlMe}_3$ . It has been reported (and discussed) previously that complexes of the type  $[\text{MoCl}_3(\text{R-SNS})]$  show negligible catalytic activity towards ethene oligomerisation.<sup>[23]</sup> Despite these results, this molybdenum system still proves to be a rich area for our research. From an EXAFS point of view, the higher energy K-edge of Mo (20 KeV) is advantageous over the Cr K-edge (6 KeV) because the higher energy X-rays have much lower probability of absorption by external factors (air, solvent, Kapton®, etc.). The Mo K-edge then allows for a higher quality collection of data over fewer scans and faster acquisition times. These properties prove useful in establishing in-time stopped-flow EXAFS and freeze-quench methods for the investigation of catalytic cycles and hope to reflect the Cr ethene oligomerisation activation by  $\text{AlMe}_3$ .<sup>[24]</sup> Preliminary UV-Vis studies have shown these Mo complexes react with  $\text{AlMe}_3$  to form new species in solution. The initial reaction with  $\text{AlMe}_3$  with the Mo complexes is similar and so, identification of these intermediates helps in elucidation of new Cr intermediates, showing how  $\text{AlMe}_3$  can interact with metal halides of this type. Moreover, this technique points to reasons why Mo gives much poorer activity relative to the Cr system, once again proving how this set-up can be used for investigations of reaction mechanisms.

These reactions with  $\text{AlMe}_3$  are investigated by Mo K-edge X-ray absorption fine structure analysis (XAFS) and UV-Vis spectroscopy. The higher X-ray energy of the Mo K-edge (20 KeV) allows for good signal to noise data and improved time resolution via transmission studies, hence real reaction intermediates are likely to be probed, instead of final (possibly decomposed) species. The Mo(III) bromide complex analogues have also been synthesised and investigated to provide a clear distinction between bromide and chloride shells in the EXAFS analysis, where in some cases the chloride and sulfur shells are indistinguishable since they are corresponding neighbours in the periodic table, with very similar Z-values and hence similar backscattering amplitudes.

Using a newly developed anaerobic freeze-quench apparatus to freeze the reaction mixture at low temperature (e.g. 100 K), it is possible to pause reactions at pre-determined time periods allowing the analysis by EXAFS spectroscopy to establish any reaction at the Mo centre. Multiple spectra can then be acquired for the same stage of the reaction, which can be averaged. This is not possible if the reaction is continually progressing.

## 4.3 Results and Discussion

### 4.3.1 Synthesis of Mo(III) Halide Complexes

All Mo(III) complexes were synthesised under inert conditions using standard Schlenk line techniques, using dry degassed solvents. Synthesis of the corresponding  $[\text{MoCl}_3(\text{L})]$  (Fig. 4.7) type complex, was from the reaction of  $[\text{MoCl}_3(\text{THF})_3] + \text{L}$  in THF.  $[\text{MoCl}_3(\text{THF})_3]$  was synthesised via the literature procedure, by reduction of  $\text{MoCl}_5$  to  $[\text{MoCl}_4(\text{Et}_2\text{O})_2]$  with Sn powder, followed by further reduction in THF.<sup>[25]</sup>

The metal precursor  $[\text{MoCl}_3(\text{THF})_3]$  is known to dimerise in non-polar solvents, such as  $\text{CH}_2\text{Cl}_2$  and toluene, and even at room temperature in the solid form, the original orange powder slowly changing to pink over *ca.* 7 days (Fig. 4.6).<sup>[26]</sup> Therefore, reactions were performed in THF to suppress this process and the powder form of the complex stored in the freezer under inert atmosphere. The bromide analogue,  $[\text{MoBr}_3(\text{THF})_3]$ , was formed from a two stage oxidation reaction using  $\text{Br}_2$  and  $[\text{Mo}(\text{CO})_6]$ .<sup>[27]</sup> In this case, no dimerisation of the precursor was observed.

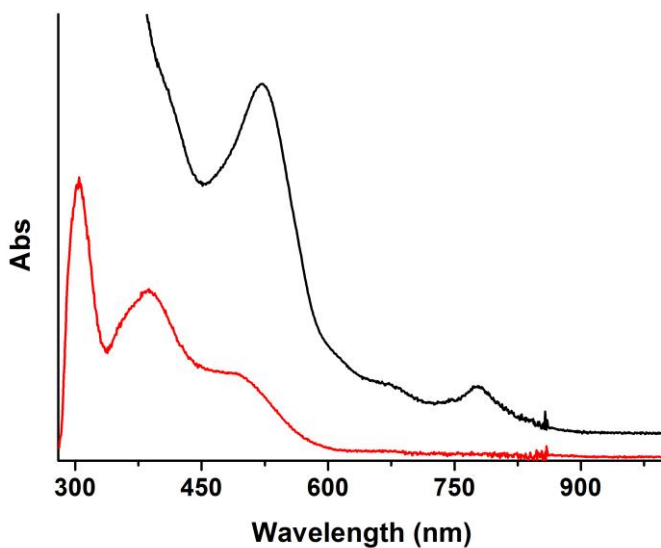


**Fig. 4.6** UV-Vis spectra of 5 mmol  $[\text{MoCl}_3(\text{THF})_3]$  in  $\text{THF}^*$  (red) and  $\text{CH}_2\text{Cl}_2$  (black) ( $^*[\text{MoCl}_3(\text{THF})_3]$  is only partially soluble in THF).

Two ligand architectures have been chosen to investigate the reactions of the Mo(III) complexes with AlMe<sub>3</sub>, one with SNS donor type and S<sub>3</sub> donor type.

The SNS type ligand was synthesised from the substitution of chloride on the bis(chloroethane)amine hydrochloride using a thiol with the desired alkyl group (alkyl = decyl or <sup>t</sup>Bu). This reaction proceeds at RT to give a yellow oil after aqueous work-up. This ligand type was selected as it had proven itself to be a highly active ligand system for chromium selective trimerisation of ethene.<sup>[28]</sup> With hard and soft donor types this tridentate ligand provides different types of coordination, coordinating via a secondary amine, providing a possible pathway for oxidation state changes on the metal.

Of the tridentate sulfur ligand (S<sub>3</sub> type donor) two classes have been used. The small macrocycle [9]aneS<sub>3</sub> was first used as purchased from Aldrich. Following this complex, an open chain form of S(CH<sub>2</sub>CH<sub>2</sub>S-<sup>n</sup>decyl)<sub>2</sub> was synthesised and successfully complexed to [MoCl<sub>3</sub>(S(CH<sub>2</sub>CH<sub>2</sub>S-<sup>n</sup>decyl)<sub>2</sub>)]. Unfortunately this complex was found to have a poor solubility in toluene, the solvent of choice for the stopped-flow system. A slight modification of this ligand to S(CH<sub>2</sub>CH<sub>2</sub>S-CH<sub>2</sub>-C<sub>6</sub>H<sub>4</sub>-*p*-<sup>t</sup>Bu)<sub>2</sub> provided the same soft tridentate ligand system with much improved solubility of the Mo complex in toluene. This ligand was synthesized from the substitution of the deprotonated thiol of S(CH<sub>2</sub>CH<sub>2</sub>SH)<sub>2</sub> for bromine, on the synthon Br-CH<sub>2</sub>-C<sub>6</sub>H<sub>4</sub>-*p*-<sup>t</sup>Bu to give a yellow oil.

Coordination to [MoX<sub>3</sub>(THF)<sub>3</sub>] in a slight excess of either the SBz or SNS (L<sub>3</sub>) ligand under inert atmosphere at RT yields the product [MoX<sub>3</sub>(L<sub>3</sub>)] (X = Cl or Br) (Fig. 4.7). A slight excess is used to push the equilibrium towards the product and any excess can be washed out using pentane or hexane after reaction. An inert N<sub>2</sub> atmosphere is kept during reaction and storage of the product as Mo(III) can be oxidised by O<sub>2</sub> or H<sub>2</sub>O to form Mo oxides.

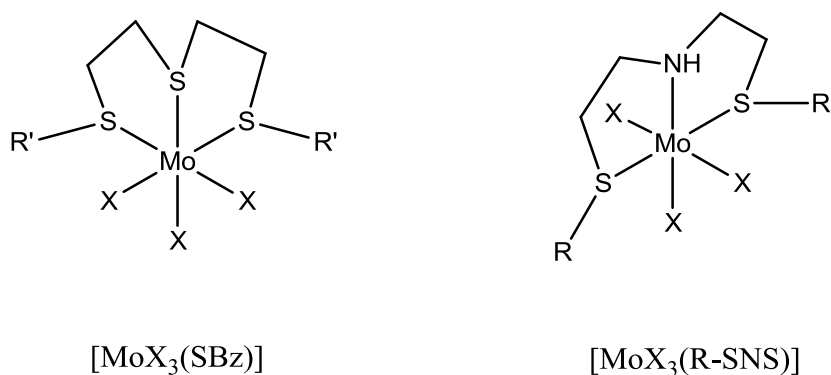


**Fig. 4.7** Showing structure of the synthesised Mo(III) complexes with coordinated ligands (L) ( $\text{R}' = p\text{-}t\text{Bu-Bz}$ ;  $\text{R} = \text{decyl, } t\text{Butyl}$ ;  $\text{X} = \text{Br, Cl}$ ).

X-ray crystal data (Figs. 4.8 and 4.9) shows the SNS type ligand coordinates in a mer- fashion to the Mo and, as expected, the macrocycle [9]aneS<sub>3</sub> coordinates as fac- to the metal centre. Poor crystallographic data of the complex  $[\text{MoBr}_3(\text{SBz})]$  established the ligand adopts a *fac*-arrangement (yet data was not of sufficient quality for an accurate structure determination). With IR data (see section below) and crystal data of complexes with similar ligands as discussed here, it is believed the ligand SBz adopts a facial arrangement around the metal centre.

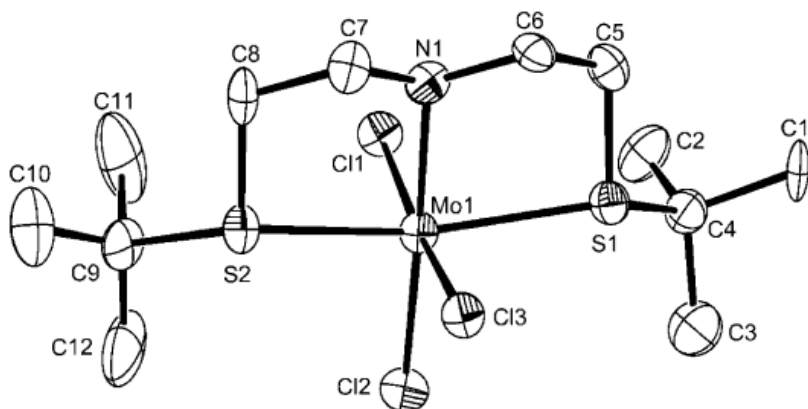


**Fig. 4.8** Structure of  $[\text{MoCl}_3(\text{HN}(\text{CH}_2\text{CH}_2\text{S}^t\text{Bu})_2)]$ . H atoms are omitted for clarity and ellipsoids are drawn at 50% probability level.

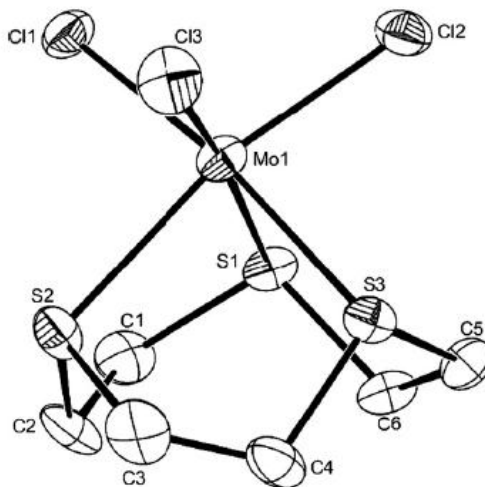


**Fig. 4.9** Structure of  $[\text{MoCl}_3([9]\text{aneS}_3)]$ . H atoms are omitted for clarity and ellipsoids are drawn at 50% probability level.

The observed bond lengths for Mo-S and Mo-Cl are generally slightly longer for  $[\text{MoCl}_3(\text{Bu-SNS})]$  than  $[\text{MoCl}_3([9]\text{aneS}_3)]$  (Table 4.5 and 4.6). The observed distances for  $[\text{MoCl}_3(\text{Bu-SNS})]$  also correspond to the distances given for the  $[\text{MoCl}_3(\text{Et-SNS})]$  complex.<sup>[23]</sup> Compared with the  $[\text{CrCl}_3(\text{Et-SNS})]$  crystal data,<sup>[28]</sup> all Mo bonds are longer by  $\sim 0.1 \text{ \AA}$  in all cases.

#### 4.3.2 Characterisation – FT-IR and UV-Vis Spectroscopy

Due to the paramagnetic nature of Mo(III) (NMR analysis is unavailable), characterisation was based on FT-IR and UV-Vis spectroscopies, (full theoretical discussion in Chapters 2 and 3) and microanalysis. The IR spectra of compounds with R-SNS type ligands, display a characteristic peak in the IR at  $\sim 3500 \text{ cm}^{-1}$ , i.e.  $\sim 250 \text{ cm}^{-1}$  to lower frequency compared to the uncoordinated ligand (Fig. 4.10). The Mo-halide stretching vibrations occur in the range  $350 - 250 \text{ cm}^{-1}$ . Fig. 4.11 shows an overlay of  $[\text{MoCl}_3(\text{decyl-SNS})]$  and  $[\text{MoCl}_3(\text{THF})_3]$ . As expected, the peaks associated with coordinated THF in  $[\text{MoX}_3(\text{THF})_3]$  ( $\sim 1100$  and  $850 \text{ cm}^{-1}$ )<sup>[29]</sup> are not evident in the SNS complexes. Similarly, the Mo-Cl stretching vibrations are shifted.

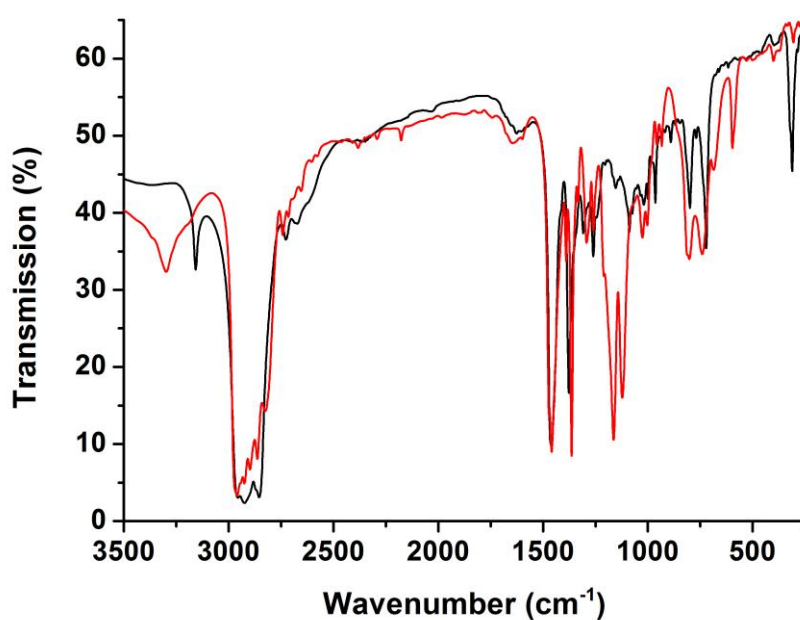


**Fig. 4.10** Displaying FT-IR spectra of  $[\text{MoCl}_3(\text{decyl-SNS})]$  as Nujol mull (black) and free ligand decyl-SNS.

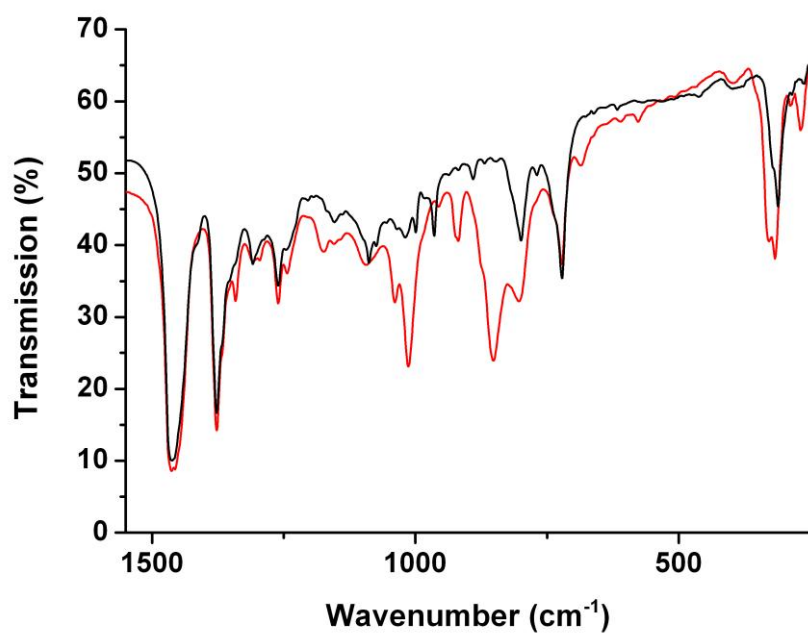


**Fig. 4.11** Displaying FT-IR spectra for  $[\text{MoCl}_3(\text{decyl-SNS})]$  (black) and  $[\text{MoCl}_3(\text{THF})_3]$  (red) as Nujol mulls.

As discussed in more detail in Chapter 3, the UV-Vis spectroscopy of Mo(III) is largely obscured as d-d transitions occur at higher energies, arising from larger Dq values. Also, Mo(III) has a smaller optical electronegativity value relative to Cr(III), therefore MLCT bands would appear at lower energies, causing further overlapping of transitions.<sup>[30]</sup>

## **4.4 Mo K-edge EXAFS Analyses**

### **4.4.1 Solid State and Solution Complexes**

For all the newly synthesised Mo(III) halide complexes, solid and solution structures were determined by Mo K-edge EXAFS analysis to confirm their integrity and starting points for their subsequent reactions. A collection of various other molybdenum complexes have also been analysed and although do not form part of the discussion, were used as references and have been put in the supplementary.

The Mo K-edge EXAFS results for the chlorides, [MoCl<sub>3</sub>(SBz)] and [MoCl<sub>3</sub>(decyl-SNS)] are presented in Table 4.1 and 4.2. The bromide analogue, [MoBr<sub>3</sub>(SBz)] is presented in Table 4.3. For the complex [MoBr<sub>3</sub>(decyl-SNS)], significant beam damage was observed that rendered EXAFS analysis unreliable (Fig. 4.12), otherwise good fits are obtained for all data, with low R-factors.

**Table 4.1** Mo K-edge EXAFS data analyses results on [MoCl<sub>3</sub>(SBz)] complex (all fitted in combined  $k^{1-3}$ -weighting).

Abs – Sc	CN	R(Å)	2σ <sup>2</sup> (Å <sup>-2</sup> )	Fitting Parameters, k (Å <sup>-1</sup> )
<i>Solid [MoCl<sub>3</sub>(SBz)]</i>				
Mo – Cl(S)	2.8(3)	2.40(2)	0.002(3)	2.0 < k < 16.8 ; 1.0 < R < 2.9
Mo – S(Cl)	2.8(3)	2.43(2)	0.003(2)	Amp = 0.85; E <sub>o</sub> = 1(1); R = 0.01
<i>Solution [MoCl<sub>3</sub>(SBz)]</i>				
Mo – Cl(S)	2.8(3)	2.39(2)	0.001(2)	3.0 < k < 16.5 ; 1.0 < R < 3.0
Mo – S(Cl)	2.8(3)	2.46(2)	0.003(3)	Amp = 0.85; E <sub>o</sub> = 1(1); R = 0.02
<i>[MoCl<sub>3</sub>(SBz)] + 8 equivs. AlMe<sub>3</sub> – stopped-flow cuvette ~ 4 min</i>				
Mo – S(Cl)	2.2(9)	2.55(1)	0.002(1)	2.0 < k < 14.6 ; 1.0 < R < 5.5
Mo – C	3.6(9)	2.26(1)	0.002(1)	Amp = 0.85; E <sub>o</sub> = 6(1); R = 0.01
Mo – Mo	1.3(8)	2.97(3)	0.010(5)	
Mo – Mo	2(1)	4.36(5)	0.011(4)	
Mo – Mo	11(9)	5.18(7)	0.015(7)	
<i>[MoCl<sub>3</sub>(SBz)] + 20 equivs. AlMe<sub>3</sub> – solution cell</i>				
Mo – S(Cl)	2.5(5)	2.55(1)	0.005(2)	2.0 < k < 15.3 ; 1.1 < R < 2.7
Mo – C	2.6(4)	2.23(1)	0.001(1)	Amp = 0.85; E <sub>o</sub> = 8(1); R = 0.03

**Table 4.2** Mo K-edge EXAFS data analyses results on  $[\text{MoCl}_3(\text{decyl-SNS})]$  complex (all fitted in combined  $k^{1-3}$ -weighting).

Abs – Sc	CN	$R(\text{\AA})$	$2\sigma^2(\text{\AA}^{-2})$	Fitting Parameters, $k (\text{\AA}^{-1})$
<i>Solid <math>[\text{MoCl}_3(\text{decyl-SNS})]</math></i>				
Mo – N	1(fixed)	2.1(1)	0.010(6)	$2.0 < k < 14.7$ ; $1.1 < R < 2.6$
Mo – Cl(S)	3(fixed)	2.41(3)	0.002(3)	$\text{Amp} = 0.85$ ; $E_o = 3(1)$ ; $R = 0.01$
Mo – S(Cl)	2(fixed)	2.50(2)	0.001(2)	
<i>Solution <math>[\text{MoCl}_3(\text{decyl-SNS})]</math></i>				
Mo – N	1(fixed)	2.1(1)	0.015(9)	$2.0 < k < 15.7$ ; $1.1 < R < 2.7$
Mo – Cl(S)	3(fixed)	2.40(2)	0.002(1)	$\text{Amp} = 0.85$ ; $E_o = 3(1)$ ; $R = 0.02$
Mo – S(Cl)	2(fixed)	2.53(2)	0.002(2)	
<i><math>[\text{MoCl}_3(\text{decyl-SNS})] + 20 \text{ equivs. AlMe}_3 - \text{solution cell}</math></i>				
Mo – N/C	3(1)	2.22(9)	0.010(9)	$2.0 < k < 11.0$ ; $1.0 < R < 3.0$
Mo – S(Cl)	1.9(9)	2.50(3)	0.003(4)	$\text{Amp} = 0.85$ ; $E_o = 3(3)$ ; $R = 0.05$

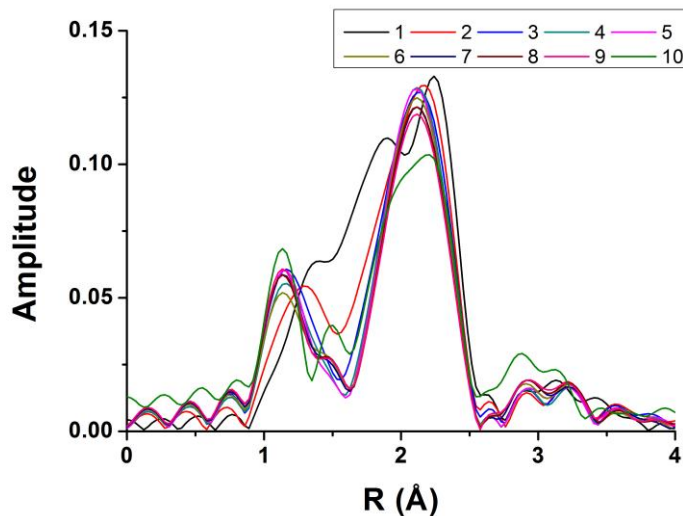


**Fig. 4.12** Mo K-edge  $k^1$ -weighted Fourier transform EXAFS data displaying subsequent scans collected for solid  $[\text{MoBr}_3(\text{decyl-SNS})]$  (legend represents scan number; 1 scan per 20 mins).

The  $[\text{MoCl}_3(\text{decyl-SNS})]$  complex was characterised by three chlorine atoms at  $2.41(3)$  Å, two sulfurs at  $2.50(2)$  Å and one nitrogen at  $2.1(1)$  Å. The crystal structure of the  $^t\text{Bu}$  analogue was used as an input model for the fit. The contribution of the one nitrogen atom is very weak and difficult to identify, as reflected by the large Debye-Waller factor and uncertainty. This can be attributed to the presence of five higher Z sulfur and chlorine atoms. The contribution can be omitted to give a good fit, however from crystal structure data of the  $[\text{MoCl}_3(^t\text{Bu-SNS})]$  (near identical UV-Vis and IR data of this complex to the decyl analogue) can confirm the presence of the Mo-N and this was included in the model. The assignment of chlorine and sulfur shells are based on the distances given by the fit (compared with XRD data), otherwise they are indistinguishable by EXAFS analysis. The Mo-Cl distance of  $2.41(3)$  Å is in good agreement with the average of three crystallographic distances given by  $[\text{MoCl}_3(^t\text{Bu-SNS})]$  ( $2.38$ ,  $2.41$  and  $2.45$  Å). The same is seen for the Mo-S distance (EXAFS =  $2.50(2)$  Å, XRD =  $2.52$ ,  $2.53$  Å). The  $[\text{MoCl}_3(\text{decyl-SNS})]$  complex was subsequently dissolved in toluene and characterised by Mo K-edge EXAFS spectroscopy and, as Table 4.2 shows, the results are similar to the solid state structure. EXAFS data and fits are shown in Fig. 4.13.

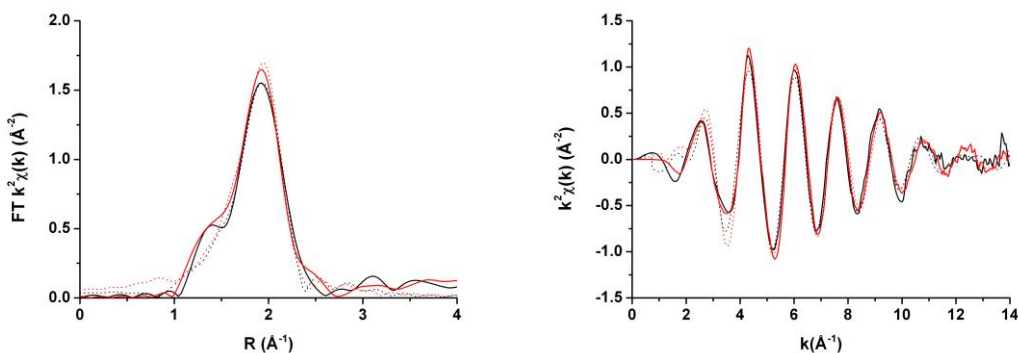


**Fig. 4.13** Mo K-edge  $k^2$ -weighted EXAFS and Fourier transform data (solid lines) and fits (dotted lines) for  $[\text{MoCl}_3(\text{decyl-SNS})]$  solid (black) and solution (red).

The solid and solution state structures of  $[\text{MoCl}_3(\text{SBz})]$  were characterised by Mo K-edge EXAFS spectroscopy and the results presented in Table 4.1. For the fits, the crystal structure of  $[\text{MoCl}_3([9]\text{aneS}_3)]$  was used to model the EXAFS data. From the Mo-Cl stretches in the FT-IR spectrum of  $[\text{MoCl}_3(\text{SBz})]$  and  $[\text{MoCl}_3([9]\text{aneS}_3)]$

complexes, both give two peaks at similar energies, suggesting both adopt  $C_{3v}$  symmetry point groups, indicating the ligands adopt a fac-geometry around the molybdenum. The results of solid fit refine for three chlorines at 2.40(2) Å and three sulfurs at 2.43(2) Å. Comparing [MoCl<sub>3</sub>([9]aneS<sub>3</sub>)] crystallographic distances (Mo-Cl = 2.345(2), 2.385(2) and 2.402(2) Å; Mo-S = 2.464(2), 2.4838(19) and 2.520(2) Å), the obtained fit values fall within the range expected. Again the solution data is in agreement with the collected solid data.

Table 4.3 presents Mo K-edge EXAFS analyses results of the bromide, [MoBr<sub>3</sub>(SBz)]. Two shells can be refined for the solid state structure; one Mo-Br shell with a coordination of 2.5(9) at distance of 2.54(2) Å with a low Debye Waller factor, and a second shell with 3.5(9) sulfur atoms at 2.45(6) Å with a higher Debye Waller factor, 0.010(6). Poor crystallographic data of [MoBr<sub>3</sub>(SBz)] established the ligand adopts a facial arrangement. This fac- assignment is also consistent with observations for Cr(III) and other transition metal complexes with ligands containing – SCH<sub>2</sub>CH<sub>2</sub>SCH<sub>2</sub>CH<sub>2</sub>S- linkages<sup>[31]</sup>. With Br being a stronger scatterer, the Mo-Br contribution dictates the overall fit. The Mo-S shell is less well defined, indicating a possible distance distribution in the solid state structure, despite fac-geometry of the ligand. The solution structure is much better defined with a similar structure and low Debye Waller factors. In this case, due to lower quality of data, coordination numbers were fixed.

EXAFS analyses of all unreacted complexes were of a similar standard and gave the same results irrespective of the observation cell containing the solution (solution cell, stopped-flow cuvette or freeze-quench capillary).

**Table 4.3** Mo K-edge EXAFS data analyses results on [MoBr<sub>3</sub>(SBz)] complex (all fitted in combined  $k^{1-3}$ -weighting).

Abs – Sc	CN	R(Å)	2σ <sup>2</sup> (Å <sup>-2</sup> )	Fitting Parameters, k (Å <sup>-1</sup> )
<i>Solid [MoBr<sub>3</sub>(SBz)]</i>				
Mo – S	3.5(9)	2.45(6)	0.010(6)	$1.7 < k < 14.2$ ; $1.2 < R < 2.6$
Mo – Br	2.5(9)	2.54(2)	0.002(3)	Amp = 0.85; $E_o = -4(1)$ ; $R = 0.01$
<i>Solution [MoBr<sub>3</sub>(SBz)]</i>				
Mo – S	3(fixed)	2.45(2)	0.003(1)	$1.8 < k < 13.5$ ; $1.1 < R < 3.0$
Mo – Br	3(fixed)	2.55(1)	0.006(1)	Amp = 0.85; $E_o = -4(1)$ ; $R = 0.01$
<i>[MoBr<sub>3</sub>(SBz)] + 20 equivs. AlMe<sub>3</sub> – stopped-flow cuvette ~ 4 min</i>				
Mo – S	2.5(3)	2.45(1)	0.003(1)	$2.0 < k < 17.0$ ; $1.1 < R < 3.0$
Mo – Br	1.4(9)	2.59(1)	0.006(4)	Amp = 0.85; $E_o = -4(1)$ ; $R = 0.01$
<i>[MoBr<sub>3</sub>(SBz)] + 20 equivs. AlMe<sub>3</sub> – stopped-flow freeze-quench ~ 5 s</i>				
Mo – S	2.9(4)	2.41(1)	0.004(3)	$2.0 < k < 14.0$ ; $1.0 < R < 3.0$
Mo – Br	2.4(7)	2.58(1)	0.005(3)	Amp = 0.85; $E_o = -5(1)$ ; $R = 0.01$
<i>[MoBr<sub>3</sub>(SBz)] + 20 equivs. AlMe<sub>3</sub> – stopped-flow freeze-quench ~ 5 min</i>				
Mo-S	3.3(3)	2.38(1)	0.005(2)	$2.0 < k < 14.0$ ; $1.0 < R < 3.0$
Mo-Br	1.6(8)	2.61(1)	0.005(3)	Amp = 0.85; $E_o = -5(1)$ ; $R = 0.01$
<i>[MoBr<sub>3</sub>(SBz)] + 20 equivs. AlMe<sub>3</sub> – solution cell</i>				
Mo – S	2.8(5)	2.43(2)	0.003(2)	$2.0 < k < 13.0$ ; $1.0 < R < 3.0$
Mo – Br	0.8(1)	2.61(2)	0.003(7)	Amp = 0.85; $E_o = -4(2)$ ; $R = 0.01$

#### 4.4.2 End state analysis

‘End-state’ analyses are defined as the Mo K-edge EXAFS analysis after the reaction of the Mo complex with AlMe<sub>3</sub> in the solution cell. Once the AlMe<sub>3</sub> was injected, a time of *ca.* 5 minutes had elapsed once data had started collecting, where the acquisition time of one scan was 35 minutes. Directly after injection, the reaction was followed by on-the-fly (otf) XAFS, where 1 scan per minute was collected to the point where the scans were identical. After >1.5 h of reaction time, precipitated Mo was visible in all cases, suggesting decomposition. All solutions was checked for beam damage, except for the [MoBr<sub>3</sub>(decyl-SNS)], no damage was observed.

The end-state EXAFS analyses are presented in Tables 4.1-4.3. From the reaction of [MoCl<sub>3</sub>(decyl-SNS)] + 20 equivs. of AlMe<sub>3</sub>, the EXAFS data can be refined to two shells, 3(1) N/C neighbours at 2.22(9) Å and 1.9(9) sulfurs at 2.50 Å. Again N/C contribution is difficult to determine as seen in solid and solution state structures, but the Mo-S shell is well defined. From an overlay of the solution [MoCl<sub>3</sub>(decyl-SNS)] EXAFS data with data collected after reaction of AlMe<sub>3</sub>, a clear decrease in overall amplitude is observed in the EXAFS spectra after reaction (Fig. 4.14). The distances and coordination obtained by the fit suggest that the sulfurs are retained with substitution of chloride for methyls (arising from the AlMe<sub>3</sub>), giving [Mo(CH<sub>3</sub>)<sub>3</sub>(decyl-SNS)]. Previous work looking at the Cr analogue with AlMe<sub>3</sub> suggested a similar reaction was observed.<sup>[24]</sup>

A similar end-state species, [Mo(CH<sub>3</sub>)<sub>3</sub>(SBz)], is seen for the reaction of [MoCl<sub>3</sub>(SBz)] + 20 equivs. of AlMe<sub>3</sub>. After reaction, the EXAFS data refines for three sulfurs at 2.55(1) Å and three carbons at 2.23(1) Å. The ligand is retained intact, with the three chlorides substituted for methyls, as seen in the SNS complex. The EXAFS analysis gives a longer Mo-S distance for the SBz ligand, than observed before reaction with AlMe<sub>3</sub>. This is consistent with an increase in trans-influence of methyl verses chloride ligand, where the methyl group provides stronger σ-donor properties (Fig. 4.15).

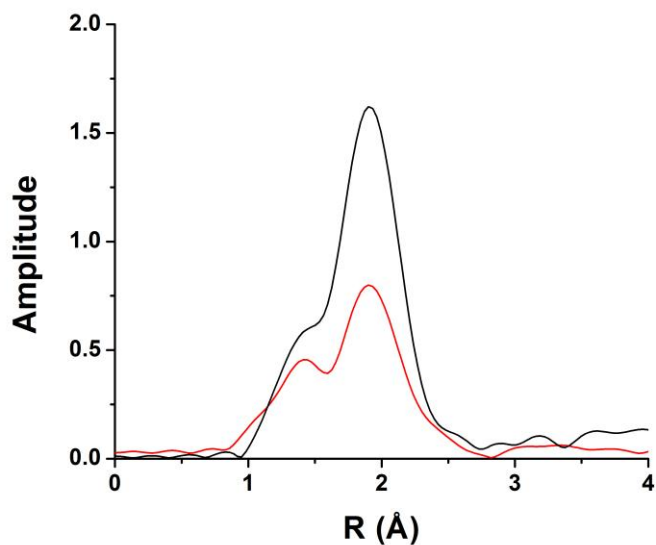


**Fig. 4.14** Mo K-edge  $k^2$ -weighted Fourier transform EXAFS data for  $[\text{MoCl}_3(\text{decyl-SNS})]$  in toluene (black) and  $[\text{MoCl}_3(\text{decyl-SNS})] + 20$  equivs.  $\text{AlMe}_3$  (red) in the solution cell.

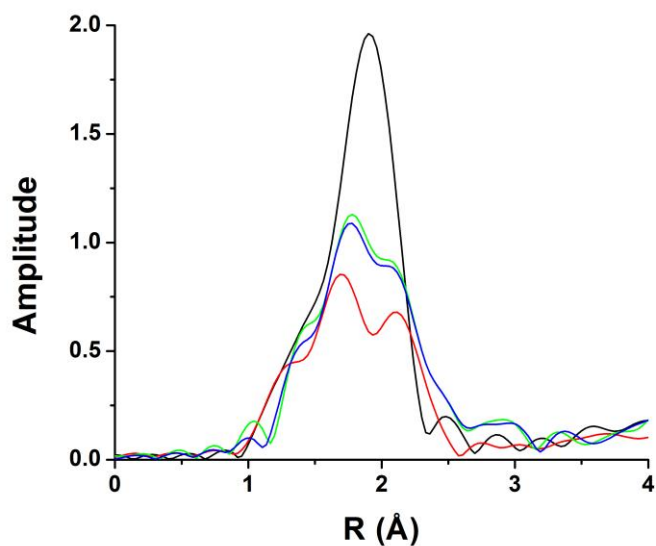


**Fig. 4.15** Mo K-edge  $k^2$ -weighted Fourier transform EXAFS data for  $[\text{MoCl}_3(\text{SBz})]$  in the solution cell (black); + 20 equivs.  $\text{AlMe}_3$  in the solution cell (red); + 4 equivs.  $\text{AlMe}_3$  in the stopped-flow cuvette (green); + 8 equivs.  $\text{AlMe}_3$  in the stopped-flow cuvette (blue).

The  $\text{MoBr}_3$  analogue displays a different behaviour to the chloride, upon reaction with 10 equivs. of  $\text{AlMe}_3$ ,  $[\text{MoBr}_3(\text{SBz})]$  shows no reaction up to one hour. When increasing the ratio of  $[\text{MoBr}_3(\text{SBz})] : \text{AlMe}_3$  to 1:20, significant changes in the EXAFS spectra are observed, but to a lesser extent than the chloride analogues. Comparison of the EXAFS data of  $[\text{MoBr}_3(\text{SBz})]$  before and after reaction shows decrease of, in amplitude where Mo-Br contribution is significant (Fig. 4.16). Refining the end-state EXAFS data led to a good fit of two shells, Mo-S; with coordination of 2.8(5) and Mo-Br; with 0.8(1) coordination. The Debye Waller factor is the same (within uncertainty) before and after reaction with  $\text{AlMe}_3$ . The overall coordination of Mo seems too low to be realistic, but no further shell could be introduced reliably. Small changes are visible in the EXAFS spectra at low k-values, which could be the introduction of lighter C scatterers, although the quality of data does not allow a reliable fit for any significant Mo-C contribution. It is plausible that the Mo-C contribution is disordered (high Debye Waller factor) and therefore too low in intensity to be determined under the strong Mo-S and Mo-Br scatterers.

$[\text{MoBr}_3(\text{SBz})]$  loses the halide ligands upon reaction with  $\text{AlMe}_3$ , albeit at a much slower rate than the chloride analogue, and so the X/Me exchange kinetics must be slower going from chloride to bromide (Scheme 4.7). For all reactions, at longer timescales  $>1.5$  h, the Mo K-edge XAS signal disappears completely and black precipitate is observed in the solution cell, indicating the formation of Mo metal.

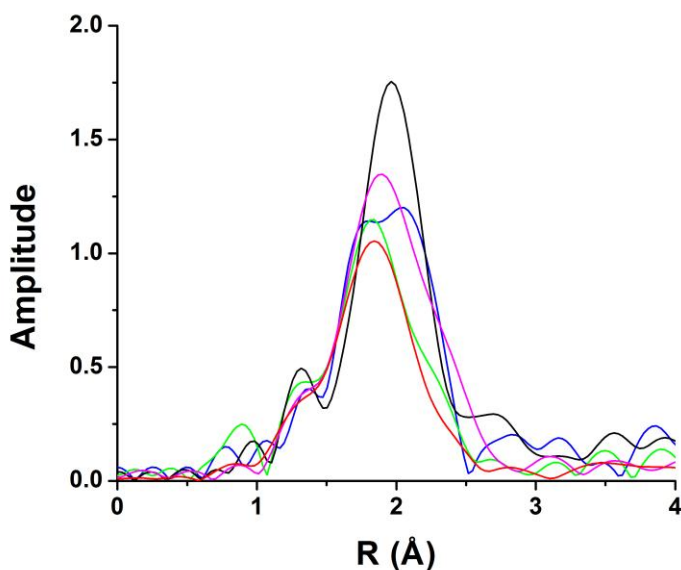
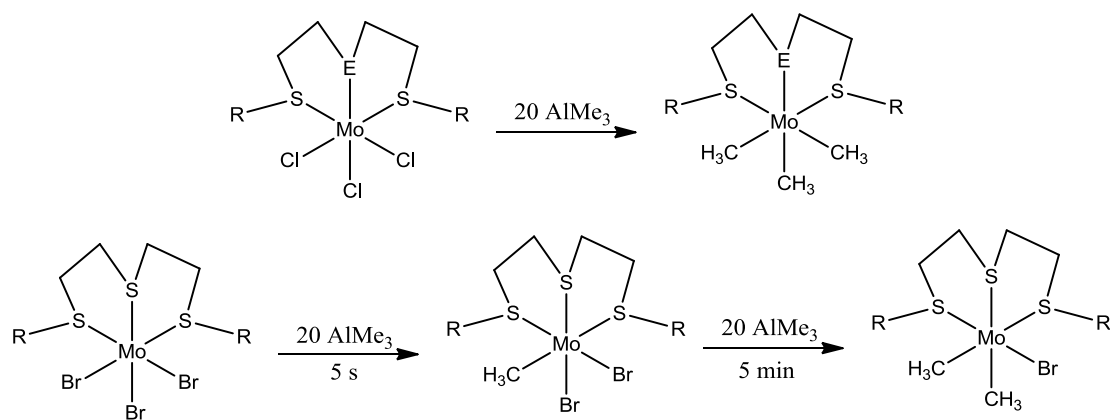


**Fig. 4.16** Mo K-edge  $k^2$ -weighted Fourier transform EXAFS data for a solution of  $[\text{MoBr}_3(\text{SBz})]$  in the solution cell (black); + 20 equivs.  $\text{AlMe}_3$  in the solution cell (red); + 20 equivs.  $\text{AlMe}_3$  in the stopped-flow cuvette (pink); + 20 equivs.  $\text{AlMe}_3$  freeze-quenched after 5 s (blue); + 20 equivs.  $\text{AlMe}_3$  freeze-quenched after 5 min (green).



**Scheme 4.7** Proposed reaction of Mo complexes upon activation with  $\text{AlMe}_3$  ( $\text{E} = \text{S}$  with  $\text{R} = \text{CH}_2\text{C}_6\text{H}_4-p\text{-C}(\text{CH}_3)_3$ ;  $\text{E} = \text{N}$  with  $\text{R} = {}^n\text{C}_{10}\text{H}_{21}$ ).

#### 4.4.3 Time-Resolved EXAFS Spectroscopy

Time-resolved spectroscopy refers to the study of chemical changes and processes followed by a spectroscopic technique. Using a stopped-flow instrument, time-resolved EXAFS spectroscopy was performed in transmission mode through the observation cuvette. Alongside this, time-resolved UV-Vis data were collected with QEXAFS spectroscopy (Quick EXAFS, 1 – 3 mins per spectrum) using optical fibre diode array UV-Vis spectroscopy, perpendicular to the XAS observation head. Reactions observed during QEXAFS collection were no different by UV-Vis spectroscopy than as observed in the lab when the X-ray beam was not present, therefore the reaction observed is in no way influenced by the X-ray beam.

The time-resolved, simultaneous QEXAFS and UV-Vis data collection of  $[\text{MoCl}_3(\text{decyl-SNS})] + 20 \text{ equivs. AlMe}_3$  is shown in Fig. 4.17. The QEXAFS and UV-Vis data were collected every 20 s. Displayed (Fig. 4.17) is a selection of the data to show the major changes of reaction. Although the quality of the EXAFS data is lower compared to the data in the solution cell (as expected due to shorter acquisition times), the same amplitude reduction as observed for the end-state EXAFS data analysis (associated with the loss of chloride from Mo). The major changes occurred within the first 1.5 minutes, as seen by loss of absorbance in both EXAFS and UV-Vis spectroscopy (explanation of UV-Vis data is discussed in Chapter 3, where same reaction is observed without the X-ray beam).

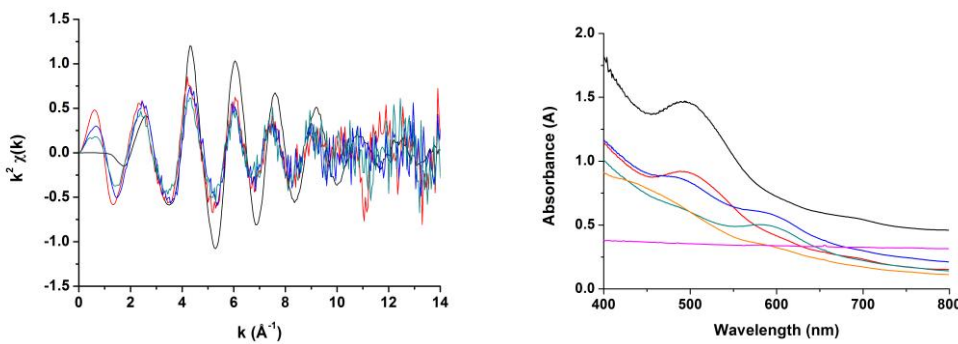


**Fig. 4.17** Combined time-resolved UV-Vis and QEXAFS data of the reaction of  $[\text{MoCl}_3(\text{decyl-SNS})] + 20 \text{ equivs of AlMe}_3$  at  $t = 0$  (black),  $t = 1 \text{ min}$  (red),  $t = 2.5 \text{ min}$  (blue),  $t = 7 \text{ min}$  (green),  $t = 18 \text{ min}$  (orange),  $t = 19 \text{ min}$  (pink) in toluene.

The combination of UV-Vis and EXAFS spectroscopy proves useful in establishing when changes in speciation occur, guiding when the EXAFS data should be collected. Here, a fast initial reaction is observed and the species lasts up to 18 min where UV-Vis and EXAFS signals are both lost simultaneously. It was also observed that when the reaction is followed in a much more confined volume (cuvette = 30  $\mu$ l, solution cell = 3 ml), the effects of the X-ray beam become more concentrated thus encouraging a quicker rate of Mo precipitation.

The UV-Vis spectroscopy of the reaction  $[\text{MoCl}_3(\text{decyl-SNS})] + 20 \text{ equivs. AlMe}_3$  indicates the substituted  $[\text{Mo}(\text{CH}_3)_3(\text{decyl-SNS})]$  is prominent in solution for between 10-20 minutes (with and without X-ray beam), indicating this is the optimum time frame for the EXAFS analysis. The fitting analysis of the end-state EXAFS spectra of the same reaction proved difficult with much background interference. As the end state analysis is the average over *ca.* 1 h of reaction, this can be attributed to possible decomposition products and lower concentration of Mo species in solution. The QEXAFS/UV-Vis spectroscopic approach has demonstrated how it can identify one or more reactive intermediates of a reaction. One of the main drawbacks is the quality of the QEXAFS data at short acquisition times, generally having poor signal-to-noise quality. To improve this, high concentrations of Mo were used to give a higher signal. Although, as the technology develops this will only get better as time goes on.

Observing the  $[\text{MoCl}_3(\text{SBz})] + 20 \text{ equivs. AlMe}_3$  in the combined stopped-flow UV-Vis QEXAFS set-up proved to be more problematic with almost immediate precipitation of Mo-Mo observed in every attempt and, due to the high concentrations used (along with high molar absorption coefficient of  $[\text{MoCl}_3(\text{SBz})]$ ) the diode array detector was instantly flooded, rendering the UV-Vis spectra useless. When looking at 1 equiv. of  $\text{AlMe}_3$ , no reaction was observed. At 8 and 4 equivs. of  $\text{AlMe}_3$  (4 and 8 equivs. giving same EXAFS profile), the displacement of chlorine for methyls is observed, although a significant contributions of Mo-Mo are also seen, indicating Mo-Mo coagulation is already occurring at 4 min after reaction (Table 4.2). At 32 equivs. of  $\text{AlMe}_3$ , EXAFS spectra starts to resemble the reference Mo foil followed by complete precipitation. Note the much higher amplitudes observed compared with reaction of 4, 8 and 20 equivs. of  $\text{AlMe}_3$  (Fig. 4.18). In all cases Mo-Mo precipitation was much quicker than observed for the solution, an indication that deactivation of

these complexes is increased by the stopped-flow cuvette. When considering that these Mo complexes under catalytic testing conditions (higher pressure, higher temperature, and much higher molar amounts of aluminium activator) one can assume this Mo-Mo particle formation is fundamentally the reason they perform such poor ethene oligomerisation.

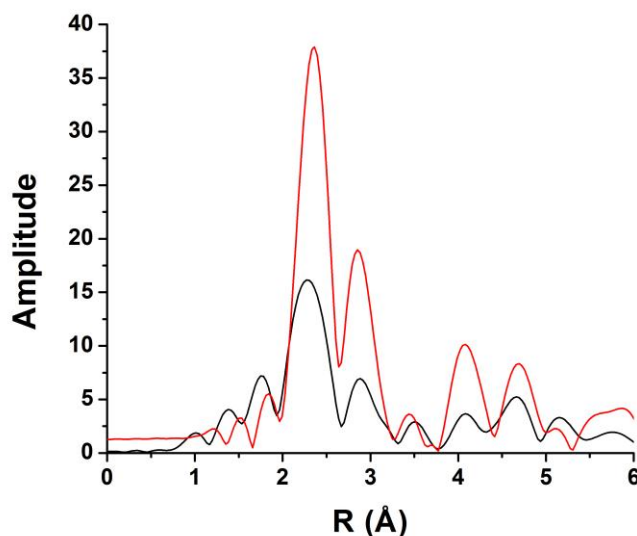


**Fig. 4.18** Mo K-edge  $k^3$ -weighted Fourier transform EXAFS data for  $[\text{MoCl}_3(\text{SBz})] + 32$  equivs.  $\text{AlMe}_3$  in stopped-flow cuvette (black) and Mo reference foil (red).

#### 4.4.4 Freeze-quench study of the alkylation of $[\text{MoBr}_3(\text{SBz})]$

The stopped-flow freeze-quench system was modified for an air moisture tight freeze-quench accessory which allows millisecond time resolution using the stopped-flow apparatus to select and isolate different intermediates, freeze-quench them and keep them frozen to allow long EXAFS data collection. The reaction solutions are injected directly into a Kapton tube, immersed in liquid nitrogen. The freezing time of the solution (commonly 75  $\mu\text{l}$ ) is very difficult to assess, but estimated to be less than 1 s.

The freeze-quench approach allowed the stepwise investigation of  $[\text{MoBr}_3(\text{SBz})]$  with 20 equivs. of  $\text{AlMe}_3$ . Initially, the starting material was frozen and analysed to give the same structural analysis as the complex in the solution cell (Chapter 3). The reaction with  $\text{AlMe}_3$  was freeze-quenched after 5 s and 5 minutes to

compare with data obtained in the stopped-flow cuvette and solution cell. Fig. 4.16 shows the EXAFS data obtained for the different frozen intermediates and the starting solution. The signal-to-noise ratio of the frozen data is lower compared to the data in the cuvette, but this could be improved by the acquisition of more scans. Comparison of data collected previously within the stopped-flow cuvette and solution cell of the same reaction, validates the new accessory as a proof of concept. Additionally, the bromide analogue is advantageous enabling the distinction of the sulfur and halide shells. As seen in the stopped-flow cuvette and solution cell, a decrease in the Mo-Br contribution in time is observed after reaction with 20 equivs. of AlMe<sub>3</sub>. When comparing the Fourier transform of the freeze-quench data after 5 min reaction, the same regions are losing intensity, the Mo-Br contribution (Fig. 4.16). The fits also agree, displaying loss of bromide and retention of the SBz ligand (Table 4.3). Freezing the reaction after 5 s allows identification of an intermediate stage, unable to be identified by QEXAFS spectroscopy in the stopped-flow instrument (30 s – 3 min /spectrum), suggesting a stepwise partial reduction of Mo-Br (Scheme 6).

The UV-Vis/EXAFS/Freeze-quench methods have clearly demonstrated the stepwise substitution of these Mo(III) halides by AlMe<sub>3</sub>, forming a mixed alkyl halide mononuclear complex as seen for some chromium systems (Scheme 4.6).<sup>[32]</sup> The high Mo K-edge energy allows time-resolved stopped-flow XAS experimentation down to a time resolution of 30 s per spectrum for good S/N quality data to allow EXAFS analyses. The new freeze-quench methodology is an extension to the stopped-flow instrument with a freezing time of less than 1 second, allowing multiple scans in fluorescence mode, enabling the analysis of very early reaction steps previously unseen by time-resolved XAS.

Although the Mo complexes have shown little or no catalytic activity towards ethene oligomerisation,<sup>[23]</sup> it is reasonable to assume the Mo systems undergo the same early stages of activation. There are literature examples of halide-bridged dimer formation at low Cr:Al ratios,<sup>[33]</sup> but no dimeric Mo species have been observed in this study. Moving from Cr to Mo analogues, a clear decrease in reaction rate was observed as expected. Moreover, the reaction kinetics were slowed further moving from the chloride to the bromide analogue. This is difficult to rationalise as the exact substitution mechanism is unknown, but possibly the bond formation of Al-Cl vs Al-Br or the difference in proximity of the Al species and the Mo centre allowed by Cl and Br ligands to allow alkylation of Mo. At the high concentrations of reactants used

in this study, it seems the alkylation of the complex is in competition with the Mo particulate precipitation, especially seen for the chloride analogues.

#### 4.5 Conclusion

This study has used the time-resolved Mo K-edge EXAFS spectroscopy with a stopped-flow system to probe the first stages of activation of the Mo analogues of the industrially important ethene trimerisation catalysts and compared the results with start and end- state studies. The results demonstrate that treatment of the Mo complex solution with excess AlMe<sub>3</sub> leads to halide loss, forming [Mo(CH<sub>3</sub>)<sub>3</sub>(L)] type complexes with strong evidence that dinuclear Mo-Mo or halide bridged dimers are not formed preferentially under these conditions (1:20 Mo:Al). At the higher AlMe<sub>3</sub> ratios, the activation reaction (formation of the mononuclear alkyl species) is in competition with the deactivation (Mo precipitation), especially seen for the trichlorides, providing insights in the low overall catalytic activity and deactivation.<sup>[23]</sup> The new freeze-quench attachment, which takes advantage of the excellent volume and timescale control offered by the stopped-flow system, allows reaction mixtures to be frozen (to liquid nitrogen temperatures) within 1 s of mixing under anaerobic conditions. This allows reactive, short-lived intermediate species to be trapped and enables multiple XAFS scans with long acquisition times of the same species, measured in fluorescence mode (as required for 3d transition metals with low X-ray absorption edge energies and low concentrations). Further experiments using this approach to examine the catalytic process associated with the [CrCl<sub>3</sub>(SNS)] ethene trimerisation system have been employed and the results presented in chapter 6.

#### 4.6 Experimental

All complexes were synthesised under inert conditions using standard Schlenk line techniques, using dry solvents, having previously been distilled from appropriate drying agents. Complexes [MoCl<sub>3</sub>(THF)<sub>3</sub>]<sup>[25]</sup> and [MoBr<sub>3</sub>(THF)<sub>3</sub>]<sup>[27]</sup> and ligand HN(CH<sub>2</sub>CH<sub>2</sub>SC<sub>10</sub>H<sub>21</sub>)<sub>2</sub> (decyl-SNS)<sup>[28]</sup> were synthesised in accordance with previously published procedures. All metal complexes were stored under inert atmosphere in a glove box. AlMe<sub>3</sub> was purchased from Aldrich (2.0 M in hexanes)

and titrated using the published procedure.<sup>[34]</sup> All solvents used in the stopped-flow instrument were purchased (anhydrous) from Aldrich and used as received.

<sup>1</sup>H and <sup>13</sup>C{<sup>1</sup>H} NMR spectra were recorded on a Bruker AV300 spectrometer. Microanalyses were obtained through Medac Ltd., Egham UK. Infrared spectra were recorded as a Nujol mull between CsI plates under inert conditions, using Perkin Elmer FT-IR Spectrum 100 Spectrometer across the range 4000 - 200 cm<sup>-1</sup>. UV-Vis spectra were recorded both using the stopped-flow instrument (Fibre optic J & M Analytic MCS-UVNIR) and using a Perkin Elmer Lambda 19 spectrometer either in solution in a 1 cm path length quartz cuvette, or as solids by diffuse reflectance (DR). All spectroscopic samples were prepared freshly in a dry N<sub>2</sub>-purged glove-box.

S(CH<sub>2</sub>CH<sub>2</sub>SCH<sub>2</sub>-C<sub>6</sub>H<sub>4</sub>-*p*-C(CH<sub>3</sub>)<sub>3</sub>)<sub>2</sub> [SBz]: Sodium (2.67 g, 116.3 mmol) was slowly dissolved in a solution of ethanol (200 mL) and bis(2-mercaptopethyl)sulfide (7.16 g, 46.40 mmol) under an N<sub>2</sub> atmosphere. The solution was heated to reflux and turned cloudy upon the dropwise addition of 4-tert-butylbenzylbromide (21.36 g, 94.03 mmol); this was then refluxed overnight under N<sub>2</sub>. Ethanol was removed *in vacuo*, and the reaction was hydrolysed using water (50 mL). After extraction with diethyl ether (3 x 30 mL), the organics were combined, dried over MgSO<sub>4</sub>, filtered and the solvent removed *in vacuo*. The yellow oil was further dried under vacuum. Yield: 18.15 g, 88 %. <sup>1</sup>H NMR (CD<sub>2</sub>Cl<sub>2</sub>): 1.32 (s, [18H], CH<sub>3</sub>), 2.63 (m, [8H], CH<sub>2</sub>S), 3.72 (s, [4H], C<sub>6</sub>H<sub>4</sub>-CH<sub>2</sub>S), 7.2, 7.4 (dd, [8H], Ar) ppm. <sup>13</sup>C{<sup>1</sup>H} NMR (CD<sub>2</sub>Cl<sub>2</sub>): 31.7 (CH<sub>3</sub>), 32.1, 32.5 (CH<sub>2</sub>S), 36.4 (C<sub>6</sub>H<sub>4</sub>-CH<sub>2</sub>S), 126.0, 129.0 (ArCH), 135.8, 150.7 (ArC) ppm.

[MoCl<sub>3</sub>{HN(CH<sub>2</sub>CH<sub>2</sub>SC(CH<sub>3</sub>)<sub>3</sub>)<sub>2</sub>}] [MoCl<sub>3</sub>(<sup>t</sup>Bu-SNS)]: HN(CH<sub>2</sub>CH<sub>2</sub>SC(CH<sub>3</sub>)<sub>3</sub>)<sub>2</sub> (0.9 g, 3.6 mmol) was added directly to a suspension of [MoCl<sub>3</sub>(THF)<sub>3</sub>] (1.0 g, 2.4 mmol) in THF (15 mL), giving an orange solution after 2 h. This was then allowed to stir overnight under N<sub>2</sub>. The solution was filtered under N<sub>2</sub> and washed with cold CH<sub>2</sub>Cl<sub>2</sub> (3 x 5 mL). The yellow solid was dried *in vacuo*. Yield: 0.7 g, 64%. DR UV-Vis Spectrum (CaF<sub>2</sub>): λ<sub>max</sub> 446 nm. IR (Nujol mull, ν/cm<sup>-1</sup>): 3144 (NH), 336, 313, 303 (Mo-Cl). Micro-analysis required for C<sub>12</sub>H<sub>27</sub>Cl<sub>3</sub>MoNS<sub>2</sub>: C = 31.9; H = 6.0; N = 3.1; found C = 32.4; H = 6.1; N = 2.6%.

[MoCl<sub>3</sub>{HN(CH<sub>2</sub>CH<sub>2</sub>SC<sub>10</sub>H<sub>21</sub>)<sub>2</sub>}][MoCl<sub>3</sub>(decyl-SNS)]: HN(CH<sub>2</sub>CH<sub>2</sub>SC<sub>10</sub>H<sub>21</sub>)<sub>2</sub>)<sub>2</sub> (1.4 g, 3.6 mmol) was added directly to a suspension of [MoCl<sub>3</sub>(THF)<sub>3</sub>] (1.0 g, 2.4 mmol) in THF (20 mL). The mixture was allowed to stir overnight under N<sub>2</sub>, giving a very dark solution. The THF was then reduced to 5 mL *in vacuo*, where CH<sub>2</sub>Cl<sub>2</sub> (15 mL) was added and the mixture was allowed to stir for a further 14 h under N<sub>2</sub>. All the solvent was then removed *in vacuo*, and dry hexane added. The solution was stirred and sonicated, the dark brown solid was then filtered under N<sub>2</sub> and dried *in vacuo*. Yield: 1.27 g, 86%. UV-Vis spectrum (toluene):  $\lambda_{\text{max}}$  455 nm,  $\epsilon = 350 \text{ mol}^{-1}\text{dm}^3\text{cm}^{-1}$ . IR (Nujol mull,  $\nu/\text{cm}^{-1}$ ): 3158 (NH), 324, 311 (Mo-Cl). Micro-analysis required for C<sub>24</sub>H<sub>51</sub>Cl<sub>3</sub>MoNS<sub>2</sub>: C = 46.5; H = 8.3; N = 2.3; found C = 46.6; H = 8.4; N = 2.5%.

[MoCl<sub>3</sub>{S(CH<sub>2</sub>CH<sub>2</sub>SCH<sub>2</sub>-C<sub>6</sub>H<sub>4</sub>-*p*-C(CH<sub>3</sub>)<sub>3</sub>)<sub>2</sub>}][MoCl<sub>3</sub>(SBz)]: S(CH<sub>2</sub>CH<sub>2</sub>SCH<sub>2</sub>-C<sub>6</sub>H<sub>4</sub>-*p*-C(CH<sub>3</sub>)<sub>3</sub>)<sub>2</sub> (0.59 g, 1.31 mmol) was added directly to a suspension of [MoCl<sub>3</sub>(THF)<sub>3</sub>] (0.5 g, 1.19 mmol) in THF (20 mL). The solution was allowed to stir for 3 d. under N<sub>2</sub> to give a very dark solution. The solvent was then removed *in vacuo* to give a very dark solid. Dry hexane (25 mL) was added and the solution was allowed to stir for 30 mins. The red solid was then filtered under N<sub>2</sub> and dried *in vacuo*. Yield: 0.56 g, 72 %. UV-Vis spectrum (toluene):  $\lambda_{\text{max}}$  476 nm,  $\epsilon = 938 \text{ mol}^{-1}\text{dm}^3\text{cm}^{-1}$ . IR (Nujol mull,  $\nu/\text{cm}^{-1}$ ): 367, 352, 322 (Mo-Cl). Micro-analysis required for C<sub>26</sub>H<sub>38</sub>Cl<sub>3</sub>MoS<sub>3</sub>: C = 48.1; H = 5.9; found C = 47.8; H = 5.8%.

[MoBr<sub>3</sub>{HN(CH<sub>2</sub>CH<sub>2</sub>SC<sub>10</sub>H<sub>21</sub>)<sub>2</sub>}][MoBr<sub>3</sub>(decyl-SNS)]: Prepared in the same manner as [MoCl<sub>3</sub>(<sup>t</sup>Bu-SNS)] above, using [MoBr<sub>3</sub>(THF)<sub>3</sub>] (0.6 g, 1.09 mmol) and HN(CH<sub>2</sub>CH<sub>2</sub>SC<sub>10</sub>H<sub>21</sub>)<sub>2</sub> (0.55 g, 1.31 mmol), with 1.5 d. stirring after the addition of CH<sub>2</sub>Cl<sub>2</sub>. UV-Vis spectrum (CH<sub>2</sub>Cl<sub>2</sub>):  $\lambda_{\text{max}}$  486 nm (sh),  $\epsilon = 1000$ ; 421 nm,  $\epsilon = 1625 \text{ mol}^{-1}\text{dm}^3\text{cm}^{-1}$ . IR (Nujol mull,  $\nu/\text{cm}^{-1}$ ): 3172 (NH), 257, 243, 228 (Mo-Br). Micro-analysis required for C<sub>24</sub>H<sub>51</sub>Br<sub>3</sub>MoNS<sub>2</sub>: C = 38.3; H = 6.8; N = 1.9; found C = 39.0; H = 7.2; N = 2.0%.

[MoBr<sub>3</sub>{S(CH<sub>2</sub>CH<sub>2</sub>SCH<sub>2</sub>-C<sub>6</sub>H<sub>4</sub>-*p*-C(CH<sub>3</sub>)<sub>3</sub>)<sub>2</sub>}][MoBr<sub>3</sub>(SBz)]: S(CH<sub>2</sub>CH<sub>2</sub>SCH<sub>2</sub>-C<sub>6</sub>H<sub>4</sub>-*p*-C(CH<sub>3</sub>)<sub>3</sub>)<sub>2</sub> (0.49 g, 1.09 mmol) was added directly to a suspension of [MoBr<sub>3</sub>(THF)<sub>3</sub>] (0.5 g, 0.91 mmol) in THF (10 mL). The solution was allowed to stir for 1 d. under N<sub>2</sub> to give an orange precipitate. The solvent was then removed *in vacuo* and CH<sub>2</sub>Cl<sub>2</sub> added to the orange solid to ensure all starting material had dissolved. This was allowed to stir overnight and then filtered under N<sub>2</sub>. The orange

solid was then washed with further CH<sub>2</sub>Cl<sub>2</sub>, filtered under N<sub>2</sub> and dried *in vacuo*. Yield: 0.38 g, 54%. UV-Vis spectrum (toluene):  $\lambda_{\text{max}}$  472 nm,  $\epsilon = 2300 \text{ mol}^{-1}\text{dm}^3\text{cm}^{-1}$ . IR (Nujol mull,  $\nu/\text{cm}^{-1}$ ): 287, 273, 265 (Mo-Br). Micro-analysis required for C<sub>26</sub>H<sub>38</sub>Br<sub>3</sub>MoS<sub>3</sub>: C = 39.9; H = 4.9; found C = 40.1; H = 4.8%.

**[MoCl<sub>3</sub>([9]aneS<sub>3</sub>)] ([9]aneS<sub>3</sub> = 1,4,7-trithiacyclononane):** Prepared by a modification of the literature method.<sup>[35]</sup> [9]aneS<sub>3</sub> (0.1 g, 0.6 mmol) in THF (5 mL) was added to [MoCl<sub>3</sub>(THF)<sub>3</sub>] (0.2 g, 0.6 mmol) in THF (5 mL). This was allowed to stir for 2 h at room temperature to give a cloudy red solution. The solvent was then reduced to ~2mL *in vacuo*, and CH<sub>2</sub>Cl<sub>2</sub> (20 mL) added. The reaction was left to stir overnight. The red precipitate was then filtered, washed with CH<sub>2</sub>Cl<sub>2</sub> (2 x 5 mL) and dried *in vacuo* to give an orange solid. Yield: 0.10 g, 48 %. DR UV-Vis spectrum (BaSO<sub>4</sub>): 480 nm. IR (Nujol mull,  $\nu/\text{cm}^{-1}$ ): 315, 292 (Mo-Cl). Micro-analysis required for C<sub>6</sub>H<sub>12</sub>Cl<sub>3</sub>MoS<sub>3</sub>: C = 18.8; H = 3.2; found C = 19.1; H = 3.1%.

#### 4.6.1 X-ray Crystallography

Crystals of [MoCl<sub>3</sub>([9]aneS<sub>3</sub>)] and weakly diffracting crystals of [MoCl<sub>3</sub>(HN(CH<sub>2</sub>CH<sub>2</sub>S<sup>t</sup>Bu)<sub>2</sub>)] suitable for single crystal X-ray analysis were obtained from a solution of the complex in THF or CH<sub>2</sub>Cl<sub>2</sub> (at -18 °C) respectively (Figs. 4.8 and 4.9). Details of the crystallographic data collection and refinement parameters are given in Table 4.4. Data collection used a Bruker-Nonius Kappa CCD diffractometer fitted with monochromated Mo K $\alpha$  radiation ( $\lambda = 0.71073 \text{ \AA}$ ), with the crystals held at 120 K in a nitrogen gas stream. Structure and refinement were straightforward using SHELXS-97 program.<sup>[36]</sup> H atoms bonded to C were introduced into models in idealised positions using default C-H distance. The crystal quality for [MoCl<sub>3</sub>(HN(CH<sub>2</sub>CH<sub>2</sub>S<sup>t</sup>Bu)<sub>2</sub>)] was modest, therefore structure determination is of modest quality, yet core geometry and isomer determination are not in doubt. Selected bond lengths and angles are presented in Tables 4.5 and 4.6.

**Table 4.4** Crystal data and structure refinement details<sup>a</sup>.

Compound	[MoCl <sub>3</sub> (HN(CH <sub>2</sub> CH <sub>2</sub> S <sup>t</sup> Bu) <sub>2</sub> )]	[MoCl <sub>3</sub> ([9]aneS <sub>3</sub> )]
Formula	C <sub>12</sub> H <sub>27</sub> Cl <sub>3</sub> MoNS <sub>2</sub>	C <sub>6</sub> H <sub>12</sub> Cl <sub>3</sub> MoS <sub>3</sub>
<i>M</i>	451.76	382.63
Crystal System	Orthorhombic	Tetragonal
Space Group (no.)	<i>P</i> 2 <sub>1</sub> 2 <sub>1</sub> 2 <sub>1</sub> (19)	<i>I</i> 4 <sub>1</sub> cd (110)
<i>a</i> (Å)	6.890(2)	17.213(2)
<i>b</i> (Å)	9.349(3)	17.213(2)
<i>c</i> (Å)	30.338(9)	16.389(2)
$\alpha$ (°)	90	90
$\beta$ (°)	90	90
$\gamma$ (°)	90	90
<i>U</i> (Å <sup>3</sup> )	1954.3(10)	4855.7(10)
<i>Z</i>	4	16
$\mu$ (Mo Kα)/mm <sup>-1</sup>	1.284	2.210
Total no. reflections	22,151	16,285
Unique reflections	3826	2579
<i>R</i> <sub>int</sub>	0.170	0.0938
No. of parameters, restraints	173, 24	118, 1
Goodness-of-fit on <i>P</i> <sup>2</sup>	1.112	1.116
<i>R</i> <sub>1</sub> <sup>b</sup> [ $I_o > 2\sigma(I_o)$ ]	0.101	0.050
<i>R</i> <sub>1</sub> (all data)	0.129	0.069
<i>wR</i> <sub>2</sub> <i>b</i> [ $I_o > 2\sigma(I_o)$ ]	0.2219	0.089
<i>wR</i> <sub>2</sub> <i>b</i> (all data)	0.237	0.097

<sup>a</sup> Common items: temperature = 120 K; wavelength (Mo Kα) = 0.71073 Å;  $\theta(\text{max}) = 27.5^\circ$ .

<sup>b</sup>  $R_1 = \Sigma |F_o| - |F_c| / \Sigma |F_o|$ .  $wR_2 = [\sum w(F_o^2 - F_c^2)^2 / \sum wF_o^4]^{1/2}$ .

**Table 4.5** Selected bond lengths ( $\text{\AA}$ ) and angles ( $^{\circ}$ ) for  $[\text{MoCl}_3(\text{HN}(\text{CH}_2\text{CH}_2\text{S}^t\text{Bu})_2)]$ .

Mo1 – N1	2.208(12)	Mo1 – Cl1	2.384(4)
Mo1 – Cl2	2.410(4)	Mo1 – Cl3	2.452(4)
Mo1 – S1	2.521(4)	Mo1 – S2	2.532(4)
N1 – Mo1 – Cl1	85.2(3)	N1 – Mo1 – Cl2	176.4(3)
Cl1 – Mo1 – Cl2	91.28(13)	N1 – Mo1 – Cl3	88.5(3)
Cl1 – Mo1 – Cl3	173.66(14)	Cl2 – Mo1 – Cl3	95.01(13)
N1 – Mo1 – S1	80.0(3)	Cl1 – Mo1 – S1	95.90(13)
Cl2 – Mo1 – S1	101.14(13)	Cl3 – Mo1 – S1	82.06(12)
N1 – Mo1 – S2	81.2(3)	Cl1 – Mo1 – S2	96.92(13)
Cl2 – Mo1 – S2	98.46(13)	Cl3 – Mo1 – S2	83.02(12)
S1 – Mo1 – S2	156.26(12)		

**Table 4.6** Selected bond lengths ( $\text{\AA}$ ) and angles ( $^{\circ}$ ) for  $[\text{MoCl}_3([9]\text{aneS}_3)]$ .

Mo1 – Cl1	2.402(2)	Mo1 – Cl2	2.345(2)
Mo1 – Cl3	2.385(2)	Mo1 – S1	2.464(2)
Mo1 – S2	2.520(2)	Mo1 – S3	2.484(2)
Cl2 – Mo1 – Cl3	96.78(9)	Cl2 – Mo1 – Cl1	99.53(8)
Cl3 – Mo1 – Cl1	96.57(9)	Cl2 – Mo1 – S1	88.60(8)
Cl3 – Mo1 – S1	172.42(9)	Cl1 – Mo1 – S1	87.77(7)
Cl2 – Mo1 – S3	86.12(7)	Cl3 – Mo1 – S3	91.41(9)
Cl1 – Mo1 – S3	169.58(8)	S1 – Mo1 – S3	83.60(7)
Cl2 – Mo1 – S2	168.16(7)	Cl3 – Mo1 – S2	89.60(9)
Cl1 – Mo1 – S2	89.59(7)	S1 – Mo1 – S2	84.20(8)
S2 – Mo1 – S3	83.76(6)		

#### 4.6.2 XAFS Experimental

All samples for solid state Mo K-edge EXAFS analysis were mixed with dry boron nitride, pressed into pellets under inert atmosphere and encapsulated in Kapton® tape. All solution data collected for Mo K-edge EXAFS spectra were obtained from solutions made up to the stated concentrations with anhydrous toluene under inert conditions. The solution was then transferred to a dry, argon-purged and

sealed solution XAFS cell<sup>[32]</sup> for analysis on the beamline. Reactions were also performed in this solution XAFS cell by adding of the stated amount of AlMe<sub>3</sub> (2.0 M in hexane) (using a syringe) directly into the solution XAFS cell. The solution was then analysed with Mo K edge EXAFS spectroscopy after ca. 5 min of reaction. Within all chapters, this cell is referred to as ‘solution cell’ (in which reaction ‘start-’ and ‘end-states’ were measured).

All stopped-flow and freeze-quench experiments were carried out using a BioLogic SFM-400 stopped-flow instrument as explained above. In stopped-flow mode, all reactions were observed in cuvette TC-100/10T with minimum dead volume of 30.2 µl. In time UV-Vis spectra was collected using J & M Analytic AG MCS-UVNIR 500-3 fibre optic diode array spectrometer. When using the freeze-quench attachment, the same set-up is used (with UV-Vis spectrometer and cuvette head removed) giving a total minimum dead volume of 19 µl from mixing to ejection, freezing time in toluene less than 1 second. Prior to all reactions using the stopped-flow instrument, the whole instrument was purged with argon, maintaining a positive pressure throughout (including waste lines) by attachment to a Schlenk line. All lines were washed with anhydrous toluene, then the subsequent reactant, followed by further washing with anhydrous toluene.

The Mo K-edge XAFS measurements were performed at different synchrotrons across Europe. Solid and solution (solution cell) preliminary experiments were performed at BM26 (DUBBLE)<sup>[37]</sup> of the European Synchrotron Radiation Facility (ESRF) in Grenoble, France. Mo K-edge XAS data were obtained using a Si(111) double crystal monochromator using ionisation chambers for transmission detection, with acquisition times of 30 minutes (three scans were averaged to improve S/N unless stated otherwise). Solid and solution (solution cell) experiments, as well as time-resolved stopped-flow QEXAFS/UV-Vis spectroscopy were performed at the SuperXAS beamline at the Swiss Light Source in Villigen, Switzerland. The time-resolved Mo K-edge QEXAFS experiments were performed using a fast scanning Si(111) double crystal monochromator, with a time resolution of 1 minute/spectrum for the stopped-flow set-up and 3 minutes/spectrum for the solids and solution cells. All data from these experiments were obtained in transmission mode using ionisation chambers. Time-resolved QEXAFS/UV-Vis spectroscopy as well as freeze-quench experiments were performed at the B18 beamline<sup>[38]</sup> at Diamond Light Source in Didcot, England. A Si(111) double crystal was used in

combination with ion chamber detectors for time-resolved transmission data and an Ortec® Ge 9 element Solid State detector for fluorescence acquisition on the frozen samples. Mo K-edge step-scans were obtained in 35 minutes, whereas the QEXAFS data was obtained with a time resolution of 30 seconds per spectrum. The time-resolved spectra shown are a combination of data obtained at the SLS and Diamond. All spectra were calibrated using a Mo foil. XAS data processing and EXAFS analysis were performed using IFEFFIT<sup>[39]</sup> with the Horae package<sup>[40]</sup> (Athena and Artemis). The amplitude, i.e.  $s_0^2$ , was derived from EXAFS data analysis of known Mo reference compounds (with known coordination numbers which were fixed during analysis) to be 0.85, which was used as a fixed input parameter in all fits to allow coordination number (CN) refinement. The organometallic complexes were fitted using single crystal models or similar complexes, as indicated. The detailed fitting parameters are given in the results section.

#### 4.7 References

- [1] R. R. Schrock, *J. Organomet. Chem.* **1986**, *300*, 249-262.
- [2] R. R. Schrock, *Accounts Chem. Res.* **1990**, *23*, 158-165.
- [3] R. H. Grubbs and W. Tumas, *Science* **1989**, *243*, 907-915.
- [4] R. R. Schrock, J. S. Murdzek, G. C. Bazan, J. Robbins, M. DiMare and M. O'Regan, *J. Am. Chem. Soc.* **1990**, *112*, 3875-3886.
- [5] a) R. R. Schrock, R. T. DePue, J. Feldman, C. J. Schaverien, J. C. Dewan and A. H. Liu, *J. Am. Chem. Soc.* **1988**, *110*, 1423-1435; b) R. R. Schrock, R. T. DePue, J. Feldman, K. B. Yap, D. C. Yang, W. M. Davis, L. Park, M. DiMare and M. Schofield, *Organomet.* **1990**, *9*, 2262-2275.
- [6] a) J. Feldman, W. M. Davis and R. R. Schrock, *Organomet.* **1989**, *8*, 2266-2268; b) J. Feldman, J. S. Murdzek, W. M. Davis and R. R. Schrock, *Organomet.* **1989**, *8*, 2260-2265.
- [7] R. R. Schrock, J. Feldman, L. F. Cannizzo and R. H. Grubbs, *Macromolecules* **1987**, *20*, 1169-1172.

- [8] W. E. Crowe, J. P. Mitchell, V. C. Gibson and R. R. Schrock, *Macromolecules* **1990**, *23*, 3534-3536.
- [9] G. Bazan, R. R. Schrock, E. Khosravi, W. J. Feast and V. C. Gibson, *Polym. Commun.* **1989**, *30*, 258-260.
- [10] G. C. Bazan, E. Khosravi, R. R. Schrock, W. J. Feast, V. C. Gibson, M. B. O'Regan, J. K. Thomas and W. M. Davis, *J. Am. Chem. Soc.* **1990**, *112*, 8378-8387.
- [11] a) T. J. Katz and J. McGinnis, *J. Am. Chem. Soc.* **1975**, *97*, 1592-1594; b) R. Grubbs and W. Tumas, *Science* **1989**, *243*, 907-915.
- [12] a) C. Pariya, K. N. Jayaprakash and A. Sarkar, *Coordin. Chem. Rev.* **1998**, *168*, 1-48; b) X. Wu and M. Tamm, *Beilstein J. Org. Chem.* **2011**, *7*, 82-93; c) M. Green, *Transit. Met. Chem.* **1985**, *10*, 196-200; d) J. A. Tallarico, P. J. Bonitatebus, Jr. and M. L. Snapper, *J. Am. Chem. Soc.* **1997**, *119*, 7157-7158; e) K. Mashima, *Macromol. Symp.* **2000**, *159*, 69-76; f) R. R. Schrock and A. H. Hoveyda, *Angew. Chem., Int. Ed.* **2003**, *42*, 4592-4633.
- [13] a) K. M. Totland, T. J. Boyd, G. G. Lavoie, W. M. Davis and R. R. Schrock, *Macromolecules* **1996**, *29*, 6114-6125; b) D. H. McConville, J. R. Wolf and R. R. Schrock, *J. Am. Chem. Soc.*, **1993**, *115*, 4413-4414.
- [14] M. Cousins and M. L. H. Green, *J. Am. Chem. Soc.* **1963**.
- [15] M. K. Trost and R. G. Bergman, *Organomet.* **1991**, *10*, 1172-1178.
- [16] M. Abrantes, A. M. Santos, J. Mink, F. E. Kühn and C. C. Romão, *Organomet.* **2003**, *22*, 2112-2118.
- [17] a) E. H. Balabolov, S. V. Kotov, T. M. Kolev and M. G. Topuzova, *React. Kinet. Catal. L.* **2009**, *97*, 51-57; b) U. Neuenschwander, E. Meier and I. Hermans, *Chem. Eur. J.* **2012**, *18*, 6776-6780; c) M. Herbert, F. Montilla, E. Alvarez and A. Galindo, *Dalton Trans.* **2012**, *41*, 6942-6956; d) C. Dinoi, R. Poli, L. Perrin and L. Maron, *Dalton Trans.* **2012**, *41*, 1131-1133; e) M. Herbert, E. Alvarez, D. J. Cole-Hamilton, F. Montilla and A. Galindo, *Chem. Commun.* **2010**, *46*, 5933-5935.
- [18] A. Comas-Vives, A. Lledos and R. Poli, *Chem. Eur. J.* **2010**, *16*, 2147-2158.

- [19] a) M. J. Calhorda and P. J. Costa, *Curr. Org. Chem.* **2012**, *16*, 65-72; b) S. Berski, F. R. Sensato, V. Polo, J. Andres and V. S. Safont, *J. Phys. Chem. A* **2011**, *115*, 514-522; c) C. Dinoi, M. Ciclosi, E. Manoury, L. Maron, L. Perrin and R. Poli, *Chem. Eur. J.* **2010**, *16*, 9572-9584; d) B. Griffe, G. Agrifoglio, F. Ruette and J. L. Brito, *Int. J. Quantum. Chem.* **2008**, *108*, 1674-1683; e) I. V. Yudanov, *J. Struct. Chem.* **2007**, *48*, S111-S124.
- [20] a) H. Mimoun, M. Mignard, P. Brechot and L. Saussine, *J. Am. Chem. Soc.* **1986**, *108*, 3711-3718; b) H. Mimoun, I. Seree de Roch and L. Sajus, *Tetrahedron* **1970**, *26*, 37-50.
- [21] Sharples, D. R. Williams and J. M. Townsend, *J. Am. Chem. Soc.* **1972**, *94*, 295.
- [22] a) W. R. Thiel and J. Eppinger, *Chem. Eur. J.* **1997**, *3*, 696-705; b) W. R. Thiel and T. Priermeier, *Angew. Chem. Int. Edit.* **1995**, *34*, 1737-1738.
- [23] S. P. Downing, M. J. Hanton, A. M. Z. Slawin and R. P. Tooze, *Organomet.* **2009**, *28*, 2417-2422.
- [24] J. O. Moulin, *X-Ray Absorption Spectroscopy for the Study of a Homogeneous Catalysis System Based Upon Chromium*, University of Southampton, Southampton, Ph. D., **2006**.
- [25] F. Stoffelbach, D. Saurenz and R. Poli, *Eur. J. Inorg. Chem.* **2001**, 2699-2703.
- [26] a) F. A. Cotton and J. Su, *Inorg. Chim. Acta* **1996**, *251*, 101-104; b) I. Boyd and A. Wedd, *Aust. J. Chem.* **1976**, *29*, 1829-1832.
- [27] B. E. Owens, R. Poli and A. L. Rheingold, *Inorg. Chem.* **1989**, *28*, 1456-1462.
- [28] D. S. McGuinness, P. Wasserscheid, W. Keim, D. Morgan, J. T. Dixon, A. Bollmann, H. Maumela, F. Hess and U. Englert, *J. Am. Chem. Soc.* **2003**, *125*, 5272-5273.
- [29] M. W. Anker, J. Chatt, G. J. Leigh and A. G. Wedd, *Dalton Trans.* **1975**, 2639-2645.
- [30] A. B. P. Lever, *Inorganic Electronic Spectroscopy*, 2nd Edition, Elsevier, The Netherlands, **1984**.

- [31] a) C. D. Beard, L. Carr, M. F. Davis, J. Evans, W. Levason, L. D. Norman, G. Reid and M. Webster, *Eur. J. Inorg. Chem.* **2006**, 4399-4406; b) G. J. Grant, K. E. Rogers, W. N. Setzer and D. G. Vanderveer, *Inorg. Chim. Acta* **1995**, 234, 35-45; c) R. E. Wolf, J. A. R. Hartman, J. M. E. Storey, B. M. Foxman and S. R. Cooper, *J. Am. Chem. Soc.* **1987**, 109, 4328-4335.
- [32] J. O. Moulin, J. Evans, D. S. McGuinness, G. Reid, A. J. Rucklide, R. P. Tooze and M. Tromp, *Dalton Trans.* **2008**, 1177-1185.
- [33] a) C. Temple, A. Jabri, P. Crewdson, S. Gambarotta, I. Korobkov and R. Duchateau, *Angew. Chem. Int. Edit.* **2006**, 45, 7050-7053; b) A. Jabri, C. Temple, P. Crewdson, S. Gambarotta, I. Korobkov and R. Duchateau, *J. Am. Chem. Soc.* **2006**, 128, 9238-9247.
- [34] D. E. Jordan, *Anal. Chem.* **1968**, 40, 2150-2153.
- [35] D. Sellmann and L. Zapf, *J. Organomet. Chem.* **1985**, 289, 57-69.
- [36] H. Flack, *Acta Crystallogr. A* **1983**, 39, 876-881.
- [37] S. Nikitenko, A. M. Beale, A. M. J. van der Eerden, S. D. M. Jacques, O. Leynaud, M. G. O'Brien, D. Detollenaere, R. Kaptein, B. M. Weckhuysen and W. Bras, *J. Synchrotron Radiat.* **2008**, 15, 632-640.
- [38] A. J. Dent, G. Cibin, S. Ramos, A. D. Smith, S. M. Scott, L. Varandas, M. R. Pearson, N. A. Krumpa, C. P. Jones and P. E. Robbins, *J. Phys. Conf. Ser.* **2009**, 190, 012039.
- [39] M. Newville, *J. Synchrotron Radiat.* **2001**, 8, 322-324.
- [40] B. Ravel and M. Newville, *J. Synchrotron Radiat.* **2005**, 12, 537-541.



## **Chapter 5.**

### **Sc(III) Complexes with Neutral N<sub>3</sub>- and SNS-Donor Ligands – A Spectroscopic Study of the Activation of Ethene Polymerisation Catalysts.**

## 5.1 Introduction

### 5.1.1 Sc Complexes for Ethene Polymerisation Catalysis

In the early 1980s, scandium Cp complexes were reported to be active towards Ziegler-Natta type polymerisation of terminal alkynes,<sup>[1]</sup> with polymerisation of alkenes reported some 20 years ago.<sup>[2]</sup> Due in part to the success in Ziegler-Natta ethene polymerisation,<sup>[3]</sup> the cyclopentadienyl (Cp) ligand has dominated much of the organometallic chemistry, in terms of the Group 3 metals.<sup>[4]</sup>

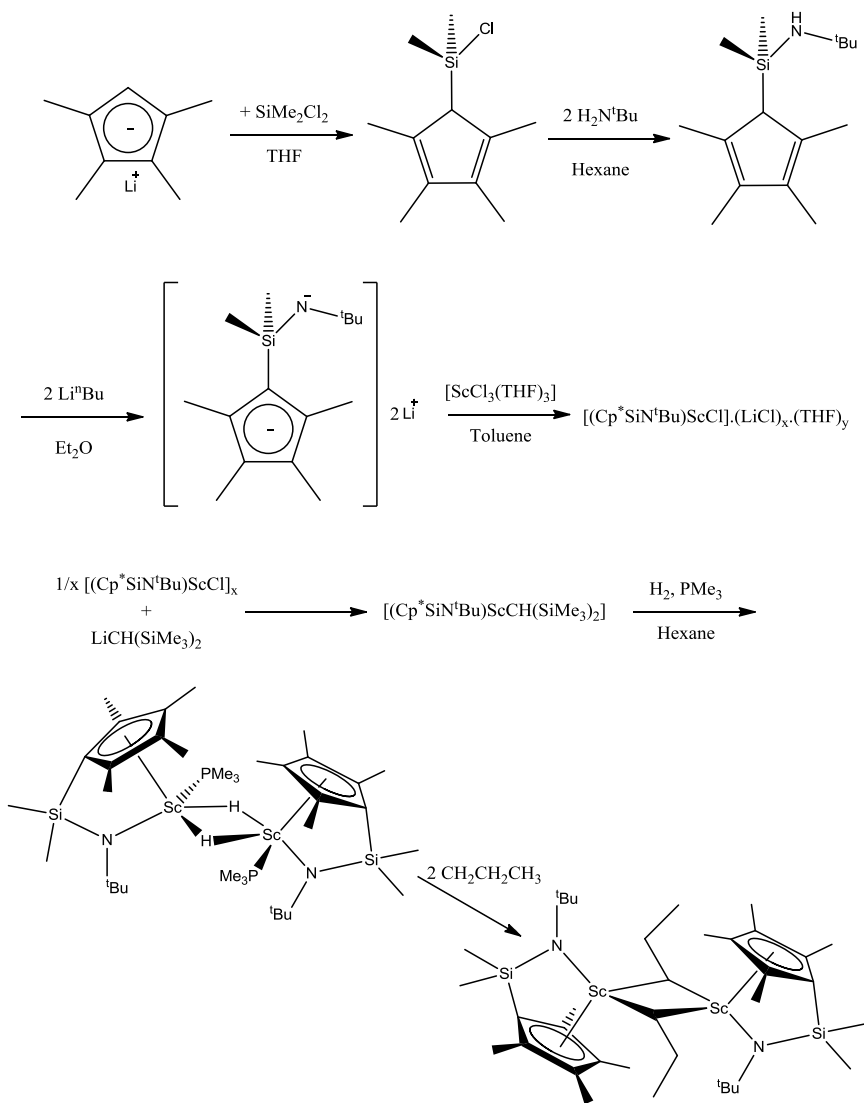
The Ziegler-Natta  $\alpha$ -olefin polymerisation by lanthanides is shown in Scheme 5.1. The olefin is directly inserted into the M-C bond and the polymer is released by  $\beta$ -hydride elimination step to form a metal hydride, where an olefin can insert to regenerate the M-C bond.<sup>[4]</sup> McKinney<sup>[5]</sup> had postulated a chain growth route by formation of a metallocycle for the  $TiCl_4$  catalyst. When considering group 3 elements, oxidative addition to form the metallocycle seems an unreasonable route because of their reluctance of redox chemistry.



### Scheme 5.1 Mechanism of Ziegler-Natta $\alpha$ -olefin polymerisation.

In 1994,<sup>[6]</sup> Bercaw and Shapiro synthesised a scandium metallocene,  $[(Cp^*SiNR)Sc(\mu-CH_2CH_2CH_3)]_2$ , capable of alkene polymerisation, forming poly(1-pentene) ( $M_w \sim 6000$ ) and poly(propylene) ( $M_w \sim 9600$ ) in toluene at 25 °C. The synthesis of the complex is shown in Scheme 5.2. The silyl functionalised cyclopentadiene (Cp) is formed by the addition of  $SiMe_2Cl_2$  to the lithiated  $Li[Cp^*-Me_4H]$  pre-cursor, followed by 2 equivs. of tert-butylamine, giving an 80 % yield of the functionalised Cp ring. This crude product is vacuum distilled and then deprotonated by butyl lithium to give the dilithium salt. Reacting this with the scandium precursor  $[ScCl_3(THF)_3]$ , gives the subsequent scandium complex with variable coordination of THF and LiCl. The THF is considered an impurity as it can block alkylation of Sc-Cl by  $LiCH_2(SiMe_2)_2$ . Therefore, before this alkylation step,

THF is removed by heating at 100 °C for 1 d and LiCl removed by Soxhlet extraction in toluene. Hydrogenation of the alkylated  $[(\text{Cp}^*\text{SiNR})\text{ScCH}(\text{SiMe}_3)_2]$  with clean  $\text{PMe}_3$  yields the hydride isolated at 83 %. The crystal structure shows the bridging hydride dimer, eliminating  $\text{CH}_2(\text{SiMe}_2)_2$ . Reacting the hydride with 1 equiv. propylene per Sc gave the complex  $[(\text{Cp}^*\text{SiNR})\text{Sc}(\mu\text{-CH}_2\text{CH}_2\text{CH}_3)]_2$ , of which a crystal structure was determined.



**Scheme 5.2** Showing method of synthesis towards dimeric scandium metallocene for Ziegler-Natta polymerisation.

From the 90's onwards, Group 3 non-cp based complexes emerged in the context of olefin polymerisation<sup>[7]</sup> Bercaw *et. al.*,<sup>[7d]</sup> synthesised  $[\text{LnCl}_3(\text{Me}_3\text{tacn})]$

and  $[\text{LnMe}_3(\text{Me}_3\text{-tacn})]$  ( $\text{Ln} = \text{Sc}, \text{Y}$ ;  $\text{Me}_3\text{-tacn} = 1,4,7\text{-trimethyl-1,4,7-triazacyclononane}$ ) complexes. The trichloride complexes were synthesised from the corresponding tris(THF) trichloride in MeCN. Although it would seem reasonable that a less donating solvent would be more ideal, it was found that the use of MeCN was essential for high yields. The crystal structure of  $[\text{ScCl}_3(\text{Me}_3\text{-tacn})]$  has previously been determined and its structure is shown in Fig. 5.1.

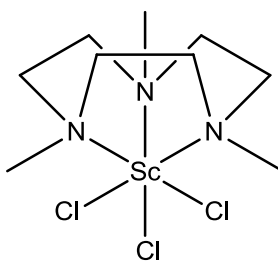


**Fig. 5.1** Displaying structure for  $[\text{ScCl}_3(\text{Me}_3\text{-[9]aneN}_3)]$ .<sup>[7d]</sup>

The two reagents are soluble in MeCN and the complex precipitates from solution, therefore the ligand competes effectively with THF and MeCN. It is perhaps this competition between THF and MeCN which allows the tacn to coordinate more effectively during solvent exchange. Methylation of the tacn complexes yields the corresponding  $[\text{LnMe}_3(\text{Me}_3\text{-tacn})]$  cleanly in THF at ambient conditions.

Activation of  $[\text{ScMe}_3(\text{Me}_3\text{-tacn})]$  with  $[\text{HN}(\text{Me})_2\text{Ph}][\text{B}(\text{C}_6\text{F}_5)_4]$ , gives the exchanged product  $[\text{ScMe}_2(\text{Me}_3\text{-tacn})][\text{B}(\text{C}_6\text{F}_5)_4]$  in  $\text{C}_6\text{D}_6$ . Addition of 1-pentene to the dense orange oil yields a highly viscous solution of oligo(1-pentene) after 2 h at room temperature.

A notable yttrium half sandwich, cp-functionalised complex with  $^{89}\text{Y}$  NMR analysis was published, which also was able to polymerise olefins.<sup>[8]</sup> The synthesis of  $[(\text{Cp}^*\text{Me}_4\text{SiMe}_2\text{NHCMe}_2\text{R})\text{Y}(\text{CH}_2\text{SiMe}_3)(\text{THF})]$  ( $\text{R} = \text{Me}$  or  $\text{Et}$ ) by reaction of  $\text{HCpMe}_4\text{SiMe}_2\text{NHCMe}_2\text{R}$  and  $[\text{Y}(\text{CH}_2\text{SiMe}_3)_3(\text{THF})_2]$  in pentane at  $0^\circ\text{C}$ , leads to the dimeric hydrido complex after hydrogenation (Fig. 5.2). A 1:2:1: triplet at  $50^\circ\text{C}$  in  $^{89}\text{Y}$  NMR spectra ( $I = \frac{1}{2}$ ), with coupling to the bridging hydrogen helped confirm the presence of the dimer in solution. This was also mirrored in the  $^1\text{H}$  NMR spectrum.

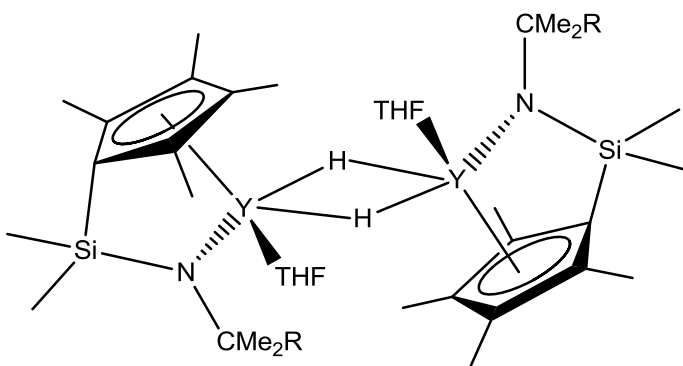
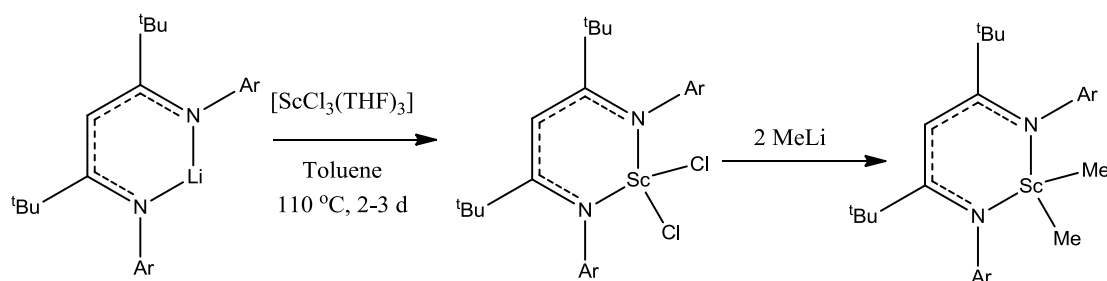


**Fig. 5.2** Dimeric yttrium hydrido complex ( $R = Me, Et$ ).

The hydrido complex was found to polymerise ethene under ambient conditions, at  $0.08 \text{ g mmol Y}^{-1} \text{ h}^{-1} \text{ bar}^{-1}$  and because of the presence of a coordinated THF occupying a free coordination site, a co-catalyst was not required. The strong Y-THF affinity may explain the lower activities observed compared with the corresponding Sc- $\text{PMe}_3$  complexes as observed above (Scheme 5.1).

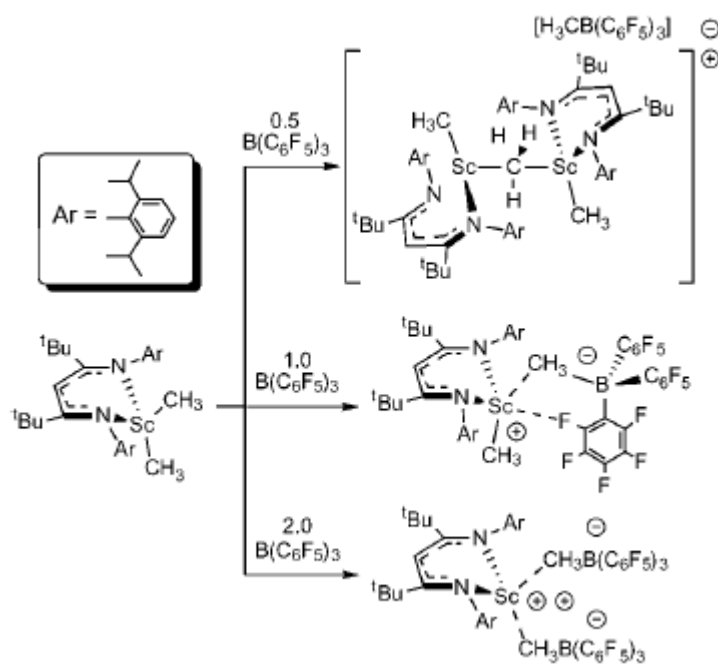
A scandium complex without the coordination of  $\text{Cp}$  was synthesised which gave comparable ethene polymerisation activity to the metallocene derivatives (Scheme 5.3).<sup>[9]</sup> The scandium dichloride  $\beta$ -diketimidato complex serves as a starting material for a variety of similar analogues. Reaction with 2 equivs. of LiMe at room temperature gave the corresponding alkylated catalyst.



**Scheme 5.3** Showing synthesis of methylated scandium  $\beta$ -diketimidato complex.

Scheme 5.4 shows the reaction of the alkylated scandium complex with 0.5, 1 and 2 equivalents of  $B(\text{C}_6\text{F}_5)_3$ , giving different conformations and products.<sup>[10]</sup> These complexes were confirmed by characteristic resonances of the terminal  $\text{Sc}-\text{CH}_3$ . An

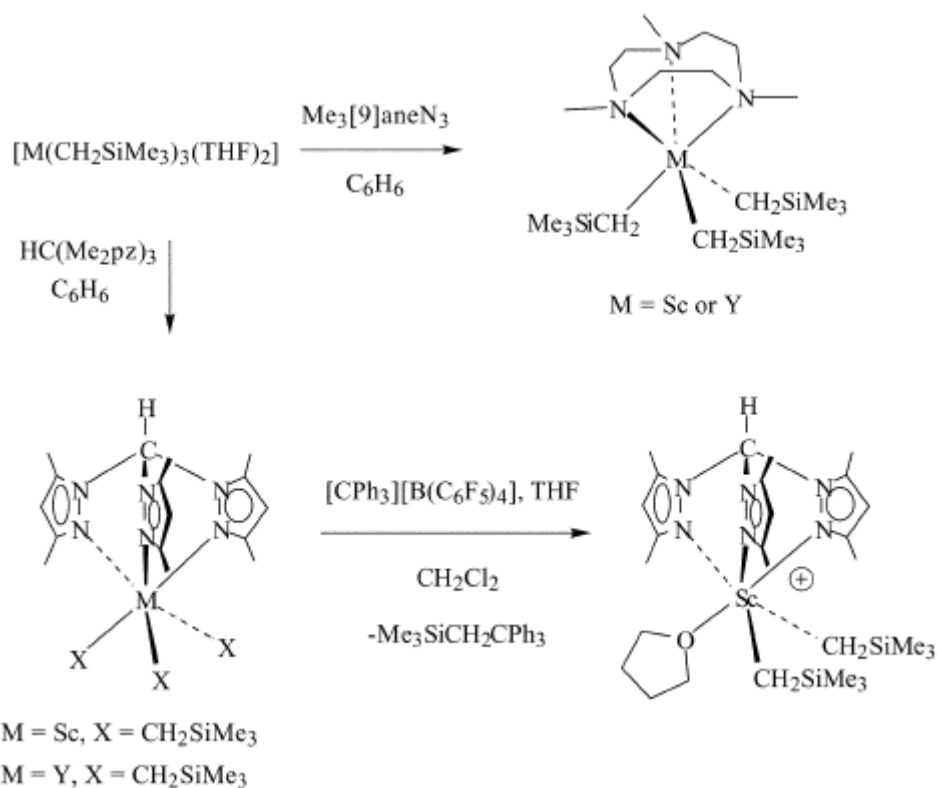
X-ray structure of the product from reaction of the scandium  $\beta$ -diketimido complex with 1 equiv.  $B(C_6F_5)_3$  was also collected. The polymerisation of ethene by the scandium dimethyl  $\beta$ -diketimido complex gave  $1.2 \times 10^6$  g PE mol $^{-1}$  h $^{-1}$ , at 50 °C in cyclohexane / toluene.



**Scheme 5.4** Reaction of scandium dimethyl  $\beta$ -diketimido complex with 0.5, 1 and 2 equivalents of  $B(C_6F_5)_3$ .<sup>[10]</sup>

Developing the Group 3 metal tacn chemistry further, Mountford used modified neutral *fac*-tridentate  $\text{N}_3$ -donor ligands to constrain metal centres, in one case forcing a similar geometry to that of the established titanium polymerisation catalyst,<sup>[7c]</sup> only to give largely inactive mixtures.

Further to this, the reaction of  $[\text{M}(\text{CH}_2\text{SiMe}_3)_3(\text{THF})_2]$  ( $\text{M} = \text{Sc, Y}$ ) with tris(pyrazolyl)methane,  $\text{HC}(\text{Me}_2\text{pz})_3$ , or  $\text{Me}_3\text{-tacn}$  yields the corresponding  $[\text{M}(\text{CH}_2\text{SiMe}_3)(\text{N}_3)]$  complex (Scheme 5.5).<sup>[11]</sup> Further reaction of the  $[\text{Sc}(\text{CH}_2\text{SiMe}_3)(\text{HC}(\text{Me}_2\text{pz})_3)]$  with  $[\text{CPh}_3][\text{B}(C_6F_5)_4]$  gave the cationic scandium(III) complex as shown in Scheme 5.5.

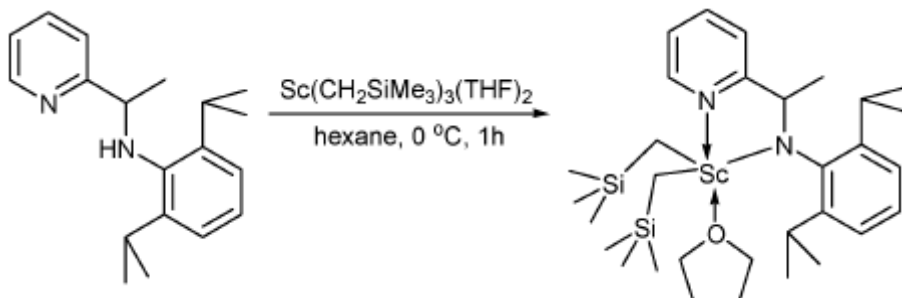


**Scheme 5.5** Synthesis of new  $[M(CH_2SiMe_3)(N_3)]$  type complexes ( $N_3 = HC(Me_2pz)_3$  or [9]aneN<sub>3</sub> ligand).<sup>[11]</sup>

Preliminary tests for the scandium Me<sub>3</sub>-tacn complex with 1 equiv. [CPh<sub>3</sub>][B(C<sub>6</sub>F<sub>5</sub>)<sub>4</sub>] at 25 °C and 5 bar ethene gave 25 g polyethylene over 1 hour. The scandium tris(pyrazolyl)methane complex gave 29 g polyethylene in the same conditions. These are significantly more active than the Bercaw [ScMe<sub>3</sub>(Me<sub>3</sub>-tacn)] complex (as discussed above). It was suggested that the Me group could facilitate bridging between Sc complexes, therefore deactivating the catalysts. Also the introduction of the –CH<sub>2</sub>SiMe<sub>3</sub> ligand, providing a relatively more stabilised cationic scandium centre by agostic interaction of β-Si-C on the alkyl ligand during initiation and/or propagation.<sup>[11]</sup>

The yttrium(III) complex,  $[Y(CH_2SiMe_3)_2(Me_2-tacn-(CH_2)_2-N^tBu)]$ , gave high molecular weight polyethylene upon activation with  $[HN(CH_3)_2Ph][B(C_6F_5)_4]$ .<sup>[12]</sup> In many cases yttrium outperforms scandium as a polymerisation catalyst and this is thought to be dictated by the difference in ionic radius and catalyst activity continues to vary down the group.<sup>[13]</sup>

Since incorporation of  $-\text{CH}_2\text{SiMe}_3$  groups at the Sc(III) site, focus has shifted to neutral and cationic complexes with these alkyl ligands.<sup>[14]</sup> Scheme 5.6 shows the synthesis of a bis(alkyl) 2-pyridinemethanamido complex.<sup>[14a]</sup>



**Scheme 5.6** Synthesis of scandium bis(alkyl) 2-pyridinemethanamido complex.<sup>[14a]</sup>

This complex was confirmed by X-ray crystallography and NMR spectroscopy. It was active towards ethene polymerisation in toluene with 1 equiv.  $[\text{CPh}_3][\text{B}(\text{C}_6\text{F}_5)_4]$  and 10 equivs.  $\text{Al}^t\text{Bu}_3$  at  $60^\circ\text{C}$  and 1 bar ethene. This catalyst gave an activity of  $3.2 \times 10^5 \text{ g PE mol}^{-1} \text{ h}^{-1} \text{ bar}^{-1}$  for a 5 min run, producing 0.27 g. A rare example of a Sc-S complex,  $[\text{Sc}(1,4,7\text{-trithiacyclononane})(\text{CH}_2\text{SiMe}_3)_3]$ ,<sup>[15]</sup> gave 11.4 g polyethylene after 1 h (toluene, 1 equiv.  $[\text{CPh}_3][\text{B}(\text{C}_6\text{F}_5)_4]$ , 250 equivs.  $\text{Al}^t\text{Bu}_3$ , 5 bar ethene). Yet this is still not as active as the tacn derivative.<sup>[16]</sup>

### 5.1.2 $^{45}\text{Sc}$ NMR Spectroscopy

Scandium-45 ( $I = 7/2$ , 100% abundant) is a sensitive NMR nucleus in terms of relative intensity to  $^1\text{H}$  NMR nucleus ( $D_c = 1780$ ).  $^{45}\text{Sc}$  has also has a significant quadrupole moment ( $Q = -0.22 \times 10^{-28} \text{ m}^2$ ) which can significantly increase line widths.<sup>[17]</sup>  $^{45}\text{Sc}$  NMR spectra can provide very useful data regarding the solution speciation. Since  $^{45}\text{Sc}$  NMR was developed,<sup>[18]</sup> one early study focused on  $\text{ScCl}_3$  and its coordination in solution with competing MeCN and  $[\text{K}][\text{NCS}]$ .<sup>[19]</sup> It found Sc(III) always took up a octahedral coordination. There was a possibility of 28 different complexes with different stoichiometries of competing  $\text{Cl}^-$ ,  $\text{SCN}^-$  and MeCN. It suggested the chemical shift was linearly dependant on the number of  $\text{Cl}^-$  or  $\text{SCN}^-$  ions coordinated to the scandium. A later study in 2003 agreed with the sensitive

nature of the  $^{45}\text{Sc}$  nucleus in terms of its chemical shift, where a  $^{45}\text{Sc}$  NMR study of  $\text{ScCl}_3$  and crown ethers demonstrated that the  $^{45}\text{Sc}$  chemical shift displays an ‘additive’ effect in terms of chloride incorporation.<sup>[15]</sup>  $[\text{ScCl}_2(18\text{-crown-6})][\text{FeCl}_4]$  ( $\delta(^{45}\text{Sc}) = 132$  ppm) with progressive addition of  $\text{FeCl}_3$  gave the mono chloride  $[\text{ScCl}(18\text{-crown-6})]^{2+}$  ( $\delta(^{45}\text{Sc}) = 101$  ppm) through to  $[\text{Sc}(18\text{-crown-6})]^{3+}$  ( $\delta(^{45}\text{Sc}) = -2$  ppm). A similar pattern was observed when using antimony chloride as a Lewis acid. In this same study, the thia-oxa crown [15]aneS<sub>2</sub>O<sub>3</sub> was reacted with  $[\text{ScCl}_3(\text{THF})_3]$  in MeCN to give the  $[\text{ScCl}_2([15]\text{aneS}_2\text{O}_3)]$  complex.  $^1\text{H}$  NMR data of the CH<sub>2</sub>S and CH<sub>2</sub>O resonances gave multiplets at 3.35-3.70 ppm. The uncoordinated thio ether macrocycle gave 2.72(t) and 2.87(t). Therefore a higher frequency shift is observed upon coordination of the thio ether. This also corresponds to  $^{45}\text{Sc}$  NMR chemical shift of 200 ppm, higher frequency to the purely oxygen containing crown ethers. These higher frequency shifts agree with the  $^1\text{H}$  and  $^{45}\text{Sc}$  NMR data discussed in this chapter.

In 2000, a  $^{45}\text{Sc}$  NMR study of scandium nitrate and its coordination to phosphine oxides demonstrated the sensitivity of the  $^{45}\text{Sc}$  NMR nucleus as influenced by the ligands coordinated.<sup>[20]</sup> The complexes  $[\text{Sc}(\text{Ph}_3\text{PO})_3(\text{NO}_3)_3]$  ( $\delta(^{45}\text{Sc}) = -7.5$  ppm) and  $[\text{Sc}(\text{Ph}_2\text{MePO})_3(\text{NO}_3)_3]$  ( $\delta(^{45}\text{Sc}) = -4.0$  ppm) show a shift of 3.5 ppm for only a change of one R group, two bonds away from the Sc nucleus. In only one case was a P-Sc splitting pattern observed in the  $^{31}\text{P}$  NMR, giving an 8 line splitting pattern for  $[\text{Sc}(\text{Me}_3\text{PO})_6]^{3+}$ . This complex is highly symmetrical ( $\text{O}_h$  symmetry) giving an EFG of effectively zero with slow quadrupolar relaxation, therefore this splitting would be expected, yet no splitting was observed in the  $^{45}\text{Sc}$  NMR spectrum.

From these relatively few investigations,  $^{45}\text{Sc}$  NMR has played a crucial role and proven to be a highly sensitive nucleus helping to understand the coordination chemistry. Therefore, it is likely it could provide a useful complementary technique alongside the XAFS studies to aid elucidation of the reaction products and possible catalytic intermediates of this study.

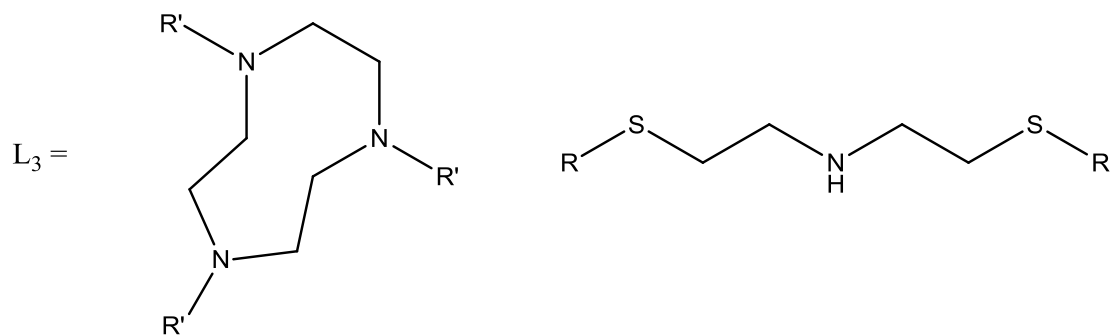
## 5.2 Aims

This aim of this study was to synthesise and characterise scandium trichloride complexes with tridentate N<sub>3</sub>- and S<sub>2</sub>N-donor ligands (L<sub>3</sub>) and, due to the diamagnetic nature of these complexes, this allows multinuclear NMR to be combined with XAFS

to help provide a high level of characterisation of the species in solution. Catalytic testing of a subset of these complexes with ethene was also undertaken in chlorobenzene. The reactions of these complexes with MeLi and AlMe<sub>3</sub> are studied by <sup>1</sup>H, <sup>13</sup>C{<sup>1</sup>H}, <sup>27</sup>Al and <sup>45</sup>Sc NMR spectroscopy and *in situ* via Sc K-edge XAFS spectroscopy. Reacting MeLi with [ScCl<sub>3</sub>(R-tacn)] and [ScCl<sub>3</sub>(R-SNS)] type complexes is studied in order to help probe the mechanism of alkylation by AlMe<sub>3</sub>. Investigations of *in situ* <sup>45</sup>Sc NMR and Sc K-edge XAFS spectroscopic studies of these scandium complexes with 10 mol. equivs. of AlMe<sub>3</sub> were undertaken to find how these complexes are activated for ethene polymerisation by AlMe<sub>3</sub>. It is hoped the chemistry of this scandium system may inform the chromium oligomerisation system for the mechanism of AlMe<sub>3</sub> reactions and the chemistry of the SNS type ligand.

### 5.3 Results and Discussion

Two sets of [ScCl<sub>3</sub>(L<sub>3</sub>)] type complexes with N<sub>3</sub> and S<sub>2</sub>N donor sets have been synthesised *via* the scandium precursor [ScCl<sub>3</sub>(THF)<sub>3</sub>] (Scheme 5.7). In a typical experiment the [ScCl<sub>3</sub>(THF)<sub>3</sub>] was dissolved in anhydrous MeCN, and after a few minutes stirring at room temperature, all volatiles were removed *in vacuo*. The resulting solid was then reacted with the ligand of choice in CH<sub>2</sub>Cl<sub>2</sub> or MeCN as described in the Experimental Section, to give the neutral products as powdered white (R<sub>3</sub>-tacn) or yellow (R-SNS) solids. The resulting complexes were characterised by IR, <sup>1</sup>H, <sup>13</sup>C{<sup>1</sup>H} and <sup>45</sup>Sc NMR spectroscopy and microanalysis.



**Scheme 5.7** General reaction scheme for the synthesis of scandium catalysts ( $R = ^t\text{Bu}$ , decyl;  $R' = \text{Me}$ , decyl).

### 5.3.1 Investigation of $R_3$ -tacn Complexes by Multinuclear NMR

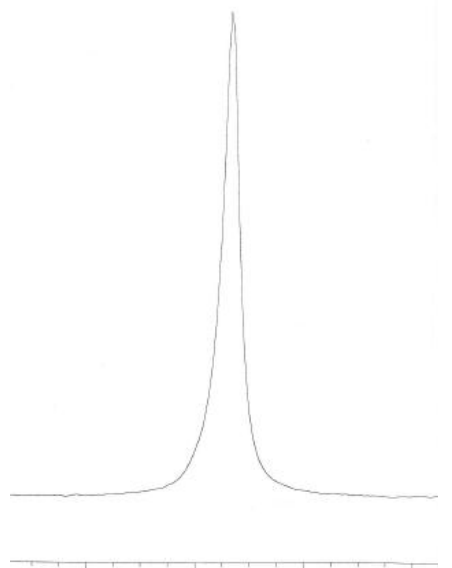
The preparation of  $[\text{ScCl}_3(\text{Me}_3\text{-tacn})]$  ( $\text{Me}_3\text{-tacn} = 1,4,7\text{-trimethyl-1,4,7-triazacyclononane}$ ) has been previously reported and the crystal structure is shown in Fig. 5.1, giving Sc-N bond distances as 2.34, 2.34 and 2.32 Å and Sc-Cl distances as 2.41, 2.41 and 2.40 Å.<sup>[7d]</sup> The  $^1\text{H}$  and  $^{13}\text{C}\{^1\text{H}\}$  NMR data of this complex agree well with that synthesised here, along with a unit cell of  $[\text{ScCl}_3(\text{Me}_3\text{-tacn})]$  that was collected. In addition, the far IR spectrum of the complex shows two peaks at 352 and 322 cm<sup>-1</sup> attributed to the  $A_1$  and E vibrational modes associated with  $\nu(\text{Sc-Cl})$  in a  $C_{3v}$  geometry. Similarly, the  $[\text{ScCl}_3(\text{decyl}_3\text{-tacn})]$  ( $\text{decyl}_3\text{-tacn} = 1,4,7\text{-tridecyl-1,4,7-triazacyclononane}$ ) was prepared and isolated as a light brown solid. The  $^1\text{H}$  and  $^{13}\text{C}\{^1\text{H}\}$  spectroscopic features are consistent with this formulation. A single broad  $\nu(\text{Sc-Cl})$  at 302 cm<sup>-1</sup> is observed in the IR spectrum; there is no evidence for water or residual THF in the spectra.

The  $^{45}\text{Sc}$  NMR data for the complexes studied in this work are presented in Table 5.1. The spectrum of  $[\text{ScCl}_3(\text{Me}_3\text{-tacn})]$  (in  $\text{CH}_2\text{Cl}_2$ ) exhibits a very sharp singlet ( $w_{1/2} \sim 20$  Hz) at 304 ppm (Fig. 5.3). The very narrow line width is a consequence of the molecular  $C_{3v}$  geometry, with the EFG being close to zero.<sup>[21]</sup> As expected, the chemical shift varies by a few ppm with solvent, but it seems clear that the  $\text{N}_3\text{Cl}_3$  donor set is retained in anhydrous  $\text{CH}_2\text{Cl}_2$ , THF, chlorobenzene and MeCN.

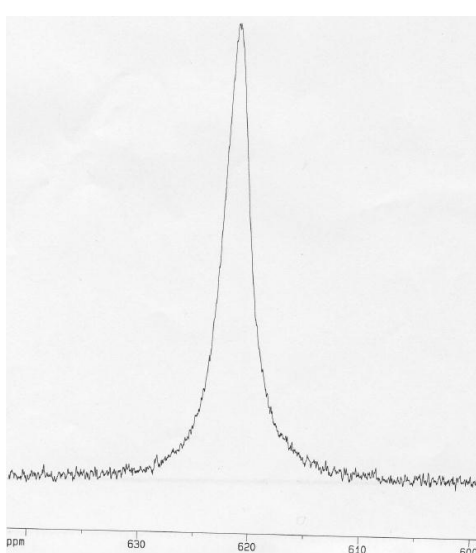
**Table 5.1**  $^{45}\text{Sc}$  NMR solution data for  $[\text{ScCl}_3(\text{R}_3\text{-tacn})]$  before and after addition of metal methyl reagents.<sup>a</sup>

Complex	Solvent and reagents	$\delta$ / ppm	$w_{1/2}$ / Hz
$[\text{ScCl}_3(\text{Me}_3\text{-tacn})]^b$	MeCN	298	20
	THF	306	20
	$\text{CH}_2\text{Cl}_2$	304	20
	PhCl	307	20
	toluene + 3.5 equiv MeLi	626	520
	PhCl + 10 equiv. AlMe <sub>3</sub>	301	250
$[\text{ScCl}_3(\text{decyl}_3\text{-tacn})]$	$\text{CH}_2\text{Cl}_2$	252	200
	toluene	227	3300
	THF	228	1400

<sup>a</sup>  $^{45}\text{Sc}$  NMR spectra recorded at 298 K, 97.17 MHz; <sup>b</sup> insoluble in toluene.



(A)



(B)

**Fig. 5.3** Displaying <sup>45</sup>Sc NMR spectra for (A) [ScCl<sub>3</sub>(Me<sub>3</sub>-tacn)] in (CH<sub>2</sub>Cl<sub>2</sub>/CDCl<sub>3</sub>) and (B) [ScMe<sub>3</sub>(Me<sub>3</sub>-tacn)] in Tol-D<sub>8</sub>.

The <sup>45</sup>Sc NMR spectrum of [ScCl<sub>3</sub>(decyl<sub>3</sub>-tacn)] varies more significantly with solvent from 252 ppm in CH<sub>2</sub>Cl<sub>2</sub> to 227 ppm in toluene, and occurs to low frequency of that for [ScCl<sub>3</sub>(Me<sub>3</sub>-tacn)]. The line-width is also highly dependent upon the solvent, varying from ~200 Hz in CH<sub>2</sub>Cl<sub>2</sub> to ~3300 Hz in toluene. Previous <sup>45</sup>Sc NMR studies on a series of Sc(III) phosphine oxide (OPR<sub>3</sub>) complexes showed that changes

in the R groups (Me *vs.* Ph, *etc.*) also lead to significant differences in  $\delta(^{45}\text{Sc})$ , e.g.  $[\text{ScCl}_2(\text{OPPh}_3)_4]^+$   $\delta(^{45}\text{Sc}) = 75$ ,  $[\text{ScCl}_2(\text{OPMe}_3)_4]^+$   $\delta(^{45}\text{Sc}) = 85$ .<sup>[20, 22]</sup> The large variation in line-width observed for  $[\text{ScCl}_3(\text{decyl}_3\text{-tacn})]$  is most likely due to the presence of the conformationally flexible *n*-decyl chains which interact differently with the solvent, depending upon its polarity, thus influencing the EFG. Since  $[\text{ScCl}_3(\text{Me}_3\text{-tacn})]$  is insoluble in toluene, direct comparison in this solvent is not possible.

### 5.3.1.1 Reaction of R<sub>3</sub>-tacn Complexes with MeLi

The reaction of  $[\text{ScCl}_3(\text{Me}_3\text{-tacn})]$  with MeLi was performed to provide a well-defined model system for the  $^{45}\text{Sc}$  NMR and Sc K-edge XAFS analysis, and as a comparison for the reactions with AlMe<sub>3</sub> (Table 5.2). Reaction of  $[\text{ScCl}_3(\text{Me}_3\text{-tacn})]$  with 3.5 mol. equivs. of MeLi in THF solution produces a yellow solution of  $[\text{ScMe}_3(\text{Me}_3\text{-tacn})]$ , with precipitation of LiCl. After removal of the volatiles *in vacuo*, the yellow complex was extracted into toluene-d<sup>8</sup> for NMR spectroscopic analysis. The <sup>1</sup>H and <sup>13</sup>C{<sup>1</sup>H} NMR spectra were in accordance with the published data (Fig. 5.4) reported by Bercaw and co-workers.<sup>[7d]</sup> In addition,  $^{45}\text{Sc}$  NMR spectroscopy showed complete disappearance of the original resonance associated with the  $[\text{ScCl}_3(\text{Me}_3\text{-tacn})]$ , which was replaced with a single new resonance at 626 ppm which was significantly broadened ( $w_{1/2} \sim 520$  Hz). (Table 5.1, Fig. 5.3). The observation of the  $^{45}\text{Sc}$  resonance is a strong indication that substitution is complete to the  $[\text{ScMe}_3(\text{Me}_3\text{-tacn})]$  complex, retaining the C<sub>3v</sub> point group symmetry, although lower symmetries are expected to have a significantly larger EFG and hence are unlikely to be observed.<sup>[21]</sup> Similar reaction of  $[\text{ScCl}_3(\text{decyl}_3\text{-tacn})]$  with 3.5 mol. equivs. of MeLi in toluene causes precipitation of LiCl, and the  $^{45}\text{Sc}$  NMR spectrum of the resulting orange solution showed complete loss of the original resonance associated with the  $[\text{ScCl}_3(\text{decyl}_3\text{-tacn})]$ . No new resonance was evident; this is most likely due to very fast quadrupolar relaxation. Due to the significant broadening of the <sup>1</sup>H and <sup>13</sup>C{<sup>1</sup>H} NMR spectra, reliable NMR data was not obtained for  $[\text{ScCl}_3(\text{decyl}_3\text{-tacn})]$  following the *in situ* reaction with MeLi.

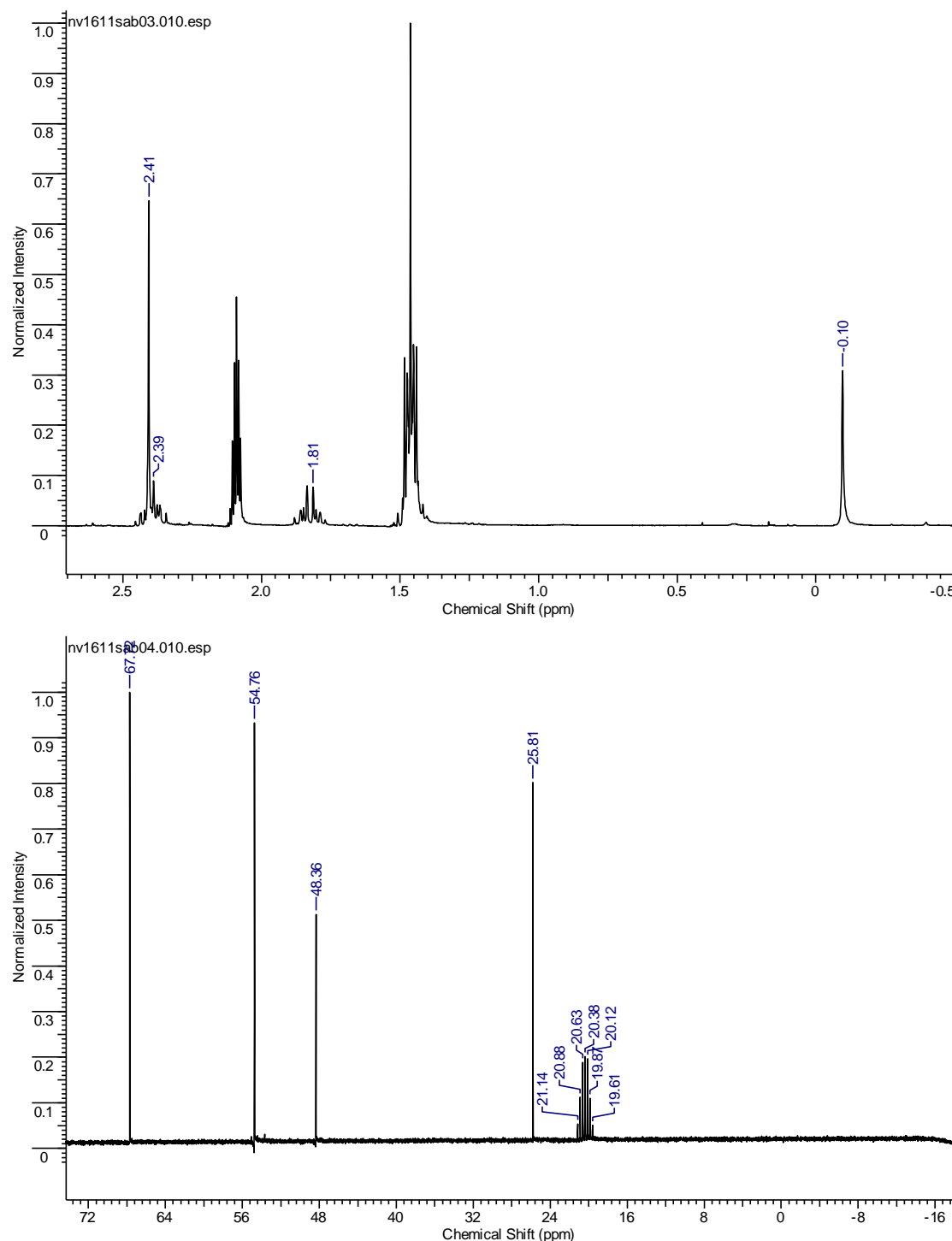


**Fig. 5.4** Displaying  $^1\text{H}$  (above) and  $^{13}\text{C}\{\text{H}\}$  (below) NMR spectra for  $[\text{ScMe}_3(\text{Me}_3\text{-tacn})]$  in  $\text{Tol-D}_8$ .

### 5.3.1.2 Reaction R<sub>3</sub>-tacn Complexes with AlMe<sub>3</sub>

The reaction of [ScCl<sub>3</sub>(Me<sub>3</sub>-tacn)] with 10 mol. equivs. of AlMe<sub>3</sub> in chlorobenzene was also monitored *in situ* by multinuclear NMR spectroscopy. The <sup>1</sup>H and <sup>13</sup>C{<sup>1</sup>H} NMR spectra showed little change from the [ScCl<sub>3</sub>(Me<sub>3</sub>-tacn)], however the <sup>45</sup>Sc NMR spectrum (d<sup>8</sup>-toluene) displayed a single resonance at 301 ppm; a very similar chemical shift to the starting material (extremely sharp singlet at 307 ppm in chlorobenzene), although this resonance is significantly broadened in the presence of AlMe<sub>3</sub> ( $w_{1/2} \sim 250$  Hz). These observations are tentatively attributed to the retention of the N<sub>3</sub>Cl<sub>3</sub> donor set at Sc(III), but with the broadening indicating a change in the secondary coordination (solvation), which could also be due to the presence of Sc-Cl-Al bridge(s).

Monitoring the reaction of [ScCl<sub>3</sub>(Me<sub>3</sub>-tacn)] with 10 mol. equivs. of AlMe<sub>3</sub> in chlorobenzene by <sup>27</sup>Al NMR (<sup>27</sup>Al: I= 5/2, D<sub>C</sub> = 0.207, Q = 0.1466 × 10<sup>-28</sup> m<sup>2</sup>)<sup>[17]</sup> (Table 5.2) showed a negligible change in the chemical shift of AlMe<sub>3</sub> itself in chlorobenzene (152 ppm,  $w_{1/2} \sim 1350$  ppm). This was expected since it is a labile system and present in an excess. However, the <sup>27</sup>Al NMR resonance is significantly broadened ( $w_{1/2} \sim 1800$  Hz). There is no evidence for any other aluminium species being formed. This too is consistent with the AlMe<sub>3</sub> not undergoing any major change, but the increased line broadening suggests the AlMe<sub>3</sub> experiences some secondary solvation or other interaction if the AlMe<sub>3</sub> forms bridging interactions with the Sc complexes *via* the Cl ligands in a rapidly exchanging system (Fig. 5.5).

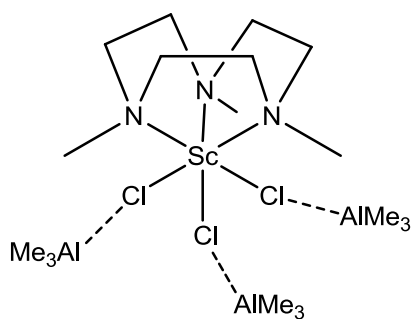


**Fig. 5.5** Proposed complex formed with [ScCl<sub>3</sub>(Me<sub>3</sub>-tacn)] + 10 AlMe<sub>3</sub> in toluene.

**Table 5.2**  $^{27}\text{Al}$  NMR solution data for  $[\text{ScCl}_3(\text{L}_3)] + 10 \text{ AlMe}_3$ .<sup>a</sup>

Compound/reaction	Solvent	$\delta / \text{ppm}$	$w_{1/2} / \text{Hz}$
$\text{AlMe}_3$	Toluene	152	1150
	PhCl	153	1350
$[\text{Ph}_3\text{C}][\text{Al}\{\text{OC}(\text{CF}_3)_3\}_4]$	toluene	35	10
	$\text{CH}_2\text{Cl}_2$	34	10
$[\text{ScCl}_3(\text{Me}_3\text{-tacn})] + 10 \text{ AlMe}_3$	PhCl	156	1800
$[\text{ScCl}_3(\text{decyl-SNS})] + 10 \text{ AlMe}_3$	Toluene	155	3200
$[\text{ScCl}_3(\text{decyl-SNS})] + 10 \text{ AlMe}_3 + 1$ $[\text{Ph}_3\text{C}][\text{Al}\{\text{OC}(\text{CF}_3)_3\}_4]$	Toluene	159 35	4300 10

<sup>a</sup>  $^{27}\text{Al}$  NMR spectra (104.23 MHz) recorded at 298 K.

### 5.3.2 Investigation of R-SNS Complexes by Multinuclear NMR

New  $[\text{ScCl}_3(\text{R-SNS})]$  complexes have been synthesised and characterised by IR and multinuclear ( $^1\text{H}$ ,  $^{13}\text{C}\{^1\text{H}\}$  and  $^{45}\text{Sc}$ ) NMR and microanalysis (Fig. 5.5). The IR of all complexes show a broad  $\nu(\text{N-H})$  peak at  $\sim 3050 \text{ cm}^{-1}$ , some  $250 \text{ cm}^{-1}$  to low frequency of the parent R-SNS ligands, and consistent with N-coordination, as well as peaks in the range  $\sim 300$  to  $350 \text{ cm}^{-1}$ , assigned to  $\nu(\text{Sc-Cl})$ . Unlike the  $\text{R}_3\text{-tacn}$  ligands which, when tridentate, can only form the *fac*-isomer, the acyclic R-SNS can in principle give *mer* or *fac* isomers in an octahedral metal complex, although crystallographic data on complexes of this ligand type with other metal ions, including the d<sup>3</sup> Cr(III) and Mo(III), always reveal the *mer* isomer in the solid state.<sup>[22a, 23]</sup> The hydrogens on the ligand in  $^1\text{H}$  NMR spectra for  $[\text{ScCl}_3(\text{R-SNS})]$  show the resonances have shifted to higher frequency compared to those of the uncoordinated ligand, and also broadened due to the  $^{45}\text{Sc}$  quadrupole, consistent with coordination to Sc. There is no evidence for residual THF or MeCN, and the NH proton appears as a broad resonance at  $\sim 8.5 \text{ ppm}$  in both complexes. NMR data for the complex  $[\text{ScCl}_3(^t\text{Bu-SNS})]$  is presented in Fig. 5.6.

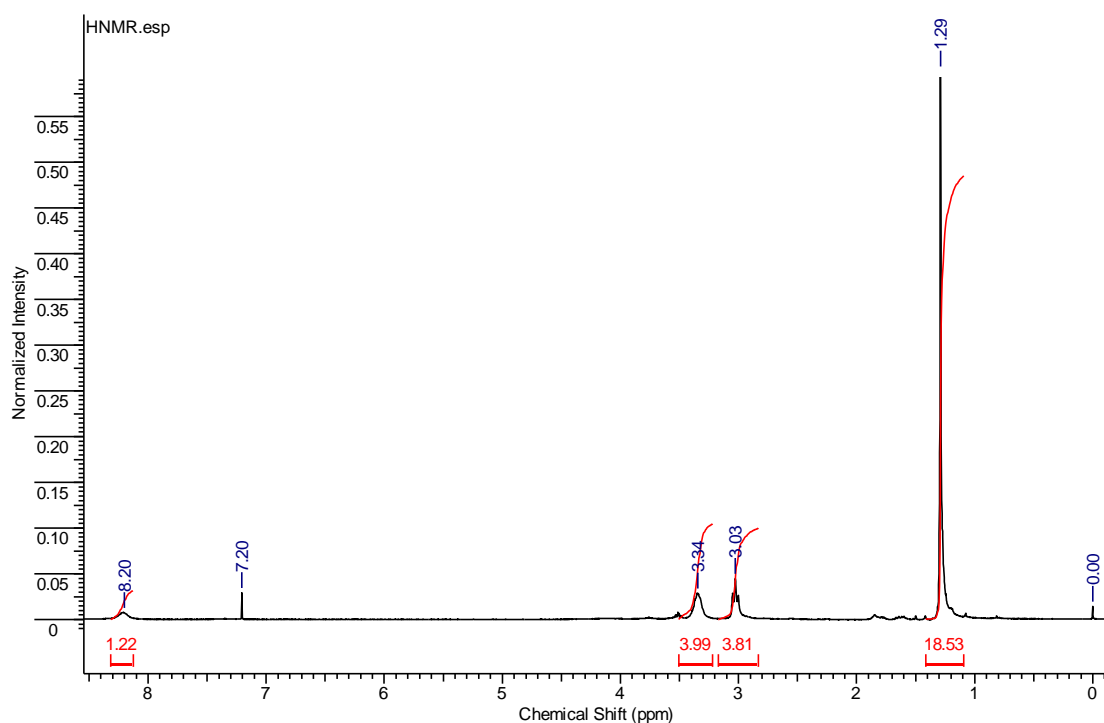
$^{45}\text{Sc}$  NMR studies on analytically pure samples of  $[\text{ScCl}_3(\text{R-SNS})]$  (R = decyl,  $^t\text{Bu}$ ) in  $\text{CH}_2\text{Cl}_2$  solution each reveal two broad resonances around  $\delta$  235 and 260, the

higher frequency resonance is usually the major species (~1:2 or 1:3), which were little affected across the temperature range 298 to 348 K. This behaviour is tentatively attributed to the presence of *mer* and *fac* isomers in the polar CH<sub>2</sub>Cl<sub>2</sub> solvent indicating less preference for the *mer* isomer in these d<sup>0</sup> complexes. The <sup>45</sup>Sc NMR spectra of [ScCl<sub>3</sub>(decyl-SNS)] gives similar <sup>45</sup>Sc NMR resonances to those of the <sup>t</sup>Bu analogue in all the solvents investigated (Table 5.3).

**Table 5.3** <sup>45</sup>Sc NMR solution data for [ScCl<sub>3</sub>(R-SNS)] before and after addition of metal methyls.<sup>a</sup>

Complex	Solvent and reagents	$\delta$ / ppm	w <sub>1/2</sub> / Hz
[ScCl <sub>3</sub> ( <sup>t</sup> Bu-SNS)]	Toluene	261, 230 (2:1)	~1200, ~1100
	CH <sub>2</sub> Cl <sub>2</sub>	260, 227 (3:1)	260, 200
	toluene + 3 equ. MeLi	560, 370 (3:1)	3000, 1300
	toluene + 4 equ. MeLi	370	2500
	toluene + 4 equ. MeLi <sup>b</sup>	560	3750
[ScCl <sub>3</sub> (decyl-SNS)]	Toluene	263, 226 (2:1)	~2500, ~2200
	CH <sub>2</sub> Cl <sub>2</sub>	261, 223 (3:1)	780, 750

<sup>a</sup> <sup>45</sup>Sc NMR spectra recorded at 298 K, 97.17 MHz, <sup>b</sup> MeLi added at -78 °C.



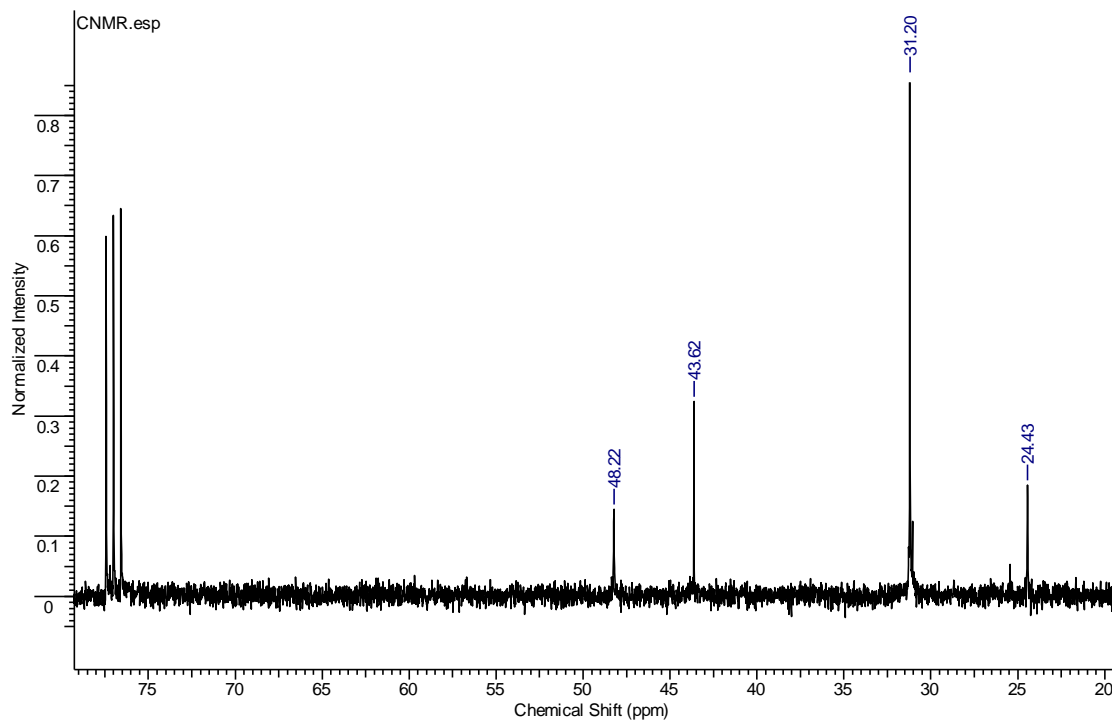


**Fig. 5.6** Displaying  $^1\text{H}$  (Top) and  $^{13}\text{C}\{^1\text{H}\}$  NMR spectra (bottom) for  $[\text{ScCl}_3(\text{tBu-SNS})]$  in  $\text{CDCl}_3$ .

### 5.3.2.1 Reactions R-SNS Complexes with MeLi

In the case of  $[\text{ScCl}_3(\text{tBu-SNS})]$ , upon reaction with 3 or 4 mol. equivs. of MeLi at room temperature, two new  $^{45}\text{Sc}$  resonances were observed at varying ratios, shifted downfield with significant broadening to  $\delta \sim 370$  and  $\sim 560$  ppm.  $^1\text{H}$  and  $^{13}\text{C}\{^1\text{H}\}$  NMR spectra and EXAFS data (below) suggest alkylation at the scandium had occurred with significant changes in chemical shifts from the starting material; also, there is the appearance of new Me resonance at  $\delta -0.5$  in the  $^1\text{H}$  NMR spectrum. Repeating the reaction using 4 mol. equivs. of MeLi at  $-78^\circ\text{C}$  leads to one new resonance in the  $^{45}\text{Sc}$  NMR spectrum at  $\delta \sim 560$  ppm (and complete loss of the original resonance associated with the trichloro precursor complex), with similar, but much cleaner  $^1\text{H}$  and  $^{13}\text{C}\{^1\text{H}\}$  NMR spectra (Figs. 5.6). In the  $^{13}\text{C}\{^1\text{H}\}$  NMR spectrum, the  $\text{CH}_2\text{N}$  resonance from the coordinated ligand is shifted to high frequency more significantly relative to that of the other carbon resonances in the ligand, consistent

with deprotonation of the secondary amine. In addition, the  $\text{CH}_2\text{S}$  resonance is closer to that of the uncoordinated ligand.

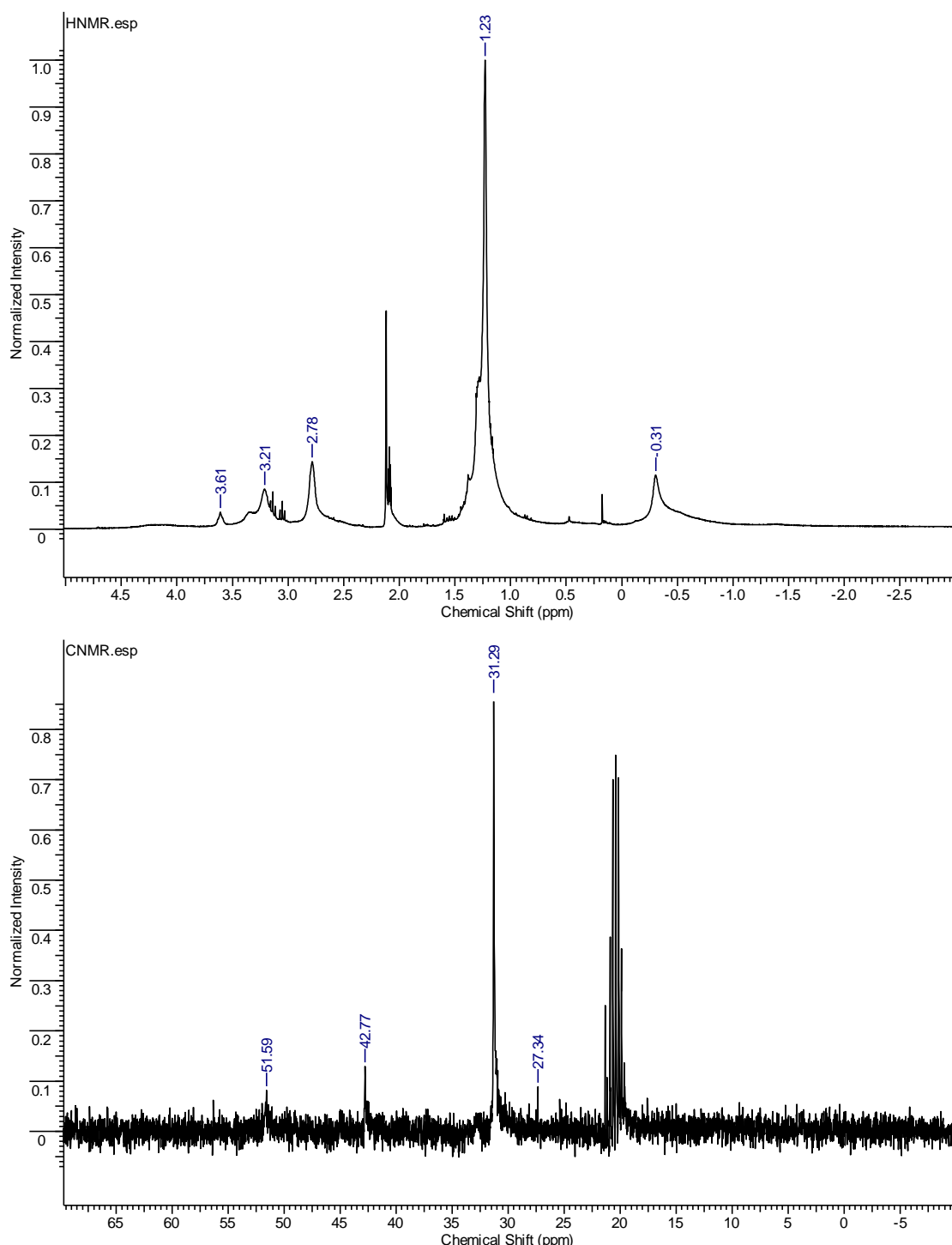


**Fig. 5.7** Displaying  $^1\text{H}$  (top) and  $^{13}\text{C}\{\text{H}\}$  (bottom) NMR for  $[\text{ScCl}_3(\text{tBu-SNS})] + 4 \text{ MeLi}$  in  $\text{Tol-D}_8$  (reacted at  $-78^\circ\text{C}$ , measured at room temperature).

Considering Sc(III) is the only stable oxidation state ( $d^0$ ), deprotonation of the secondary amine function in the  $^t\text{Bu-SNS}$  ligand would not lead to a change of oxidation state (contrasting with the analogous Cr(III)-(R-SNS) systems<sup>[24]</sup>). More likely it could cause a structural change from a six- to five-coordinate species. There is literature precedent for this using similar tridentate  $\text{Li-N}[2\text{-P}(\text{CHMe}_2)_2\text{-4-methylphenyl}]_2$  or  $\text{Li-N}(\text{Si}(\text{Me}_2)\text{CH}_2\text{P}(\text{iPr})_2)_2$  ( $\text{P}_2\text{N}$ ) ligand.<sup>[25]</sup> In these instances the ligand is deprotonated beforehand using  $^n\text{BuLi}$ , then coordinated to  $[\text{ScCl}_3(\text{THF})_3]$  to give the five-coordinate  $[\text{ScCl}_2(\text{P}_2\text{N})]$  complex (Fig. 5.7). This was then reacted with alkyl lithium reagents to give complexes of the type  $[\text{ScR}_2(\text{P}_2\text{N})]$ , which were also characterised crystallographically. In light of these studies, the same procedure was followed with the  $\text{Li}[\text{Et-SNS}]$  ligand,<sup>[26]</sup> where the ligand was deprotonated beforehand using  $^n\text{BuLi}$ , then reacted with  $[\text{ScCl}_3(\text{THF})_3]$  in toluene at 70 °C for 1 day to give the five-coordinate  $[\text{ScCl}_2(\text{Et-SNS})]$  (Scheme 5.8). This complex was isolated and the NH peak was absent in the IR and  $^1\text{H}$  NMR data. Also the  $\text{CH}_2$  resonances are shifted and broadened relative to the six-coordinate species and free ligand. This was then reacted with 3 mol equiv. of MeLi to give one signal in the  $^{45}\text{Sc}$  NMR, 372 ppm (Scheme 5.8). This is the same chemical shift as one of the signals given by the reaction of the six-coordinate  $[\text{ScCl}_3(^t\text{Bu-SN(H)S})]$  with 4 mol equivs. of MeLi at room temperature (Table 5.3). The  $^1\text{H}$  and  $^{13}\text{C}\{\text{H}\}$  NMR of this reaction give similar  $\text{SCH}_2\text{CH}_2\text{N}$  chemical shifts to that of the  $^t\text{Bu}$  complex after reaction with MeLi at -78 °C (Figs. 5.7). Formation of the similar  $[\text{ScCl}_2(\text{P}_2\text{N})]$  complexes in the literature are reacted over ~1 day at 70-100 °C, suggesting that an input of energy is required to form the five-coordinate species. Therefore in this case, the supposed six-coordinate complex  $[\text{ScMe}_3(\text{SN(Li)S})]$  (tentatively assigned to the 560 ppm resonance) is the most likely exclusively formed product when carried out at low temperature.

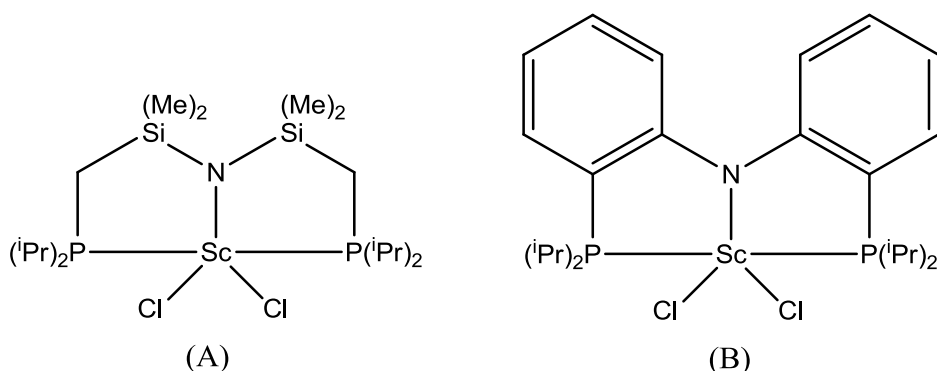
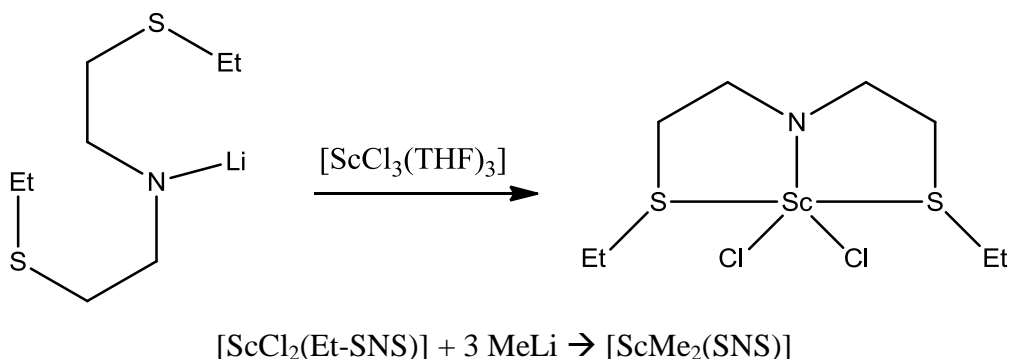


**Fig. 5.8** Displaying two complexes formed from the reaction of  $[\text{ScCl}_3(\text{THF})_3]$  and the lithiated free ligand PN(Li)P. (A);<sup>[25c]</sup> (B).<sup>[25b]</sup>



**Scheme 5.8** Showing formation of five coordinate scandium SNS complex and subsequent alkylation by MeLi.

Reaction of  $[\text{ScCl}_3(\text{decyl-SNS})]$  with 3.5 mol. equivs. of MeLi in toluene saw the same precipitation of LiCl, and the  $^{45}\text{Sc}$  NMR spectrum of the resulting orange solution showed complete loss of the original resonance associated with the  $[\text{ScCl}_3(\text{decyl-SNS})]$ . No new resonances were evident, most likely due to the product(s) with the long decyl groups having lower symmetry and therefore leading to very fast quadrupolar relaxation (as observed for the  $[\text{ScCl}_3(\text{decyl-tacn})]$ ). Addition of 10 mol. equivalents of  $\text{AlMe}_3$  to a toluene solution of  $[\text{ScCl}_3(\text{decyl-SNS})]$  also led to the disappearance of the resonance from the chloro-complex, with no new signal observed between  $\delta$  -100 to +800 ppm. The same observations resulted for the  $[\text{ScCl}_3(\text{tBu-SNS})] + 10 \text{ AlMe}_3$  system, indicating that any species formed exhibited a resonance with a very large linewidth.

### 5.3.2.2 Reactions R-SNS Complexes with $\text{AlMe}_3$

The  $^{27}\text{Al}$  NMR spectrum from the reaction between  $[\text{ScCl}_3(\text{decyl-SNS})] + 10$  equivs.  $\text{AlMe}_3$  shows a negligible change in chemical shift for the  $\text{AlMe}_3$ , but again a significant broadening of the resonance is observed (by a factor of ~3). When adding

the Lewis acid  $[\text{Ph}_3\text{C}][\text{Al}\{\text{OC}(\text{CF}_3)_3\}_4]$  (Trityl Aluminate) again no major speciation changes are observed with no new resonances occurring (Table 5.2).

### 5.3.3 Ethene Polymerisation Catalysis Testing

The scandium complexes of the decyl<sub>3</sub>-tacn and decyl-SNS ligands were tested for catalytic activity in ethene oligo/polymerisation using the decyl-substituted variants in order to maximise solubility (Table 5.4). For comparison, blank runs with  $[\text{ScCl}_3(\text{THF})_3]$  were also conducted. It is well established that different pre-catalysts show varying behaviour depending upon the method of activation, and, based upon the results reported herein, it was of interest to screen the catalysts using two different types of modified methylaluminoxane (MMAO) which have differing levels of trialkylaluminium present: one with a low ‘active’ aluminium content (PMAO-IP, ~24%) and one with a high ‘active’ aluminium content (MMAO-3A, ~40%).

Examination of the results reveals that MMAO-3A consistently gave the more active and productive catalyst compared to PMAO-IP, suggesting that higher levels of  $\text{AlR}_3$  are preferred, consistent with the Sc-Cl-Al bridges proposed by the NMR studies (above) and observed by EXAFS (below). A further difference is that whilst MMAO-3A gave almost exclusively polymer, PMAO-IP gave a more even split between polymer and liquid fraction, although the TON was extremely low in these cases. In the liquid fraction 1-butene was the only product observed in all reactions, no heavier products or other C<sub>4</sub> isomers being detected. In comparison to the runs with  $[\text{ScCl}_3(\text{THF})_3]$  both the decyl<sub>3</sub>-tacn and decyl-SNS ligands enhanced productivity and activity, more so with the latter. With MMAO-3A the ancillary ligands gave a small increase in the selectivity towards polymer, this already being quite high, whilst with PMAO-IP it is interesting to note that a dramatic change was induced, the polymer selectivity rising from 63 wt % to >97 wt %.

**Table 5.4** Results of catalyst testing with ethene.<sup>a</sup>

Pre-catalyst	Aluminium Co-Catalyst	Time (min)	TON <sup>b</sup>	Activity <sup>c</sup>	Total Product (g)	Polymer (wt%)	Liquid Product (wt%)	C <sub>4</sub> (wt%) <sup>d</sup>	1-C <sub>4</sub> in C <sub>4</sub> (%)	C <sub>6</sub> (wt%) <sup>d</sup>
[ScCl <sub>3</sub> (decyl-SNS)]	MMAO-3A	17	7,290	25,740	2.046	99.8	0.2	100	100	0
[ScCl <sub>3</sub> (decyl-SNS)]	PMAO-IP	10	150	880	0.041	97.3	2.7	100	100	0
[ScCl <sub>3</sub> (decyl <sub>3</sub> -tacn)]	MMAO-3A	10	1,930	11,590	0.542	98.5	1.5	100	100	0
[ScCl <sub>3</sub> (decyl <sub>3</sub> -tacn)]	PMAO-IP	10	270	1,630	0.076	99.5	0.5	100	100	0
[ScCl <sub>3</sub> (THF) <sub>3</sub> ]	MMAO-3A	13	1,290	5,970	0.363	97.9	2.1	100	100	0
[ScCl <sub>3</sub> (THF) <sub>3</sub> ]	PMAO-IP	10	20	100	0.005	63.0	37.0	100	100	0

<sup>a</sup> General conditions: 10 μmol Sc; 500 eq Al co-catalyst; PhCl solvent (74 mL); 40 bar ethene; 60°C. <sup>b</sup> (mol ethene)(mol Sc)<sup>-1</sup>. <sup>c</sup> (mol ethene)(mol Sc)<sup>-1</sup>h<sup>-1</sup>. <sup>d</sup> Weight percentage of liquid fraction.

The most active complex,  $[\text{ScCl}_3(\text{decyl}_3\text{-SNS})]$  gave an activity comparable with the scandium bis(silyl) 2-pyridinemethanamido complex as discussed above.<sup>[14a]</sup> Comparing with the  $[\text{MoCl}_3(\text{decyl}_3\text{-SNS})]$  complex,<sup>[27]</sup> the Sc analogue is significantly more active towards polymerisation, where the Mo analogue is effectively inactive. This could be because of the reluctance of Sc(III) to form clusters and this is postulated as one of the main reasons for the inactivity of Mo (Chapter 4). In comparison with the ethene trimerisation catalyst,  $[\text{CrCl}_3(\text{decyl}_3\text{-SNS})]$ , the scandium analogue gave no selectivity for 1-hexene.<sup>[23]</sup>

### 5.3.4 XAFS Measurements and Analysis

The scandium K-edge (4492 eV) is relatively soft for *in situ* studies and so the penetration depth into solutions across the EXAFS spectral range is small (400 – 500  $\mu\text{m}$  in pure toluene), hence spectra were acquired in fluorescence mode using the  $K_{\alpha}$  lines of scandium ( $\sim 4090$  eV, penetration depth  $\sim 360$   $\mu\text{m}$ ).

#### 5.3.4.1 Complexes in the Solid State and in Solution

The structures of the chloro-complexes  $[\text{ScCl}_3(\text{R-SNS})]$  ( $\text{R} = \text{decyl}, \text{'Bu}$ ) and  $[\text{ScCl}_3(\text{Me}_3\text{-tacn})]$  were studied in the powder (pressed with dry boron nitride) and, where possible, solution phase by Sc K-edge XAFS under inert atmosphere, contained in an XAFS solution cell, details of which are given in the Experimental Section. All samples were carefully checked for X-ray beam damage, but no effects were observed. In addition, each scan for every separate sample collection was overlaid prior to averaging to ensure data was comparable. The powder and solution structures of the complexes were confirmed by EXAFS and compared to the other characterisation obtained. The powder and solution data were collected for 3 or 4 scans, taking 20 mins per spectrum.

The Sc K-edge EXAFS results are presented in Table 5.5. Good fits have been obtained for all data sets, with low R-factors. Representative EXAFS data and fits are presented in Fig. 5.8 for  $[\text{ScCl}_3(\text{decyl-SNS})]$  powder and solution, while others samples are presented in the Supplementary Chapter.

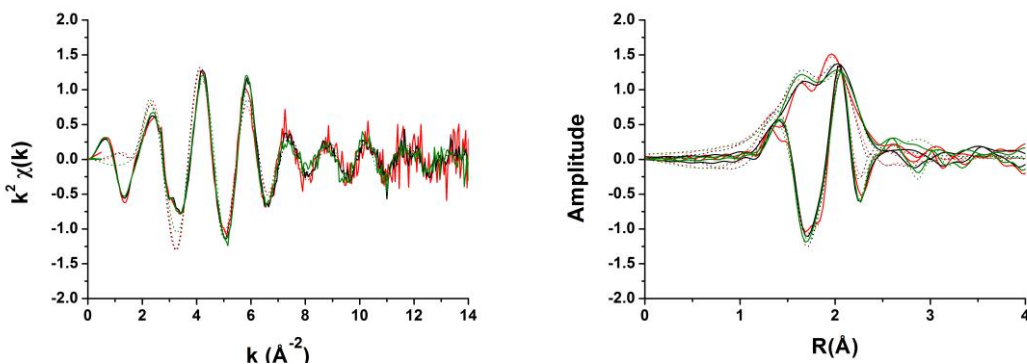


**Fig. 5.9** Sc K-edge  $k^2$ -weighted EXAFS and Fourier transform data (solid lines) and fits (dotted lines) for  $[\text{ScCl}_3(\text{decyl-SNS})]$  solid (black), solution in toluene (red) and  $[\text{ScCl}_3({}^t\text{Bu-SNS})]$  solid (green).

EXAFS analysis of the  $[\text{ScCl}_3(\text{Me}_3\text{-tacn})]$  complex shows three nitrogen atoms at 2.34  $\text{\AA}$ , three chlorine atoms at 2.36(3)  $\text{\AA}$  and two long range carbon shells at 2.65(3) and 2.9(1)  $\text{\AA}$ . In order to obtain a good fit, the Sc-N distance was fixed (taken from X-ray crystal data)<sup>[7d]</sup> and two Sc-C shells were included. Comparing the distances with the X-ray crystal data which was used as the model to fit the EXAFS data, the Sc-C shells are fitted at a much shorter distance in the EXAFS. This shorter distance is due to the fact that there are many more Sc-C contributions in the complex present at distances from 3.4  $\text{\AA}$  and upwards (both single and multiple scattering), which are not included in the fit, but overlap considerably with the fitted EXAFS here. These contributions are not included in the fit due to the limited data quality and their consequential very low statistical and mathematical relevance. This also explains the large Sc-C Debye-Waller values. Due to the overlap at low  $R$  and  $k$  of all Sc-C and Sc-N shells, unless fixing the Sc-N, the distance of that shell moves up automatically to compensate for the other, not fitted, contributions. Since this complex has been fully characterised from other techniques (see Experimental), the Sc-N contribution was fixed in the fit and refined it reliably, which is important since it serves as a starting point for reactions performed later.

The  $[\text{ScCl}_3(\text{decyl-SNS})]$  complex was dissolved in toluene (50 mmol) and characterised *via* Sc K-edge EXAFS (Fig. 5.9, Table 5.5) to give one nitrogen atom at 2.05(3)  $\text{\AA}$ , three chlorine atoms at 2.39(6)  $\text{\AA}$  and two sulfur atoms at 2.51(7)  $\text{\AA}$ . The  $[\text{ScCl}_3(\text{decyl-SNS})]$  powder was also confirmed by EXAFS to give similar distances

and Debye-Waller factors. [ScCl<sub>3</sub>(<sup>t</sup>Bu-SNS)] EXAFS data provided analyses consistent with the expected structure.

**Table 5.5** Sc K-edge EXAFS data analyses for [ScCl<sub>3</sub>(R-SNS)] and [ScCl<sub>3</sub>(Me<sub>3</sub>-tacn)] (fitted in k<sup>1-3</sup> weighting).

Sample	CN Absorber - Scatterer <sup>a</sup>	R /(\AA)	2σ <sup>2</sup> /(Å <sup>-2</sup> )	Fitting Factors <sup>b</sup>
[ScCl <sub>3</sub> (Me <sub>3</sub> -tacn)] (powder)	3 Sc-N	2.34 <sup>a</sup>	0.003(8)	1.8< k < 15.1, 1.2 < R < 3.7
	3 Sc-Cl	2.36(3)	0.002(1)	E <sub>0</sub> = -8(4)
	3 Sc···C	2.65(3)	0.001(1)	R=0.02
	6 Sc···C	2.9(1)	0.04(4)	
[ScCl <sub>3</sub> (decyl-SNS)] (solution in toluene (50 mmol))	1 Sc-N	2.05(3)	0.001(4)	1.8 < k < 14.4, 1.3 < R < 2.9
	3 Sc-Cl	2.39(6)	0.008(8)	E <sub>0</sub> = -2(2)
	2 Sc-S	2.51(7)	0.005(6)	R=0.04
[ScCl <sub>3</sub> (decyl-SNS)] (powder)	1 Sc-N	2.06(6)	0.001(5)	2.6 < k < 13.1, 1.2 < R < 2.8
	3 Sc-Cl	2.36(6)	0.009(9)	E <sub>0</sub> = -4(3)
	2 Sc-S	2.49(5)	0.004(5)	R=0.03
[ScCl <sub>3</sub> ( <sup>t</sup> Bu-SNS)] (powder)	1 Sc-N	2.11(4)	0.002(5)	1.8 < k < 14.5, 1.2 < R < 3.5
	3 Sc-Cl	2.41(5)	0.015(7)	E <sub>0</sub> = 0(1)
	2 Sc-S	2.49(3)	0.004(2)	R=0.03
	4 Sc···C	3.33(3)	0.002(4)	

<sup>a</sup>Fixed coordination numbers. <sup>b</sup>Amplitude factor 0.9.

### 5.3.4.2 Reactions of [ScCl<sub>3</sub>(L<sub>3</sub>)] with MeLi

The [ScCl<sub>3</sub>(decyl-SNS)] and [ScCl<sub>3</sub>(Me<sub>3</sub>-tacn)] complexes were reacted with 3.5 equivs. of MeLi, by injection of the required amount in diethyl ether to the complex in a toluene or THF solution at ambient temperature. The XAFS data acquisition time for all these systems were started around 5 min after injection, with an acquisition time of 20 min per spectrum, data averaged over six scans (Table 5.6).

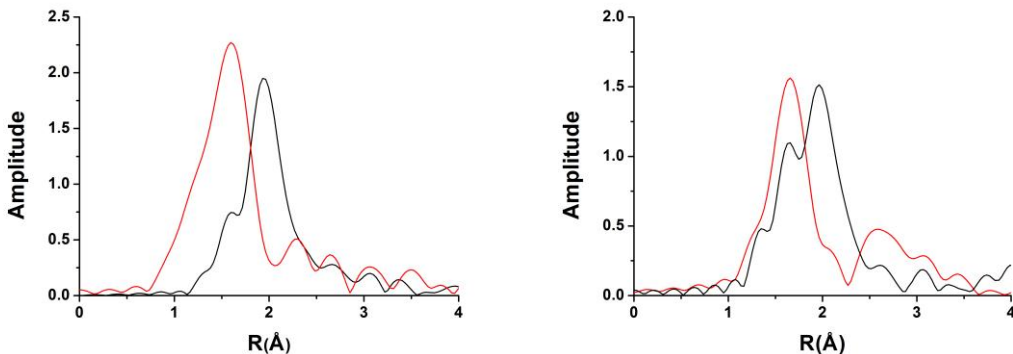


**Fig. 5.10** Sc K-edge  $k^2$ -weighted Fourier transform EXAFS data. **Left:** [ScCl<sub>3</sub>(Me<sub>3</sub>-tacn)] powder (black) and [ScCl<sub>3</sub>(Me<sub>3</sub>-tacn)] + 3.5 MeLi in THF (red). **Right:** [ScCl<sub>3</sub>(decyl-SNS)] solid (black) and [ScCl<sub>3</sub>(decyl-SNS)] + 3.5 MeLi in toluene (red).

**Table 5.6** Sc K-edge EXAFS data analyses of [ScCl<sub>3</sub>(L)] + 3.5 MeLi in toluene (L = decyl-SNS, Me<sub>3</sub>-tacn) (fitted in  $k^{1-3}$  weighting).

Reaction	CN Absorber - Scatterer	R (Å)	$2\sigma^2(\text{\AA}^{-2})$	Fitting Factors <sup>a</sup>
[ScCl <sub>3</sub> (Me <sub>3</sub> -tacn)] + 3.5 MeLi in THF	8(2) Sc-C/N	2.17(2)	0.003(4)	$1.3 < k < 11.1$ , $1.2 < R < 2$ $E_0 = -7(1)$ $R = 0.01$
[ScCl <sub>3</sub> (decyl-SNS)] + 3.5 MeLi in toluene (45 mmol)	3.5(8) Sc-C/N 1(1) Sc-S 0.5(9) Sc-S	2.13(2) 2.96(5) 3.39(5)	0.003(2) 0.002(9) 0.003(9)	$1.9 < k < 12.5$ , $1.2 < R < 23.3$ $E_0 = 1(2)$ $R = 0.02$

<sup>a</sup>Amplitude Factor 0.9.

As the model reaction, the [ScCl<sub>3</sub>(Me<sub>3</sub>-tacn)] was reacted with 3.5 mol. equivs. of MeLi in THF, and following precipitation of LiCl, the product ([ScMe<sub>3</sub>(Me<sub>3</sub>-tacn)]) remained in solution with sufficient solubility for Sc K-edge EXAFS analysis. One Sc-N/C shell was fitted at 2.17(2) Å, with a coordination of 8(2), giving a good fit and low R-factor. The EXAFS analyses confirm the disappearance of chloride from the coordination sphere, to leave only C/N contributions, as predicted from the NMR analyses, confirming the formation of [ScMe<sub>3</sub>(Me<sub>3</sub>-tacn)].

In a similar fashion, the complex  $[\text{ScCl}_3(\text{decyl-SNS})]$  was reacted with 3.5 mol. equivs. MeLi to give 3 or 4 Sc-C/N at 2.13 Å and two separate Sc-S shells at 2.96 and 3.39 Å. In the five-coordinate  $[\text{ScMe}_2(\text{PNP})]$  complex reported previously (Fig. 5.8 (B)),<sup>[25a]</sup> the crystallographic Sc-C distances are 2.21 Å. The  $^{45}\text{Sc}$  NMR studies of the SNS systems indicate that reaction with MeLi affords at least two products when reacted at room temperature. Since EXAFS spectroscopy is a macroscopic technique probing the weighted average of all the species in the mixture, it is difficult to identify any single species in the EXAFS analysis in this instance. What we can ascertain from the analysis of this reaction is the reduction of heavy atoms, (LiCl is also precipitated after reaction) in conjunction with a significant increase of light atom scatters at lower distance, as seen in the  $[\text{ScMe}_3(\text{Me}_3\text{-tacn})]$  complex; the reduced Sc-C/N distances are consistent with a lower coordination number. The EXAFS data also displays heavy contributions at ~3-3.5 Å, assigned as long distance Sc–S contributions. The  $^{13}\text{C}\{^1\text{H}\}$  NMR spectrum of  $[\text{ScCl}_3(^t\text{Bu-SNS})] + 4$  mol. equivs. MeLi shows the  $\text{CH}_2\text{S}$  resonance shifts toward the free ligand chemical shift value, suggesting that some dissociation of the Sc–S bond is observed for this reaction.

The Sc K-edge XANES shows clear changes upon addition of MeLi, with disappearance of the double white-line feature and a simultaneous growth of the overall white-line intensity, as well as an upwards energy shift of the edge position and an increase in the intensity of the first pre-edge feature (Fig. 5.10). Similar XANES changes were observed during the alkylation of some Cr(III) complexes by  $\text{AlMe}_3$ .<sup>[28]</sup> These changes can sometimes be indicative of changes in the coordination site and the electronics, unfortunately it is difficult to predict how due to the fact that there is not an extensive series of Sc K-edge XANES reference data available here or in literature. The derivative of the XANES actually seems to suggest an increased number of pre-edge and/or edge positions are present, which could indicate a mixture of species.

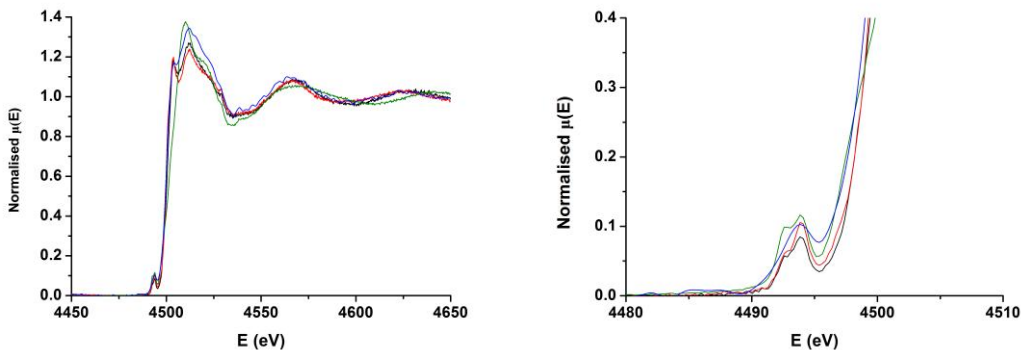


**Fig. 5.11** Sc K-edge XANES spectra for  $[\text{ScCl}_3(\text{decyl-SNS})]$  solution (black), with 10 mol. equiv.  $\text{AlMe}_3$  frozen after 1 s (blue), with 10 mol. equiv.  $\text{AlMe}_3$  at ambient temperature (red), with 3.5 mol. equiv.  $\text{MeLi}$  (green).

#### 5.3.4.3 Reaction of $[\text{ScCl}_3(\text{decyl-SNS})]$ with $\text{AlMe}_3$

Sc K-edge XAFS was used to follow the reaction of a toluene solution of  $[\text{ScCl}_3(\text{decyl-SNS})]$  with 10 mol. equivalents of  $\text{AlMe}_3$ , to determine if the catalyst is firstly methylated, as observed from similar studies of the Group 6 metal analogues  $[\text{MoCl}_3(\text{R-SNS})]$ <sup>[29]</sup> and  $[\text{CrCl}_3(\text{R-SNS})]$ .<sup>[28]</sup>

The toluene solution of  $[\text{ScCl}_3(\text{decyl-SNS})]$  was activated at room temperature with  $\text{AlMe}_3$  by injecting the required amount of  $\text{AlMe}_3$  in toluene (where indicated,  $[\text{Ph}_3\text{C}][\text{Al}\{\text{OC}(\text{CF}_3)_3\}_4]$  and 1-hexene were added to the scandium complex prior to the  $\text{AlMe}_3$ ). The XAFS data acquisition for all these systems started *ca.* 5 min after injection at room temperature, with an acquisition time of 16 mins per scan, with data averaged over 10 scans, the spectra being unchanged over the period of acquisition. (Fig. 5.11).

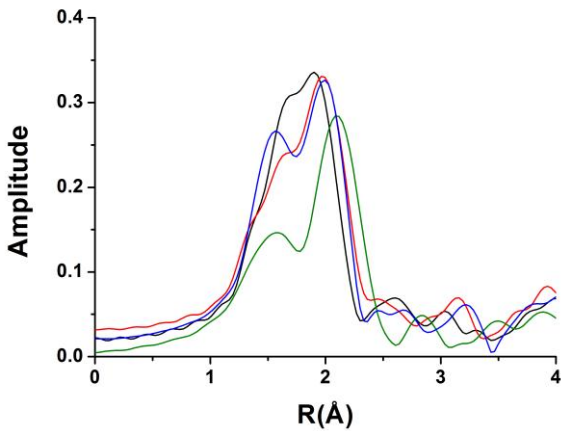


**Fig. 5.12** Sc K-edge  $k^1$ -weighted Fourier transform EXAFS data for  $[\text{ScCl}_3(\text{decyl-SNS})]$  solution (black) and with 10 mol. equiv.  $\text{AlMe}_3$  (red), with further addition of 1 mol. equiv. of  $[\text{Ph}_3\text{C}][\text{Al}\{\text{OC}(\text{CF}_3)_3\}_4]$  (green), and with further addition of 100 mol. equivs. 1-hexene (blue).

**Table 5.7** Sc K-edge EXAFS data analyses for  $[\text{ScCl}_3(\text{decyl-SNS})]$  upon activation in toluene (fitted in  $k^{1-3}$  weighting).

[ $\text{ScCl}_3(\text{decyl-SNS})$ ]	CN Absorber- Scatterer	R (Å)	$2\sigma^2(\text{\AA}^{-2})$	Fitting Parameters <sup>a</sup>
+ 10 $\text{AlMe}_3$ in toluene (25 mmol)	1(fixed) Sc-N 5(1) Sc-S/Cl	2.02(5) 2.44(2)	0.001(6) 0.006(3)	$1.8 < k < 13.6$ , $1.3 < R < 2.8$ $E_0 = 4(2)$ $R = 0.04$
+ 10 $\text{AlMe}_3$ + 1 trityl aluminate in toluene (21 mmol)	1.2(8) Sc-C/N 4(1) Sc-S/Cl	2.11(4) 2.60(2)	0.002(5) 0.003(4)	$2.9 < k < 12.3$ , $1.3 < R < 2.6$ $E_0 = 5(2)$ $R = 0.01$
+ 10 $\text{AlMe}_3$ + 1 trityl aluminate + 100 1-hexene in toluene (17 mmol)	2(1) Sc-C/N 4(1) Sc-S/Cl	2.10(4) 2.57(3)	0.002(8) 0.004(4)	$1.8 < k < 12.4$ , $1.3 < R < 2.6$ $E_0 = 1(2)$ $R = 0.02$

<sup>a</sup>Amplitude factor 0.9

XAFS data were also collected and analysed for the reactions of [ScCl<sub>3</sub>(decyl-SNS)] with 10 mol. equivs. of AlMe<sub>3</sub> in the presence of 1 mol. equivalent of trityl aluminate and 100 mol. equivalents of 1-hexene. Good fits are obtained for all data sets with low R-factors. After the initial reaction with AlMe<sub>3</sub>, no major chemical changes at the scandium centre are observed. One nitrogen atom at a similar distance to the starting material, 2.02(5) Å is still observed, and the sulfur and chlorine shells are now indistinguishable, giving an overall sulfur/chlorine contribution of 5(1) at 2.44 Å. This suggests that no alkylation has taken place, but only some small changes in distances and order of S/Cl around the scandium, compared with the starting complex. The Sc K-edge XANES spectra also only show very small changes (Fig. 5.12), indicating little change in the coordination geometry around the Sc metal centre. Using the freeze-quench technique previously described,<sup>[29]</sup> we see from the normalised XANES spectra that the reaction of [ScCl<sub>3</sub>(decyl-SNS)] with 10 mol. equivs. of AlMe<sub>3</sub> (frozen after 1s) (Fig. 5.10) does occur within 1 second, with only small changes occurring thereafter. In no case does addition of AlMe<sub>3</sub> cause the change in edge position, as observed from reaction with MeLi. Taking into account the <sup>45</sup>Sc and <sup>27</sup>Al NMR evidence as well as the catalysis testing results, we suggest that this arises from aluminium bridging the scandium through the chloride(s), causing the observed changes in the distance.

After the addition of AlMe<sub>3</sub> to a mixture of the Sc complex with trityl aluminate and 1-hexene, a significant increase in distance is seen for S/Cl to ~2.60 Å, with lower Debye-Waller factors compared to the AlMe<sub>3</sub> only. Moreover, a lower coordination of 4(1) S/Cl is observed. This could indicate the removal of a chloride ligand, with the distance of Sc-N/C increased to 2.11(4) Å, and the remaining S/Cl scatterers now more equidistant from the scandium. Moreover, as the reaction proceeds with 1-hexene, the N/C coordination further increases. Again, the XANES spectra of the reaction species formed do not display significant changes, only some very small shifts in pre-edge features and intensities, indicating the overall geometry around the Sc, with retention of the decyl-SNS ligand and significant Sc-Cl still present throughout the activation process.

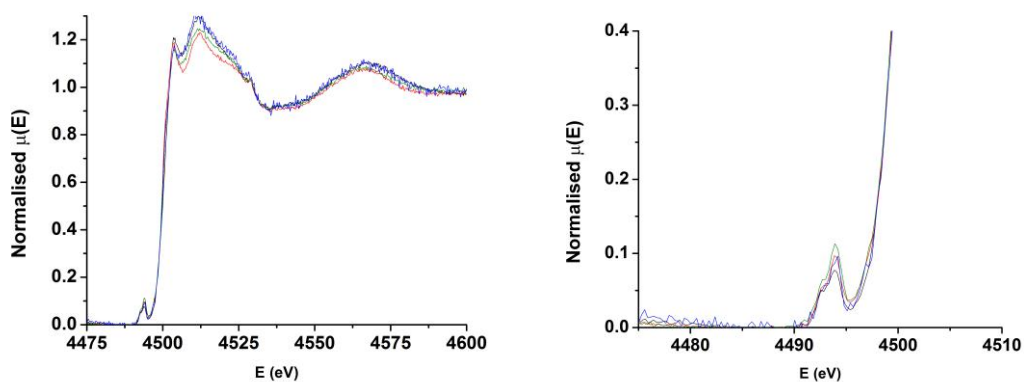


**Fig. 5.13** Sc K-edge normalised XANES spectra for  $[\text{ScCl}_3(\text{decyl-SNS})]$  solution (black) and with 10 mol. equiv.  $\text{AlMe}_3$  (red), with further addition of 1 mol. equivs.  $[\text{Ph}_3\text{C}][\text{Al}\{\text{OC}(\text{CF}_3)_3\}_4]$  (green), with further addition of 100 mol. equivs. 1-hexene (blue).

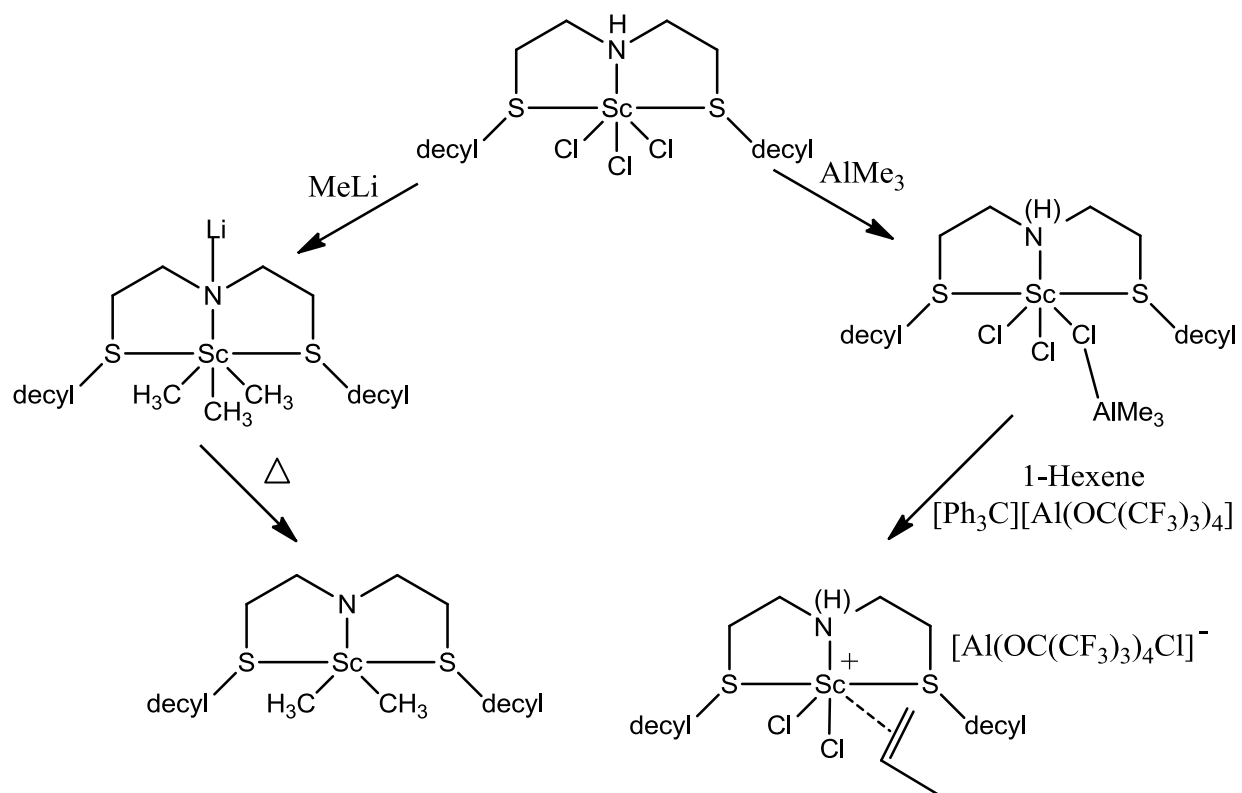
#### 5.4 Conclusions

The  $^{45}\text{Sc}$  NMR spectroscopy of the  $[\text{ScCl}_3(\text{R-SNS})]$  with  $\text{MeLi}$  has given strong indications of the possible mechanism of the important SNS type ligand used in the highly active chromium ethene oligomerisation catalysts. The evidence suggests that the secondary amine can be deprotonated and, in the case of Sc(III) complexes, cause a structural change (Scheme 5.9). Therefore, it is entirely possible that when coordinated to chromium under catalytic conditions, this same mode of action could provide structural and/or electronic changes to the metal centre contributing towards high activity of the catalyst.

The EXAFS analyses strongly suggest that the  $\text{AlMe}_3$  reagent alone does not alkylate the metal centres in the Sc(III) complexes, in contrast to previous studies on analogous complexes of Group 6 metals,<sup>[28-29]</sup> but rather ‘activates’ the Sc-Cl bond (*via* formation of bridging to the  $\text{AlMe}_3$ ). This is strongly supported by the  $^{45}\text{Sc}$  NMR studies on the reactions with  $\text{MeLi}$  compared to  $\text{AlMe}_3$ . Rather the  $\text{AlMe}_3$  appears to interact with the chloride ligands rather than directly perturb the scandium centre. When this activation occurs in the presence of the Lewis acid such as  $[\text{Ph}_3\text{C}][\text{Al}\{\text{OC}(\text{CF}_3)_3\}_4]$ , this allows a route for one chloride to be removed. When this

reaction proceeds in the presence of a large excess of an  $\alpha$ -olefin (such as the 1-hexene used here), the  $\text{AlMe}_3$  and  $[\text{Ph}_3\text{C}][\text{Al}\{\text{OC}(\text{CF}_3)_3\}_4]$  may be facilitating coordination of the 1-hexene to scandium (Scheme 5.9). This sequence is in accordance with ethene polymerisation (simple chain growth) observed in the catalytic studies.

In addition to Sc chemistry being dominated by a single oxidation state (III), this resistance of the Sc-Cl bonds to alkylation by  $\text{AlMe}_3$  may contribute to the very different catalysis reactivity and selectivity as compared to chromium analogues, for which the R-SNS complexes are highly active trimerisation catalysts<sup>[23, 30]</sup> and the tacn complexes form oligomers, while the Sc systems described in this Chapter lead to ethene polymerisation.



**Scheme 5.9** Proposed reaction pathways of  $[\text{ScCl}_3(\text{decyl-SNS})]$  by  $\text{AlMe}_3$  +  $[\text{Ph}_3\text{C}][\text{Al}\{\text{OC}(\text{CF}_3)_3\}_4]$  for olefin polymerisation.

## 5.5 Experimental

Infrared spectra were recorded as Nujol mulls between CsI plates using a Perkin-Elmer Spectrum100 spectrometer over the range 4000-200 cm<sup>-1</sup>. <sup>1</sup>H and <sup>13</sup>C{<sup>1</sup>H} NMR spectra were recorded using a Bruker AV300 or DPX400 spectrometer. <sup>27</sup>Al and <sup>45</sup>Sc NMR spectra used a Bruker DPX400 spectrometer and are referenced to external aqueous [Al(H<sub>2</sub>O)<sub>6</sub>]<sup>3+</sup> and [Sc(H<sub>2</sub>O)<sub>6</sub>]<sup>3+</sup> respectively ( $\delta = 0$ ). Microanalyses were undertaken by Medac Ltd. Solvents were dried by distillation prior to use, CH<sub>2</sub>Cl<sub>2</sub> from CaH<sub>2</sub>, hexane, pentane, THF and toluene from sodium benzophenone ketyl. MMAO-3A and PMAO-IP were obtained from Akzo Nobel. Reagents Me<sub>3</sub>Al (2.0 mol. dm<sup>-3</sup> in toluene) and MeLi (1.6 mol. dm<sup>-3</sup> in Et<sub>2</sub>O) were obtained from Aldrich and titrated to determine their concentrations prior to use.<sup>[31]</sup> [ScCl<sub>3</sub>(THF)<sub>3</sub>] was prepared from ScCl<sub>3</sub>·6H<sub>2</sub>O (Aldrich) by the literature procedure.<sup>[32]</sup> ( $\delta$  <sup>45</sup>Sc = 206). Ligands Me<sub>3</sub>-tacn,<sup>[33]</sup> decyl<sub>3</sub>-tacn,<sup>[28]</sup> HN(CH<sub>2</sub>CH<sub>2</sub>SC<sub>10</sub>H<sub>21</sub>)<sub>2</sub> (decyl-SNS) and HN(CH<sub>2</sub>CH<sub>2</sub>S<sup>t</sup>Bu)<sub>2</sub> ('Bu-SNS)<sup>[23, 29]</sup> were prepared by literature methods. Li-N(CH<sub>2</sub>CH<sub>2</sub>S<sup>t</sup>Bu)<sub>2</sub> ('Bu-SN(Li)S) was made *in situ* and prepared based on literature methods.<sup>[26, 34]</sup> The co-catalyst trityl aluminate ([Ph<sub>3</sub>C][Al{OC(CF<sub>3</sub>)<sub>3</sub>}<sub>4</sub>]) was also prepared by the literature method.<sup>[35]</sup> All reactions were performed using pre-dried glassware and Schlenk techniques. Samples were stored and handled in a dry, N<sub>2</sub>-purged glove box.

### 5.5.1 Preparations

**[ScCl<sub>3</sub>(Me<sub>3</sub>-tacn)]:**<sup>[7d]</sup> [ScCl<sub>3</sub>(THF)<sub>3</sub>] (0.98 g, 2.7 mmol) was dissolved in MeCN (10 mL). To this the ligand Me<sub>3</sub>-tacn (0.5 g, 2.9 mmol) was added in a dry, N<sub>2</sub> purged glove-box. With stirring, almost immediately a white solid precipitated which was collected by Schlenk filtration, washed with small amount of MeCN and dried *in vacuo*. Yield: 0.45 g, 1.3 mmol, 52%. Required for C<sub>9</sub>H<sub>21</sub>Cl<sub>3</sub>N<sub>3</sub>Sc: C, 33.5; H, 6.6; N, 13.0. Found: C33.6; H, 6.4; N, 13.0%. <sup>1</sup>H NMR (CD<sub>3</sub>CN):  $\delta$  = 3.2 (m, [6H], CH<sub>2</sub>), 3.0 (m, [6H], CH<sub>2</sub>), 2.9 (s, [9H], CH<sub>3</sub>) ppm. <sup>13</sup>C{<sup>1</sup>H} NMR (CD<sub>3</sub>CN):  $\delta$  = 55.0 (CH<sub>2</sub>), 49.4 (CH<sub>3</sub>) ppm. <sup>45</sup>Sc NMR (THF, 298 K):  $\delta$  = 306; (CD<sub>3</sub>CN): 298; (CH<sub>2</sub>Cl<sub>2</sub>): 304. IR (Nujol,  $\nu$ /cm<sup>-1</sup>): 352, 322 (Sc-Cl).

**[ScCl<sub>3</sub>(decyl<sub>3</sub>-tacn)]:** [ScCl<sub>3</sub>(THF)<sub>3</sub>] (0.5 g, 1.4 mmol) dissolved in CH<sub>2</sub>Cl<sub>2</sub> (15 mL). To this, the ligand decyl<sub>3</sub>-tacn (0.9 g, 1.6 mmol) was added dropwise with stirring. The light brown solution was left to stir for 5 h, at which point the volatiles were removed *in vacuo*, dry degassed pentane (25 mL) was added and the mixture left to stir overnight. The solution was filtered under N<sub>2</sub> and the solids washed with further pentane (2 x 10 ml) and dried *in vacuo*. Yield: 0.62 g, 0.9 mmol (66 %). Required for C<sub>36</sub>H<sub>75</sub>Cl<sub>3</sub>N<sub>3</sub>Sc: C 61.6, H 10.8, N 6.0. Found: C 61.8, H 10.8, N 5.7%. <sup>1</sup>H NMR (CDCl<sub>3</sub>): δ = 0.75 (t, [9H], CH<sub>3</sub>), 1.25 (br, [48H], CH<sub>2</sub>), 1.7 (br, [6H], CH<sub>2</sub>), 2.95 (br, [6H], CH<sub>2</sub>N), 3.2 (br, [6H], CH<sub>2</sub>N), 3.7 (br, [6H], CH<sub>2</sub>N). <sup>13</sup>C{<sup>1</sup>H} NMR (CDCl<sub>3</sub>): δ = 57.7 (CH<sub>2</sub>N), 49.8 (CH<sub>2</sub>N), 16.9, 19.2, 22.7, 24.3, 27.0, 29.3, 29.5, 29.8, 31.9 (CH<sub>2</sub>), 14.1 (CH<sub>3</sub>). <sup>45</sup>Sc NMR (CH<sub>2</sub>Cl<sub>2</sub>): 252 (w<sub>1/2</sub> 200 Hz); (toluene): 227 (w<sub>1/2</sub> 3300 Hz). IR (Nujol, ν/cm<sup>-1</sup>): 302 br (Sc-Cl).

**[ScCl<sub>3</sub>(decyl-SNS)]:** [ScCl<sub>3</sub>(THF)<sub>3</sub>] (0.5 g, 1.4 mmol) was dissolved in MeCN (15 mL), where it was allowed to stir for 30 min. All volatiles were then removed *in vacuo*, and further MeCN (15 mL) was added and the solution was stirred for 10 min. Following removal of the volatiles once more, CH<sub>2</sub>Cl<sub>2</sub> (20 mL) was added to the white solid. The ligand, decyl-SNS, (0.68 g, 1.6 mmol) was then added dropwise to the solution, which changed from colourless to pale yellow. This was left to stir for 3 h with no further changes observed. The solvent was then removed *in vacuo* to give a yellow solid which was washed with pentane, filtered and dried to give an orange/yellow solid. Yield: 0.6 g, 75%. Required for C<sub>24</sub>H<sub>51</sub>Cl<sub>3</sub>NS<sub>2</sub>Sc: C, 50.7; H, 9.0; N, 2.5. Found: C, 50.2; H, 9.0; N, 2.3%. <sup>1</sup>H NMR (CDCl<sub>3</sub>): δ 0.8 (t, [6H], CH<sub>3</sub>), 1.2 (m, [28H], decyl CH<sub>2</sub>), 1.5 (m, decyl NCH<sub>2</sub>CH<sub>2</sub>), 2.5 (br, [4H], SCH<sub>2</sub>), 3.0, 3.4 (br, each [4H], SCH<sub>2</sub>CH<sub>2</sub>N). <sup>13</sup>C{<sup>1</sup>H} NMR (CDCl<sub>3</sub>): δ 14.1 (CH<sub>3</sub>), 22.7, 25.5, 28.0, 28.5, 28.8, 29.4, 29.5, 29.6, 29.6 (CH<sub>2</sub>), 47.0 (CH<sub>2</sub>NH). <sup>45</sup>Sc NMR (CH<sub>2</sub>Cl<sub>2</sub>): 223, 261 (780, 750). IR (Nujol, ν/cm<sup>-1</sup>): 3097 (NH), 333, 305 cm<sup>-1</sup> (Sc-Cl).

**[ScCl<sub>3</sub>(<sup>t</sup>Bu-SNS)]:** Prepared as above, yellow solid. Yield: 55%. Required for C<sub>12</sub>H<sub>27</sub>Cl<sub>3</sub>NS<sub>2</sub>Sc: C, 36.0; H, 6.8; N, 3.5. Found: C, 35.7; H, 7.2; N, 3.3%. <sup>1</sup>H NMR (CDCl<sub>3</sub>): 1.3 (s, [18H], CH<sub>3</sub>), 3.0, 3.3 (br, each [4H], SCH<sub>2</sub>CH<sub>2</sub>N), 8.2 (br, [1H], NH) ppm. <sup>13</sup>C{<sup>1</sup>H} NMR (CDCl<sub>3</sub>): 24.4 (CH<sub>2</sub>S), 31.2 (CH<sub>3</sub>), 43.6 (C(CH<sub>3</sub>)<sub>3</sub>), 48.2 (NCH<sub>2</sub>) ppm. <sup>45</sup>Sc NMR (CDCl<sub>3</sub>): 260, 233 (w<sub>1/2</sub> ~2000 and 1000 Hz respectively) ppm. IR (Nujol, ν/cm<sup>-1</sup>): 3045 (NH), 302 cm<sup>-1</sup> (Sc-Cl).

**[ScCl<sub>2</sub>(Et-SNS)]:** [ScCl<sub>3</sub>(THF)] (0.8 g, 2.2 mmol) was suspended in dry/degassed toluene (20 mL) at 60 °C. To this, the ligand Li(SNS-Et) (0.5 g, 2.5 mmol) was added in toluene (15 mL) to the suspension. This was stirred overnight at 60 °C, leading to an orange-brown solution and some white precipitate. The toluene was removed *in vacuo* and dry/degassed hexane was added and the mixture stirred at room temperature for 2 h. The solution was filtered and the LiCl was washed out through the frit using hexane (3 x 10 ml). The solid was then dried and stored under inert atmosphere. Yield: 0.32 g, 76%. <sup>1</sup>H NMR (CDCl<sub>3</sub>): 1.3 (br t, [6H], CH<sub>3</sub>), 2.6, 2.7, 2.8 (br m, each [4H], CH<sub>2</sub>), no NH. <sup>1</sup>H NMR (CDCl<sub>3</sub>): 1.3 (br t, [6H], CH<sub>3</sub>), 2.6, 2.7, 2.8 (br m, each [4H], CH<sub>2</sub>), no NH. <sup>45</sup>Sc NMR (CDCl<sub>3</sub>): 300 ppm. IR (Nujol,  $\nu/\text{cm}^{-1}$ ): No NH, 501(br) (Sc-S).

**[ScMe<sub>3</sub>(Me<sub>3</sub>-tacn)]:** [ScCl<sub>3</sub>(Me<sub>3</sub>-tacn)] (0.15 g, 0.5 mmol) was suspended in THF (10 mL) and MeLi (3.5 mol. equivalents 1.8 mmol, 1.6 mol. dm<sup>-3</sup> in hexane) was added to the solution and stirred for 20 mins. at room temperature before removal of the volatiles *in vacuo*. Toluene-d<sub>8</sub> ca. 1 mL was added and the white precipitate (LiCl) was allowed to settle before removing the clear yellow solution for NMR spectroscopy. <sup>1</sup>H NMR (toluene-d<sub>8</sub>): -0.1 (br s, [9H], ScMe), 1.8 (m, [6H], CH<sub>2</sub>), 2.3 (m, [6H], CH<sub>2</sub>), 2.4 (s, [9H], NMe). <sup>13</sup>C{<sup>1</sup>H} NMR (toluene-d<sub>8</sub>): 48.4 (NMe), 54.8 (CH<sub>2</sub>) ppm (the ScMe resonance was not observed at any temperature between 223 and 353 K, consistent with the literature<sup>[7d]</sup>). <sup>45</sup>Sc NMR (toluene-d<sub>8</sub>): 626 ppm ( $w_{1/2}$  ~ 520 Hz).

**[ScMe<sub>3</sub>(<sup>t</sup>Bu-SN(Li)S)]:** [ScCl<sub>3</sub>(<sup>t</sup>Bu-SNS)] (0.15 g, 0.4 mmol) was dissolved in toluene (10 ml) and cooled to -78 °C. MeLi (4 mol. equivalents) was added and stirred for 10 mins., then allowed to slowly warm to room temperature. The mixture was stirred for 15 mins. at room temperature before removal of the volatiles *in vacuo*. Toluene-d<sub>8</sub> (ca. 1 mL) was added and the LiCl precipitate was allowed to settle before decanting the clear yellow solution *via* syringe for NMR spectroscopy. <sup>1</sup>H NMR (toluene-d<sub>8</sub>): -0.31 (br, ScMe), 1.2 (br, [18H], C(CH<sub>3</sub>)<sub>3</sub>, 2.8, 3.2 (br, each [4H], CH<sub>2</sub>). <sup>13</sup>C{<sup>1</sup>H} NMR (toluene-d<sub>8</sub>): 27.34 (CH<sub>2</sub>S), 31.3 (CH<sub>3</sub>), 42.8 (C(CH<sub>3</sub>)<sub>3</sub>), 51.6 (CH<sub>2</sub>N) ppm.

**Li[Al{OC(CF<sub>3</sub>)<sub>3</sub>}<sub>4</sub>]<sup>[36]</sup>:** Purified LiAlH<sub>4</sub> (0.38 g, 10 mmol) was suspended in toluene (60 ml). Perfluro-tert-butanol (10 g, 42.4 mmol) in toluene (20 ml) was added at 0 °C over 30 min. This was allowed to stir overnight where the solution changed to pink through to green with precipitate. This mixture was then heated to 45 °C for ½ day where bubbles were being formed. The solution was then raised to 70 °C over 4 hrs then kept at this temperature overnight to give a clear yellow solution and white precipitate. The solution was cooled to 0 °C for 1 hr and the solution filtered to give a white precipitate. If any black precipitate has formed (Al<sub>x</sub>O<sub>y</sub>), this can be filtered out by dissolving the white precipitate in Et<sub>2</sub>O and then evaporation of the solvent to give the desired product. The solid was then dried under vacuum for 1 day at 80 °C. The product was stored under inert atmosphere. Yield: 6.81 g, 70 %. <sup>13</sup>C{<sup>1</sup>H} NMR (CDCl<sub>3</sub>): 120 (qC), 293 (CF<sub>3</sub>) ppm. <sup>19</sup>F NMR (CDCl<sub>3</sub>): -77 ppm. <sup>27</sup>Al NMR (CDCl<sub>3</sub>): 34 ppm.

### 5.5.2 Catalysis Testing

Catalytic experiments were performed in 250 mL Buchi Miniclavettes equipped with stainless steel vessels with integral thermal-fluid jackets, internal cooling coils and mechanical mixing *via* gas-entraining stirrers. Ethene (Grade 4.5) was supplied by Linde and passed through oxygen and moisture scrubbing columns prior to use; ethene flow was measured using a Siemens Sitrans F C Massflo system (Mass 6000-Mass 2100) and the data logged. Liquid phase sample GC-FID analysis was performed using an Agilent Technologies 6850N GC System equipped with a PONA column (50 m × 0.20 mm × 0.50 μm) using hydrogen as carrier gas.

An autoclave was heated to 90 °C under vacuum for 30 minutes then cooled to 60 °C. After back-filling with ethene to ambient pressure, solvent (70 mL, PhCl) was added *via* syringe, followed by the pre-catalyst as a stock solution in PhCl. The vessel was vigorously stirred and the temperature maintained at the desired temperature throughout. In order to initiate reaction, MMAO was added *via* syringe and the vessel immediately charged with 40 bar of ethene and the pressure kept constant throughout the reaction by the continuous addition of ethene, which was monitored *via* a flow-meter. Once ethene uptake had ceased, the gas supply was closed and the reactor cooled to 5 °C. The reactor was carefully vented. The reactor contents were treated sequentially with 1000 μL of nonane (GC internal standard) and 10% HCl. A sample

of the organic phase was taken for GC-FID analysis. Any solid formed was collected, washed repeatedly with 10% HCl and EtOH, dried overnight and weighed.

### 5.5.3 XAFS Experimentation

All samples for powder Sc K-edge EXAFS analyses were mixed with boron nitride, pressed into pellets under inert atmosphere and encapsulated in Kapton tape. All solution data collected for Sc K-edge XAFS were obtained from solutions made up to the stated concentrations with anhydrous toluene or THF under inert conditions. The solution was then transferred to a dry, argon-purged and sealed liquid XAFS cell for analysis on the beamline.<sup>[28]</sup> Reactions were also performed in the same liquid XAFS cell by addition of the stated amount of AlMe<sub>3</sub> (2.0 mol dm<sup>-3</sup> in hexane) directly into the XAFS cell at ambient temperature. Stopped-flow-freeze-quench sampling was carried out as previously described,<sup>[29]</sup> with the sample as a frozen glass maintained as such using an Oxford Instruments Cryojet. The solution was then analysed with Sc K-edge EXAFS after *ca.* 5 min of reaction with each scan taking 20 minutes. The Sc K-edge XAFS measurements were all collected in fluorescence mode using a 9-element Ge detector (Ortec), performed on the B18 beamline<sup>[37]</sup> at Diamond Light Source in Didcot, England using a Si(111) double crystal monochromator and a beamsize of ~ 100 μm. Energy calibration was carried out using a Ti foil. Constant scan-rate (QEXAFS) data were recorded with an acquisition time of 20 mins per spectrum. XAS data processing and EXAFS analysis were performed using IFEFFIT<sup>[38]</sup> with the Horae package<sup>[39]</sup> (Athena and Artemis). The complexes were fitted using single crystal models from similar complexes, as indicated. The detailed fitting parameters are given in the results section.

### 5.6 References

- [1] Z. Shen and M. F. Farona, *J. Polym. Sci. Pol. Chem.* **1984**, *22*, 1009-1015.
- [2] a) W. E. Piers, E. E. Bunel and J. E. Bercaw, *J. Organomet. Chem.* **1991**, *407*, 51-60; b) P. Shapiro and J. E. Bercaw, *Abstr. Pap. Am. Chem. Soc.* **1990**, *199*, 381.
- [3] S. Arndt and J. Okuda, *Chem. Rev.* **2002**, *102*, 1953-1976.
- [4] P. L. Watson, *J. Am. Chem. Soc.* **1982**, *104*, 337-339.

- [5] R. J. McKinney, *Chem. Commun.* **1980**, 490-492.
- [6] P. J. Shapiro, W. P. Schaefer, J. A. Labinger, J. E. Bercaw and W. D. Cotter, *J. Am. Chem. Soc.* **1994**, *116*, 4623-4640.
- [7] a) P. Mountford and B. D. Ward, *Chem. Commun.* **2003**, 1797-1803; b) W. E. Piers and D. J. H. Emslie, *Coord. Chem. Rev.* **2002**, 233–234, 131-155; c) V. C. Gibson and S. K. Spitzmesser, *Chem. Rev.* **2002**, *103*, 283-316; d) S. Hajela, W. P. Schaefer and J. E. Bercaw, *J. Organomet. Chem.* **1997**, *532*, 45-53.
- [8] K. C. Hultsch, P. Voth, K. Beckerle, T. P. Spaniol and J. Okuda, *Organomet.* **2000**, *19*, 228-243.
- [9] P. G. Hayes, W. E. Piers, L. W. M. Lee, L. K. Knight, M. Parvez, M. R. J. Elsegood and W. Clegg, *Organomet.* **2001**, *20*, 2533-2544.
- [10] P. G. Hayes, W. E. Piers and R. McDonald, *J. Am. Chem. Soc.* **2002**, *124*, 2132-2133.
- [11] S. C. Lawrence, B. D. Ward, S. R. Dubberley, C. M. Kozak and P. Mountford, *Chem. Commun.* **2003**, 2880-2881.
- [12] S. Bambirra, D. van Leusen, A. Meetsma, B. Hessen and J. H. Teuben, *Chem. Commun.* **2001**, 637-638.
- [13] a) G. Paolucci, M. Bortoluzzi, M. Napoli, P. Longo and V. Bertolasi, *J. Mol. Catal. A-Chem.* **2010**, *317*, 54-60; b) S. Bambirra, D. van Leusen, C. G. J. Tazelaar, A. Meetsma and B. Hessen, *Organomet.* **2007**, *26*, 1014-1023; c) S. Bambirra, M. W. Bouwkamp, A. Meetsma and B. Hessen, *J. Am. Chem. Soc.* **2004**, *126*, 9182-9183.
- [14] a) Z. Jian and D. Cui, *Dalton Trans.* **2012**, *41*, 2367-2373; b) D. Li, S. Li, D. Cui, X. Zhang and A. A. Trifonov, *Dalton Trans.* **2011**, *40*, 2151-2153; c) L. T. J. Evans, M. P. Coles, F. G. N. Cloke and P. B. Hitchcock, *Inorg. Chim. Acta* **2010**, *363*, 1114-1125; d) S. Ge, S. Bambirra, A. Meetsma and B. Hessen, *Chem. Commun.* **2006**, 3320-3322; e) S. Ge, A. Meetsma and B. Hessen, *Organomet.* **2007**, *26*, 5278-5284; f) S. Li, W. Miao, T. Tang, D. Cui, X. Chen and X. Jing, *J. Organomet. Chem.* **2007**, *692*, 4943-4952; g) G. Paolucci, M. Bortoluzzi, S. Milione and A. Grassi, *Inorg.*

*Chim. Acta* **2009**, *362*, 4353-4357; h) P. M. Zeimentz, T. P. Spaniol and J. Okuda, *Inorg. Chim. Acta* **2006**, *359*, 4769-4773.

[15] M. D. Brown, W. Levason, D. C. Murray, M. C. Popham, G. Reid and M. Webster, *Dalton Trans.* **2003**, 857-865.

[16] C. S. Tredget, F. Bonnet, A. R. Cowley and P. Mountford, *Chem. Commun.* **2005**, 3301-3303.

[17] E. A. V. Ebsworth, D. W. H. Rankin and S. Cradock, *Structural Methods in Inorganic Chemistry*, Blackwell Scientific Publications, Great Britain, **1987**.

[18] G. A. Melson, D. J. Olszanski and E. T. Roach, *Chem. Commun.* **1974**, 229-230.

[19] Y. A. Buslaev, G. A. Kirakosyan and V. P. Tarasov, *Koord. Khim.* **1980**, *6*, 361-371.

[20] L. Deakin, W. Levason, M. C. Popham, G. Reid and M. Webster, *Dalton Trans.* **2000**, 2439-2447.

[21] J. Mason, *Multinuclear NMR*, Springer, New York and London, **1987**.

[22] a) N. J. Hill, W. Levason, M. C. Popham, G. Reid and M. Webster, *Polyhedron* **2002**, *21*, 1579-1588; b) W. Levason, B. Patel, M. C. Popham, G. Reid and M. Webster, *Polyhedron* **2001**, *20*, 2711-2720.

[23] D. S. McGuinness, P. Wasserscheid, W. Keim, D. Morgan, J. T. Dixon, A. Bollmann, H. Maumela, F. Hess and U. Englert, *J. Am. Chem. Soc.* **2003**, *125*, 5272-5273.

[24] D. S. McGuinness, *Chem. Rev.* **2011**, *111*, 2321-2341.

[25] a) J. Scott, H. Fan, B. F. Wicker, A. R. Fout, M.-H. Baik and D. J. Mindiola, *J. Am. Chem. Soc.* **2008**, *130*, 14438-14439; b) J. Scott, T. Basuli, A. R. Fout, J. C. Huffman and D. J. Mindiola, *Angew. Chem. Int. Edit.* **2008**, *47*, 8502-8505; c) M. D. Fryzuk, G. Giesbrecht and S. J. Rettig, *Organomet.* **1996**, *15*, 3329-3336.

[26] A. A. Danopoulos and P. G. Edwards, *Polyhedron* **1989**, *8*, 1339-1344.

- [27] S. P. Downing, M. J. Hanton, A. M. Z. Slawin and R. P. Tooze, *Organomet.* **2009**, 28, 2417-2422.
- [28] J. O. Moulin, J. Evans, D. S. McGuinness, G. Reid, A. J. Rucklidge, R. P. Tooze and M. Tromp, *Dalton Trans.* **2008**, 1177-1185.
- [29] S. A. Bartlett, P. P. Wells, M. Nachtegaal, A. J. Dent, G. Cibin, G. Reid, J. Evans and M. Tromp, *J. Catal.* **2011**, 284, 247-258.
- [30] D. S. McGuinness, P. Wasserscheid, D. H. Morgan and J. T. Dixon, *Organomet.* **2005**, 24, 552-556.
- [31] a) D. E. Jordan, *Anal. Chem.* **1968**, 40, 2150-2153; b) H. Gilman and F. K. Cartledge, *J. Organomet. Chem.* **1964**, 2, 447-454.
- [32] L. E. Manzer, J. Deaton, P. Sharp and R. R. Schrock *Tetrahydrofuran Complexes of Selected Early Transition Metals*, 21 John Wiley & Sons, Inc., **1982**, pp. 135-140.
- [33] K. Wieghardt, P. Chaudhuri, B. Nuber and J. Weiss, *Inorg. Chem.* **1982**, 21, 3086-3090.
- [34] W. Weng, L. Yang, B. M. Foxman and O. V. Ozerov, *Organomet.* **2004**, 23, 4700-4705.
- [35] I. Krossing, H. Brands, R. Feuerhake and S. Koenig, *J. Fluorine Chem.* **2001**, 112, 83-90.
- [36] I. Krossing, *Chem. Eur. J.* **2001**, 7, 490-502.
- [37] A. J. Dent, G. Cibin, S. Ramos, A. D. Smith, S. M. Scott, L. Varandas, M. R. Pearson, N. A. Krumpa, C. P. Jones and P. E. Robbins, *J. Phys Conf. Ser.* **2009**, 190, 012039.
- [38] M. Newville, *J. Synchotron Radiat.* **2001**, 8, 322-324.
- [39] B. Ravel and M. Newville, *J. Synchotron Radiat.* **2005**, 12, 537-541.



## **Chapter 6.**

### **Freeze-quench Cr K-edge EXAFS: Insights into the Early Activation of Chromium Catalysed Ethene Oligomerisation.**

## 6.1 Introduction

The chromium catalysed trimerisation/tetramerisation of ethene is a very active and very specific route to produce highly desirable  $\alpha$ -olefins. The discovery and understanding of the exact activation and subsequent catalytic mechanism is of great academic and commercial interest. The intention of this introduction is to present published work from 2006 onwards, focusing on the activation of the pre-catalytic chromium complex. This is hoped to give a more relevant overview for the research presented in this chapter. The background and history of the chromium catalysed trimerisation and tetramerisation of ethene is given in the introduction chapter and has been published previously.<sup>[1]</sup>

### 6.1.1 Chromium SNS

In 2006, Gambarotta and coworkers investigated the reaction of  $[\text{CrCl}_x(\text{Cy-SNS})]$  ( $X = 2$  or  $3$ , Cy = cyclohexyl, SNS =  $\text{HN}(\text{CH}_2\text{CH}_2\text{S}-)_2$ ) with alkyl aluminiums, with the aim of isolating and characterising products from the reaction.<sup>[2]</sup> When reacting  $[\text{CrCl}_3(\text{Cy-SNS})]$  with 10 equivs. of  $\text{AlMe}_3$ , the dimeric complex shown in Fig. 6.1 was isolated as green crystals and characterised by X-ray crystallography. The amine had not been deprotonated and this was confirmed by IR spectroscopy and reflected by the bond length and the deviation of the nitrogen from the plane in the crystal structure.

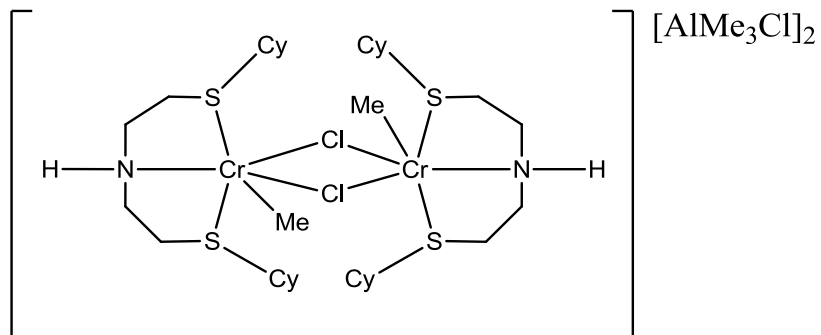
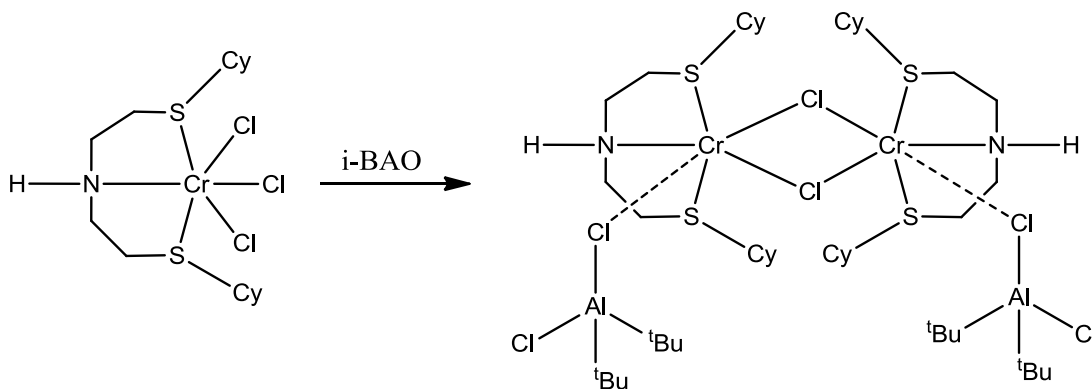


**Fig. 6.1** Chromium dimer complex formed after addition of 10  $\text{AlMe}_3$  to  $[\text{CrCl}_3(\text{Cy-SNS})]$ .

Reaction of  $[\text{CrCl}_3(\text{Cy-SNS})]$  with MAO (Methylaluminoxane) also afforded similar green crystals, although these were not suitable for X-ray crystallography. EPR (Electron paramagnetic resonance) spectra of these products from  $\text{AlMe}_3$  and MAO gave similar profiles, implying that the products are similar and no reduction by MAO has occurred. The IR spectrum of the chromium product after reaction with MAO gave an unaffected N-H peak.

Reaction of  $[\text{CrCl}_3(\text{Cy-SNS})]$  with iso-butyl aluminoxane (i-BAO) produced the Cr(II) dimer (Scheme 6.1). Both Cr(II) and Cr(III) dimers gave similar activities and >98 % selectivity, suggesting  $[\text{CrCl}_3(\text{Cy-SNS})]$  precursor leads to both oxidation states, which are both active for selective trimerisation.



**Scheme 6.1** Reduction of  $[\text{CrCl}_3(\text{Cy-SNS})]$  with iso-butyl aluminoxane (i-BAO) to give chromium(II) dimer.

On the basis of this evidence,  $[\text{CrCl}_2(\text{Cy-SNS})(\text{THF})]$  was synthesised directly and characterised by X-ray crystallography, where Cr-S bond distances were determined at  $\sim 2.85 \text{ \AA}$ . This Cr(II) complex gave similar activity and selectivity to that of trivalent chromium. This might suggest the Cr(III) species is a precursor to the active Cr(II) species.<sup>[2]</sup>

In contrast to this, the same group published research that suggested Cr(II) is the inactive oxidation state.<sup>[3]</sup> When reacting  $[\text{CrCl}_2(\text{THF})_2]$  with  $\text{AlEt}_2\text{Cl}$  in the presence of R-SNS (R = Ph or Cy), a cationic, monomeric square planar complex was obtained (Fig. 6.2). This complex was significantly less active than the dimeric products discussed above (Fig. 6.1).

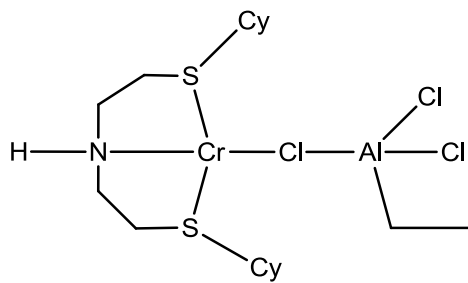
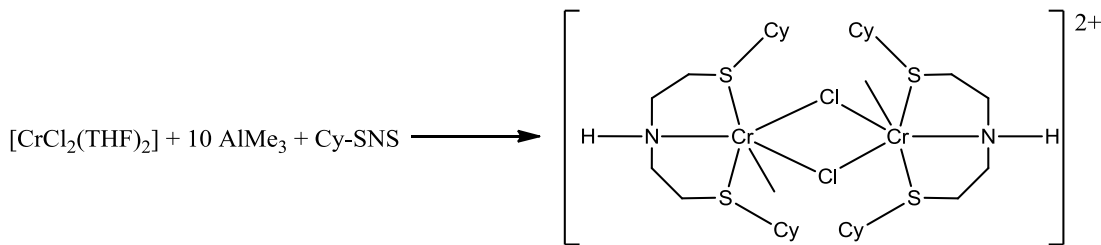


**Fig. 6.2** Isolated product from reaction of  $[\text{CrCl}_2(\text{THF})_2]$  + Cy-SNS +  $\text{AlEt}_2\text{Cl}$ .

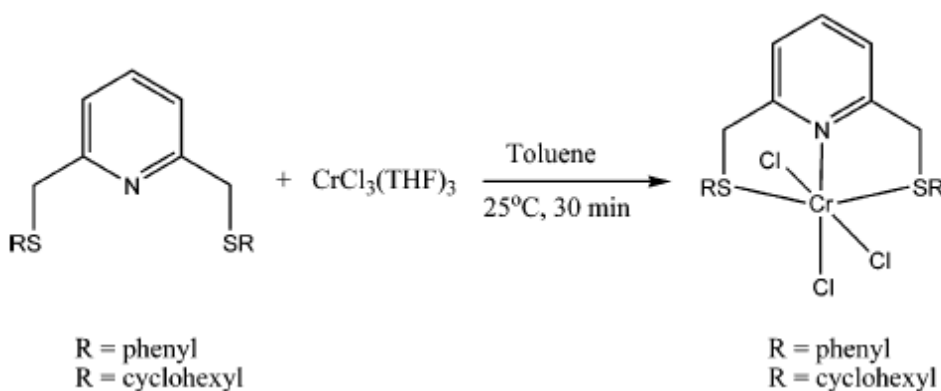
When using  $\text{AlMe}_3$  in place of  $\text{AlEt}_2\text{Cl}$ , Cr(II) had oxidised to give a Cr(III) dimer in one instance (Scheme 6.2). It was suggested the initial Cr(II) complex undergoes disproportionation to give the Cr(I)/Cr(III) complexes in solution.<sup>[3]</sup> This would explain why the Cr(II) dimer isolated originally gave comparable activities with Cr(III). This contradicts the original study, suggesting Cr(II) as the active oxidation state.<sup>[2]</sup>



**Scheme 6.2** Oxidation of Cr(II) precursor giving oxidised dimeric  $[\text{Cr}(\text{SNS})\text{Cl}]^{2+}$ .

A new type of SNS ligand incorporating a pyridine ring, 2,6-(CySCH<sub>2</sub>)<sub>2</sub>-pyridine, was coordinated to Cr(III) and Cr(II) chlorides complexes, and their activity towards ethene trimerisation was investigated.<sup>[4]</sup> The Cr(III) analogue was synthesised without difficulty (Scheme 6.3), whereas the corresponding Cr(II) complex could not be isolated cleanly and was reluctant to dissolve in any common organic solvent. When dissolved in CH<sub>2</sub>Cl<sub>2</sub>, the same product as given in Scheme 6.3 was isolated. When dissolved in THF, large amounts of the starting material,  $[\text{CrCl}_2(\text{THF})_2]$ , were

collected. This implies that the 2,6-(CySCH<sub>2</sub>)<sub>2</sub>-pyridine ligand is labile towards Cr(II) oxidation state. The catalytic activity of the impure [CrCl<sub>2</sub>(2,6-(CySCH<sub>2</sub>)<sub>2</sub>-py)] was comparable to the Cr(III) analogue but the selectivity of 1-C<sub>6</sub> production was significantly reduced (Cr(III) = 99.8 % [3883 g gCr<sup>-1</sup> h<sup>-1</sup>]; Cr(II) = 57. 2 % [5200 g gCr<sup>-1</sup> h<sup>-1</sup>]) for the same conditions (Al:Cr = 1000). This research suggest that the Cr(III) is the active and selective species for trimerisation. Also, as the [CrCl<sub>x</sub>(2,6-(CySCH<sub>2</sub>)<sub>2</sub>-py)] (X = 2 or 3) complexes gave modest activity at best, it is possible that removing the NH function of the SNS ligand stops the redox process and possibly inhibits the disproportionation from the Cr(II) complex to give the corresponding Cr(I)/Cr(III) pair.



**Scheme 6.3** Synthesis of [CrCl<sub>3</sub>(2,6-(CySCH<sub>2</sub>)<sub>2</sub>-py)] complex.<sup>[4]</sup>

In 2011, a self-activating catalyst was isolated from [CrCl<sub>3</sub>(2,6-(<sup>t</sup>BuSCH<sub>2</sub>)<sub>2</sub>-py)] and AlMe<sub>3</sub> (Fig. 6.3).<sup>[5]</sup>

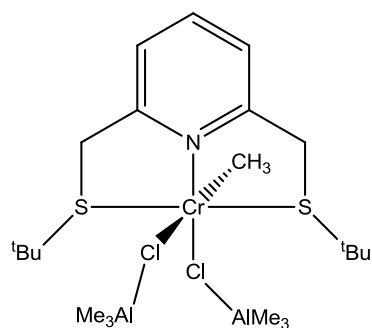
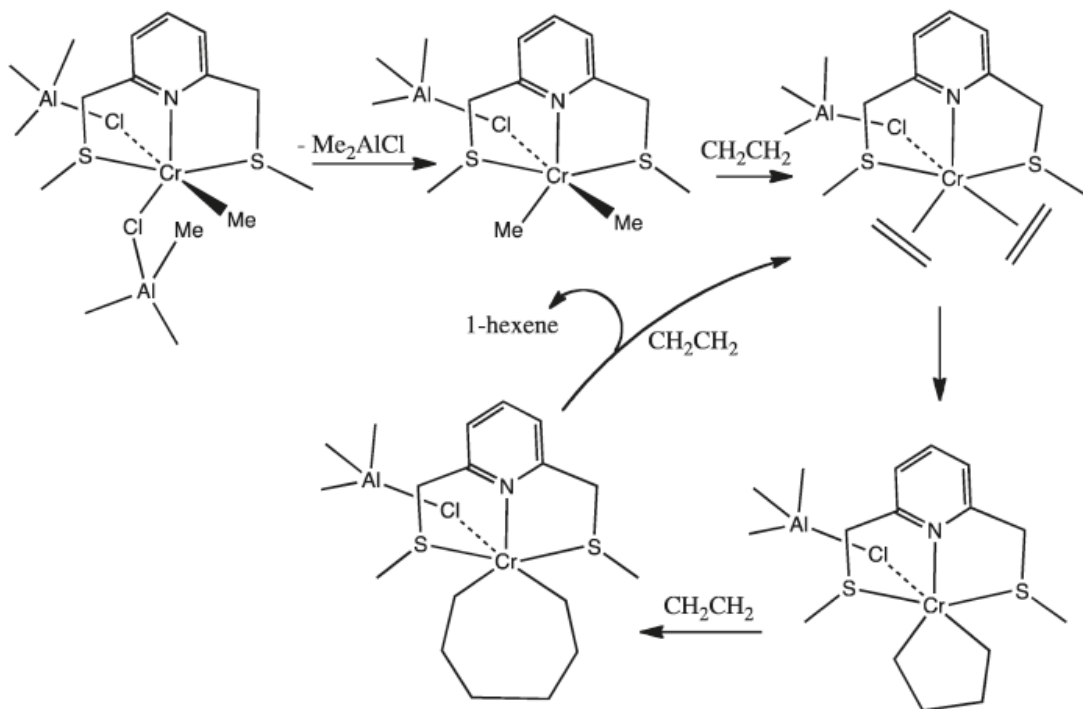


**Fig. 6.3** Self-activating catalyst formed from [CrCl<sub>3</sub>(2,6-(<sup>t</sup>BuSCH<sub>2</sub>)<sub>2</sub>-py)] and AlMe<sub>3</sub>.

Without further addition of aluminium activator, the chromium chloro bridged aluminium complex produced high purity 1-hexene. Scheme 6.4 shows the proposed pathway towards the production of 1-hexene by the chromium complex in Fig. 6.3. Self-activation was thought to proceed by dissociation of  $[\text{Me}_3\text{AlCl}]^-$ , followed by reductive elimination of the corresponding chromium dialkyl complex. The presence of  $\text{Al}-\text{Cl}_{\mu}-\text{Cr}$  would enhance the Lewis acidity of the Cr complex and the presence of higher ratios of aluminium activator would enhance this. This is observed as the activity is doubled in the presence of 1000 equivils of MAO.<sup>[5]</sup>



**Scheme 6.4** Proposed mechanism towards the production of 1-hexene from the isolated self-activating chromium catalyst.<sup>[5]</sup>

In contrast to Gambarotta, McGuinness reported that the amine function of  $[\text{CrCl}_3(\text{R-SNS})]$  should deprotonate during catalysis.<sup>[6]</sup> This conclusion was gathered after reacting  $[\text{CrCl}_3(\text{R-SNS})]$  with  $\text{LiCH}_2\text{SiMe}_3$  and DABCO (1,4-diazabicyclo(2.2.2)octane), where the N-H peak was not observed in the IR spectrum after reaction. Therefore they proposed it to be likely that MAO and  $\text{AlMe}_3$  would also deprotonate the amine.

The Cr(II) complex  $[\text{CrCl}_2(\text{THF})_2]$  was reacted with  $^t\text{Bu-SN}(\text{Li})\text{S}$  to give the amide bridged dimer, of which the crystal structure is shown in Fig. 6.4.

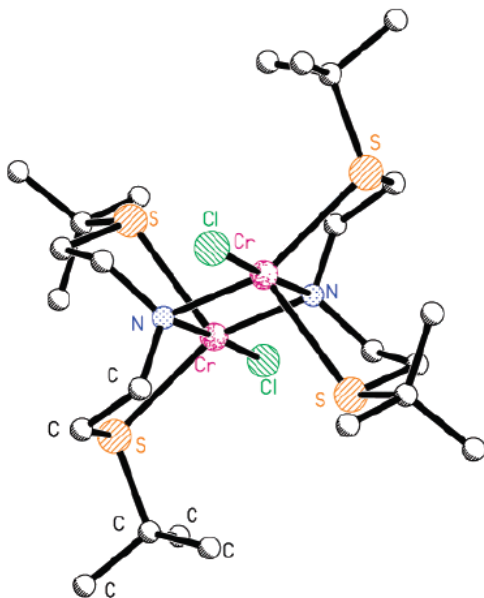
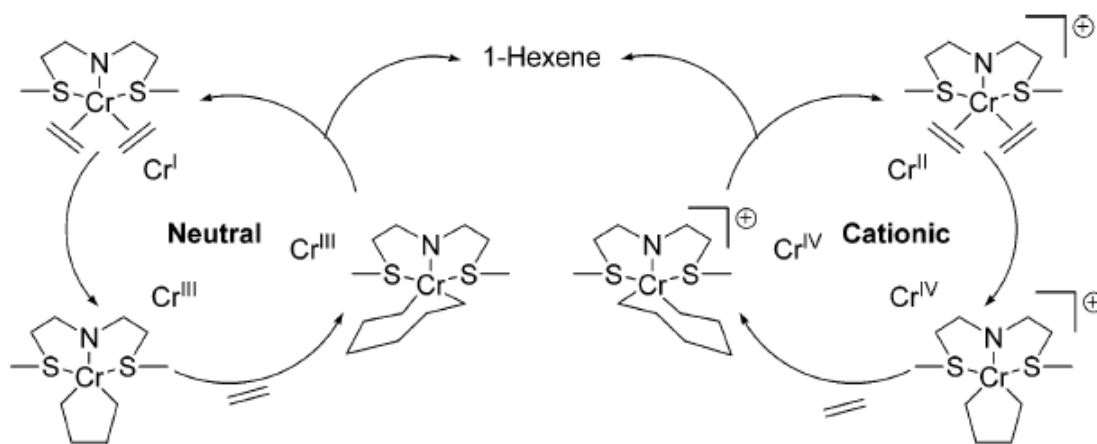


**Fig. 6.4** Crystal structure for  $[\text{CrCl}(^t\text{Bu-SNS})]_2$  with bridging amide.<sup>[6]</sup>

This structure gives Cr-N bond distances of  $\sim 2.07 \text{ \AA}$ , Cr-S<sup>t</sup>Bu of  $\sim 2.60 \text{ \AA}$  and a Cr···Cr distance of  $2.98 \text{ \AA}$ . When reacted with 300 MAO and tested for ethene oligomerisation, it gave an activity of 4785 mol ethene /mol Cr/h and selectivity of C<sub>6</sub> of 45.2 %, which is  $\frac{1}{4}$  of the activity given by the  $[\text{CrCl}_3(^t\text{Bu-SNS})]$ . It is claimed that because this species is active, it lends support to process of deprotonation of the amine during catalysis. Reaction of  $[\text{CrCl}_3(\text{THF})_3]$  and  $^t\text{Bu-SN}(\text{Li})\text{S}$  gave an unwanted side product of  $[\text{Cr}(\text{THF})_2\text{Cl}_2(\mu\text{-Cl})_2\text{Li}(\text{THF})_2]$ .<sup>[6]</sup>

The same study investigated a similar ligand of  $\text{HN}(\text{CH}_2\text{CH}_2\text{PPh}_2)_2$ . When complexed to Cr(II) to give  $[\text{CrCl}_2(\text{HN}(\text{CH}_2\text{CH}_2\text{PPh}_2)_2)]$ , this complex readily converted to  $[\text{CrCl}_3(\text{HN}(\text{CH}_2\text{CH}_2\text{PPh}_2)_2)]$  in  $\text{CH}_2\text{Cl}_2$ . In this case the Cr(II) complex gave similar activity to that of the corresponding Cr(III) complex with MAO,  $\sim 25,000$  mol ethene /mol Cr/h. This suggests the Cr is reduced upon reaction with aluminium activator, supposing the complex is not oxidised by MAO indirectly, which was discussed as possibility by Gambarotta, which would mean the Cr(II) could also be oxidised to the active Cr(III).<sup>[2]</sup>

Based on the evidence of these  $^t\text{Bu-SNS}$  and  $\text{HN}(\text{CH}_2\text{CH}_2\text{PPh}_2)_2$  complexes, it is thought the role of MAO is to deprotonate the ligand, reduce the complex and generate the counterion. In light of this, two possible mechanistic cycles were proposed to generate 1-C<sub>6</sub> selectively; a neutral Cr(I)/Cr(III) cycle or the cationic Cr(II)/Cr(IV) cycle (Scheme 6.5).<sup>[6]</sup>



**Scheme 6.5** Proposed mechanistic cycles of Cr-SNS complex for selective ethene trimerisation; neutral Cr(I)  $\rightarrow$  Cr(III) and cationic Cr(II)  $\rightarrow$  Cr(IV) cycles where the amine is deprotonated in both case.<sup>[6]</sup>

Chromium(III) complexes with all hard ( $\text{N}_3$ ) or soft ( $\text{S}_3$ ) ligands were investigated by UV-Vis and XAFS spectroscopy.<sup>[7]</sup> The compound  $[\text{CrCl}_3(\text{decyl-S}_3)]$  (decyl-S<sub>3</sub> =  $\text{S}(\text{CH}_2\text{CH}_2\text{S}^n\text{C}_{10}\text{H}_{21})_2$ ) gave selective 1-C<sub>6</sub> activity, but was only active for a few minutes. It was supposed that the complex decomposed as the thioether ligand was lost, which was based on EXAFS analysis. The UV-Vis data of  $[\text{CrCl}_3(\text{decyl-S}_3)]$  with 5 equivs. of  $\text{AlMe}_3$  displayed a colour change of purple to yellow/green and the two original bands ( $14,300$  and  $19,330 \text{ cm}^{-1}$ ) change to give single band at ( $16015 \text{ cm}^{-1}$ ). The EPR data of the same reaction goes silent upon reaction. These observations would suggest an oxidation state change from Cr(III) to Cr(II). The EXAFS of this reaction shows complete substitution of chloride for carbon at  $\sim 2.10 \text{ \AA}$  and a coordination of only 0.3 S at  $\sim 2.45 \text{ \AA}$ . This suggests the complex is

decomposing, especially after long EXAFS data acquisition time of 1-3 h at which this data was obtained.<sup>[7]</sup>

### 6.1.2 Chromium PNP

The activation of the chromium R-N(PPh<sub>2</sub>)<sub>2</sub> (PNP) ethene terramerisation system has been investigated by Gambarotta (where R = Cy).<sup>[8]</sup> The reaction of [(PNP)CrCl<sub>3</sub>]<sub>2</sub> with 10 AlMe<sub>3</sub> yielded the divalent monomer shown in Fig. 6.5.

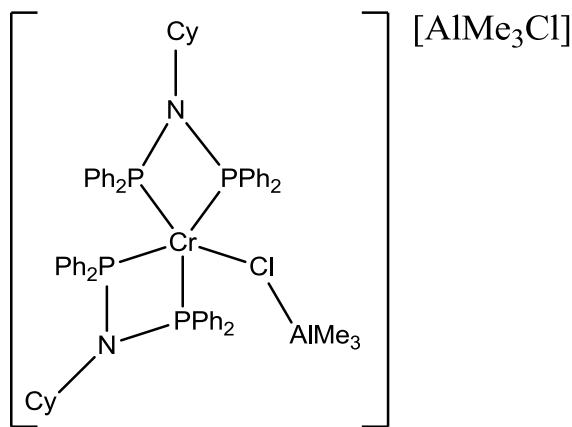


**Fig. 6.5** Isolated monomeric divalent Cr(PNP) species upon reaction with 10 equivalents of AlMe<sub>3</sub>.

The pre-catalyst has been reduced to Cr(II), which was confirmed by X-ray crystallography and magnetic susceptibility measurements. The catalysis of this complex gave very similar results to that of its precursor, [(PNP)CrCl<sub>3</sub>]<sub>2</sub>. As the product contains two PNP ligands, this would imply another chromium species is present in solution, which in this case is completely unknown.<sup>[8]</sup>

The reaction of [CrCl<sub>2</sub>(THF)<sub>2</sub>] with the PNP ligand did not proceed, even after reflux in THF or toluene for 12 h. The reaction of [CrCl<sub>2</sub>(THF)<sub>2</sub>] with the PNP ligand only proceeded upon addition of AlMe<sub>3</sub>, giving the same product as seen in Fig. 6.5. This implies that the Cr(II) can only be stabilised by two PNP ligands and a counterion.<sup>[8]</sup>

Many of these studies have arisen from the isolation and characterisation of intermediates and their subsequent performance in catalysis. This could be

problematic because as the complexes crystallise from solution they will most likely take up lowest energy forms and possibly undergo reversible or irreversible transformations. Therefore, the real species may not be observed under these conditions and the active species may not drop out of solution without decomposition.

## 6.2 Aims

The research of this chapter investigates already existing chromium trimerisation catalysts  $[\text{CrCl}_3(\text{decyl-SNS})]$  and  $[\text{CrCl}_3(\text{decyl-S}_3)]$ , and the tetramerisation catalyst  $[\text{CrCl}_3(\text{PNP})(\text{THF})]$ , using the previously validated, stopped-flow freeze-quench EXAFS spectroscopy (Chapter 3). This technique provides an insight into the activation of these highly selective catalysts, using 20 equivs. of  $\text{AlMe}_3$  and characterisation at predetermined time scales. Once the reaction is frozen, it effectively stalls the reaction to allow the structural characterisation of the intermediates that have been formed.

Typically, EXAFS data was collected for samples frozen at 1s and 5 min reaction time for the chromium complexes  $[\text{CrCl}_3(\text{decyl-SNS})]$  and  $[\text{CrCl}_3(\text{decyl-S}_3)]$  with 20 equivs.  $\text{AlMe}_3$ . Proceeding reactions with trityl aluminate and 1-hexene were also investigated by freezing reactions at 1 min.

The catalyst  $[\text{CrCl}_3(\text{PNP})(\text{THF})]$  was also investigated by the freeze-quench technique with the same reagents. Due to the insolubility in toluene, this reaction was analysed at 1 min and 5 min reaction with 20  $\text{AlMe}_3$ , and again at 1 min using trityl aluminate and 1-hexene. As the stopped-flow freeze-quench apparatus could not be used, the reaction was done in a Schlenk tube under anaerobic conditions and injected into a pre-purged Kapton tube at the pre-determined times, which was instantly frozen using liquid  $\text{N}_2$ .

From these experiments it is possible to identify the products that exist in the solution phase at the early stages of the reaction, rather than previous experiments by EXAFS spectroscopy where, because of the long EXAFS data acquisition times of hours for these *in situ* solutions at the Cr K edge, end state and decomposition products were more likely to be investigated.<sup>[7]</sup>

## 6.3 Results and Discussion

### 6.3.1 Synthesis of Chromium Complexes

The chromium complexes  $[\text{CrCl}_3(\text{decyl-SNS})]$  (decyl-SNS =  $\text{HN}(\text{CH}_2\text{CH}_2\text{S}^-\text{decyl})_2$ ) and  $[\text{CrCl}_3(\text{decyl-S}_3)]$  (decyl-S<sub>3</sub> =  $\text{S}(\text{CH}_2\text{CH}_2\text{S}^-\text{decyl})_2$ ) were synthesised with no deviations from reported methods.<sup>[7, 9]</sup> The precursor complex  $[\text{CrCl}_3(\text{THF})_3]$  was dissolved in dry  $\text{CH}_2\text{Cl}_2$  where the ligand was added and stirred overnight under inert atmosphere (Ar). The solvent was then removed *in vacuo* and the remaining solid was washed with dry hexane to yield a dark green ( $[\text{CrCl}_3(\text{decyl-SNS})]$ ) or purple ( $[\text{CrCl}_3(\text{decyl-S}_3)]$ ) powder which was stored under inert atmosphere in the glove-box. IR and UV-Vis spectroscopy were in accordance with the previously published data.

The chromium complex  $[\text{CrCl}_3(\text{PNP})(\text{THF})]$  (PNP =  ${}^i\text{PrN}(\text{PPh}_2)_2$ ) was synthesised ca. 6 h before EXAFS analysis using the previously published method.<sup>[10]</sup> This was to minimise the possibility of forming an insoluble dimeric complex, as observed by X-ray crystallography.<sup>[11]</sup> This was done by dissolving the  $[\text{CrCl}_3(\text{THF})_3]$  in dry  $\text{CH}_2\text{Cl}_2$ , at which point the ligand was added in dry  $\text{CH}_2\text{Cl}_2$ . This was allowed to stir for 1 h under inert atmosphere (Ar) where the solution was removed *in vacuo* and the subsequent solid was stored in the glove box under inert atmosphere. This gave a dark blue solid with no traces of the light purple starting material.

### 6.3.2 Cr K-edge XAFS analysis

Solution Cr K-edge XAFS spectra were collected for the starting materials under inert atmosphere at 6 mmol in toluene, at room temperature. Three spectra were collected at 15 mins per spectrum and the data averaged for each of the three complexes  $[\text{CrCl}_3(\text{decyl-SNS})]$ ,  $[\text{CrCl}_3(\text{decyl-S}_3)]$  and  $[\text{CrCl}_3(\text{PNP})(\text{THF})]$ . The analyses of these complexes are shown in Table 6.1. Solid state spectra were also collected for each, pressed in dry BN under inert atmosphere. These were overlaid with the solution spectra and are near identical in each case. A representative EXAFS fit is shown in Fig. 6.6 for  $[\text{CrCl}_3(\text{decyl-SNS})]$  in toluene.

**Table 6.1** Cr K-edge EXAFS data analyses for solutions of  $[\text{CrCl}_3(\text{L})]$  in toluene.

CN Absorber - Scatterer <sup>a</sup>	$R / (\text{\AA})$	$2\sigma^2 / (\text{\AA}^{-2})$	Fitting Factors
$[\text{CrCl}_3(\text{decyl-SNS})]$			
1 Cr-N	2.07(4)	0.003(3)	$2.4 < k < 14$ , $1.1 < R < 2.7$
2 Cr-S	2.45 <sup>a</sup>	0.009(4)	$E_0 = 4(1)$ , $R = 0.0007$
3 Cr-Cl	2.32 <sup>a</sup>	0.004(1)	$k_w = 3$
$[\text{CrCl}_3(\text{decyl-S}_3)]$			
3 Cr-S	2.45 <sup>a</sup>	0.008(5)	$3.3 < k < 12$ , $1.1 < R < 2.6$
3 Cr-Cl	2.30 <sup>a</sup>	0.005(1)	$E_0 = 2(2)$ , $R = 0.009$ $k_w = 2,3$
$[\text{CrCl}_3(\text{PNP})(\text{THF})]$			
1 Cr-O	2.10 <sup>a</sup>	0.001(8)	$2.2 < k < 10$ , $1.1 < R < 2.8$
2 Cr-P	2.40(7)	0.006(3)	$E_0 = 4(2)$ , $R = 0.009$
3 Cr-Cl	2.26 <sup>a</sup>	0.009(6)	$k_w = 1,2,3$

<sup>a</sup>Fixed parameters, Amp = 0.85.

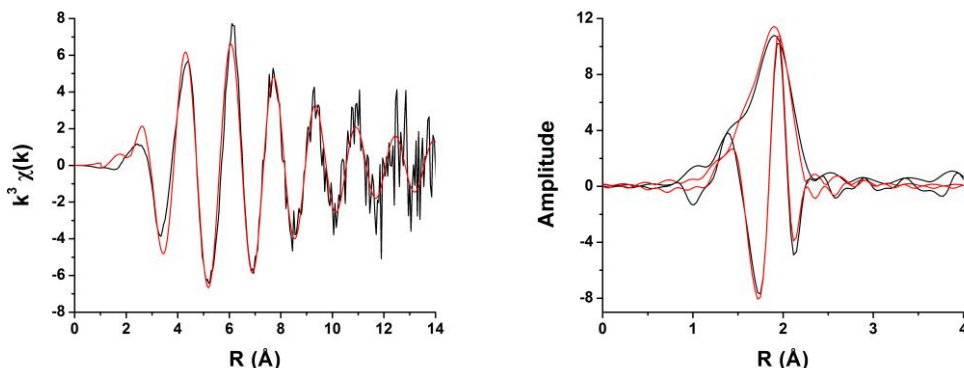


**Fig. 6.6** Cr K-edge  $k^2$ -weighted EXAFS and Fourier transform data (black) and fits (red) for  $[\text{CrCl}_3(\text{decyl-SNS})]$  in toluene.

The fitting of this data was modelled using the reported crystal structures;  $[\text{CrCl}_3(\text{Et-SNS})]^{[9]}$  for  $[\text{CrCl}_3(\text{decyl-SNS})]$ ,  $[\text{CrCl}_3(\text{[18]aneS}_6)]^{[12]}$  for  $[\text{CrCl}_3(\text{decyl-S}_3)]$  and  $[\text{CrCl}_3(\text{PNP})(\text{MeCN})]^{[13]}$  for  $[\text{CrCl}_3(\text{PNP})(\text{THF})]$ . In cases where the

distances were fixed, these were based on the data provided from the crystal structures. The bond distances were first fixed at the reported lengths given by the crystal data and then the distance was adjusted accordingly to the point at which the fixed distance gave the best fit value to the raw data. In this way the bond distances in the above table are either the same as the reported crystal distances for that bond or very close to the reported value. The data were required to be fit in this way due in part to poor data and because of neighbouring atoms of chromium having similar atomic numbers (i.e. sulfur, chlorine, phosphorus) and so, have similar backscattering amplitudes making contributions difficult to distinguish in the EXAFS. Moreover, these contributions are overlapping, so when all fitting parameters are set as variables, one shell is found with an average of all values given at the minimum, giving a high Debye-Waller factor as the distances between Cl and S are relatively large (seeing a high static disorder). The low Debye-Waller factors given for the fixed distances provide good evidence that the contribution and coordination is genuine at that distance.

### 6.3.2.1 Freeze-quench [CrCl<sub>3</sub>(decyl-SNS)] + 20 AlMe<sub>3</sub> in Toluene

The [CrCl<sub>3</sub>(decyl-SNS)] complex was reacted with 20 mol equivs. of AlMe<sub>3</sub> and freeze-quenched at 1s and 5 min. These were then analysed by EXAFS spectroscopy. No major speciation changes were observed between the samples characterised after 1s and after 5 min and so only the analysis at 1 s is presented in Table 6.2.

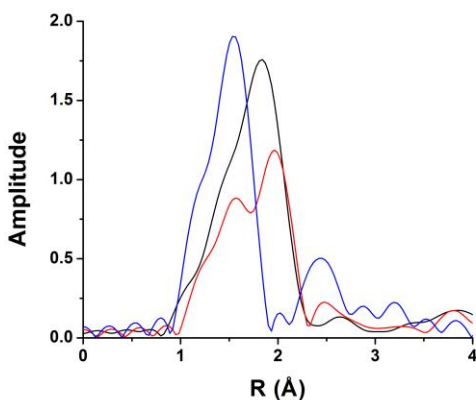


**Fig. 6.7** Cr K-edge  $k^2$ -weighted Fourier transform EXAFS data for  $[\text{CrCl}_3(\text{decyl-SNS})]$  (black),  $[\text{CrCl}_3(\text{decyl-SNS})] + 20 \text{ AlMe}_3$ , freeze-quenched at 1 s (red) and  $[\text{CrCl}_3(\text{decyl-SNS})] + 4 \text{ MeLi}$  in the XAFS solution cell (blue) in toluene.

**Table 6.2** Cr K-edge EXAFS data analyses for the reaction of  $[\text{CrCl}_3(\text{decyl-SNS})]$  with 20 equivs.  $\text{AlMe}_3$  in toluene, freeze-quenched after 1 s.

CN Absorber - Scatterer	$R /(\text{\AA})$	$2\sigma^2/(\text{\AA}^{-2})$	Fitting Factors
1.4(3) Cr-N	2.02(2)	0.000(2)	$2.4 < k < 13, 1.1 < R < 3.5$
2 <sup>a</sup> Cr-S	2.46(2)	0.002(2)	$E_0 = 3(1)$
1 <sup>a</sup> Cr-Cl	2.32(3)	0.000(3)	$R = 0.008$

<sup>a</sup>Fixed parameters, Amp = 0.85, k-weight = 1,2,3

The EXAFS analysis of the reaction  $[\text{CrCl}_3(\text{decyl-SNS})]$  with 20 mol equivs. of  $\text{AlMe}_3$  gives a low overall coordination number of four around the chromium. The Cr-N at  $2.02(2) \text{ \AA}$  was refined to coordination of 1.4(3) which is shorter than the distance given for the starting material ( $2.07(4) \text{ \AA}$ ) and the crystallographically determined distance for  $[\text{CrCl}_3(\text{Et-SNS})]$  ( $2.10 \text{ \AA}$ ). Coordination of two sulfurs at  $2.46(3) \text{ \AA}$  show the SNS ligand is still coordinated and remains intact. Also, one Cl is still coordinated at  $2.32(3) \text{ \AA}$ . The coordination of these shells were set at these values because higher or lower coordination numbers were reflected in the Debye-Waller

factor as giving too high or too low contribution to the overall fit. Setting these values as variables gave high uncertainty around the set values as given in Table 6.2, most likely due to the problem of Cl and S having similar backscattering amplitudes as discussed previously. From this analysis, a complex of similar geometry to a crystal structure determined by Gambarotta is proposed (Fig. 6.2) and so, this data was used to help model the EXAFS data.<sup>[3]</sup> The determined complex is shown in Fig. 6.8. The Gambarotta crystal structure shows a long interaction of Al-Cl- - -Cr(II) along the z-axis. This was not seen in the EXAFS spectrum but may not be observable due to it being a long range interaction or having a high disorder because of the solution EXAFS and so, its presence cannot be discounted completely.

The XANES analysis of the edge position also corroborates with the EXAFS analysis, which shows that if any alkylation at the chromium (of Cr(II) or Cr(III)) occurred, this would shift the edge to a higher energy with respect to the starting material, whereas an edge shift to lower energy is observed when chloride is retained without any alkylation for a Cr(II) oxidation state.<sup>[14]</sup>

The change in pre-edge features before and after reaction with AlMe<sub>3</sub> also suggest a change in the geometry around chromium has occurred, moving from a weak pre-edge absorption for the starting complex, to a slightly more intense absorption after reaction with AlMe<sub>3</sub>, which XANES simulations indicated a change from octahedral to square planar coordination (Fig. 6.9).

The proposed four-coordinate complex from the EXAFS analysis was predicted to give the experimentally observed edge shift, based on the crystal structure collected by Gambarotta (Fig. 6.2). This crystal structure gives a cationic Cr(II) complex where the amine remains protonated, formed from an intial Cr(II) complex. In our case, we have an oxidation state change from Cr(III) to Cr(II) and the EXAFS analysis suggests a shorter Cr-N distance then that given by the four-coordinate complex determined by Gambarotta at 2.09 Å, this may be a small indication that the amine has formed an amide.

Not many crystallographic examples of Cr(II) methyl bonds are available in the literature, but two of the more similar systems give Cr-C bond lengths as 2.13 Å for a [(N<sub>2</sub>P<sub>2</sub>)CrMe] complex of distorted trigonal bipyramidal geometry<sup>[15]</sup> {N<sub>2</sub>P<sub>2</sub> = <sup>t</sup>BuN(H)SiMe<sub>2</sub>N(CH<sub>2</sub>CH<sub>2</sub>P<sup>i</sup>Pr<sub>2</sub>)<sub>2</sub>} and 2.09 Å for a Y-shape [(nacnac)CrMe] complex<sup>[16]</sup> (nacnac = (2,6-<sup>i</sup>Pr<sub>2</sub>C<sub>6</sub>H<sub>3</sub>)NC(<sup>t</sup>Bu)]<sub>2</sub>CH<sup>-</sup>). These complexes also give Cr amide distances shorter at 2.07 and 1.98 Å respectively. Based on this evidence, the

distance given by EXAFS of Cr-N indicates the observed 2.02(2) Å is likely to be a nitrogen bond rather than a carbon bond.

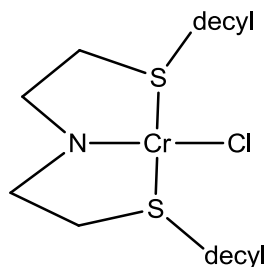


**Fig. 6.8** Activated  $[\text{CrCl}_3(\text{decyl-SNS})]$  catalyst proposed by XAFS.

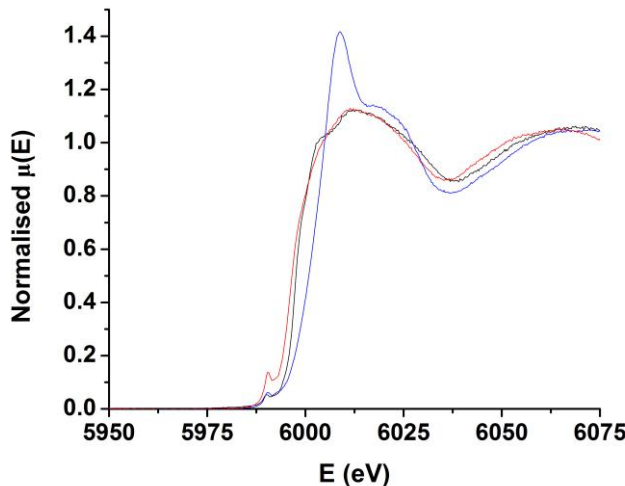


**Fig. 6.9** Cr K-edge normalised XANES spectra for solution  $[\text{CrCl}_3(\text{decyl-SNS})]$  (black),  $[\text{CrCl}_3(\text{decyl-SNS})] + 20 \text{ AlMe}_3$ , freeze-quenched at 1 s (red) and  $[\text{CrCl}_3(\text{decyl-SNS})] + 4 \text{ MeLi}$  in the XAFS cell (blue), in toluene.

Further reactions with the addition of a Lewis acid, trityl aluminate ( $[\text{Ph}_3\text{C}][\text{Al}(\text{OC}^{\text{t}\text{Bu}^{\text{F}}})_3]_4$ ) and 1-hexene with the addition of  $\text{AlMe}_3$  were undertaken in similar fashion, and samples were frozen after 1 min of reaction. The addition of trityl aluminate in this case gave no significant changes, giving identical spectra to that observed for  $[\text{CrCl}_3(\text{decyl-SNS})] + 20 \text{ AlMe}_3$  at 1s and 5 min.

The spectra obtained with the addition of trityl aluminate and 1-hexene had high signal-to-noise and was only reliable up to  $\sim 10 \text{ \AA}^{-1}$  in  $k$ , upto which no changes were observed from the intial reaction with  $\text{AlMe}_3$ .

### 6.3.2.1.1 Stopped-flow UV-Vis Analysis of $[\text{CrCl}_3(\text{decyl-SNS})] + 10 \text{ AlMe}_3$

As shown in Chapter 3, the reaction of  $[\text{CrCl}_3(\text{decyl-SNS})]$  with 10 equivs. of  $\text{AlMe}_3$  was observed by UV-Vis spectroscopy in the stopped-flow instrument. A fast initial reaction occurs, at which point the absorbance decreases slowly over time. This data is shown again in Fig. 6.10 and 6.11. The same reaction was repeated with 20 mol equivs. of  $\text{AlMe}_3$  to give the same changes, except at a faster rate making it more difficult to follow by UV-Vis spectroscopy, especially as the early stages are difficult to follow due to the turbulence of the system. The reaction of  $[\text{CrCl}_3(\text{decyl-SNS})]$  with 10 mol equivs. of  $\text{AlMe}_3$  was freeze-quenched at 1 s to give identical EXAFS data to that using 20 equivs.  $\text{AlMe}_3$ .

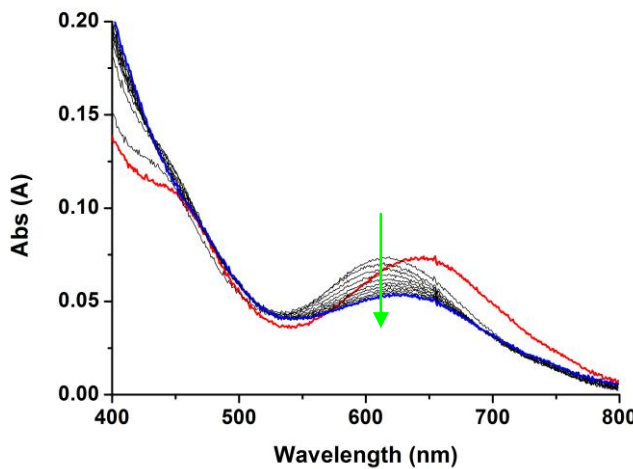


**Fig. 6.10** UV-Vis spectra showing reaction of 5 mM  $[\text{CrCl}_3(\text{decyl-SNS})]$  + 10  $\text{AlMe}_3$  in toluene at 2 s intervals, with red spectrum representing start point and blue representing last collected spectrum (red = 2s, black = 2s intervals, Blue = 29 s; green arrow = direction of time).

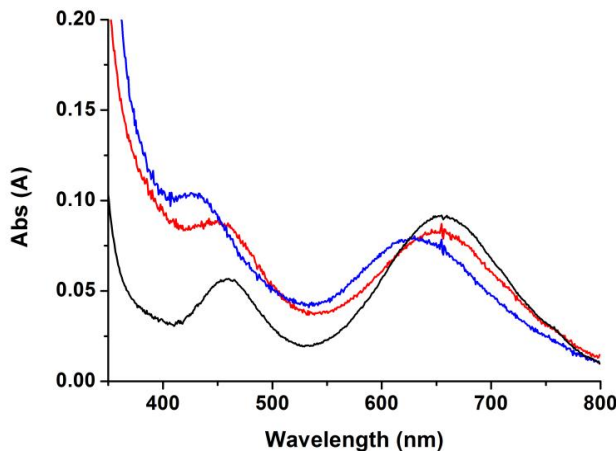


**Fig. 6.11** UV-Vis spectra showing reaction of 5 mM  $[\text{CrCl}_3(\text{decyl-SNS})]$  + 10  $\text{AlMe}_3$  in toluene at rate of 2 ms/spectrum (black = unreacted complex, red = 1.120 s, blue = 1.122 s).

The XAFS analysis suggests a square planar complex is formed after reaction with  $\text{AlMe}_3$ . Using the Russell-Saunders coupling scheme for Cr(II) ( $d^4$ ), this gives a free ion ground state term of  ${}^5\text{D}$ . This leads to  ${}^5\text{T}_{2g}$  +  ${}^5\text{E}_g$  terms in an octahedral field which further splits in a square planar ligand field to give the ground state term  ${}^5\text{E}_g$  leading to three spin allowed  ${}^5\text{A}_{1g}$  +  ${}^5\text{B}_{1g}$  +  ${}^5\text{B}_{2g}$ .<sup>[17]</sup>

After the reaction a significant shift of the transitions is observed to give 16,200 and 23,530 (sh)  $\text{cm}^{-1}$ . The solvent cut-off point moves up to  $\sim 450$  nm from 350 nm obscuring much of the spectrum. For a high-spin complex, the observed transition most likely correspond to the  ${}^5\text{E}_g (\text{d}_{xz}, \text{d}_{yz}) \rightarrow {}^5\text{B}_{1g} (\text{d}_x^2 - \text{d}_y^2)$  and  ${}^5\text{B}_{2g} (\text{d}_{xy}) \rightarrow {}^5\text{B}_{1g} (\text{d}_x^2 - \text{d}_y^2)$  transitions.

### 6.3.2.2 $[\text{CrCl}_3(\text{decyl-SNS})] + 4 \text{ MeLi}$

$[\text{CrCl}_3(\text{decyl-SNS})] + 4$  mol equivs. of MeLi was reacted at  $-78^\circ\text{C}$  to give a red solution in toluene, which was analysed by XAFS at room temperature in the XAFS solution cell. It was then characterised by Cr K-edge EXAFS spectroscopy. The analysis is presented in Table 6.3 and the Fourier Transform EXAFS data shown in Fig. 6.7.

**Table 6.3** Cr K-edge EXAFS data analyses for the reaction of [CrCl<sub>3</sub>(decyl-SNS)] with 4 mol equivs. MeLi in toluene.

CN Absorber - Scatterer <sup>a</sup>	R /(\Å)	2σ <sup>2</sup> /(\Å <sup>-2</sup> )	Fitting Factors <sup>b</sup>
5(1) Cr-C/N	2.03(2)	0.001(2)	3.0< k <11, 1.1< R <3.1
2 <sup>a</sup> Cr-S	3.10(5)	0.006(7)	E <sub>0</sub> = -4(2), R=0.03 kw = 1,2

<sup>a</sup>Fixed parameters, Amp = 0.85.

The EXAFS analysis of the reaction [CrCl<sub>3</sub>(decyl-SNS)] with 4 mol equivs. MeLi in toluene gives Cr-N/C at 2.03(2) Å with a coordination of 5(1) and 2 Cr-S at long distance of 3.10(5) Å. This shows all chloride has been substituted for methyl groups and a long interaction from the sulfur atoms on the ligand are observed at 3.10(5) Å. This indicates the Cr-S bond has weakened to a long-range interaction. The reaction of [CrCl<sub>3</sub>(SNS)] with LiCH<sub>2</sub>SiMe<sub>3</sub>, a similar alkyl lithium, has previously been shown to deprotonate the amine and so it is highly likely this occurs within this system forming an amide which most likely helps keep the SNS ligand coordinated.<sup>[6]</sup> It has been suggested previously that the sulfurs of the SNS ligand can act as hemilabile donors, which is possibly why long distance Cr-S interaction is observed here. Study of the similar [ScCl<sub>3</sub>(decyl-SNS)] + MeLi (Chapter 5) indicated the ligand did deprotonate and exchange chlorides for methyl groups where the Sc-S bonds had moved to much longer ~ 3 Å.

As Cl and S are indistinguishable by EXAFS analysis, this contribution is assigned as a long distance Cr-S contribution as a large edge shift to higher energy is observed, where retention of Cl is not likely to shift the edge quite so significantly. Inclusion of a Cl shell raised the E<sub>0</sub> value closer to -10 eV, indicating a Cr-Cl contribution would give a significant shift which is not observed. XANES calculations have shown alkylated systems with similar geometry would shift the edge position to higher energy, this would be true for other coordinated light elements. Where an edge shift is not observed or shifted to lower energy, this indicates that Cl is still retained and/or the coordination has decreased from six as seen in the reaction with AlMe<sub>3</sub> for this system. Based on these theoretical observations and the

experimental observation of LiCl precipitation, helps conclude that the chlorides have been substituted by methyl groups.

### 6.3.2.3 [CrCl<sub>3</sub>(decyl-S<sub>3</sub>)] + 20 AlMe<sub>3</sub>

The [CrCl<sub>3</sub>(decyl-S<sub>3</sub>)] complex was reacted with 20 mol equivs. of AlMe<sub>3</sub> and freeze-quenched at 1 s and 5 min, in toluene. These were then analysed by Cr K-edge EXAFS spectroscopy. The analyses at both these time frames are presented in Table 6.4 and Fourier Transform EXAFS data shown in Fig. 6.12.

**Table 6.4** Cr K-edge EXAFS data analyses for the reaction of [CrCl<sub>3</sub>(decyl-S<sub>3</sub>)] with 20 equivs. AlMe<sub>3</sub> in toluene, freeze-quenched after 1 s and 5 min.

CN Absorber - Scatterer <sup>a</sup>	R /(\AA)	2σ <sup>2</sup> /(\AA <sup>-2</sup> )	Fitting Factors <sup>b</sup>
<i>[CrCl<sub>3</sub>(decyl-S<sub>3</sub>)] + 20 AlMe<sub>3</sub> – RT = 1 s</i>			
1 <sup>a</sup> Cr-C	2.05(7)	0.002(6)	2.4< k < 12, 1.1 < R < 3.3
1 <sup>a</sup> Cr-Cl	2.32(4)	0.000(5)	E <sub>0</sub> = 3(2), R = 0.003
2.7(9) Cr-S	2.46(3)	0.003(5)	k <sub>w</sub> = 2,3
<i>[CrCl<sub>3</sub>(decyl-S<sub>3</sub>)] + 20 AlMe<sub>3</sub> – RT = 5 min</i>			
1 <sup>a</sup> Cr-C	2.10(6)	0.003(6)	2.4 < k < 12, 1.1 < R < 2.9
3.7(8) Cr-S	2.47(2)	0.009(3)	E <sub>0</sub> = 3(1), R = 0.02 k <sub>w</sub> = 1,2,3

<sup>a</sup>Fixed parameters. Amp = 0.85.

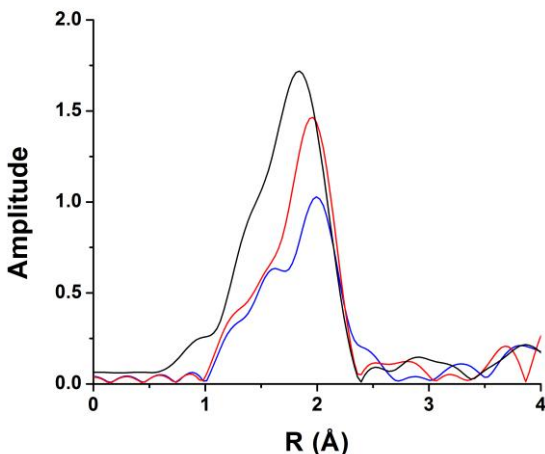
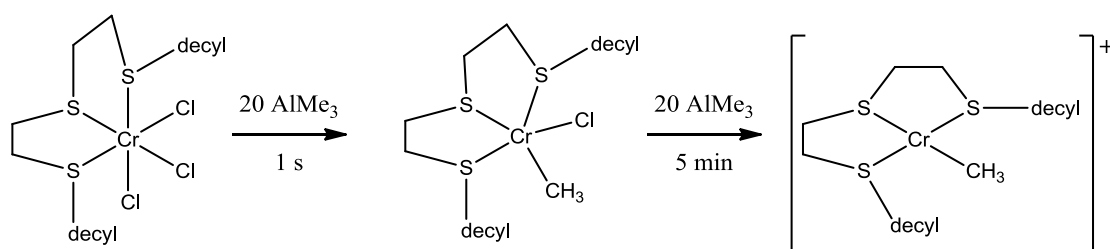


**Fig. 6.12** Cr K-edge  $k^2$ -weighted Fourier transform EXAFS data for  $[\text{CrCl}_3(\text{decyl-S}_3)]$  in toluene (black),  $[\text{CrCl}_3(\text{decyl-S}_3)] + 20 \text{ AlMe}_3$ , freeze-quenched at 1 s (red) and  $[\text{CrCl}_3(\text{decyl-S}_3)] + 20 \text{ AlMe}_3$  freeze-quenched at 5 min (blue).

The EXAFS analysis of the reaction  $[\text{CrCl}_3(\text{decyl-S}_3)]$  with 20 mol equivs. of  $\text{AlMe}_3$ , freeze-quenched at 1 s gives one Cr-C contribution at  $2.05(7)$  Å with one Cr-Cl at  $2.32(4)$  Å and  $2.7(9)$  Cr-S at  $2.46(3)$  Å. After 5 min an ‘end state’ product is observed, where a similar 4 coordinate complex to that of the decyl-SNS analogue is seen, i.e. the ligand is retained, with  $3.7(8)$  Cr-S at  $2.47$  Å, but now with one Cr-C at  $2.11(4)$  Å. (Scheme 6.6). The observed Cr-C length is similar to  $2.13$  Å given for the  $(\text{N}_2\text{P}_2)\text{CrMe}$  complex as discussed earlier, in line with a Cr(II) carbon bond.<sup>[15]</sup>

The intermediate state at 1 s is a five coordinate, partially alkylated complex where the oxidation state is thought to be Cr(II) based on the edge shift. In this case the distances are set as variables and give values similar to that of the starting material. This then further reacts to yield a four coordinate complex where one chloride has been further abstracted. The coordination of Cr-S is slightly high at 3.7 but within the error value to allow the supposed 3 S coordination. It is unlikely this signifies four coordinate from residual chloride as this would be a significant distance increase for Cr-Cl from the starting material and from an overlay of the Fourier Transform EXAFS of raw data, of the reaction at 1s and 5 min, the product at 5 min has significantly decreased in amplitude (Fig. 6.12). This would also explain the higher Debye-Waller factor given for this product, implying the given coordination is

slightly high. This value is most likely increased due to noisy data. The product at 5 min has the same edge value as the intermediate at 1s, suggesting both are the same oxidation state where, most likely, the final product forms a cation when the chloride is abstracted (Scheme 6.6; Fig. 6.13). XANES analysis was in agreement with the direction of the observed edge shift, as discussed for the SNS analogue.



**Scheme 6.6** Reaction scheme of  $[\text{CrCl}_3(\text{decyl-S}_3)] + 20 \text{ AlMe}_3$  as proposed by freeze-quench Cr K-edge EXAFS spectroscopy.

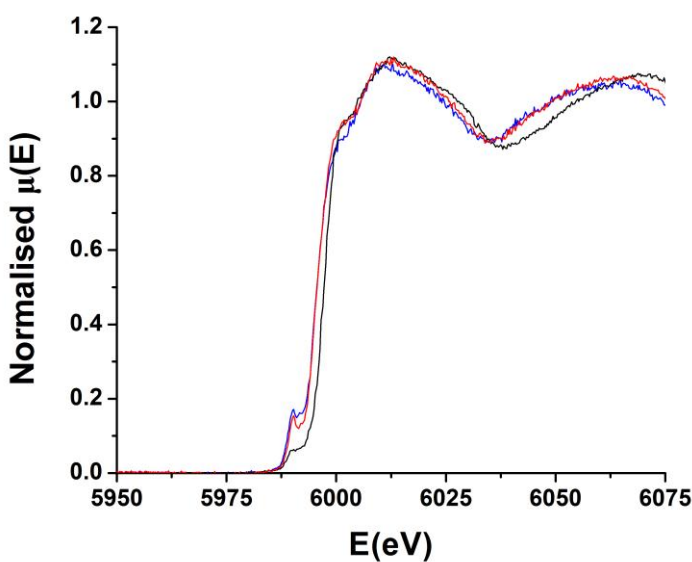


**Fig. 6.13** Displaying XANES region for solution  $[\text{CrCl}_3(\text{decyl-S}_3)]$  in toluene (black),  $[\text{CrCl}_3(\text{decyl-SNS})] + 20 \text{ AlMe}_3$  at 1s (red) and  $[\text{CrCl}_3(\text{decyl-S}_3)] + 20 \text{ AlMe}_3$  at 5 min (blue).

### 6.3.2.4 [CrCl<sub>3</sub>(PNP)(THF)] + 20 AlMe<sub>3</sub>

The [CrCl<sub>3</sub>(PNP)(THF)] complex was reacted with 20 mol equivs. of AlMe<sub>3</sub> and freeze-quenched at 1 min and 5 min. These were then analysed by Cr K-edge EXAFS spectroscopy. The analyses at both these time frames are presented in Table 6.5 and Fourier Transform EXAFS data shown in Fig. 6.14.

**Table 6.5** Cr K-edge EXAFS data analyses for the reaction of [CrCl<sub>3</sub>(PNP)(THF)] with 20 equivs. AlMe<sub>3</sub> in toluene, freeze-quenched after 1 min and 5min.

CN Absorber - Scatterer <sup>a</sup>	R /(\AA)	2σ <sup>2</sup> /(Å <sup>-2</sup> )	Fitting Factors
<i>[CrCl<sub>3</sub>(PNP)(THF)] + 20 AlMe<sub>3</sub> - RT = 1 min</i>			
2 Cr-C/O	2.04(5)	0.002(4)	2.1 < k < 12, 1.1 < R < 2.6
2 Cr-P	2.54(6)	0.006(7)	E <sub>0</sub> = 3(3), R = 0.004
2 Cr-Cl	2.38(2)	0.000(2)	k <sub>w</sub> = 2,3
<i>[CrCl<sub>3</sub>(PNP)(THF)] + 20 AlMe<sub>3</sub> - RT = 5 min</i>			
1 Cr-C	2.06(4)	0.003(3)	2.4 < k < 14, 1.1 < R < 3
2 Cr-P	2.46(5)	0.009(3)	E <sub>0</sub> = -1(2), R = 0.003
2 Cr-Cl	2.39(1)	0.002(1)	k <sub>w</sub> = 2,3

<sup>a</sup>Fixed parameters. Amp = 0.85.

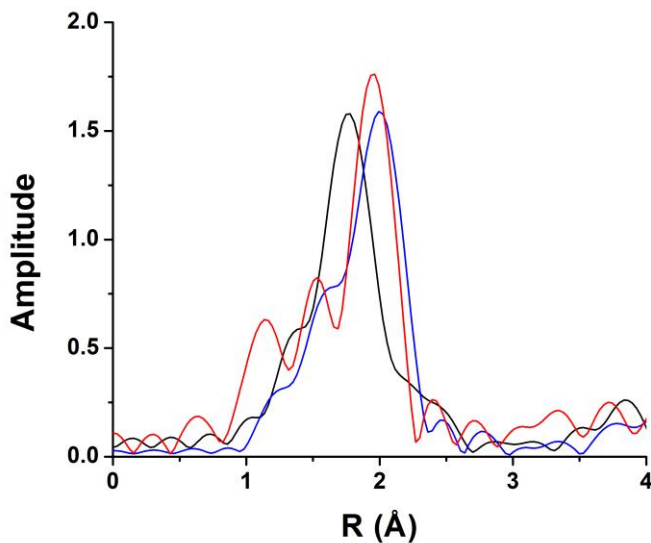


**Fig. 6.14** Cr K-edge  $k^2$ -weighted Fourier transform EXAFS data for solid  $[\text{CrCl}_3(\text{PNP})(\text{THF})]$  in BN (black),  $[\text{CrCl}_3(\text{PNP})(\text{THF})] + 20 \text{ AlMe}_3$ , freeze-quenched at 1 min (red) and  $[\text{CrCl}_3(\text{PNP})(\text{THF})] + 20 \text{ AlMe}_3$  freeze-quenched at 5 min (blue).

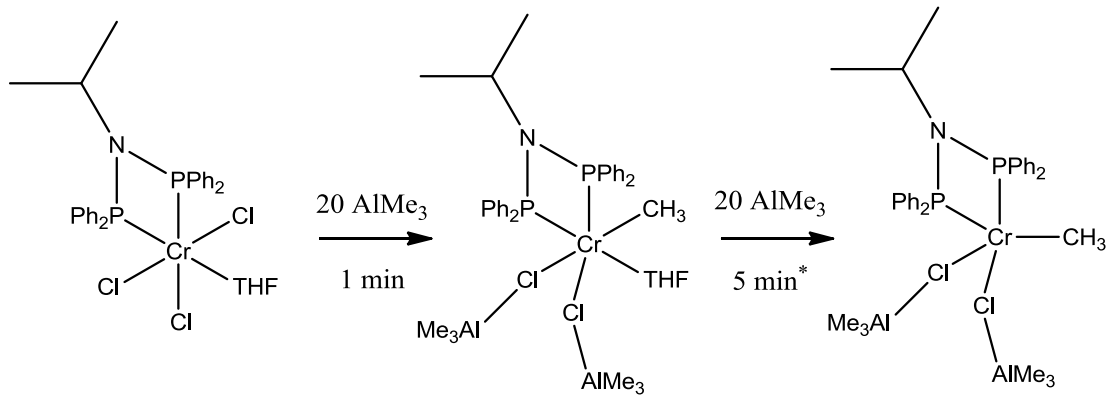
The EXAFS analysis of the reaction  $[\text{CrCl}_3(\text{PNP})(\text{THF})]$  with 20 mol equivs. of  $\text{AlMe}_3$  freeze-quenched at 1 min gives a six coordinate chromium complex. A two coordinate shell of Cr-O/C at  $2.04(5)$  Å indicates that the chromium has been alkylated and retained coordination of a solvent molecule of THF. The two-coordinate shell of Cr-Cl at  $2.38(2)$  Å is longer compared with the starting material. The third shell was determined as two coordinate P at  $2.54(6)$  Å and is longer than the starting material. As Cl and P are hard to distinguish by EXAFS analysis, they were assigned as such based on their X-ray crystallography data of  $[\text{CrCl}_3(\text{PNP})(\text{MeCN})]$  and  $[\text{CrCl}(\text{PNP})_2]$ . Also, XANES analysis indicates reduction of the Cr(III) to Cr(II), which could be the reason for the observed increase in bond lengths. This complex has been previously synthesised in 2007, using  $[\text{CrCl}_2(\text{Me})(\text{THF})_3]$  and PNP to give a  $[\text{CrCl}_2(\text{Me})(\text{THF})(\text{PNP})]$  complex.<sup>[11]</sup>

Analysis of the same reaction after 5 min gives a different EXAFS profile. The analysis of this reaction gave similar results with Cr-Cl and Cr-C/O shells at similar distances to that at 1 min except a coordination of only 1 Cr-C/O. The Cr-P shell also gives same coordination at a shorter distance of  $2.48(2)$  Å. This suggests loss of THF

coordination, leading to a five-coordinate complex. The Cr-P moves to a shorter distance after 5 mins, which is most likely because of steric reasons as the Cr complex becomes a five-coordinate species. A computational study has previously stated that initial alkylation of  $[\text{CrCl}_3(\text{PNP})]$  is a highly favourable process by  $\text{AlMe}_3$  and even suggested that complete alkylation would be expected in an excess of  $\text{AlMe}_3$ .<sup>[18]</sup>

Considering the increased length of Cr-Cl upon reaction with  $\text{AlMe}_3$ , this would suggest the formation of a chloro bridged aluminium bimetallic complex (Scheme 6.7). Similar bond lengths have been observed for a Cr-Cl-Al.<sup>[19]</sup> Such examples include  $[\text{Cr}(\text{SNS})(\mu\text{-Cl})\text{AlCl}_2\text{Et}]^{[3]}$  and  $[\text{Cr}(\text{SNS})(\mu\text{-Cl})\text{AlMe}_3]^{[19]}$  where the given distances for Cr(II)-Cl-Al are 2.397 and 2.372 Å respectively. These systems provide some indication as to why long Cr-Cl bonds are being observed.

XANES simulations on the below structures reproduced the experimental changes observed in edge position (Fig. 6.15). Upon single alkylation of the Cr(PNP) species, remaining a 6 coordinated species, no significant change in edge position is predicted. It is likely the change in oxidation state counteracts the loss of one chlorine, in the same coordination geometry. Upon dissociation of the solvent molecule to form a 5 coordinated complex, however, the downward shift in edge energy was reproduced as observed for the raw data (Fig. 6.15).



**Scheme 6.7** Reaction of  $[\text{CrCl}_3(\text{PNP})(\text{THF})]$  with 20  $\text{AlMe}_3$  as proposed by Cr K-edge EXAFS analysis (\*same product seen after 5 min reaction with 20  $\text{AlMe}_3$  as observed with addition of trityl aluminate and 20  $\text{AlMe}_3$  at 1 min).

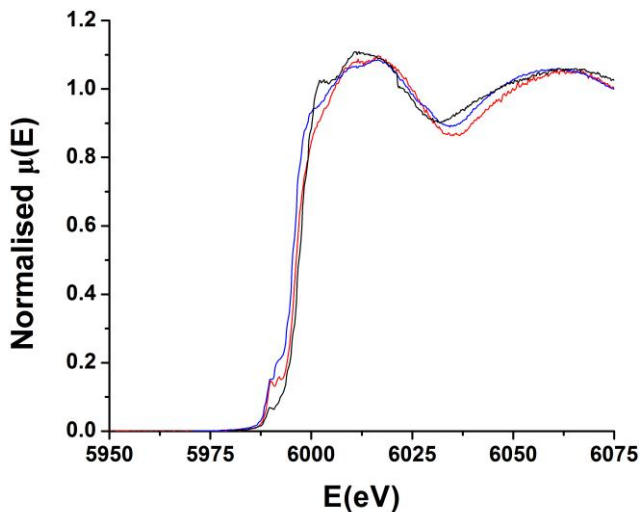


**Fig. 6.15** Displaying XANES region for solid  $[\text{CrCl}_3(\text{PNP})(\text{THF})]$  (black),  $[\text{CrCl}_3(\text{PNP})(\text{THF})] + 20 \text{ AlMe}_3$  at 1 min (red) and  $[\text{CrCl}_3(\text{PNP})(\text{THF})] + 20 \text{ AlMe}_3$  at 5 min (blue).

#### 6.4 Conclusion

This study has investigated the early activation steps of highly active and selective ethene oligomerisation chromium catalysts using  $\text{AlMe}_3$ . By freeze-quenching the reaction at 1 s, 1 min or 5 min it was possible to propose new reactive intermediate species being formed using fluorescence EXAFS spectroscopy. This technique gave evidence of  $[\text{CrCl}(\text{decyl-SNS})]$  formation very quickly at 1 s from the reaction of  $[\text{CrCl}_3(\text{decyl-SNS})]$  and  $\text{AlMe}_3$ . XANES calculations gave support to this product, suggesting reduction of the chromium to 2+, signifying no alkylation had taken place. EXAFS analysis of the reaction  $[\text{CrCl}_3(\text{decyl-SNS})]$  and  $\text{MeLi}$  indicated the complete substitution of Cl for Me, with some dissociation of the ligand to give a long Cr-S interaction.

Probing the similar complex  $[\text{CrCl}_3(\text{decyl-S}_3)]$  with  $\text{AlMe}_3$  which is initially active for the trimerisation of ethene, gave a similar four coordinate complex,  $[\text{CrMe}(\text{decyl-S}_3)]$  which was formed at a slower rate than that of  $[\text{CrCl}(\text{decyl-SNS})]$ , where at 1 s an intermediate five coordinate species was identified,  $[\text{CrClMe}(\text{decyl-S}_3)]$ . It may be possible that the reason this complex is alkylated where the SNS

analogue is not, is because of the absence of amine or amide interaction. As reaction of  $[\text{CrCl}_3(\text{decyl-SNS})]$  and  $\text{MeLi}$  indicated a longer Cr-S interaction after alkylation, it is possible the decyl- $S_3$  ligand dissociates from the complex after a few minutes during catalysis as the complex becomes alkylated, losing activity and selectivity for ethene trimerisation.

Finally, the reaction of the selective ethene tetramerisation catalyst  $[\text{CrCl}_3(\text{PNP})(\text{THF})]$  with  $\text{AlMe}_3$  was studied at 1 min and 5 min, to give a partially alkylated species with the retention of THF at 1 min,  $[\text{CrCl}_2\text{Me}(\text{PNP})(\text{THF})]$ , and without to form a five-coordinate species at 5 min,  $[\text{CrCl}_2\text{Me}(\text{PNP})]$ . Based on the given bond lengths, it is possible the chlorides bridge an aluminium species giving slightly longer Cr-Cl bonds.

The freeze-quenching EXAFS technique has demonstrated its power in identifying reactive intermediates that exist in solution. It has shown that this technique can probe at pre-determined reaction times down to 1 s, allows multiple scans to be collected to provide high quality data which in turn allows secure data analysis giving evidence for new catalytic species in their natural medium. This technique has given excellent insight into the early activation pathway of these highly active and selective ethene oligomerisation catalysts, providing strong evidence of coordination, ligand environment and oxidation state of the Cr. Fig. 6.16 is the raw and fit data for  $[\text{CrCl}_3(\text{PNP})(\text{THF})] + 20 \text{ AlMe}_3$  at 5 min. This demonstrates the quality of data that can be obtained using the newly developed freeze-quench methodology. This is the average of 20 scans at 1 spectrum every 20 mins. As the sample remains frozen, it is now possible to probe one species for multiple scans giving very low signal-to-noise data.

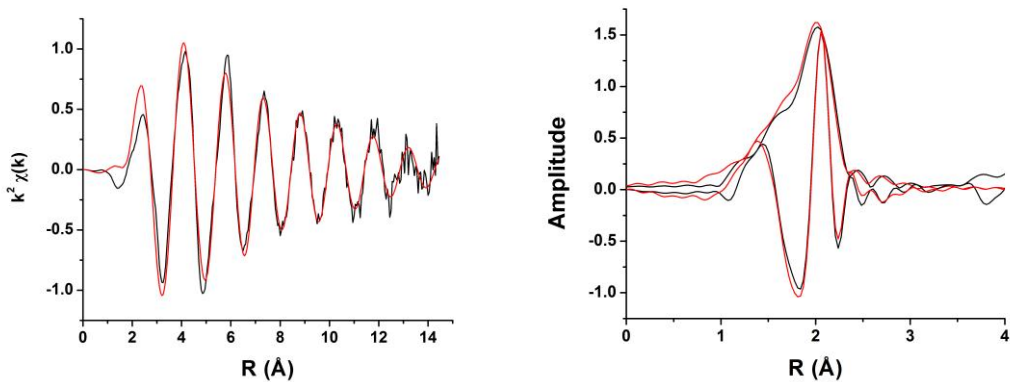


**Fig 6.16** Cr K-edge  $k^2$ -weighted EXAFS and Fourier transform data (black) and fits (red) for  $[\text{CrCl}_3(\text{PNP})(\text{THF})] + 20 \text{ AlMe}_3$  freeze-quenched at 5 min (blue).

## 6.5 Experimental

All complexes were synthesised under inert conditions using standard Schlenk line techniques, using dry solvents, having previously been distilled from appropriate drying agents. Complexes  $[\text{CrCl}_3(\text{THF})_3]$ ,<sup>[20]</sup>  $[\text{CrCl}_3(\text{decyl-SNS})]$ ,<sup>[9]</sup>  $[\text{CrCl}_3(\text{decyl-S}_3)]$ ,<sup>[7]</sup>  $[\text{CrCl}_3(\text{PNP})(\text{THF})]$ ,<sup>[10]</sup> and ligands  ${}^i\text{PrN}(\text{PPh}_2)_2$  (PNP),<sup>[10a]</sup>  $\text{HN}(\text{CH}_2\text{CH}_2\text{SC}_{10}\text{H}_{21})_2$  (decyl-SNS)<sup>[9]</sup> and  $\text{S}(\text{CH}_2\text{CH}_2\text{SC}_{10}\text{H}_{21})_2$  (decyl-S<sub>3</sub>)<sup>[7]</sup> were synthesised in accordance with previously published procedures. All metal complexes were stored under inert atmosphere in a glove box. MeLi (1.6 M in Et<sub>2</sub>O) and AlMe<sub>3</sub> (2.0 M in hexanes) were purchased from Aldrich and titrated using the published procedures.<sup>[21]</sup> All solvents used in the stopped-flow instrument were purchased (anhydrous) from Aldrich and used as received.

<sup>1</sup>H and <sup>13</sup>C{<sup>1</sup>H} NMR spectra were recorded on a Bruker AV300 spectrometer. Microanalyses were obtained through Medac Ltd., Egham UK. Infrared spectra were recorded as a Nujol mull between CsI plates under inert conditions, using Perkin Elmer FT-IR Spectrum 100 Spectrometer across the range 4000 - 200 cm<sup>-1</sup>. UV-Vis spectra were recorded both using the stopped-flow instrument (Fibre optic J & M Analytic MCS-UVNIR) and using a Perkin Elmer Lambda 19 spectrometer either in solution in a 1 cm path length quartz cuvette, or as solids by

diffuse reflectance (DR). All spectroscopic samples were prepared freshly in a dry N<sub>2</sub>-purged glove-box.

The stopped freeze-quench system (as described in Chapter 3 and 4) was utilised for all samples freeze-quenched at 1 s. All samples freeze-quenched at 1 min and 5 min were collected using Schlenk line techniques under Ar, where the reaction mixture was injected into a fully purged Kapton® capillary under Ar and frozen using liquid N<sub>2</sub>.

### 6.5.1 XAFS Experimental

All samples for solid state Cr K-edge EXAFS analyses were mixed with dry boron nitride, pressed into pellets under inert atmosphere and encapsulated in Kapton® tape. All room temperature solution data collected for Cr K-edge EXAFS spectra were obtained from solutions made up to the stated concentrations with anhydrous toluene under inert conditions. The solution was then transferred to a dry, argon-purged and sealed solution XAFS cell<sup>[7]</sup> for analysis on the beamline. The room temperature reactions were performed in the solution XAFS cell by the addition of MeLi (using a syringe) directly into the solution XAFS cell. The solution was then analysed with Cr K-edge EXAFS spectroscopy after ca. 5 min of reaction.

All Cr K-edge XAFS measurements were performed at the B18 beamline<sup>[22]</sup> at Diamond Light Source in Didcot, England. A Si(111) double crystal was used in combination with an Ortec® Ge 9 element Solid State detector for fluorescence acquisition on all samples. Cr K-edge scans were obtained in 20 min. All spectra were calibrated using a Cr foil. XAS data processing and EXAFS analysis were performed using IFEFFIT<sup>[23]</sup> with the Horae package<sup>[24]</sup> (Athena and Artemis). The organometallic complexes were fitted using single crystal models or similar complexes, as indicated. The detailed fitting parameters are given in the results section.

## 6.6 References

- [1] a) P. W. N. M. van Leeuwen, N. D. Clement and M. J. L. Tschan, *Coord. Chem. Rev.* **2011**, 255, 1499-1517; b) D. S. McGuinness, *Chem. Rev.* **2011**, 111, 2321-2341; c) T. Agapie, *Coord. Chem. Rev.* **2011**, 255, 861-880; d) J. T. Dixon, M. J. Green, F. M. Hess and D. H. Morgan, *J. Organomet. Chem.* **2004**, 689, 3641-3668.
- [2] A. Jabri, C. Temple, P. Crewdson, S. Gambarotta, I. Korobkov and R. Duchateau, *J. Am. Chem. Soc.* **2006**, 128, 9238-9247.
- [3] C. Temple, A. Jabri, P. Crewdson, S. Gambarotta, I. Korobkov and R. Duchateau, *Angew. Chem. Int. Edit.* **2006**, 45, 7050-7053.
- [4] C. N. Temple, S. Gambarotta, I. Korobkov and R. Duchateau, *Organomet.* **2007**, 26, 4598-4603.
- [5] K. Albahily, Y. Shaikh, Z. Ahmed, I. Korobkov, S. Gambarotta and R. Duchateau, *Organomet.* **2011**, 30, 4159-4164.
- [6] D. S. McGuinness, D. B. Brown, R. P. Tooze, F. M. Hess, J. T. Dixon and A. M. Z. Slawin, *Organomet.* **2006**, 25, 3605-3610.
- [7] J. O. Moulin, J. Evans, D. S. McGuinness, G. Reid, A. J. Rucklidge, R. P. Tooze and M. Tromp, *Dalton Trans.* **2008**, 1177-1185.
- [8] A. Jabri, P. Crewdson, S. Gambarotta, I. Korobkov and R. Duchateau, *Organomet.* **2006**, 25, 715-718.
- [9] D. S. McGuinness, P. Wasserscheid, W. Keim, D. Morgan, J. T. Dixon, A. Bollmann, H. Maumela, F. Hess and U. Englert, *J. Am. Chem. Soc.* **2003**, 125, 5272-5273.
- [10] a) A. Bollmann, K. Blann, J. T. Dixon, F. M. Hess, E. Killian, H. Maumela, D. S. McGuinness, D. H. Morgan, A. Neveling, S. Otto, M. Overett, A. M. Z. Slawin, P. Wasserscheid and S. Kuhlmann, *J. Am. Chem. Soc.* **2004**, 126, 14712-14713; b) J. Moulin *X-Ray Absorption Spectroscopy for the Study of a Homogeneous Catalysis System based upon Chromium*, PhD University of Southampton, Southampton, **2006**.

- [11] D. S. McGuinness, M. Overett, R. P. Tooze, K. Blann, J. T. Dixon and A. M. Z. Slawin, *Organomet.* **2007**, *26*, 1108-1111.
- [12] G. J. Grant, K. E. Rogers, W. N. Setzer and D. G. VanDerveer, *Inorg. Chim. Acta* **1995**, *234*, 35-45.
- [13] Z. Weng, S. Teo and T. S. Andy Hor, *Dalton Trans.* **2007**, 3493-3498.
- [14] M. Tromp, J. Moulin, G. Reid, J. Evans, *AIP Conf. Proc.* **2007**, *882*, 699-701.
- [15] S. S. Rozenel, W. A. Chomitz and J. Arnold, *Organomet.* **2009**, *28*, 6243-6253.
- [16] H. Fan, D. Adhikari, A. A. Saleh, R. L. Clark, F. J. Zuno-Cruz, G. Sanchez Cabrera, J. C. Huffman, M. Pink, D. J. Mindiola and M.-H. Baik, *J. Am. Chem. Soc.* **2008**, *130*, 17351-17361.
- [17] S. F. A. Kettle, *Physical Inorganic Chemistry*, Spektrum Academic Publishers, Guildford, **1996**.
- [18] W. Janse van Rensburg, J.-A. van den Berg and P. J. Steynberg, *Organomet.* **2007**, *26*, 1000-1013.
- [19] K. Albahily, S. Gambarotta and R. Duchateau, *Organomet.* **2011**, *30*, 4655-4664.
- [20] W. Herwig and H. Zeiss, *J. Org. Chem.* **1958**, *23*, 1404-1404.
- [21] a) D. E. Jordan, *Anal. Chem.* **1968**, *40*, 2150-2153; b) H. Gilman and F. K. Cartledge, *J. Organomet. Chem.* **1964**, *2*, 447-454.
- [22] A. J. Dent, G. Cibin, S. Ramos, A. D. Smith, S. M. Scott, L. Varandas, M. R. Pearson, N. A. Krumpa, C. P. Jones and P. E. Robbins, *J. Phys. Conf. Ser.* **2009**, *190*, 012039.
- [23] M. Newville, *J. Synchrotron Radiat.* **2001**, *8*, 322-324.
- [24] B. Ravel and M. Newville, *J. Synchrotron Radiat.* **2005**, *12*, 537-541.



7.

## **Final Discussion and Conclusions.**

This research into the early activation steps within ethene oligomerisation catalysis utilised a stopped-flow instrument throughout many areas of the project, for which it has proven to be a robust and reliable piece of apparatus which, after some minor modifications to exclude air and moisture *via* a rigorous purging procedure and a constant gas tight flow of Ar, allowed the use of quite harsh and sensitive reagents (such as AlMe<sub>3</sub>). With the addition of a new freeze-quench attachment, this allowed reaction mixtures to be injected into a capillary at ~20 ms to be frozen (to liquid nitrogen temperatures) within 1 s under anaerobic conditions. This allows reactive, short-lived intermediate species to be trapped and enables multiple XAFS scans with long acquisition times of the same species, measured in fluorescence mode.

The stopped-flow apparatus was employed for time-resolved Mo K-edge EXAFS spectroscopy in order to probe the first stages of Mo analogues for the Sasol ethene trimerisation catalysts, which proved useful because of its hard X-ray edge allowing for good data collection especially for fast acquisition times. These experiments demonstrated the value of using a stopped-flow instrument within this technique and for such sensitive chemistry of homogeneous ethene oligomerisation catalysis.

These results indicated that these Mo analogues gave [Mo(CH<sub>3</sub>)<sub>3</sub>(L)] type complexes with reaction of AlMe<sub>3</sub>. No observation of Mo dimers under these conditions (1:20 Mo:Al) were observed but at higher levels of AlMe<sub>3</sub>, Mo precipitation was favourable, providing insights in the low overall catalytic activity and deactivation.

When investigating the Sc(III) analogues, these gave no selectivity to give only polyethylene. Interestingly, when complexed with the SNS ligand, an increase in activity was observed to give moderately active Sc ethene polymerisation catalysts in some cases.

Using <sup>45</sup>Sc NMR spectroscopy to study reactions with MeLi, the [ScCl<sub>3</sub>(R-SNS)] complex gave indications towards the importance of this active SNS type ligand. These studies gave strong evidence that the secondary amine could be deprotonated and prompt a change in the coordination of the Sc from six to five.

The EXAFS analyses of the same Sc complexes with AlMe<sub>3</sub> suggest they are not alkylated but rather ‘activated’, as the Sc-Cl bond forms a chloro bridged AlMe<sub>3</sub> species. This is strongly supported by <sup>45</sup>Sc NMR studies, helped by comparison with MeLi, which alkylates Sc. The ‘activation’ of Sc-Cl would allow for a simple chain

growth mechanism observed as given by ethene polymerisation catalysis. As Sc(III) is such a stable oxidation state, perhaps its reluctance to be reduced, along with the strength of Sc-Cl, does not allow a Sc metallocyclo to form, where only one chloride was abstracted in the presence of a Lewis acid and  $\alpha$ -olefin, to provide one coordination site, allowing chain growth for polyethylene.

An investigation into the early activation steps of the highly active and selective ethene oligomerisation Cr catalysts, by AlMe<sub>3</sub> was undertaken by freeze-quenching the reaction at 1 s, 1 min or 5 min. Fluorescence Cr K-edge XAFS spectroscopy supported the formation of [Cr<sup>II</sup>Cl(decyl-SNS)] very quickly at 1 s from [Cr<sup>III</sup>Cl<sub>3</sub>(decyl-SNS)] and AlMe<sub>3</sub>. XANES calculations gave support to this species, suggesting reduction to Cr(II), signifying no alkylation had taken place. At 5 min no observable changes from 1 s were observed. Based on the studies of the Sc(III) SNS reactions with MeLi, where the amine was likely deprotonated to give an amide, it is possible that this same process occurs for the reaction of [CrCl<sub>3</sub>(SNS)] + 20 AlMe<sub>3</sub>, which may facilitate coordination and oxidation state changes at Cr.

Reaction of the selective ethene tetramerisation catalyst [CrCl<sub>3</sub>(PNP)(THF)] with AlMe<sub>3</sub> was also studied at 1 min and 5 min, to give a partially alkylated species with the retention of THF at 1 min, [CrCl<sub>2</sub>Me(PNP)(THF)], and without to form a five-coordinate species at 5 min, [CrCl<sub>2</sub>Me(PNP)].

The much larger bite angle and different donor atoms of the SNS ligand compared to the relatively small bite angle of the PNP ligand, most likely plays a significant role in the product that is formed upon reaction with the aluminium co-catalyst. One previous study demonstrated that a small modification of the PNP ligand can cause a switch from tetramerisation to trimerisation.<sup>[1]</sup> Adding a methoxy substituent to the phenyl groups switched the Cr catalysis to give a high selectivity for trimerisation. It is likely the ligand changes from PNP coordination to the larger bite angle coordination *via* the methoxy substituent which then favours formation of 1-hexene.

A similar four coordinate product was observed from [CrCl<sub>3</sub>(decyl-S<sub>3</sub>)] + AlMe<sub>3</sub>, meaning the secondary amine on the ligand is not essential in forming the four coordinate [Cr(L<sub>3</sub>)Cl] species, but the SNS analogue was formed <1 s whereas the S<sub>3</sub> is formed > 1 s, which could have significant impact on the catalytic activity between the two complexes. Investigation of [CrCl<sub>3</sub>(decyl-SNS)] with MeLi showed how the Cr-S interaction lengthens significantly moving to ~ 3 Å. It is therefore possible that

the amine within the SNS ligand stops it dissociating fully, providing labile sulfur donors. Without this amine, as in the case for the  $[\text{CrCl}_3(\text{decyl-S}_3)]$  complex, the ligand would most likely dissociate throughout the catalysis. This provides a distinct possibility as to why the  $[\text{CrCl}_3(\text{decyl-SNS})]$  is highly active relative to the  $[\text{CrCl}_3(\text{decyl-S}_3)]$  complex, which was found to be active for only a few minutes.<sup>[2]</sup>

Previous investigations of  $[\text{CrCl}_3(\text{N}_3)]$  donors have been shown to give only a Shultz-Flory distribution of ethene oligomers. The research presented in this thesis suggests that because the  $\text{N}_3$  ligand does not provide a hemi-labile donor and restricts the geometry, especially for the  $[\text{CrCl}_3(\text{R}_3\text{-tacn})]$  complexes, this would not allow for the formation of the square planar type complex as observed in this study.<sup>[2]</sup>

### 7.3 References

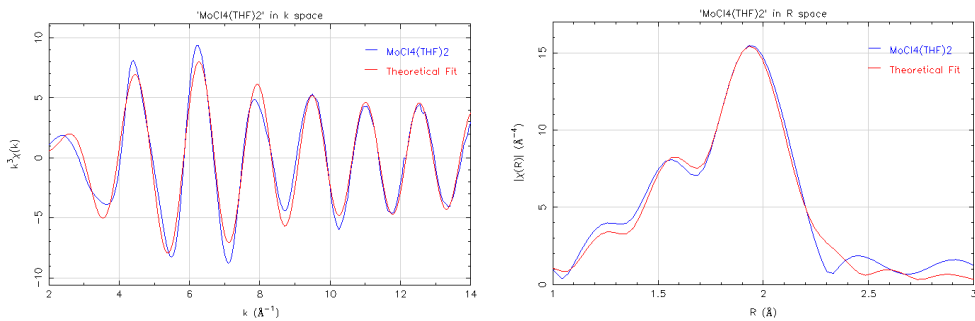
- [1] a) A. Carter, S. A. Cohen, N. A. Cooley, A. Murphy, J. Scutt and D. F. Wass, *Chem. Commun.* **2002**, 858-859; b) A. Bollmann, K. Blann, J. T. Dixon, F. M. Hess, E. Killian, H. Maumela, D. S. McGuinness, D. H. Morgan, A. Neveling, S. Otto, M. Overett, A. M. Z. Slawin, P. Wasserscheid and S. Kuhlmann, *J. Am. Chem. Soc.* **2004**, 126, 14712-14713.
- [2] J. O. Moulin, J. Evans, D. S. McGuinness, G. Reid, A. J. Ruckridge, R. P. Tooze and M. Tromp, *Dalton Trans.* **2008**, 1177-1185.



**8.**

**Supplementary.**

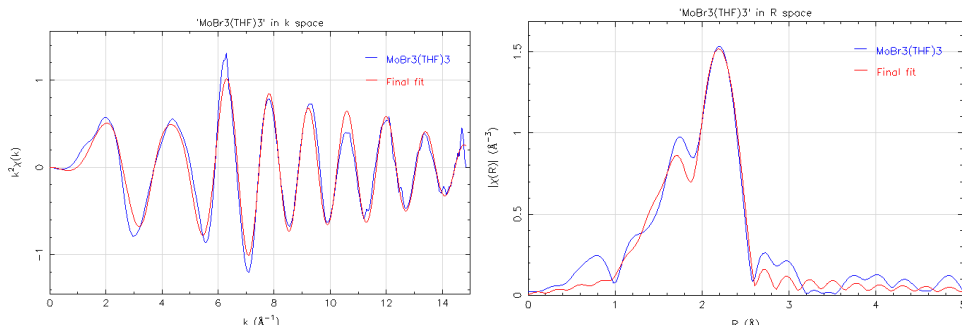
### 8.1 Chapter 4



CN Absorber - Scatterer <sup>a</sup>	R / (Å)	2σ <sup>2</sup> / (Å <sup>-2</sup> )	Fitting Factors
2 Mo-O	2.07(3)	0.004(3)	2 < k < 14, 1 < R < 2.5
4Mo-Cl	2.36(1)	0.003(1)	E <sub>0</sub> = 1(1) eV

R-factor = 0.02, k-weight = 2, 3.

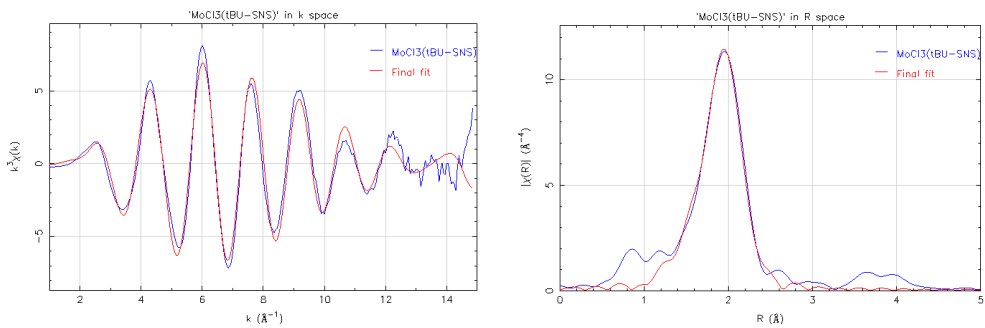
**Fig. S4.1** Mo K-edge  $k^2$ -weighted EXAFS and Fourier transform data (magnitude) (blue) and fits (red) for  $[\text{MoCl}_4(\text{THF})_2]$  in BN.<sup>[1]</sup>



CN Absorber - Scatterer <sup>a</sup>	R / (Å)	2σ <sup>2</sup> / (Å <sup>-2</sup> )	Fitting Factors
3 Mo-Br	2.58(1)	0.006(2)	3.7 < k < 14.4, 1.1 < R < 2.6
3 Mo-O	2.12(3)	0.004(3)	E <sub>0</sub> = 0(1) eV

R-factor = 0.02, k-weight = 1.

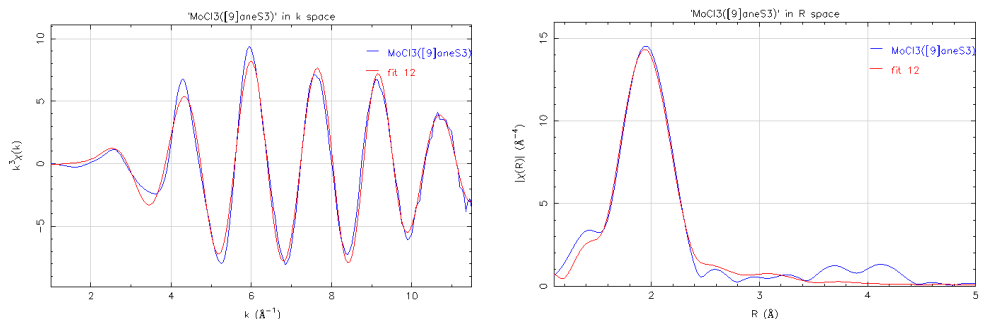
**Fig. S4.2** Mo K-edge  $k^2$ -weighted EXAFS and Fourier transform data (magnitude) (blue) and fits (red) for  $[\text{MoBr}_3(\text{THF})_3]$  in BN.<sup>[2]</sup>



CN Absorber - Scatterer <sup>a</sup>	$R /(\text{\AA})$	$2\sigma^2/(\text{\AA}^2)$	Fitting Factors
1 Mo-N	2.16(5)	0.009(2)	$2.8 < k < 14, 1 < R < 2.5$
2 Mo-S	2.51(2)	0.004(2)	$E_0 = 2(3) \text{ eV}$
3 Mo-Cl	2.45(2)	0.004(3)	

R-factor = 0.009, k-weight = 1, 3.

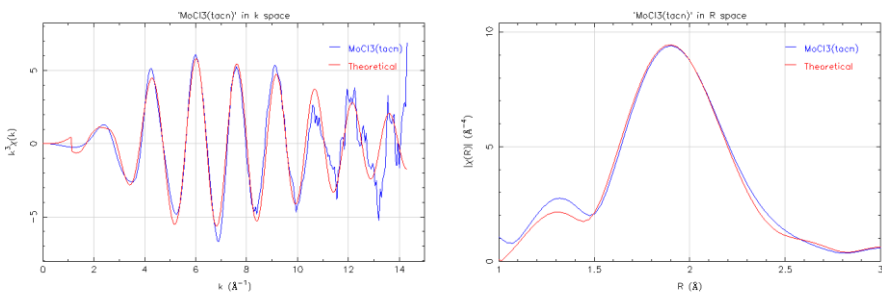
**Fig. S4.3** Mo K-edge  $k^2$ -weighted EXAFS and Fourier transform data (magnitude) (blue) and fits (red) for  $[\text{MoCl}_3(\text{tBu-SNS})]$  in BN.



CN Absorber - Scatterer <sup>a</sup>	$R /(\text{\AA})$	$2\sigma^2/(\text{\AA}^2)$	Fitting Factors
3 Mo-Cl	2.40(2)	0.002(2)	$1 < k < 11.5, 1.1 < R < 5$
3 Mo-S	2.41(1)	0.003(3)	$E_0 = 0.86(9) \text{ eV}$
3 Mo-C	3.29(5)	0.007(4)	

R-factor = 0.025, k-weight = 1, 3.

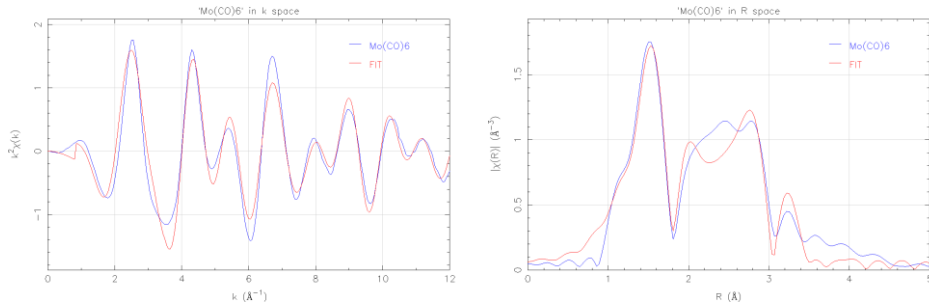
**Fig. S4.4** Mo K-edge  $k^2$ -weighted EXAFS and Fourier transform data (magnitude) (blue) and fits (red) for  $[\text{MoCl}_3([9]\text{aneS}_3)]$  in BN.



CN Absorber - Scatterer <sup>a</sup>	$R$ / $(\text{\AA})$	$2\sigma^2/(\text{\AA}^2)$	Fitting Factors
3 Mo-Cl	2.421(8)	0.003(1)	$2 < k < 10$ , $1.1 < R < 2.8$
3 Mo-N	2.33(4)	0.011(8)	$E_0 = 4(1)$ eV

R-factor = 0.006, k-weight = 1, 2, 3.

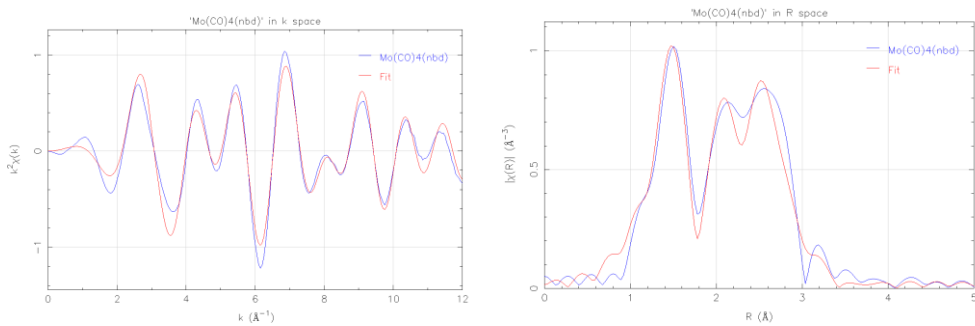
**Fig. S4.5** Mo K-edge  $k^2$ -weighted EXAFS and Fourier transform data (magnitude) (blue) and fits (red) for  $[\text{MoCl}_3(9\text{-aneN}_3)]$  in BN.



CN Absorber - Scatterer <sup>a</sup>	$R$ / $(\text{\AA})$	$2\sigma^2/(\text{\AA}^2)$	Fitting Factors
6 Mo-C	2.07(1)	0.002(2)	$2 < k < 11.8$ , $1 < R < 4.2$
36 Mo-O-C	3.24(1)	0.003(1)	$E_0 = 2.5(8)$ eV

R-factor = 0.06, k-weight = 1, 2.

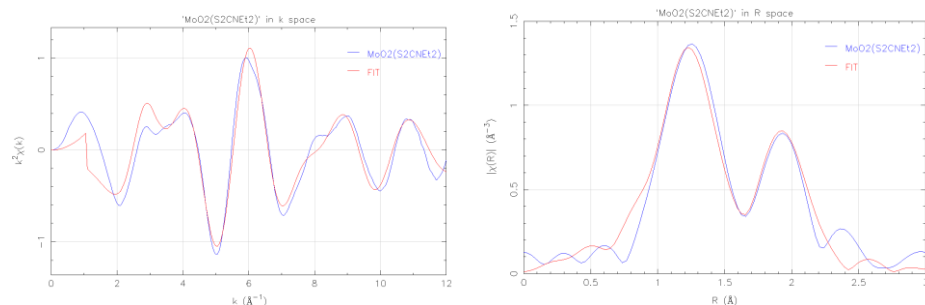
**Fig. S4.6** Mo K-edge  $k^2$ -weighted EXAFS and Fourier transform data (magnitude) (blue) and fits (red) for  $[\text{Mo}(\text{CO})_6]$  in BN.<sup>[3]</sup>



CN Absorber - Scatterer <sup>a</sup>	R /(Å)	2σ <sup>2</sup> /(Å <sup>-2</sup> )	Fitting Factors
4 Mo-C <sub>(CO)</sub>	2.00(1)	0.002(2)	2< k < 12, 1 < R < 4.5
4 Mo-C <sub>(nbd)</sub>	2.41(1)	0.000(2)	E <sub>0</sub> = -4(1) eV
16 Mo-O-C	3.16(1)	0.002(1)	

R-factor = 0.05, k-weight = 1, 2.

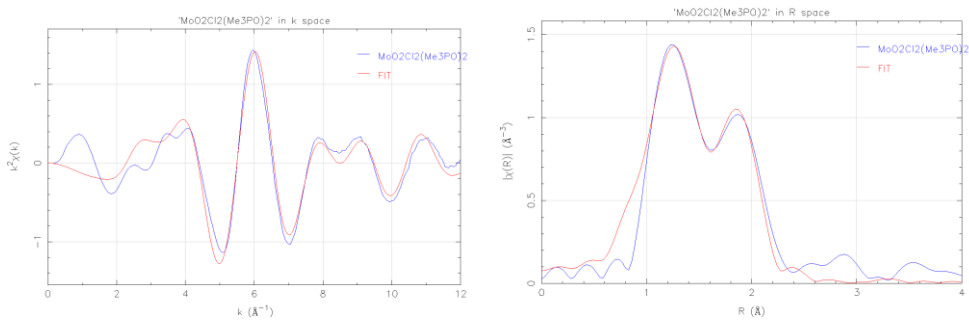
**Fig. S4.7** Mo K-edge  $k^2$ -weighted EXAFS and Fourier transform data (magnitude) (blue) and fits (red) for  $[\text{Mo}(\text{CO})_4(\text{norbornadiene})]$  in BN.<sup>[4]</sup>



CN Absorber - Scatterer <sup>a</sup>	R /(Å)	2σ <sup>2</sup> /(Å <sup>-2</sup> )	Fitting Factors
2 Mo-O	1.69(6)	0.001(2)	2 < k < 11.7, 1 < R < 2.3
4 Mo-S	2.47(3)	0.011(4)	E <sub>0</sub> = 4(4) eV

R-factor = 0.02, k-weight = 2, 3.

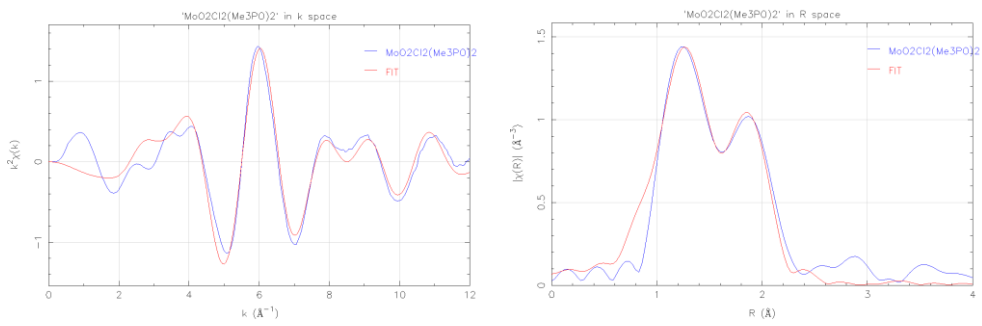
**Fig. S4.8** Mo K-edge  $k^2$ -weighted EXAFS and Fourier transform data (magnitude) (blue) and fits (red) for  $[\text{MoO}_2(\text{S}_2\text{N}\text{Et}_2)_2]$  in BN.<sup>[5]</sup>



CN Absorber - Scatterer <sup>a</sup>	R /(Å)	2σ <sup>2</sup> /(Å <sup>-2</sup> )	Fitting Factors
2 Mo=O	1.71(1)	0.003(2)	2< k < 12, 1 < R < 3.7
2 Mo-O	2.18(3)	0.002(5)	E <sub>0</sub> = -1(3) eV
2 Mo-Cl	2.44(2)	0.003(2)	

R-factor = 0.03, k-weight = 1, 2, 3.

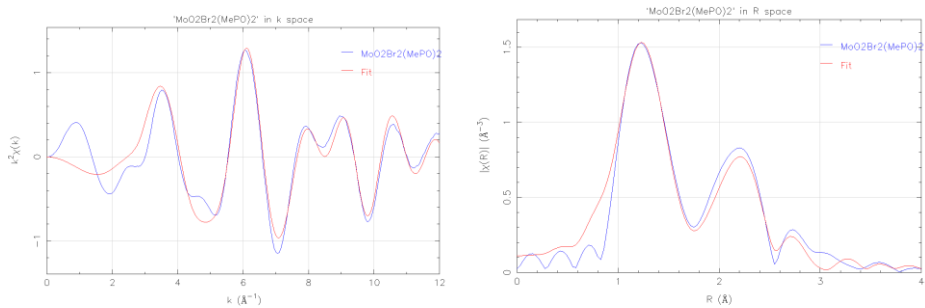
**Fig. S4.9** Mo K-edge  $k^2$ -weighted EXAFS and Fourier transform data (magnitude) (blue) and fits (red) for  $[\text{MoO}_2\text{Cl}_2(\text{Ph}_3\text{PO})_2]$  in BN.<sup>[6]</sup>



CN Absorber - Scatterer <sup>a</sup>	$R /(\text{\AA})$	$2\sigma^2/(\text{\AA}^{-2})$	Fitting Factors
2 Mo=O	1.69(2)	0.003(2)	$2 < k < 12$ , $1 < R < 3.2$
2 Mo-O	2.17(3)	0.002(5)	$E_0 = 0(4)$ eV
2 Mo-Cl	2.43(2)	0.003(3)	

R-factor = 0.02, k-weight = 1, 2, 3.

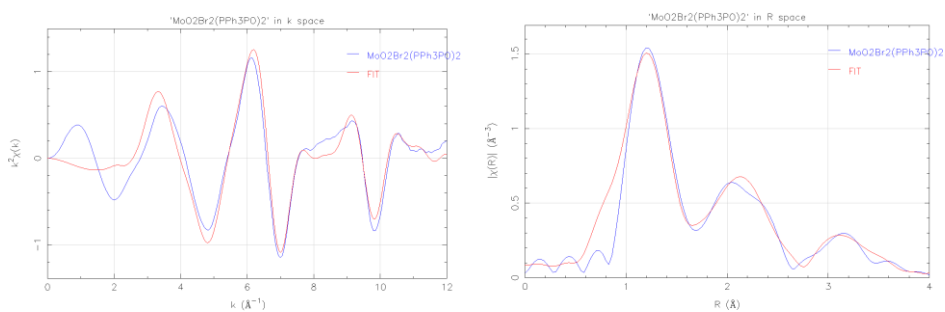
**Fig. S4.10** Mo K-edge  $k^2$ -weighted EXAFS and Fourier transform data (magnitude) (blue) and fits (red) for  $[\text{MoO}_2\text{Cl}_2(\text{Me}_3\text{PO})_2]$  in BN.<sup>[7]</sup>



CN Absorber - Scatterer <sup>a</sup>	R /(Å)	2σ <sup>2</sup> /(Å <sup>-2</sup> )	Fitting Factors
2 Mo=O	1.69(6)	0.003(2)	2< k < 12, 1 < R < 3.5
2 Mo-O	2.14(2)	0.003(5)	E <sub>0</sub> = -1(3) eV
2 Mo-Br	2.57(2)	0.003(1)	
2 Mo-P	3.46(5)	0.004(5)	

R-factor = 0.03, k-weight = 1, 2, 3.

**Fig. S4.11** Mo K-edge  $k^2$ -weighted EXAFS and Fourier transform data (magnitude) (blue) and fits (red) for  $[\text{MoO}_2\text{Br}_2(\text{Me}_3\text{PO})_2]$  in BN.<sup>[7]</sup>



CN Absorber - Scatterer <sup>a</sup>	R /(Å)	2σ <sup>2</sup> /(Å <sup>-2</sup> )	Fitting Factors
2 Mo=O	1.67(1)	0.003(2)	2< k < 12, 1 < R < 3.7
2 Mo-O	2.17(3)	0.008(5)	E <sub>0</sub> = -1(3) eV
2 Mo-Br	2.57(2)	0.006(2)	
2 Mo-P	3.74(3)	0.002(3)	

R-factor = 0.03, k-weight = 1, 2, 3.

**Fig. S4.11** Mo K-edge  $k^2$ -weighted EXAFS and Fourier transform data (magnitude) (blue) and fits (red) for  $[\text{MoO}_2\text{Br}_2(\text{Me}_3\text{PO})_2]$  in BN.<sup>[8]</sup>

## 8.2 Chapter 5

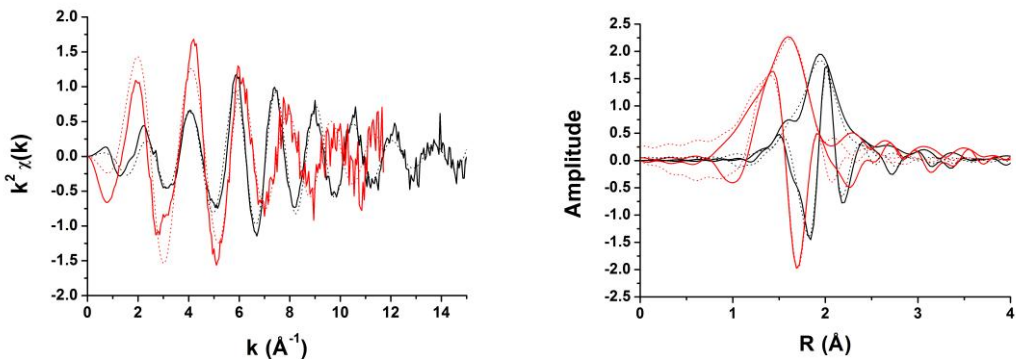


**Fig. S5.1** Sc K-edge  $k^2$ -weighted EXAFS and Fourier transform data (magnitude and imaginary part) (solid) and fits (dotted) of  $[\text{ScCl}_3(\text{Me}_3\text{-tacn})]$  solid (black) and with 3.5 mol. equivs. MeLi in THF (red).

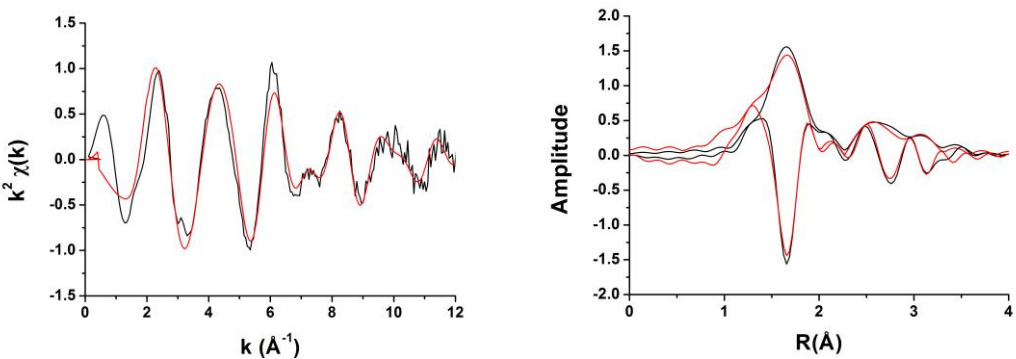


**Fig. S5.2** Sc K-edge  $k^2$ -weighted EXAFS and Fourier transform data (magnitude and imaginary part) (black) and fits (red) for  $[\text{ScCl}_3(\text{decyl-SNS})]$  with 3.5 mol. equivs. MeLi in THF.

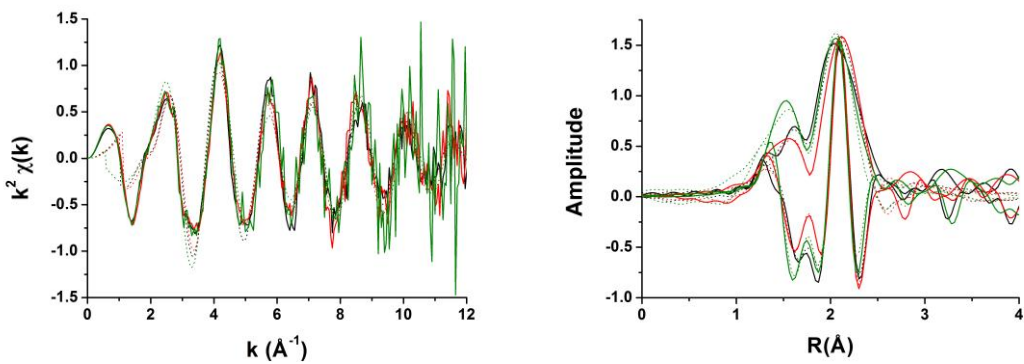


**Fig. S5.3** Sc K-edge  $k^2$ -weighted EXAFS and Fourier transform data (magnitude and imaginary part) (solid) and fits (dotted) for  $[\text{ScCl}_3(\text{decyl-SNS})]$  solution with 10 mol equiv.  $\text{AlMe}_3$  (black), with further addition of 1 mol equivs.  $[\text{Ph}_3\text{C}][\text{Al}\{\text{OC}(\text{CF}_3)_3\}_4]$  (red), with further addition of 100 mol equivs. 1-hexene (green).

**8.3 Chapter 6**

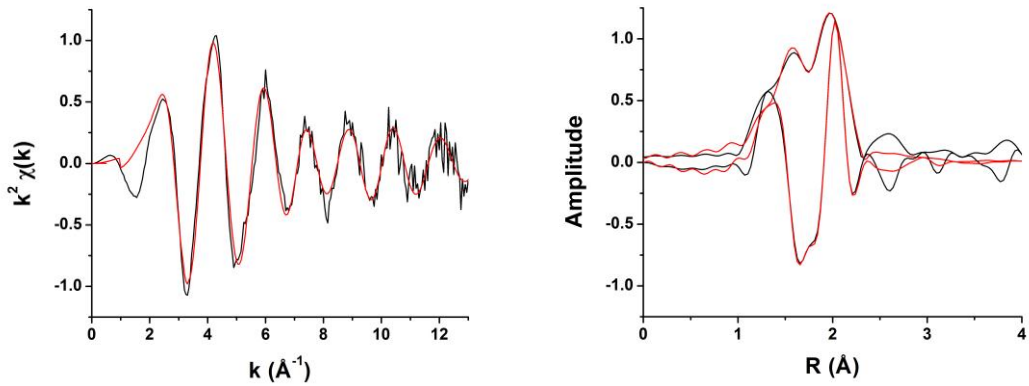


**Fig. S6.1** Cr K-edge  $k^2$ -weighted EXAFS and Fourier transform data (magnitude and imaginary part) (black) and fits (red) for  $[\text{CrCl}_3(\text{decyl-SNS})] + 20 \text{ AlMe}_3$  at 1 s in toluene.

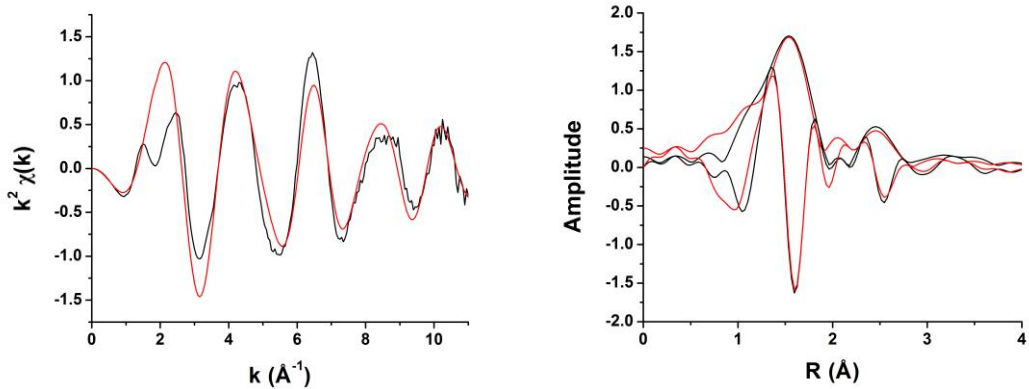


**Fig. S6.2** Cr K-edge  $k^2$ -weighted EXAFS and Fourier transform data (magnitude and imaginary part) (black) and fits (red) for  $[\text{CrCl}_3(\text{decyl-SNS})] + 4 \text{ MeLi}$  in toluene.

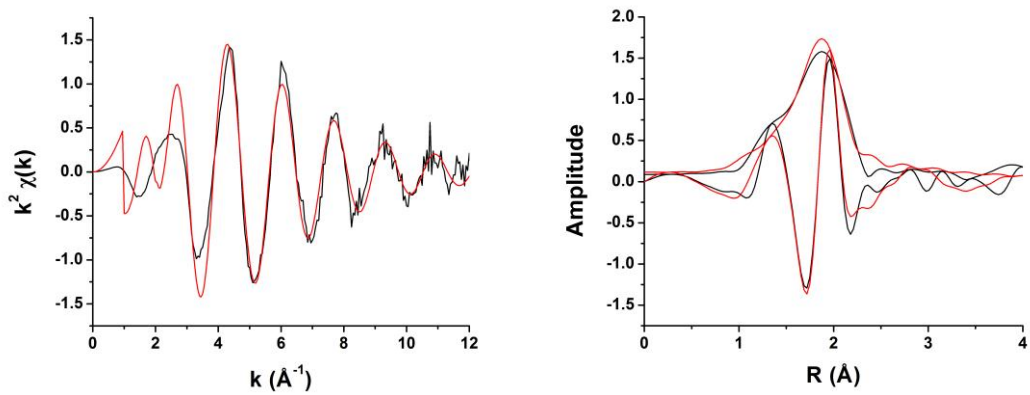


**Fig. S6.3** Cr K-edge  $k^2$ -weighted EXAFS and Fourier transform data (magnitude and imaginary part) (black) and fits (red) for  $[\text{CrCl}_3(\text{decyl-S}_3)]$  in toluene.

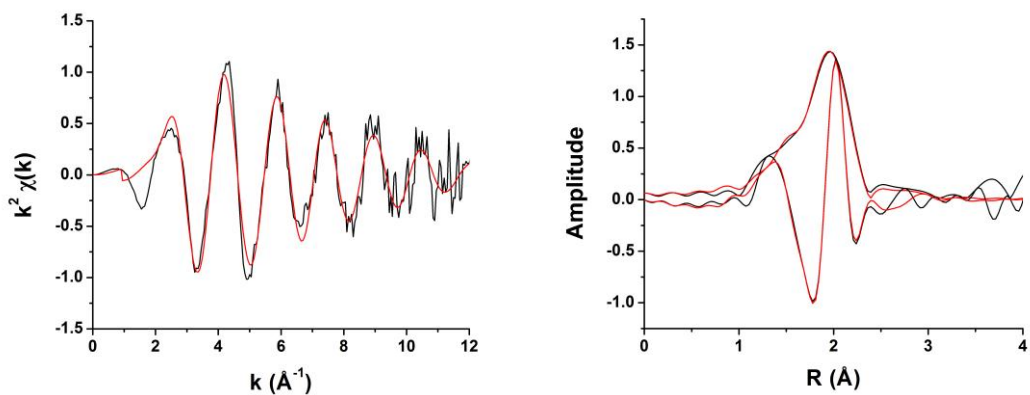


**Fig. S6.4** Cr K-edge  $k^2$ -weighted EXAFS and Fourier transform data (magnitude and imaginary part) (black) and fits (red) for  $[\text{CrCl}_3(\text{decyl-S}_3)] + 20 \text{ AlMe}_3$  at 1 s in toluene.

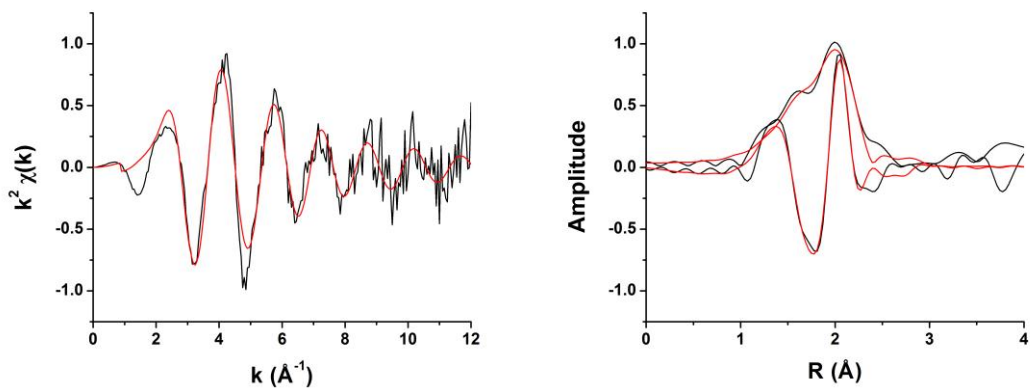


**Fig. S6.5** Cr K-edge  $k^2$ -weighted EXAFS and Fourier transform data (magnitude and imaginary part) (black) and fits (red) for  $[\text{CrCl}_3(\text{decyl-S}_3)] + 20 \text{ AlMe}_3$  at 1 s in toluene.

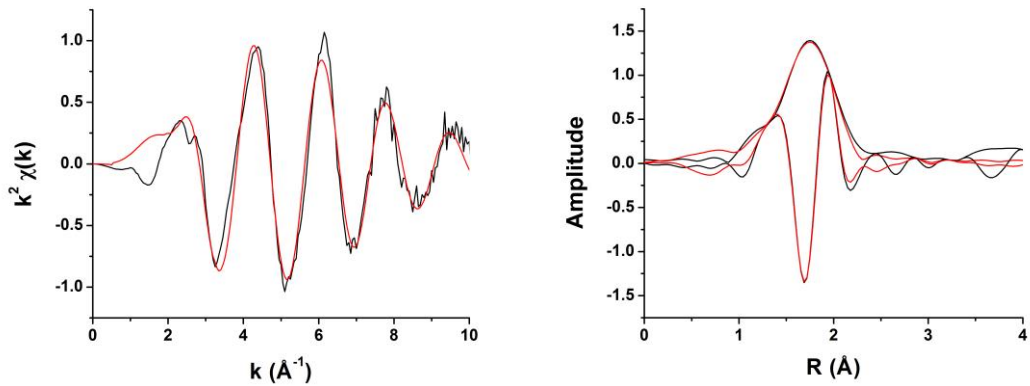


**Fig. S6.6** Cr K-edge  $k^2$ -weighted EXAFS and Fourier transform data (magnitude and imaginary part) (black) and fits (red) for  $[\text{CrCl}_3(\text{PNP})(\text{THF})]$  in BN.

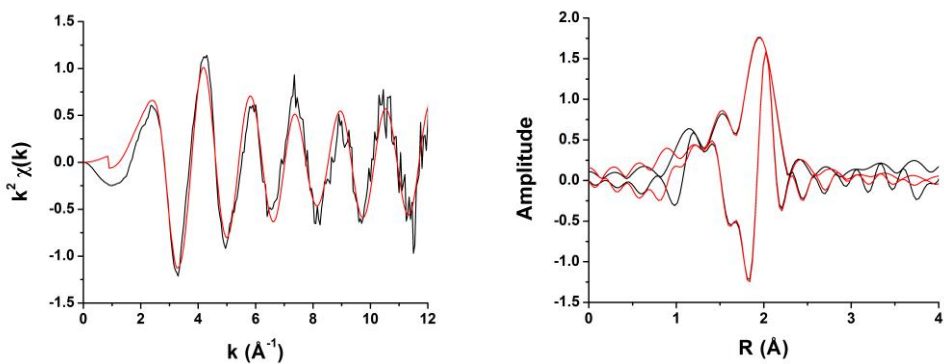


**Fig. S6.7** Cr K-edge  $k^2$ -weighted EXAFS and Fourier transform data (magnitude and imaginary part) (black) and fits (red) for  $[\text{CrCl}_3(\text{PNP})(\text{THF})] + 20 \text{ AlMe}_3$  at 1 min.

#### 8.4 References

- [1] A. Hills, G. J. Leigh, J. Hutchinson, J. A. Zubieta, *J. Chem. Soc. Dalton Trans.*, **1985**, 1069.
- [2] F. Calderazzo, C. Maichle-Mössmer, G. Pampaloni, J. Strähle, *Dalton Trans.*, **1993**, 655.
- [3] T. C. W. Mak, *Z. Kristallogr.*, **1984**, 166, 277.
- [4] L. Liu, *Bull. Inst. Chem. Acad. Sin.*, **1989**, 36, 45.
- [5] J. M. Berg, K. O. Hodgson, *Inorg. Chem.*, **1980**, 19, 2180.
- [6] F. R. Fronczek, R. L. Luck, G. Wang, *Inorg. Chem. Commun.*, **2002**, 5, 384.
- [7] M. B. Hursthouse, W. Levason, R. Ratnani, G. Reid, *Polyhedron*, **2004**, 23, 1915.
- [8] R. J. Butcher, B. R. Penfold, E. Sinn, *Dalton Trans.*, **1979**, 668.



**END**